

Cosmic Structures

– Theory, Statistics, Numerics

Prof. Oliver Hahn
Institute for Astrophysics
Institute for Mathematics
University of Vienna
oliver.hahn@univie.ac.at

This document was generated on June 25, 2024

Copyright ©2024 Oliver Hahn
Do not redistribute outside of class without permission.

Contents

1 The homogeneous Universe	7
The cosmological principle	7
Philosophical considerations	7
Observational evidence	8
The cosmic microwave background (CMB)	8
Galaxies as probes of the evolved Universe on the largest scales	10
Spatial structure – A primer in differential geometry	11
Manifolds	11
Geodesics	16
Curvature	17
Space-time	21
Einstein’s general relativity	23
Friedmann equations and the energy content of the Universe	24
Maximally symmetric space-times	24
Evolution of $a(t)$ from Einstein’s equations	26
The current expansion rate	27
Cosmological density parameters	28
Cosmic geodesy – measuring distances	29
Equations of state, co-dimension	31
Horizons	34
Newtonian cosmology	36
2 The inhomogeneous universe	39
Random fields	39
Fourier space: conventions and basic properties	39
Definitions and key properties	40
Convolution products and the inverse Fourier transform	41
Correlations and their Fourier transform	44
Random field statistics	45
Basic statistical concepts	45
Gaussian random variables	47
Random fields and their distributional properties	48
Gaussian random fields	48
Homogeneous and isotropic GRFs	49
Higher-order statistics	50
GRFs in Fourier space	50
Generating a Gaussian random field	51
Generating uncorrelated Gaussian random numbers	52
The Discrete Fourier Transform (DFT): basics	54
Python implementation of Gaussian random field generation	55

One-point statistics and coarse-grained fields	58
One-point covariance	58
Coarse-grained fields	59
One-point statistics of derivatives of random fields	61
The eigenvalue distributions of Hessians of Gaussian fields	63
Joint distributions of GRFs and its derivatives	63
The coordinate invariant probability measure	64
Eigenvalue distributions	65
Statistics of critical points of GRFs	67
Excursion sets, geometric and topological properties of GRFs	70
Higher-order correlators	75
Moments and cumulants	75
Cumulant expansion	75
3 Dynamical Equations	79
Vlasov–Poisson equations	79
Vlasov–Poisson and phase-space distributions in physical coordinates	79
Marginal/kinetic moments and the Vlasov hierarchy	83
The Vlasov–Poisson equations in comoving coordinates	85
Continuity equations	86
Fluid equations	87
Fluid in physical coordinates	87
Fluid in comoving coordinates	88
Linear analysis of fluid equations	89
Finite temperatures: the Jeans scale	90
Cold solutions	90
Zel'dovich approximation from early-time asymptotics	92
Early-time asymptotic behaviour	92
The Zel'dovich map	93
Non-gaussianity and non-linear structure	97
Two-point correlation function in the ZA	97
Eulerian (standard) perturbation theory	99
Matter power spectrum at one loop	101
Numerical Evaluation of Loop Integrals	103
4 N-body simulations	107
Discretising the Universe	107
The (in-)finite numerical Universe	107
The N -body universe: discretising mass	109
Symplectic integration of Hamiltonian systems	115
Perturbation theory inspired integrators	117
N -body experiments in 1+1 dimensions	118
Solving Poisson's equation in 1D	118
Time integration, cosmological parameters and units	119
Plane Wave Initial Conditions	119
Hierarchical structure formation	121
Poisson solvers beyond 1D	124
Taming the infinite sum: Direct Ewald summation	124
Particle mesh methods	126
Two-dimensional N -body simulations – a comparison with LPT .	138
Non-uniform Fast Fourier transforms	140

Trees for hierarchical multipole expansions	141
Particle-Mesh-Ewald – the P ³ M and TreePM hybrid methods	150
The frontier: fast-multipole methods	151
Force softening	151
Discreteness errors in cosmological simulations	153
Initial conditions for cosmological <i>N</i> -body simulations	155
Beyond <i>N</i> -body: tessellation and metric methods	155
Metric methods	155
Tessellation methods	159
Analysis of <i>N</i> -body simulations	162
Measuring the density field	162
Measuring power spectra and correlation functions	164
Measuring the abundance of collapsed structures	166

Chapter 1

The homogeneous Universe

It is a remarkable achievement of modern physics to put the field of cosmology on a scientific footing. Questions about the origin of our Universe, its history and the development of structure from ‘nothing’ in our Universe became testable predictions. At the heart of this is the theory of General Relativity and a very bold simplification of the complexity of our Universe that enables the calculation of its dynamics: the cosmological principle. In this chapter we will state it, formulate it rigorously which means that we immediately have to make statistical statements about the Universe, and then we will discuss the dynamics that follows when combining this principle with the theory of General Relativity.

The cosmological principle

Definition 1.1 — Cosmology. Cosmology is the study of the large-scale properties of the Universe as a whole, i.e. in particular its structure and temporal evolution.

Philosophical considerations

Humankind has sought to identify its place in the cosmos since ancient times. Following Rudnicki (1993); Lahav and Suto (2004) , we can summarise the historically most important (western) cosmological principles as the following:

- *The ancient Greek cosmological principle* – Our Earth is the natural center of the Universe.
- *The Copernican cosmological principle* – The Universe as observed from any planet looks much the same.
- *The (modern) cosmological principle* – The Universe is approximatively homogeneous and isotropic when averaged over large volumes. The meaning is
 - *Homogeneity* – The Universe looks the same everywhere. There is no preferred location in the Universe. Mathematically: invariance with respect to translation.
 - *Isotropy* – The Universe looks the same in every direction. There is no preferred direction in the Universe. Mathematically: invariance w.r.t. rotations.

- *Averaging* – The Universe is not homogeneous and isotropic on scales smaller than 100 Mpc¹ (for example, the Earth is not homogeneous and isotropic). Therefore we have to think about a Universe with small scales averaged out, when talking about homogeneity and isotropy. This means that inhomogeneities and anisotropies must get smaller as we consider larger and larger scales in a well-defined limiting process.
- *The anthropic principle* – Human beings, as they are, can exist only in the Universe as it is. (Or weaker: given a multitude of Universes, conscious observers will only exist in Universes very similar to ours)

Historically, there has thus been a process of de-centralizing cosmology: from earth as the center of the Universe, to a Universe with neither a center nor a preferred direction as implied by homogeneity and isotropy. Note that isotropy at every point would automatically enforce homogeneity, however since humanity lives (so far) only at one designated point in space, the statement of homogeneity remains, to some degree, an assumption.

Furthermore, homogeneity and isotropy should be considered in a *statistical* and *scale-dependent* sense which is a weaker statement than enforcing homogeneity and isotropy for a single realisation. We will in detail explore what we mean by this in the following sections.

Most theoretical models assume the modern cosmological principle. For example, the principle is applied in Einstein's theory of General Relativity when assuming that we live, on average, in a [Friedmann–Lemaître–Robertson–Walker \(FLRW\) space-time](#) (see section 1). That space-time has the largest possible symmetry group, namely those of independent translations and rotations, and an important physical consequence of this symmetry group is the so-called Hubble law: It states that the observed physical velocity V of objects is proportional to the distance r between them, i.e., $V = H(t)r$, where $H(t)$ is in principle an arbitrary time-dependent function – the so-called Hubble parameter.

Observational evidence

The cosmic microwave background (CMB)

The standard model of cosmology includes the hypothesis that the Universe began with a hot big bang: At the initial stage, the whole Universe was very hot with a mean temperature of $\sim 10^{27}$ K (though this value is model dependent). After an inflationary period where all spatial separations and thus, the spatial volume V , inflated in an accelerated manner, the mean temperature of the Universe dropped significantly (essentially since the matter energy density is $\propto 1/V$). About 380,000 years later, at the time period of [recombination](#), the mean temperature of the whole Universe is just a shy 3000 K. This afterglow can also be detected nowadays e.g. with the Planck satellite, which measures the temperature of the incoming photons from this time period. What we observe are spatially varying temperature fluctuations of the order of 10^{-5} with respect to the mean temperature; see Fig. 1.1. These small temperature fluctuations are evidence that the matter in the Universe was almost perfectly but not exactly homogeneous at the time of recombination (photons have to climb out of [matter-made] potential

¹ $100 \text{ Mpc} \approx 3 \times 10^{21} \text{ km} \approx 3 \times 10^8 \text{ lightyears.}$

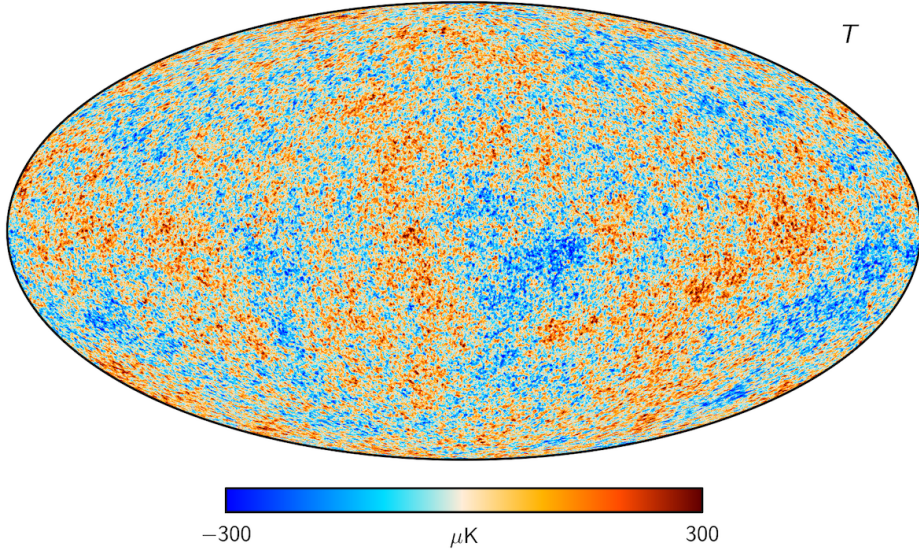


Figure 1.1: The early Universe: Full-sky Planck 2018 CMB temperature map (Planck Collaboration et al., 2020) in Mollweide projection. The map shows the local shift in the CMB photon energy due to the Sachs-Wolfe effect, where photons last scattering in denser regions lose energy (red) compared to those from underdense regions (blue). The shown fluctuations have a relative amplitude of only $\simeq 10^{-5}$. [Click for data source]

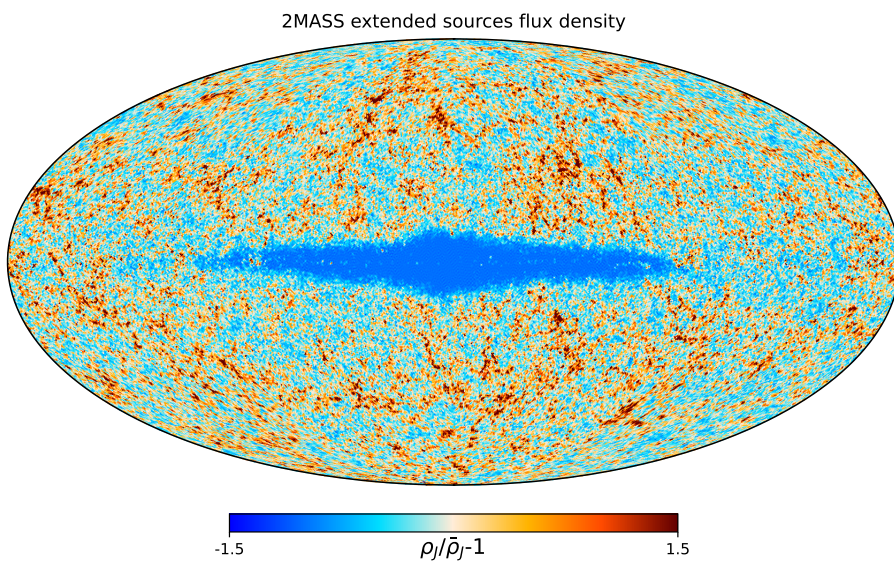


Figure 1.2: The late Universe: Full-sky J-band photon flux density of 1.4 million ‘extended sources’, i.e. galaxies, in the 2MASS (2 micron all-sky survey; Skrutskie et al., 2006) reflecting the distribution of galaxies in the nearby Universe. Unlike the CMB temperature map Figure 1.1, this map shows strong evidence for large fluctuations (of order 1) and gravity induced non-Gaussianity leading to the characteristic filamentary structures. The central region is covered by the Milky Way, but unlike for the CMB map, no ‘in-painting’ has been performed here to simulate the missing data. [Click for data source]

wells which make them lose momentum on their way to us). Still, pronounced cosmic structures did not exist at that time.

However, several billions year later, the Universe contains a rich web of cosmic structures, themselves comprised of clusters of galaxies (see Fig. 1.2). It is one of the main targets of cosmology to investigate precisely the origin and evolution of these cosmic structures.

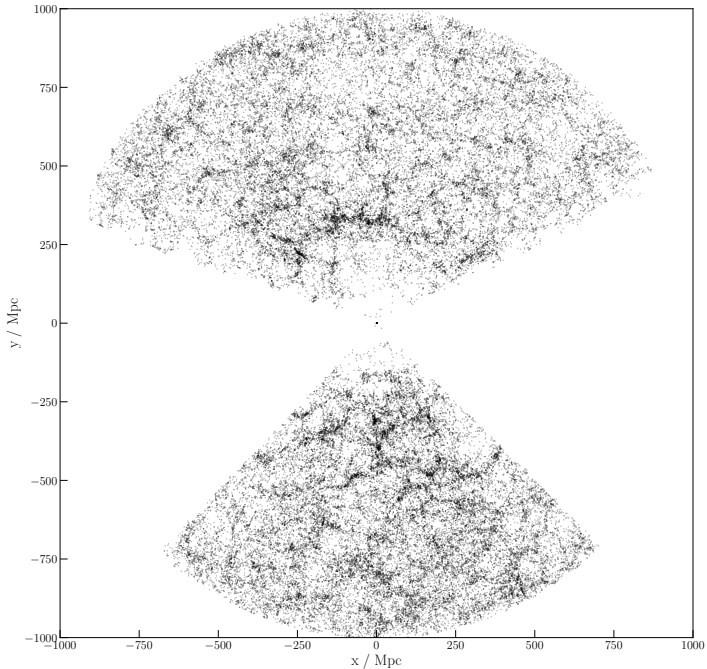


Figure 1.3: Our cosmic neighbourhood: The distribution of galaxies around the Milky Way (located at the origin) as observed by the Sloan digital sky survey (SDSS) of galaxies. Each dot corresponds to a galaxy. Shown are all galaxies detected by the SDSS within ± 15 degrees of the equatorial plane out to a co-moving distance of ≈ 1 Gpc (where $1\text{ pc} \approx 3.09 \times 10^{16}\text{ m}$), which corresponds to redshift $z \approx 0.25$ (see Eq. 1.66 for related definitions). Data courtesy the SDSS collaboration is available from <https://data.sdss.org/sas/dr12/boss/lss/>.

Galaxies as probes of the evolved Universe on the largest scales

The question whether many of the diffuse ‘Nebulae’, that are visible in the night sky with even a modest telescope, are part of the Milky Way or not, was settled already in the 19th century in favour of their interpretation as ‘Island Universes’ just like our own Milky Way. This became possible since some of the Nebulae could be resolved as systems of individual stars (‘star clusters’ that are part of the Milky Way) with increasingly better telescopes, while others remained diffuse and presented large internal velocities indicating that they are as massive as the Milky Way and much more distant than the star clusters. It then became quickly clear that these systems of (as we know today consisting of billions of stars) actually

probe the properties of our Universe. By measuring their recession velocities from the Milky Way, around 1930, the expansion of the Universe was first measured (see Figure 1.5). With increasingly better distance measurements and larger catalogues of galaxies the cosmic ‘large-scale’ environment began to be charted out. Already in the 1930s it became clear that large groups (‘clusters’) of such galaxies exist localised in space. By 1977, the CfA galaxy survey had collected 3D positions of 2200 galaxies, but the field really exploded in the last two decades. By 2002, the 2DF survey had mapped 220,000 galaxies; the SDSS survey by 2007 about one million, and the ongoing LSST survey and upcoming Euclid satellite will map billions of galaxies.

The distribution of some galaxies from the SDSS survey is shown in Figure 1.3, where each point represents a galaxy, and Earth along with the Milky Way is located at the very center. The missing portions correspond to regions that were not observed (e.g. in the plane of the Milky Way disk, which obscures observations, or not observable from the used telescope).

If we look at the distribution of galaxies in the nearby Universe, and assume that these galaxies trace to some degree the overall matter distribution, then it is obvious from Fig. 1.3 that the Universe around us is neither homogeneous nor isotropic, and thus seemingly in violation of the cosmological principle. One can see by eye that this distribution is not the result of a Poisson point process, but that points are spatially correlated.

How exactly the distribution of galaxies relates to the underlying matter distribution and to structure formation processes, is what we will study in this course. We will see that the observed distribution of galaxies is a result of the interplay of gravity, the expansion of the Universe, and the initial conditions set by the early Universe. The distribution of galaxies or other matter on such large scales is thus not only a probe of the large-scale structure of the Universe, but also of the fundamental physics of the Universe.

Spatial structure – A primer in differential geometry

Before we introduce the physical concept of a space-time, we shall first concern ourselves with the spatial structure of the Universe. Specifically, we will discuss the notions of manifolds, topology, and geometry.

Manifolds

As in daily experience, we assume a three-dimensional space for the Universe. However, it is not a simple three-dimensional Euclidean space, but rather a three-dimensional Riemannian manifold. This means that the Universe’s curvature can be non-zero and vary from point to point. The curvature is a measure of how much the geometry of the Universe deviates from that of a flat space. If we include the time-dimension, we will end up with a four-dimensional pseudo-Riemannian manifold as we will see. Ultimately, the curvature is determined by the distribution of matter and energy in the Universe over time, an aspect we will consider once we familiarised ourselves with some basic concepts.

Definition 1.2 — Manifold. A topological space \mathcal{M} is a d -manifold if it can be covered by open sets and where every point in M has a neighbourhood that is homeomorphic to Euclidean d -dimensional space. Therefore, locally, i.e. when

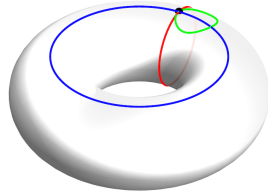
'zooming in', looks like flat Euclidean space.

We define the **spatial section** of the Universe as a 3-manifold. 'Spatial section' means that we are considering the Universe at a given time, i.e. we are ignoring the time dimension.

Topology

A general d -manifold allows for a multitude of possible spatial topologies. A key distinction is whether the manifold is simply connected or not.

Definition 1.3 — Simply connected. A topological space is called **simply connected** if it is path-connected and every loop in the space can be contracted to a single point. Otherwise it is called **multiply connected**.



A torus is not simply connected: Only the green loop is reducible to a point, the red and blue loops are not.

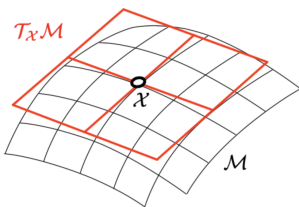
■ **Example 1.1 — Simply connected 3-manifolds.** Simply connected 3-manifolds are the 3-sphere S^3 , the 3-hyperboloid H^3 , and the 3-Euclidean space E^3 , but also $E \times H^2$ or $E \times S^2$, and a few more. In fact there are exactly 8 in total by a theorem of William Thurston.

An example for a multiply connected 3-manifold is the 3-torus $T^3 \equiv S^1 \times S^1 \times S^1$ which is the product of three circles. We can picture it as a cube with opposite faces identified, i.e. a cube with periodic boundary conditions. A loop around any of the circles (i.e. connecting opposite faces of the cube) cannot be contracted to a point without leaving the manifold. ■

Geometry

The geometry of a d -manifold \mathcal{M} is expressed by its curvature. The curvature is in turn determined by the metric. We will introduce these notions next. We will use the index notation for tensors, which is most commonly used in the physics literature. There exist also coordinate-free notations, which are more common in the mathematics literature.

Let us define a general d -dimensional coordinate system $x^i = (x^1, x^2, \dots, x^d)$ on \mathcal{M} . A coordinate line passing through a given point $P \in \mathcal{M}$ is a curve that is obtained by fixing $d - 1$ of the coordinates and letting the other one vary.



A manifold \mathcal{M} and the tangent vector space $T_X \mathcal{M}$ at a point X spanned by the vectors e_1 and e_2 .

Definition 1.4 — Coordinate basis and tangent space. The set $\{e_k\}$ of vectors $e_k \equiv \partial/\partial x^k$ (tangent to the coordinate lines at P) is called a **coordinate basis** (or natural frame) at P . The set $\{e^k\}$ of co-vectors $e^k \equiv dx^k$ is defined such that $e^i(e_j) = \delta^i_j$ and is called the **dual basis** at P . Co-vectors are also called 1-forms and the dual basis is also called the **co-frame** at P : it is a linear map from the tangent space to the real numbers. We say that the set of vectors $\{e_k\}$ spans the **tangent space** T_P at P , and the set of co-vectors $\{e^k\}$ spans the **co-tangent space** T_P^* at P .

Definition 1.5 — Einstein notation. We will from now on use Einstein notation, i.e. we will implicitly sum over repeated pairs of upper and lower index, i.e. $a^i b_i \equiv \sum_{i=1}^d a^i b_i$.

Definition 1.6 — Tensor. A **tensor** is a multi-linear map from a set of vectors and co-vectors to the real numbers. A tensor A of rank $\left\{ \begin{smallmatrix} p \\ q \end{smallmatrix} \right\}$ is a map that takes p

vectors and q co-vectors and returns a real number,

$$A : \underbrace{T_P^* \times \dots \times T_P^*}_{p \text{ times}} \times \underbrace{T_P \times \dots \times T_P}_{q \text{ times}} \rightarrow \mathbb{R}. \quad (1.1)$$

The space of tensors of fixed rank $\left\{ \begin{smallmatrix} p \\ q \end{smallmatrix} \right\}$ forms a vector space. The basis of this vector space is given by the tensor product of the basis of the tangent and co-tangent spaces, i.e. we have the coordinate representation

$$A = A^{i_1 \dots i_p}_{j_1 \dots j_q} e_{i_1} \otimes \dots \otimes e_{i_p} \otimes e^{j_1} \otimes \dots \otimes e^{j_q}. \quad (1.2)$$

Lemma 1.1 The components of a rank $\left\{ \begin{smallmatrix} p \\ q \end{smallmatrix} \right\}$ tensor A transform under a change of coordinates $x \mapsto \tilde{x}$ according to the rule

$$\tilde{A}^{i_1 \dots i_p}_{j_1 \dots j_q} = \frac{\partial \tilde{x}^{i_1}}{\partial x^{k_1}} \dots \frac{\partial \tilde{x}^{i_p}}{\partial x^{k_p}} \frac{\partial x^{l_1}}{\partial \tilde{x}^{j_1}} \dots \frac{\partial x^{l_q}}{\partial \tilde{x}^{j_q}} A^{k_1 \dots k_p}_{l_1 \dots l_q}, \quad (1.3)$$

i.e. with the Jacobians and inverse Jacobians of the coordinate transformation.

Proof. The components of the tensor are given by the action of the tensor on the basis vectors and co-vectors, i.e. $A^{i_1 \dots i_p}_{j_1 \dots j_q} = A(e_{i_1}, \dots, e_{i_p}, e^{j_1}, \dots, e^{j_q})$. Using the chain rule, the result (1.3) follows. ■

Definition 1.7 — Metric tensor. A point P' infinitesimally close to P is described by the displacement vector $dx = e_i dx^i$. We define the metric as a symmetric non-degenerate bi-linear map $g : T_P \times T_P \rightarrow \mathbb{R}$ that takes two vectors and returns a real number. Note that the metric is symmetric and non-degenerate, i.e. $g(v, w) = g(w, v)$ and $\det g \neq 0$. If it is positive definite, i.e. if $\det g > 0$ everywhere, the manifold (M, g) is called [Riemannian](#), if it is not, it is called [pseudo-Riemannian](#).

The [metric tensor](#) g – or (g_{ij}) in index notation – is then defined via the line element ds^2 which is given by the inner product of the displacement vector with itself, i.e.

$$ds^2 \equiv g(dx, dx) \equiv g_{ij} dx^i dx^j. \quad (1.4)$$

As a consequence of the definition, one immediately finds that

$$g_{ij} = e_i \cdot e_j \quad \text{and} \quad e_i = g_{ij} e^j. \quad (1.5)$$

The [inverse of the metric tensor](#) exists due to the condition that the metric is non-degenerate, i.e. $\det g \neq 0$. It is given by

$$g^{ik} g_{jk} = \delta_j^i \quad \text{and thus} \quad g^{ij} = e^i \cdot e^j \quad (1.6)$$

where δ_j^i is the Kronecker delta.

Definition 1.8 — Raising and lowering indices. The metric tensor and its inverse can be used to raise and lower indices, i.e. to transform a co-vector to a vector (i.e. they generate linear maps $T_p^* M \rightarrow T_p M$) and vice versa. In such cases, we denote the corresponding pair with the same symbol. For a co-vector A_i , the corresponding vector is given by $A^i \equiv g^{ij} A_j$, and for a vector B^i , the

corresponding co-vector is given by $B_i \equiv g_{ij}B^j$. The same applies to tensors of higher rank, e.g.

$$A^i_j \equiv g^{ik}A_{kj}, \quad A^j_i \equiv g_{ik}A^{kj}. \quad (1.7)$$

Definition 1.9 — Signature of the metric and normal coordinates. It follows from linear algebra that for any $p \in \mathcal{M}$ we can find *local* coordinates (x^1, \dots, x^d) so that the metric tensor can be written

$$g = \begin{pmatrix} -I_p & 0 \\ 0 & I_q \end{pmatrix}, \quad (1.8)$$

where I_p and I_q are the $p \times p$ and $q \times q$ identity matrices, and $p + q = d$. The number of positive and negative eigenvalues of the metric tensor is called the **signature** of the metric. Given a signature (p, q) , the manifold is called a **Lorentzian manifold** if $p = 1$ and $q = d - 1$, and a **Riemannian manifold** if $p = d$ and $q = 0$. The coordinates in which the metric tensor takes this form are called **normal coordinates**. Often this signature is also given in the form $(- \dots - + \dots +)$, where the number of + and - signs correspond to the number of positive and negative eigenvalues of the metric tensor.

■ **Example 1.2 — Curve length.** We can use the metric tensor to compute the length of a path between two points P and Q . Let $\gamma : [a, b] \rightarrow \mathcal{M}$ be a continuously differentiable curve with $\gamma(a) = P$ and $\gamma(b) = Q$, then its length is given from (1.4) by

$$L(\gamma) = \int_a^b \sqrt{g(\dot{\gamma}, \dot{\gamma})} d\lambda = \int_a^b \sqrt{g_{ij}\dot{\gamma}^i \dot{\gamma}^j} d\lambda, \quad (1.9)$$

where $\dot{\gamma}^i = d\gamma^i/d\lambda$ is the tangent vector to the curve, and λ is the parameter along the curve. The distance between P and Q for a Riemannian manifold is then defined as the infimum of all such lengths

$$\text{dist}(P, Q) = \inf_{\gamma} L(\gamma). \quad (1.10)$$

For a Lorentzian manifold, curve lengths might not be positive, and there is therefore no equivalently simple notion of distance, in particular, lengths defined by (1.9) might be complex numbers. We will come back to this problem later. ■

Exercise 1.1 Show that a Riemannian manifold (\mathcal{M}, g) equipped with distance (1.10) is a metric space, i.e. that the distance function satisfies the triangle inequality, is symmetric, and that $\text{dist}(P, Q) = 0$ if and only if $P = Q$. ■

Definition 1.10 — Christoffel symbols. Consider again a point P' infinitesimally close to P , described by the displacement vector $dx = e_i dx^i$. The natural frame $\{e'_k\}$ at P' is related to the natural frame $\{e_k\}$ at P by the transformation

$$e'_i = e_i + \Gamma_{ik}^j dx^k e_j, \quad (1.11)$$

where the Γ_{ik}^j are called the [Christoffel symbols](#)^a. They are given by

$$\Gamma_{ik}^j = \frac{1}{2} g^{jl} \left(\frac{\partial g_{il}}{\partial x^k} + \frac{\partial g_{kl}}{\partial x^i} - \frac{\partial g_{ik}}{\partial x^l} \right). \quad (1.12)$$

Christoffel symbols obey the symmetries

$$\Gamma_{ik}^j = \Gamma_{ki}^j, \quad \Gamma_{ik}^j = g^{jl} \Gamma_{ik}^m g_{ml}. \quad (1.13)$$

^aThe Christoffel symbols are not tensors, but they are the components of the connection, which is a tensor. The connection is a measure of how vectors change as one moves along a curve on the manifold.

Observation 1.1 The Christoffel symbols are not tensors, but they transform under a change of coordinates according to the rule

$$\tilde{\Gamma}_{ik}^j = \frac{\partial \tilde{x}^j}{\partial x^l} \frac{\partial x^m}{\partial \tilde{x}^i} \frac{\partial x^n}{\partial \tilde{x}^k} \Gamma_{mn}^l + \frac{\partial \tilde{x}^j}{\partial x^l} \frac{\partial^2 x^l}{\partial \tilde{x}^i \partial \tilde{x}^k}. \quad (1.14)$$

This implies that they are tensors only under a linear coordinate transformation. The result follows from the transformation rule of the metric tensor and the chain rule. We leave the details to the reader.

Definition 1.11 — Covariant derivative. The [covariant derivative](#) of a basis vector e_i along the basis vector e_j is defined by

$$\nabla_{e_j} e_i = \Gamma_{ij}^k e_k. \quad (1.15)$$

This definition yields the Levi-Civita connection, which is the unique connection that is compatible with the metric, i.e. that satisfies $\nabla_{e_j} g_{ik} = 0$.

It quantifies how the basis vectors change as one moves along a curve on the manifold. We will sometimes denote partial derivatives by a comma-separated index and a covariant derivative by a semicolon-separated index for brevity, i.e.

$$\partial_j v_i \equiv v_{i,j} \quad \text{and} \quad \nabla_{e_j} v \equiv v^i_{;j} e_i. \quad (1.16)$$

■ **Example 1.3 — Covariant derivative of a vector.** The covariant derivative of a vector u along a basis vector e_j is

$$\nabla_{e_j} u^i = \frac{\partial u^i}{\partial x^j} + \Gamma_{jk}^i u^k. \quad (1.17)$$

The result follows from the Leibniz rule and the definition of the covariant derivative:

$$\nabla_{e_j} u = \nabla_{e_j} (u^k e_k) \stackrel{\text{Leibniz}}{=} e_k \partial_{e_j} u^k + u^k \nabla_{e_j} e_k \stackrel{(1.15)}{=} \left(\frac{\partial u^i}{\partial x^j} + \Gamma_{jk}^i u^k \right) e_i. \quad \blacksquare$$

■ **Example 1.4 — Covariant derivative of a tensor.** The covariant derivative of a tensor A is obtained by applying repeatedly the Leibniz rule, i.e.

$$\nabla_{e_j} A^{i_1 \dots i_p}_{j_1 \dots j_q} = \partial_j A^{i_1 \dots i_p}_{j_1 \dots j_q} + \Gamma_{jk}^{i_1} A^{i_2 \dots i_p}_{j_1 \dots j_q} + \dots - \Gamma_{jj_1}^k A^{i_1 \dots i_p}_{k \dots j_q} - \dots \quad (1.18) \quad \blacksquare$$

■ **Example 1.5 — Metric compatibility.** It is easy to show that the covariant derivative of the metric tensor vanishes, i.e.

$$\nabla_{e_j} g_{ik} = 0 .$$

This is a consequence of the definition of the Christoffel symbols. The result is obtained by simply inserting definitions. We leave the explicit calculation as an exercise. ■

Geodesics

In Euclidean space it is trivial to translate a vector along a curve. This is not the case on a curved manifold, where the vector has to be parallel transported and will in general change direction.

Definition 1.12 — Parallel Transport. Given a curve $\gamma : [a, b] \rightarrow \mathcal{M}$ and a vector $v_0 \in T_{\gamma(a)} \mathcal{M}$, define the **parallel transport** of v along $\gamma(\lambda)$ as the unique solution $v(\lambda)$ to the differential equation

$$\nabla_{\dot{\gamma}} v = 0 , \quad (1.19a)$$

with the initial condition $v(a) = v_0$ and $\lambda \in [a, b]$. In coordinate notation, this is equivalent to (proof below)

$$\frac{dv^k}{d\lambda} + v^j \Gamma_{ij}^k \dot{\gamma}^i = 0 . \quad (1.19b)$$

In terms of local coordinates, the coordinates of the curve are $\gamma^i(\lambda) = x^i \circ \gamma(\lambda)$, and $v(t) = v^i(t) e_i$, so we have

$$\dot{\gamma}(\lambda) = \dot{\gamma}^i(\lambda) e_i \quad (1.20)$$

and along the curve

$$\nabla_{\dot{\gamma}} v = \nabla_{\dot{\gamma}^i e_i} (v^j(t) e_j) \stackrel{(1.17)}{=} \dot{\gamma}^i \left(\frac{\partial v^j}{\partial x^i} e_j + v^j \Gamma_{ij}^k e_k \right) = \frac{dv^k}{d\lambda} e_k + v^j \Gamma_{ij}^k \dot{\gamma}^i e_k ,$$

which holds for any k and thus yields the parallel transport equation (1.19b).

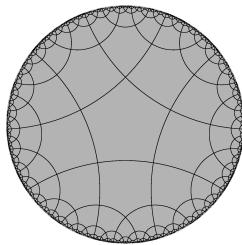
Theorem 1.1 Assume a Riemannian manifold \mathcal{M} . We call the line of shortest distance a **geodesic**. A curve $\gamma : [a, b] \rightarrow \mathcal{M}$ is a geodesic if and only if its tangent vector $\dot{\gamma}$ is parallel transported along the curve, i.e. if and only if it is autoparallel

$$\nabla_{\dot{\gamma}} \dot{\gamma} = 0 , \quad (1.21)$$

Since the coordinates of the curve are $\gamma^i = x^i \circ \gamma$, this can also be written in coordinate form as

$$\ddot{\gamma}^i + \Gamma_{jk}^i \dot{\gamma}^j \dot{\gamma}^k = 0 , \quad (1.22)$$

if the curve is arc-length parametrised, i.e. if the length of the curve is given by $\int_a^b \sqrt{g_{ij} \dot{\gamma}^i \dot{\gamma}^j} d\lambda = b - a$.



Straight lines on the hyperbolic Poincaré disc are ordinary circles in the embedding space, intersecting the boundary at right angles. The Poincaré disk can be tiled by regular pentagons.

Proof. The statements (1.21) and (1.22) are equivalent as follows from (1.19b) by setting $v^k = \dot{\gamma}^k$.

The shortest distance property follows as a sketch. We require that the length of the curve is stationary under variations of the curve, which is a variational problem. The functional (1.9)

$$L(\gamma) = \int_a^b \sqrt{g_{ij}\dot{\gamma}^i\dot{\gamma}^j} d\lambda =: \int_a^b \mathcal{L}(\gamma, \dot{\gamma}) d\lambda$$

is stationary if the integrand obeys the Euler-Lagrange equation

$$\frac{\partial \mathcal{L}}{\partial \gamma^i} - \frac{d}{d\lambda} \frac{\partial \mathcal{L}}{\partial \dot{\gamma}^i} = 0. \quad (1.23)$$

One finds

$$\frac{\partial \mathcal{L}}{\partial \gamma^i} = -\frac{1}{2\mathcal{L}}\gamma^j\gamma^k \frac{\partial g_{jk}}{\partial x^i} \quad \text{and} \quad \frac{\partial \mathcal{L}}{\partial \dot{\gamma}^i} = -\frac{1}{\mathcal{L}}g_{ij}\dot{\gamma}^j,$$

and from the second follows

$$\frac{d}{d\lambda} \frac{\partial \mathcal{L}}{\partial \dot{\gamma}^i} = \frac{d}{d\lambda} \left(-\frac{1}{\mathcal{L}}g_{ij}\dot{\gamma}^j \right) = -\frac{1}{\mathcal{L}} \left(\frac{\partial g_{ij}}{\partial x^k} \dot{\gamma}^j \dot{\gamma}^k + g_{ij}\ddot{\gamma}^j - g_{ij}\dot{\gamma}^j \frac{d \log \mathcal{L}}{d\lambda} \right).$$

Inserting these into the Euler-Lagrange equation and using that $\frac{\partial g_{ij}}{\partial x^k} \dot{\gamma}^j \dot{\gamma}^k = \frac{\partial g_{ik}}{\partial x^j} \dot{\gamma}^k \dot{\gamma}^j$, we find

$$\underbrace{\frac{1}{2}g^{li} \left(-\frac{\partial g_{jk}}{\partial x^i} + \frac{\partial g_{ij}}{\partial x^k} + \frac{\partial g_{ik}}{\partial x^j} \right) \dot{\gamma}^j \dot{\gamma}^k}_{\stackrel{(1.12)}{=} \Gamma_{jk}^l} + \ddot{\gamma}^l = g_{ij}\dot{\gamma}^j \frac{d \log \mathcal{L}}{d\lambda}$$

which is equivalent to (1.22) iff $\mathcal{L} = \text{const}$. Let this constant be C , then the length of the curve is given by $L(\gamma) = C(b-a)$, and the curve is a geodesic. If we set $C=1$, the curve is arc-length parametrised. ■

Curvature

In any metric space, one can define the following important quantities.

Definition 1.13 — Riemann curvature tensor. The **Riemann curvature tensor** R^i_{jkl} is defined by

$$R^i_{jkl} = \frac{\partial \Gamma^i_{jl}}{\partial x^k} + \Gamma^i_{mk}\Gamma^m_{jl} - \frac{\partial \Gamma^i_{jk}}{\partial x^l} - \Gamma^i_{ml}\Gamma^m_{jk}. \quad (1.24)$$

The components are not all independent, but satisfy the symmetries

$$R^i_{jkl} = -R^i_{jlk} = -R^i_{klj} = R^i_{ljk}. \quad (1.25)$$

The number of independent components is thus $\frac{1}{12}d^2(d^2-1)$, where d is the dimension of the manifold.

Note that we use in index-free notation R for Riemann curvature tensor, Ric for Ricci tensor, and R for the Ricci scalar, while we use R_{ijkl} for the components of the Riemann curvature tensor, R_{ij} for the Ricci tensor, and R for the Ricci scalar.

Definition 1.14 — Ricci tensor, Ricci scalar, and curvature scalar. Describing the curvature of the manifold in terms of the metric tensor, we define the [Ricci tensor](#) Ric with components R_{ij} and the scalar curvature R (also called the ‘[Ricci scalar](#)’) as the traces of the Riemann curvature tensor, i.e.

$$R_{ij} = R^k_{ikj}, \quad R = g(\text{Ric}) = g^{ij}R_{ij}. \quad (1.26)$$

The Ricci tensor is symmetric, i.e. $R_{ij} = R_{ji}$.

■ **Example 1.6** For two-dimensional surfaces ($d = 2$) the curvature tensor has only one independent component, say $R_{1212} =: \mu$. Then

$$R_{ij} = g_{ij} \frac{\mu}{\det(g)}, \quad R = 2 \frac{\mu}{\det(g)}. \quad (1.27)$$

Note that $R = -2K$, where K is the Gaussian curvature of the surface. While the value μ is coordinate dependent, K (and R) is an intrinsic property of the surface. ■

■ **Example 1.7** In three dimensions ($d = 3$), the curvature tensor has six independent components, which are however coordinate-dependent. Generically, a coordinate-independent characterisation of the curvature is formed by the Ricci principal curvatures, or [sectional curvatures](#), which are given by the roots $\{\kappa\}$ of the characteristic equation

$$\det(R_{ij} - \kappa g_{ij}) = 0. \quad (1.28)$$

For $d = 3$, these are given by

$$\kappa = \left\{ R, R_{ij}R^{ij}, \det(\text{Ric})/\det(g) \right\}. \quad (1.29)$$

These are only half of the independent components of the curvature tensor in three dimensions. ■

Exercise 1.2 Show that (1.29) are indeed the roots of the characteristic equation (1.28). ■

Lemma 1.2 — Local Taylor expansion of the line element. The [Riemann tensor](#) can be understood as quantifying the deviation from a flat geometry. In particular, a Taylor expansion of the line element ds in terms of [normal coordinates](#), defining the distance between a point P with coordinates x^i and a nearby point P' with coordinates $x^i + dx^i$, yields to second order

$$ds^2 \asymp \gamma_{ij} dx^i dx^j + \frac{1}{12} R_{ijkl} (x^i dx^j - x^j dx^i) (x^k dx^l - x^l dx^k), \quad (1.30)$$

where $(\gamma_{ij}) = \text{diag}(-1_p, 1_q)$ (see 1.9) is the flat metric in normal coordinates given the signature (p, q) . The Riemann tensor thus quantifies the deviation from the Euclidean geometry at second order in the displacement vector dx^i . Note that there is no first order term. The derivation of this result can be found e.g. in Berger (2007) (Section 4.4).

Definition 1.15 — Constant curvature. A manifold is said to have [constant curvature](#) if the sectional curvatures have all the same value $K = \text{const}$. In that case $R_{ij} = \kappa g_{ij}$ holds.

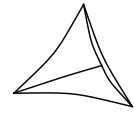
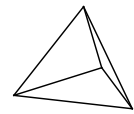
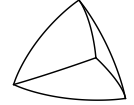
As an immediate consequence, in dimension $d = 3$, a manifold has constant

curvature iff the sectional curvatures (1.29) are all equal.

Theorem 1.2 — Constant curvature 3-geometries. A Riemannian manifold that is locally homogeneous and isotropic necessarily has constant curvature. The only geometries in $d = 3$ dimensions that permit constant curvature are the following

- the Euclidean space \mathbb{E}^3 if $\kappa = 0$
- the three-sphere \mathbb{S}^3 if $\kappa > 0$
- the hyperbolic three-space \mathbb{H}^3 if $\kappa < 0$.

Tetrahedra of constant curvature
(top to bottom: $\kappa > 0$, $\kappa = 0$,
 $\kappa < 0$)



Proof. This follows directly from a theorem of Thurston (1982), which classifies the homogeneous 3-manifolds into eight distinct types. The three above are the ones permitting constant curvature, the five others do not. We do not reproduce the proof here. It is intuitively clear that e.g. a topology $\mathbb{R} \times \mathbb{S}^2$ is not isotropic. ■

The spaces of constant curvature are the only ones compatible with global spatial isotropy and homogeneity. This is a key result for cosmology, as it implies that the spatial sections of the Universe are necessarily of constant curvature.

Definition 1.16 — Reduced circumference polar coordinates. A common choice of coordinates for constant curvature 3-geometries are the ‘reduced circumference polar coordinates’ $x = (r, \theta, \phi)$ where $r \in [0, \infty)$, $\theta \in [0, \pi]$, and $\phi \in [0, 2\pi]$. The line element is then given by

$$dx^2 = \frac{dr^2}{1 - \kappa r^2} + r^2 d\Omega^2, \quad \text{with} \quad d\Omega^2 \equiv d\theta^2 + \sin^2 \theta d\phi^2. \quad (1.31)$$

Be aware that in these coordinates, r is not the radial distance from the origin if $\kappa \neq 0$. However, the circumference of a circle of radius r is always $2\pi r$.

Note that, if $\kappa \neq 0$, the line element remains unchanged under the simultaneous exchange $\kappa \rightarrow \kappa/|\kappa|$, $r \rightarrow r\sqrt{|\kappa|}$ and $a \rightarrow a/\sqrt{|\kappa|}$, implying that the relevant curvature parameter is actually $\kappa/|\kappa| = \pm 1$. We can therefore restrict ourselves to a curvature parameter $k \in \{-1, 0, +1\}$.

The non-zero Christoffel symbols for the metric (1.31) are given by

$$\begin{aligned} \Gamma_{rr}^r &= \frac{\kappa r}{1 - \kappa r^2} & \Gamma_{\theta\theta}^r &= -r(1 - \kappa r^2) & \Gamma_{\phi\phi}^r &= -r(1 - \kappa r^2) \sin^2 \theta \\ \Gamma_{r\theta}^\theta &= \frac{1}{r} & \Gamma_{\phi\theta}^\theta &= -\sin \theta \cos \theta & & \\ \Gamma_{r\phi}^\phi &= \frac{1}{r} & \Gamma_{\theta\phi}^\phi &= \cot \theta & & . \end{aligned} \quad (1.32)$$

Which yields the following non-zero components of the Ricci tensor

$$R_{rr} = \frac{2\kappa}{1 - \kappa r^2} \quad R_{\theta\theta} = 2\kappa r^2 \quad R_{\phi\phi} = 2\kappa r^2 \sin^2 \theta \quad (1.33)$$

along with the scalar curvature

$$R = 6\kappa. \quad (1.34)$$

Exercise 1.3 Determine the sectional curvatures of the metric (1.31). ■

Exercise 1.4 — Hyperspherical coordinates. Show that the spatial metric (1.31) using another radial coordinate ϱ can be written also in the form

$$dx^2 = d\varrho^2 + \varrho^2 S_\kappa^2(\varrho) d\Omega^2. \quad (1.35)$$

These coordinates are called ‘hyperspherical coordinates’. Show further that (requiring the reduced circumference $r \rightarrow \varrho$ for $\kappa \rightarrow 0$) we have $r(\varrho) = \varrho S_\kappa(\varrho)$ with

$$S_\kappa(\varrho) = \begin{cases} \frac{1}{\sqrt{\kappa}\varrho} \sin \sqrt{\kappa}\varrho & \text{for } \kappa > 0 \\ 1 & \text{for } \kappa = 0 \\ \frac{1}{\sqrt{-\kappa}\varrho} \sinh \sqrt{-\kappa}\varrho & \text{for } \kappa < 0 \end{cases}. \quad (1.36)$$

These coordinates have the advantage that ϱ (unlike r in the reduced circ. coordinates) is directly the radial distance from the origin, in contrast to the previous coordinates, the circumference of a circle of radius R is however not $2\pi\varrho$ if $\kappa \neq 0$. ■

Exercise 1.5 Compute the scalar curvature and the sectional curvatures of the metric (1.35). ■

Proposition 1.1 — Computing volume on manifolds and submanifolds. An infinitesimal hypervolume^a element on a d -manifold is spanned by d co-vectors dx^1, \dots, dx^d and its measure is given by

$$dV(x) \equiv \sqrt{|\det g|} dx^1 \dots dx^d. \quad (1.37a)$$

In the case of an m -dimensional submanifold, spanned by a subset of the co-vectors $dx^{i_1}, \dots, dx^{i_m}$, the corresponding measure is given by the square root of the absolute value of the determinant of the sub-metric tensor

$$dA(x) \equiv \sqrt{|\det g^{(m)}|} dx^{i_1} \dots dx^{i_m}, \quad (1.37b)$$

where $g^{(m)}$ is the m -dimensional sub-metric tensor with entries corresponding to pairs of indices (i_1, \dots, i_m) .

^aNote that integration is better defined using external calculus, which we will however not cover here, in which case we would have $dV = \sqrt{|\det g|} dx^1 \wedge \dots \wedge dx^d$. This makes area and volume an oriented structure, as they should be.

Proof. These formulae follow from the transformation properties of integral measures under coordinate transformations, the metric determinant taking the role of the Jacobian determinant. ■

■ **Example 1.8 — Unit 3-balls and 3-spheres.** Assume hyperspherical coordinates $x = (r, \theta, \phi)$ following (1.35). Then the distance from the origin is $\|x\| \equiv r$. It is easily possible to compute the surface area A_2 and volume V_3 of a unit ball $\mathcal{B} = \{x \in M \mid \|x\| \leq 1\}$ in a three-dimensional manifold with constant sectional

curvature κ in these coordinates. We find $\det g = r^4 S_\kappa^4(r) \sin^2 \theta$. The surface $\partial\mathcal{B}$ is defined by the submanifold on which $r = 1$. The volume measure therefore given by

$$dV(x) = r^2 S_\kappa^2(r) \sin \theta \, dr \, d\theta \, d\phi, \quad (1.38)$$

while the surface area measure at constant r is

$$dA(x) = r^2 S_\kappa^2(r) \sin \theta \, d\theta \, d\phi. \quad (1.39)$$

One finds for the surface area

$$A_2^\kappa := \int_{\partial\mathcal{B}_3} dA = 4\pi S_\kappa^2(1) = 4\pi \begin{cases} \frac{\sin^2 \sqrt{\kappa}}{\kappa} < 1 & \text{for } \kappa > 0 \\ 1 & \text{for } \kappa = 0 \\ \frac{\sinh^2 \sqrt{|\kappa|}}{|\kappa|} > 1 & \text{for } \kappa < 0 \end{cases}$$

and for the volume

$$V_3^\kappa := \int_{\mathcal{B}} dV = 4\pi \int_0^1 dr r^2 S_\kappa^2(r) = \pi \begin{cases} -\frac{\sin(2\sqrt{\kappa}) - 2\sqrt{\kappa}}{\kappa^{3/2}} < \frac{4}{3} & \text{for } \kappa > 0 \\ \frac{4}{3} & \text{for } \kappa = 0 \\ \frac{\sinh(2\sqrt{|\kappa|}) - 2\sqrt{|\kappa|}}{|\kappa|^{3/2}} > \frac{4}{3} & \text{for } \kappa < 0 \end{cases}$$

Therefore unit balls (in terms of surface and volume) are smaller in spherical space and larger in hyperbolic space compared to Euclidean space. ■

Space-time

In Einstein's theory of general relativity, the Universe is described by a four-dimensional pseudo-Riemannian manifold, called space-time. We have already introduced the relevant concepts for the spatial part of the Universe, and we will now extend these to the full space-time.

General relativity considers [Lorentzian manifolds](#), a special case of 4-dimensional pseudo-Riemannian manifolds where the metric has [signature](#) $(- + ++)$, i.e. time takes a role distinct from that of space. The signature is defined by the signs of the eigenvalues of the metric tensor (remember 1.9). We add a time coordinate as the zeroth coordinate, and define the line element of [space-time](#) as

$$ds^2 = g_{\mu\nu} dx^\mu dx^\nu, \quad (1.40)$$

where now greek indices by convention indicate four dimensions ($\mu, \nu = 0, 1, 2, 3$).

Definition 1.17 — Minkowski space-time. The simplest example of a Lorentzian manifold is Minkowski space-time, which is the space-time of [special relativity](#). It is a flat space-time, and its line element is given by

$$ds^2 = \eta_{\mu\nu} dx^\mu dx^\nu := -d\tau^2 + dx^2, \quad \text{i.e. } (\eta_{\mu\nu}) = \text{diag}(-1, 1, 1, 1), \quad (1.41)$$

where dx^2 is the line-element of the three-dimensional spatial submanifold $\Sigma = \mathbb{E}^3$.

Often the speed of light is included explicitly in the metric to denote its importance, i.e. $ds^2 = -c^2 dt^2 + dx^2$, where c is the speed of light and $d\tau = cdt$.

Proposition 1.2 The Minkowski metric is the unique metric tensor that is invariant under the Poincaré group (the 10 parameter group of space-time translations, spatial rotations, and Lorentz boosts).

A general Lorentzian manifold is locally isometric to Minkowski space-time, by Lemma 1.2. This follows directly from the existence of normal coordinates, see (1.30), which can be chosen to be Minkowski coordinates in a small enough neighbourhood of any point.

Definition 1.18 The metric of Minkowski space-time illustrates the causal structure of space-time. Consider a point P' infinitesimally close to P on a Lorentzian manifold, described by the displacement vector $\mathrm{d}x = e_\mu \mathrm{d}x^\mu$. This vector is called, depending on the sign of the line element $\mathrm{d}s^2 = g_{\mu\nu} \mathrm{d}x^\mu \mathrm{d}x^\nu$,

- | | |
|---------------------|--------------------------|
| time-like | if $\mathrm{d}s^2 < 0$, |
| null, or light-like | if $\mathrm{d}s^2 = 0$, |
| space-like | if $\mathrm{d}s^2 > 0$. |

In the case of Minkowski space-time, the displacements can be non-infinitesimal (since the metric is constant), say Δx^μ and the same classification applies. The $\mathrm{d}s^2 = 0$ conditions selects a submanifold of the space-time, called the **light-cone**.

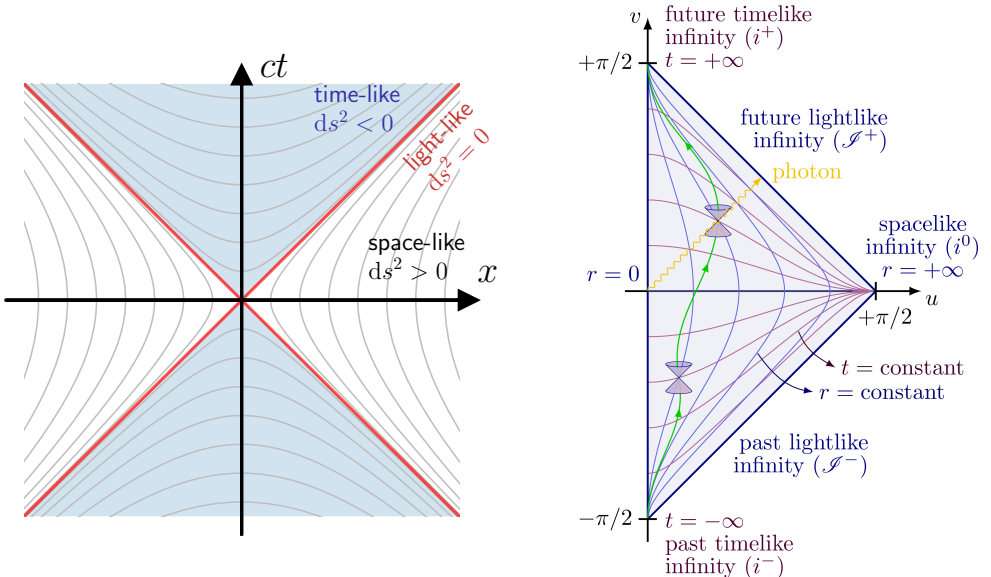


Figure 1.4: **Left:** Lightcone diagram of Minkowski space-time demonstrating lines of constant space-time distance (gray lines) that are space-like (white area), time-like (blue area), and light-like (red lines). The lightcone (red) is the boundary between the time-like and space-like regions and represents the propagation of light in the rest-frame. **Right:** Penrose diagram of Minkowski space-time. The vertical direction represents time, and the horizontal direction represents space. The light-cone is the boundary between the time-like and space-like regions. The diagonal lines represent the world-lines of light rays. The Penrose diagram is a compact representation of the causal structure of space-time. [Source of right figure: https://tikz.net/relativity_penrose_diagram/]

Penrose diagrams are a compact representation of the causal structure of space-time. They are constructed by a conformal transformation of the metric, which maps the entire space-time to a finite region. Lightcones are preserved as 45-degree lines. The Penrose diagram of Minkowski space-time is shown in Fig. 1.4.

Definition 1.19 — Null-geodesic. A curve in space-time is called a **null-geodesic** if it is parametrised by an affine parameter λ and satisfies the geodesic equation (1.22) with $ds^2 = 0$. Null-geodesics are the world-lines of light rays.

Einstein's general relativity

Definition 1.20 — Einstein tensor. The **Einstein tensor** is defined as

$$G_{\mu\nu} := R_{\mu\nu} - \frac{1}{2}Rg_{\mu\nu}, \quad (1.42)$$

where $R_{\mu\nu}$ and R are the Ricci tensor and scalar, which are fully determined by the metric coefficients $g_{\mu\nu}$. The Einstein tensor has 10 independent components in 4-dimensional space.

Lemma 1.3 — Contracted Bianchi identity. The Einstein and the metric tensor satisfy the **contracted Bianchi identity**

$$\nabla^\mu G_{\mu\nu} = 0 \quad \nabla^\mu g_{\mu\nu} = 0. \quad (1.43)$$

Proof. The contracted Bianchi identity follows from the definition of the Einstein tensor and the Bianchi identities. We refer to a textbook on differential geometry/relativity for the details. ■

Definition 1.21 — Einstein's field equations. The field equations are given by

$$G_{\mu\nu} + \Lambda g_{\mu\nu} = \frac{8\pi G}{c^4} T_{\mu\nu}, \quad (1.44)$$

where G is the gravitational constant, Λ the cosmological constant, c the speed of light, $G_{\mu\nu}$ the Einstein tensor. The right-hand side contains $T_{\mu\nu}$ which is the so-called **energy-momentum tensor**. These equations make up a set of 10 coupled non-linear partial differential equations for the metric tensor.

The energy-momentum tensor is a symmetric tensor that describes the distribution of energy and momentum in space-time. It is the source of the gravitational field in Einstein's theory.

Theorem 1.3 — Conservation of energy-momentum. The energy-momentum tensor satisfies the **conservation law**

$$\nabla^\mu T_{\mu\nu} = 0. \quad (1.45)$$

It is a direct consequence of the contracted Bianchi identity (1.43) and the field equation (1.44). We will see later why this is called a conservation law for energy and momentum.

Observation 1.2 Einstein's field equations (1.44) can be derived from the **Einstein-Hilbert action** through the principle of least action. The action is given by the

functional

$$S[g] = \int \left[\frac{1}{2\kappa} (R - 2\Lambda) + \mathcal{L}_m \right] \sqrt{|\det g|} d^4x , \quad (1.46)$$

where $\kappa \equiv \frac{8\pi G}{c^4}$, R is the scalar curvature, Λ the cosmological constant, and \mathcal{L}_m is the Lagrangian density of matter (e.g. the Lagrangian of the standard model of particle physics).

The cosmological constant Λ and the coupling constant κ are free parameters in the theory and are determined by astronomical observation and by experiments. Physicists have long speculated whether the functional form $(R - 2\Lambda)$ of the geometry Lagrangian tells us something about whether general relativity is the ultimate theory of gravity. Clearly in the $R \rightarrow 0$ limit, the cosmological constant Λ becomes the only relevant parameter. At the same time, there is no natural regulation that would prevent the Lagrangian to diverge in the $R \rightarrow \infty$ limit. This has led to more general functional forms $f(R)$ to be investigated other than the linear one of general relativity. Is GR just the lowest order Taylor expansion of $f(R)$? Generally, this field of research is called '[modified gravity](#)'.

Theorem 1.4 — Field equations. Einstein's field equations can be derived by requiring stationarity of the variational derivative of the Einstein-Hilbert action with respect to the metric tensor, i.e.

$$\frac{\delta S}{\delta g_{\mu\nu}} = 0. \quad (1.47)$$

This yields the field equations (1.44).

Proof. The proof can be found in all standard textbooks on general relativity, also e.g. the Wikipedia page on the Einstein-Hilbert action. It is somewhat involved and we shall not reproduce it here. ■

Friedmann equations and the energy content of the Universe

As we have seen, the high degree of symmetry imposed by the cosmological principle (spatial translation and rotation invariance) allows only for three types of spaces with simple topology, namely \mathbb{E}^3 , \mathbb{S}^3 , and \mathbb{H}^3 corresponding to (1) flat space, (2) a three-dimensional sphere with constant positive curvature, and (3) a three-dimensional hyperbolic space with constant negative curvature. As a consequence, the only allowed dynamical degree of freedom is a global time-dependent re-scaling of space (the cosmic scale factor a) which is the only degree of freedom that preserves the spatial symmetries.

Maximally symmetric space-times

Proposition 1.3 — FLRW metric. The only metric that is globally spatially homogeneous and isotropic for all times is the so-called [FLRW metric](#) (found by Friedmann, Lemaître, Robertson and Walker) with line element:

$$ds^2 = -c^2 dt^2 + a^2(t) dx^2, \quad (1.48)$$

where c is a constant (the speed of light), $a(t)$ is the single dynamical degree of freedom allowed, x are called [co-moving coordinates](#), and dx^2 is the metric of the spatial submanifold Σ of constant curvature κ .

Adopting the reduced circumference polar coordinates, the FLRW metric can be written in its most common form as

$$ds^2 = -c^2 dt^2 + a^2(t) \left(\frac{dr^2}{1 - \kappa r^2} + r^2 d\Omega^2 \right), \quad (1.49)$$

where $d\Omega^2 = d\theta^2 + \sin^2 \theta d\phi^2$ is the line element of the unit two-sphere, and κ is the curvature parameter of the spatial sections.

Proof. The proof that FLRW is indeed the only globally spatially homogeneous and isotropic metric can be found in most standard textbooks on general relativity, we shall not reproduce it here but refer the reader e.g. to chapter 10 of Straumann (2013.). ■

Definition 1.22 — Cosmic scale factor. The only dynamical degree of freedom of this metric is the function $a(t)$, which is called the [scale factor of the Universe](#) as it describes how length scales evolve over time.

We can thus say that $\dot{a} > 0$ corresponds to an expanding universe and $\dot{a} < 0$ to a contracting universe. Similarly, a universe in which $\ddot{a} > 0$ is accelerating, while one in which $\ddot{a} < 0$ is decelerating. A universe would be static if $\dot{a} = 0$ and only remain static if also $\ddot{a} = 0$ (which however is unstable to perturbations; cf. Einstein's so-called biggest blunder).

Definition 1.23 — Co-moving and physical coordinates. We call coordinates defined on Σ co-moving, since they simply label coordinates on the temporally constant spatial hypersurface. In contrast, the *physical coordinates* are obtained by multiplying the comoving coordinate by the respective scale factor, i.e.

$$x_{\text{phys}} := a(t) x \quad (1.50)$$

Exercise 1.6 — Comoving and physical velocities. Consider the trajectory of a galaxy, i.e. a 1-parameter family of points on the spatial hypersurface, $x(t)$. Show that, defining the comoving velocity as $v_{\text{comoving}} := \dot{x}$, its physical velocity is given by

$$v_{\text{physical}} = a v_{\text{comoving}} + \dot{a} x = a v_{\text{comoving}} + H(a) x_{\text{phys}}. \quad (1.51)$$

What does this imply for the observed recession velocity of galaxies? What is the comoving velocity of a photon – does it agree with what you find for a light-like geodesic with $ds^2 = 0$ from the FLRW metric? ■

We remind the reader that light-like distances, i.e. the [lightcone](#) itself, are described by the submanifold $ds^2 = 0$. For this choice of signature of the metric, it separates space-time into the part of space that is time-like connected with $ds^2 > 0$ and that which is space-like connected with $ds^2 < 0$.

Evolution of $a(t)$ from Einstein's equations

The evolution of the cosmic scale factor must be obtained from solving Einstein's field equations, which dictates how certain energy constituents deform the space-time.

Definition 1.24 — Energy-momentum of ideal fluid. For an ideal fluid, the energy-momentum tensor is defined as

$$T_{\mu\nu} = (\rho + p/c^2)u_\mu u_\nu + p g_{\mu\nu}. \quad (1.52a)$$

We assume that the fluid is at rest in the co-moving frame, i.e., its 4-velocity is $u^\mu = (c, 0, 0, 0)$. The requirement of homogeneity and isotropy requires that ρ and p are functions of time alone. We have the following particularly simple form:

$$T^\mu_\nu = \text{diag}(-\rho c^2, p, p, p).$$

Proposition 1.4 — Friedmann equations. The so-called **Friedmann equations** fully describe the evolution of the single degree of freedom $a(t)$ of Einstein's field equations under the assumption of spatial homogeneity and isotropy. They are

$$H^2 := \left(\frac{\dot{a}}{a}\right)^2 = \frac{8\pi G\rho}{3} - \frac{\kappa c^2}{a^2} + \frac{\Lambda c^2}{3}, \quad (1.53a)$$

$$\frac{\ddot{a}}{a} = -\frac{4\pi G}{3} \left(\rho + \frac{3p}{c^2}\right) + \frac{\Lambda c^2}{3}, \quad (1.53b)$$

where $H = H(t) = \dot{a}(t)/a(t)$ is the **Hubble parameter**. H measures the rate of expansion of the Universe, and is a function of time that depends on what the Universe is made of.

Proof. The nonzero Christoffel symbols of the FLRW with curvature κ are found to be

$$\begin{aligned} \Gamma_{11}^0 &= \frac{a\dot{a}}{c^2(1-\kappa r^2)} & \Gamma_{22}^0 &= \frac{1}{c^2}a\dot{a}r^2 & \Gamma_{33}^0 &= \frac{1}{c^2}a\dot{a}r^2 \sin^2 \theta \\ \Gamma_{10}^1 &= \Gamma_{01}^1 = \frac{\dot{a}}{a} & \Gamma_{11}^1 &= \frac{kr}{1-\kappa r^2} & \Gamma_{22}^1 &= -r(1-\kappa r^2) & \Gamma_{33}^1 &= -r(1-\kappa r^2) \sin^2 \theta \\ \Gamma_{20}^2 &= \Gamma_{02}^2 = \frac{\dot{a}}{a} & \Gamma_{21}^2 &= \Gamma_{12}^2 = \frac{1}{r} & \Gamma_{33}^2 &= -\sin \theta \cos \theta \\ \Gamma_{30}^3 &= \Gamma_{03}^3 = \frac{\dot{a}}{a} & \Gamma_{31}^3 &= \Gamma_{13}^3 = \frac{1}{r} & \Gamma_{32}^3 &= \Gamma_{23}^3 = \cot \theta. \end{aligned}$$

From this one calculates the Ricci tensor as

$$\begin{aligned} R_{00} &= -3\frac{\ddot{a}}{a} & R_{11} &= \frac{(c^{-2}(\ddot{a}a + 2\dot{a}^2) + 2\kappa)}{1-\kappa r^2} \\ R_{22} &= (c^{-2}(\ddot{a}a + 2\dot{a}^2) + 2\kappa)r^2 & R_{33} &= (c^{-2}(\ddot{a}a + 2\dot{a}^2) + 2\kappa)r^2 \sin^2 \theta. \end{aligned}$$

and the Ricci scalar as

$$R = 6 \left(\frac{1}{c^2} \left(\frac{\ddot{a}}{a} + \frac{\dot{a}^2}{a^2} \right) + \frac{\kappa}{a^2} \right).$$

The Einstein tensor is then finally given by

$$G^0_0 = -3 \left[\frac{1}{c^2} \left(\frac{\dot{a}}{a} \right)^2 + \frac{\kappa}{a^2} \right] \quad G^i_j = - \left[\frac{1}{c^2} \left[\left(\frac{\dot{a}}{a} \right)^2 + 2 \frac{\ddot{a}}{a} \right] + \frac{\kappa}{a^2} \right] \delta^i_j.$$

Eq. (1.53a) is then obtained from the 0_0 -component of Einstein's field equations, and Eq. (1.53b) from the trace, i.e. by computing $G^\mu_\mu + 4\Lambda = \frac{8\pi G}{c^4} T^\mu_\mu$ and then combining the result with the 0_0 -component to eliminate the second derivative. ■

Proposition 1.5 — Conservation law. In addition one finds a continuity equation arising from the covariant conservation of the energy-momentum tensor (specifically from $\nabla_\mu T^\mu_0 = 0$), i.e.,

$$\dot{\rho} + 3 \left(\frac{p}{c^2} + \rho \right) \frac{\dot{a}}{a} = 0. \quad (1.54)$$

If we assume a relation $w \equiv \frac{p}{\rho c^2}$, i.e. a so-called equation of state with parameter $w \in \mathbb{R}$ relating the pressure and the energy density, then we can write this as

$$\dot{\rho} + 3(1+w) \frac{\dot{a}}{a} \rho = 0. \quad (1.55)$$

with solution (assuming $\rho_0 := \rho(a=1)$)

$$\rho(a) = \rho_0 a^{-3(1+w)}. \quad (1.56)$$

Proof. Left as an exercise. ■

Variants of these equations have been first derived in 1922 by the Russian physicist Alexander Friedmann (Friedmann, 1922). These equations should be supplemented with an equation of state relating p and ρ , which we discuss in section 1. Note that the three equations (1.53)-(1.54) are not independent, any two of them yield the third.

The current expansion rate

The Hubble parameter $H(t)$ evaluated at the present time t_0 is called the **Hubble constant**, and is usually written as

$$H_0 := H(t_0) = 100 h \frac{\text{km/s}}{\text{Mpc}}, \quad (1.57)$$

where h is the dimensionless **Hubble parameter**. Here and in the following we denote arbitrary functions $f(t)$ evaluated at the present time t_0 with f_0 .

Hubble and Lemaître were the first to measure the Doppler shift of nearby galaxies. Knowing their distance through other means, they were able to deduce the (local) Hubble law, which holds when $H \approx H_0$,

$$v_{\text{Galaxy}} = H_0 d_{\text{Galaxy}}, \quad (1.58)$$

which states a simple linear relation between the physical distance d_{Galaxy} to a galaxy and its apparent recession velocity v_{Galaxy} from us. Hubble's original measurement is reproduced in Figure 1.5, along with his linear fit to the

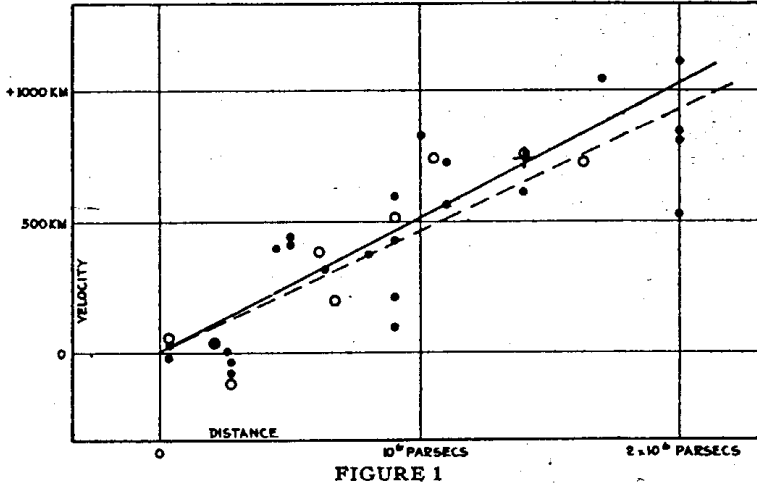


FIGURE 1

Figure 1.5: The original diagram that Edwin Hubble made in 1929 relating the distance and the recession velocity of nearby galaxies and the linear fit he provided of the form $v = H_0 d$. Hubble's original value ($H_0 \sim 500 \text{ km/s/Mpc}$) is quite different from the precision value we have today ($H_0 = 67.74 \pm 0.46 \text{ km/s/Mpc}$ Planck Collaboration et al. 2016). The discrepancy is mainly due to Hubble's determination of distances being wrong by about a factor of 7. However, the factor was roughly the same for all his galaxies, so that he indeed measured the expansion of the Universe.

velocity/distance pairs Hubble (1929). Although his distance measurements were wrong by about a factor of seven, this is commonly seen as the discovery of the expansion of the Universe and thus marked the beginning of the century of physical cosmology. Lemaître had similar measurements at the time Lemaître (1927), and in fact published them two years before Hubble in a Belgian journal in French (that apparently not many people read), but did not bother to re-publish them in English after Hubble's results came out.

Cosmological density parameters

The value of the curvature term κ is uniquely defined in terms of the total density at the present time ρ_0 and the Hubble constant. The total density includes the contribution from the cosmological constant, so that we can write

$$\rho_0 := \rho(a=1) + \rho_\Lambda \quad \text{where} \quad \rho_\Lambda := \frac{\Lambda c^2}{8\pi G} \quad (1.59)$$

Definition 1.25 — Critical density. The curvature term is zero exactly iff the total density $\rho + \rho_\Lambda$ is equal to the **critical density of the Universe** ρ_{crit} , defined as

$$\rho_{\text{crit}}(a) := \frac{3H^2(a)}{8\pi G} \quad \rho_{\text{crit},0} := \rho_{\text{crit}}(a=1) = \frac{3H_0^2}{8\pi G}. \quad (1.60)$$

Using the definition of the critical density, we can non-dimensionalise all densities. In particular, we can express the mean density in units of this critical density as a

density parameter

$$\Omega_0 := \rho_0 / \rho_{\text{crit},0}. \quad (1.61)$$

This allows us to write the curvature in a particularly simple form as $\kappa = H_0^2(\Omega_0 - 1)/c^2$ so that the curvature parameter k can be expressed in terms of the density parameter Ω_0 as

$$k = \begin{cases} -1 & : \text{negative curvature} \\ 0 & : \text{no curvature} \\ +1 & : \text{positive curvature} \end{cases} \quad \text{corresponds to} \quad \begin{cases} \Omega_0 < 1 \\ \Omega_0 = 1 \\ \Omega_0 > 1 \end{cases}. \quad (1.62)$$

The density parameter of curvature can then be defined as

$$\Omega_{k,0} := 1 - \Omega_0 = \frac{\kappa c^2}{H_0^2} = \kappa R_H^2, \quad (1.63)$$

where $R_H := c/H_0$ is the [Hubble radius](#). The density parameter of the cosmological constant becomes

$$\Omega_{\Lambda,0} := \frac{\rho_{\Lambda}}{\rho_{\text{crit},0}} = \frac{\Lambda c^2}{3H_0^2}. \quad (1.64)$$

Finally, one customarily defines the [deceleration parameter](#) (measured at $a_0 = 1$ today)

$$q_0 = -\frac{\ddot{a}_0}{a_0} \left(\frac{\dot{a}_0}{a_0} \right)^{-2} = -\frac{\ddot{a}_0 a_0}{\dot{a}_0^2} \quad (1.65)$$

that characterises whether the expansion of the universe is currently accelerating ($q_0 < 0$) or decelerating ($q_0 > 0$). *Usually one fixes the scale of the Universe today to $a_0 = 1$.*

Cosmic geodesy – measuring distances

The redshifting of light We note that the expansion with time as $a(t)$ causes all length scales to expand, so also the wavelength of photons.

Definition 1.26 — Cosmological redshift. A photon emitted at a time t_E and observed at $t_O > t_E$ will thus experience a scaling of its wavelength proportional to the change of all physical length-scales in the Universe. Assume its wavelength at emission is λ_E then it is observed with $\lambda_O = \lambda_E a(t_O)/a(t_E)$. Since the universe has expanded between t_E and t_O , wavelengths are re-scaled by the respective scale factors at those epochs. For this purpose one defines the [cosmological redshift](#) z as

$$1 + z := \frac{\lambda_O}{\lambda_E} = \frac{a(t_O)}{a(t_E)}. \quad (1.66)$$

If a photon is emitted and immediately (i.e. compared to cosmological time scales), then its redshift vanishes. Since all observations take place at the same time (now!), it is customary to set $a(t_O) \equiv a_0 = 1$. As a consequence, to-day correspond to a cosmological redshift of zero.

If $a(t)$ is monotonous, then cosmological redshift can be used to label time in an expanding Universe. Since photons travel with the speed of light, we will see distant photons coming from a time when the Universe was smaller (and thus



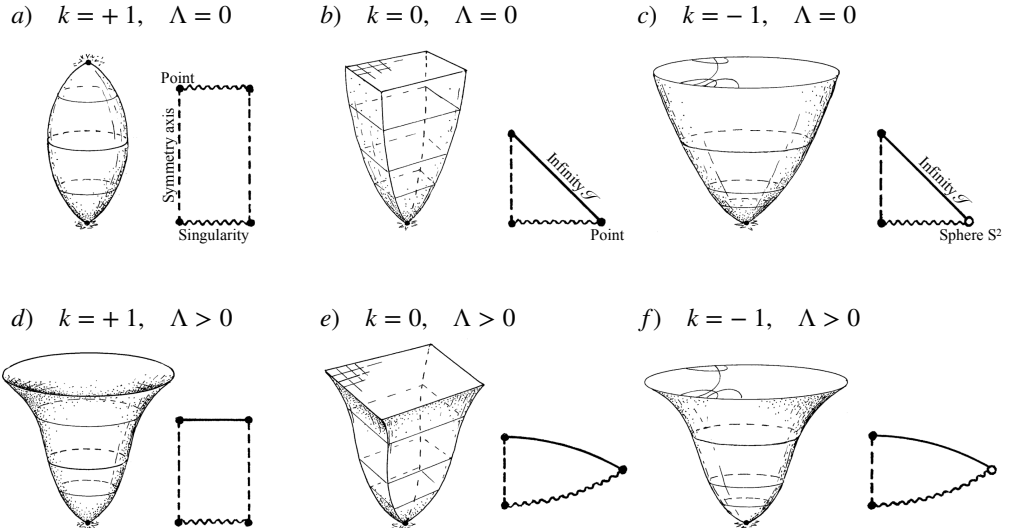


Figure 1.6: Evolution of FLRW Universes (i.e. maximally symmetric space-times) with, from left to right, supercritical density ($k = +1$), critical density ($k = 0$), and subcritical density ($k = -1$), as well as with vanishing (top) or non-zero (bottom) cosmological constant. In each case a sketch of the evolution with time going upwards, along with a schematic conformal diagram is shown. In all cases shown, we have a singularity at the origin. Figure adapted from Penrose (2006).

younger) than today. The redshift of a photon thus indicates both its distance and the age of the Universe when it was emitted, rendering it possible to peek into ‘the past’ when observing the “high-redshift Universe”.

Longitudinal distances

Proposition 1.6 — Co-moving distance. Assume an observer O with a (co-moving) spatial coordinate $\chi_O = 0$ who observes at time t_0 light that was emitted at some time $t_E < t_O$ from an emitter E with a spatial coordinate $\chi_E > 0$.

1. The light propagation in co-moving coordinates $\chi(t)$ is described by the ODE

$$\frac{d\chi}{dt} = \frac{c}{a(t)} \quad (1.67)$$

2. The co-moving distance χ_{EO} between emitter and observer is therefore related to emission and observation time as

$$\chi_{EO} = \chi_E - \chi_O = \int_{t_E}^{t_O} \frac{dt}{a(t)} = \int_{a_E}^{a_O} da \frac{c}{a^2 H(a)}. \quad (1.68)$$

where the explicit expression depends on the energy content of the Universe through the Ω_X , and the current expansion rate H_0 .

Proof. The proof is straightforward:

1. A photon trajectory is by definition a null geodesic (1.19), i.e. the 4-distance

is $ds^2 = 0$. It follows from the metric (1.48) that then

$$c^2 dt^2 = a^2 dx^2 \quad (1.69)$$

which is fulfilled by the ODE (1.67) for $d\chi/dx = 1$.

2. The first equality in (1.68) follows straightforwardly from integrating the ODE from t_E to t_O . The second equality follows by a change of variables respecting that the Jacobian is related to the Friedmann equation (1.53a), i.e. $da/dt = aH(a)$.

■

Note that this is readily translated into a co-moving distance as a function of the redshift z_E (z_O) of the light at emission (observation) by setting $a_E = 1/(1+z_E)$ and $a_O = 1/(1+z_O)$. Since all cosmological observations are made by humans here and today, it is customary to fix $a_O = 1$ and therefore $z_O = 0$. Therefore a redshift of zero corresponds to today.

Proposition 1.7 — Comoving transverse distance. The comoving distance between two points at the same redshift, and therefore at the same comoving distance R , separated by an angle $\delta\phi$ is given by $\chi_T \delta\phi$ where

$$\chi_T = RS_k(R) \quad (1.70)$$

Proof. Employing hyperspherical coordinates, the result follows readily from (1.35) by integrating over the angle at fixed R . ■

Equations of state, co-dimension

As we have mentioned above, the set of equations is not closed in the absence of an [equation of state](#) (EOS) relating pressure p and rest energy density ρ , cf. (1.56). We have already seen that if w is constant then eq. (1.54) can be readily integrated to give

$$\rho \propto a^{-3(1+w)} = a^{-n}, \quad (1.71)$$

where $n := 3(1+w)$ reflects the co-dimension of the energy component, as summarised in Table 1.1. The most important components are the ultrarelativistic and non-relativistic particles, which are respectively abbreviated with “r” and “m”. Recent measurements find that the Universe is consistent with being flat, non-relativistic and ultrarelativistic components making up about 30% of the critical density, and the remainder has an equation of state parameter w very close to -1 allowing basically only a cosmological constant, but there is no evidence of a contribution from domain walls and cosmic strings to the cosmic energy budget.

Proposition 1.8 — Friedmann equation in terms of Ω_X . All these components can be conveniently expressed in terms of their density parameters Ω and contribute jointly to the [Friedmann equation](#) eq. (1.53a) for the total energy budget of the Universe,

$$H^2(t) = \left(\frac{\dot{a}}{a}\right)^2 = H_0^2 \left[\Omega_{\text{r},0} a^{-4} + \Omega_{\text{m},0} a^{-3} + \Omega_{k,0} a^{-2} + \Omega_{\Lambda,0} \right], \quad (1.72)$$

w	n	type
-1	0	volume-like, cosmological constant
-2/3	1	sheet-like, domain walls
-1/3	2	line-like, cosmic strings
0	3	point-like, non-relativistic particle (index "m")
1/3	4	4d-point-like, ultrarelativistic particle/radiation (index "r")

Table 1.1: Energy components in an expanding universe: different forms of energy behave differently under expansion due to their co-dimension. This is reflected in the equation of state parameter w , and their co-dimension n , related as $w = n/3 - 1$. Either of them directly determines the scaling of the energy fraction with the expansion of the universe as $\Omega_X(a) = \Omega_{X,0}a^{-n}$.

where for convenience one defines $\Omega_{k,0} := 1 - \Omega_{r,0} - \Omega_{m,0} - \Omega_{\Lambda,0}$ as the contribution from curvature ($\Omega_{k,0} = 0$ if $\rho_0 = \rho_{\text{crit},0}$). Note that we have not added the $\propto a^{-1}$ component due to a lack of evidence for it being significant. Also, current observations point to $\Omega_{k,0} \simeq 0$.

Exercise 1.7 — Friedmann equations. Prove that indeed eq. (1.72) follows from eq. (1.53a). ■

From now on we drop the o index in $\Omega_{\Lambda,0}$, as Λ is a constant. Note that it is common in the literature to omit the o in all indices, which for clarity, we will not do here. We remark that the background energy density of photons (which all essentially come from the cosmic microwave background) has a blackbody spectrum and thus scales as $\rho_r \sim T^4$ as follows from the Stefan–Boltzmann law, while $T \sim 1/a$; this explains the a^{-4} scaling of the radiation term in (1.72). In the massless limit, neutrinos are relativistic and are grouped with Ω_r .

Fact 1.0.1 — Cosmological Parameters. So far we have no fundamental theory that predicts the set of constants (or cosmological parameters) of the cosmological standard model

$$\{H_0, \Omega_{m,0}, \Omega_{r,0}, \Omega_\Lambda\} \quad (1.73)$$

that appear in the Friedmann equation and determine the dynamics of the homogeneous Universe; instead they have to be measured from observations. The most recent values for these constants are found from the combination of various measurements (Planck Collaboration et al., 2016) and are $H_0 = 67.74 \pm 0.46 \text{ km/s/Mpc}$, $\Omega_{m,0} = 0.3089 \pm 0.0062$, $\Omega_\Lambda = 0.6911 \pm 0.0062$, $\Omega_{k,0} \lesssim 10^{-3}$ and $\Omega_{r,0} \simeq 8.4 \times 10^{-5}$ (assuming massless neutrinos which applies at sufficiently early times).

Exercise 1.8 — Cosmic epochs and asymptotics. While today $\Omega_\Lambda > \Omega_m > \Omega_r$, this was not always the case.

1. Determine the moment (in terms of z and a) of equality between the cosmological constant and the matter energy density, as well as that of matter and radiation equality.
2. For each of the three epochs (radiation domination, matter domination,

Λ -domination), determine the asymptotically valid form of the Friedmann equation, i.e., by setting all non-dominating energy constituents to zero.

3. While the full Friedmann equation has no known closed-form solution in general, the asymptotic equations do. Find them.
4. Einstein originally introduced the cosmological constant Λ to be able to obtain a static universe. Show that a static universe composed of matter and a cosmological constant is indeed allowed by the equations. Show that this solution is however unstable.

Exercise 1.9 — Big Crunch. Closed Universes can have multiple singularities.

1. Show that in a closed universe with vanishing cosmological constant and radiation content (i.e. $\Omega_{\Lambda,0} = 0, \Omega_r = 0, \Omega_{m,0} > 1$) the Friedmann equation possesses the following parametric solution for the scale factor

$$a(\theta) = \frac{\Omega_{m,0}}{2(\Omega_{m,0} - 1)}(1 - \cos \theta) \quad (1.74a)$$

$$t(\theta) = \frac{\Omega_{m,0}}{2H_0(\Omega_{m,0} - 1)^{3/2}}(\theta - \sin \theta). \quad (1.74b)$$

2. When does Big Crunch happen in units of the Hubble time ($t_H = 1/H_0$)?

Exercise 1.10 — Numerical Integration of Friedmann Equation. Use the `PYTHON` script below as a starting point for your own program to numerically integrate the Friedmann equation (1.72).

1. Plot the solution $a(t)$ for the Planck satellite best-fit Λ CDM model given above. Play with the parameters and observe how the expansion history of the universe changes.
2. If one assumes a universe containing only matter ($\Omega_m = 1$), or only radiation ($\Omega_r = 1$), or only a cosmological constant ($\Omega_\Lambda = 1$), then analytic solutions for the Friedmann equation exist, as you have shown above. Include them in your plot and compare your numerical solution against the analytic solutions for these cases.

Program Code 1.1 — Numerical integration of the Friedmann equation. In general, there are no closed form solutions in the presence of all density parameters. We therefore want to find numerical solutions of the Friedmann equation. We could use a routine to solve initial value problems such as `scipy.integrate.solve_ivp`. However, in this case it is simpler to directly integrate the equation since it is a first order equation. We will thus use the `scipy` routine `quad` to numerically integrate a function. We will need the

following **PYTHON** packages

```

1 import numpy as np
2 import matplotlib.pyplot as plt
3 from scipy.integrate import quad
4 %matplotlib inline

```

The main problem we have to circumvent is that the limits of integration that are passed to `quad` cannot be vectors. This means that we will have to write a function around `quad` that loops over an array of values, passes them one by one to `quad` and stores the result in a new array. The skeleton to integrate the Friedmann equation in order to find $t(a)$, i.e. the cosmic time as a function of the scale factor, then might look like this:

```

1 def Hubble_a(a):
2     return ...
3
4 def t_of_a(a):
5     res = np.zeros_like(a)
6     for i,ai in enumerate(a):
7         t,err = quad(lambda ap : 1.0/(ap*Hubble_a(ap)),0,ai)
8
9     res[i] = t
10    return res
11
12 a = np.logspace(-8,1,100)
13
14 plt.loglog(t_of_a(a)*H0,a)
15 plt.xlabel('t * H0')
16 plt.ylabel('a(t)')

```

We have not provided the implementation for the function `Hubble_a` = $\frac{\dot{a}}{a}$, but leave this as the main purpose of the exercise besides learning how to integrate such functions numerically. There is one more advanced bit in this listing. We are making use of **PYTHON** lambda expressions. This is just a short hand notation for a function definition, i.e., we define in-place a nameless function that maps $a_p \mapsto (a_p H(a_p))^{-1}$, which is the function that we want to integrate over. Finally, we create an array of 100 values of logarithmically spaced scale factors $10^{-8} \leq a \leq 10$, calculate the cosmic times (in units of the Hubble time after multiplying with H_0), and plot the result as time against a . Note that a Hubble time $1/H_0 \approx 1.44 \times 10^{10}$ years.

Horizons

Definition 1.27 — Conformal time. The metric (1.48), for $k = 0$, can be written as a scaled version of Minkowski space

$$ds^2 = a^2(t) (d\eta^2 - dx^2) \quad (1.75)$$

using the **conformal time** $\eta(t) = c \int_0^t dt a^{-1}$. In terms of conformal time, light rays travel along straight lines with unit velocity, i.e. $\|x_O - x_E\| = \eta_O - \eta_E$.

The causal structure of FLRW space-times is most clearly visualised in conformal time, which is shown in Figure 1.7. Several important concepts are of note.

Definition 1.28 — Particle horizon. The particle horizon is the comoving distance

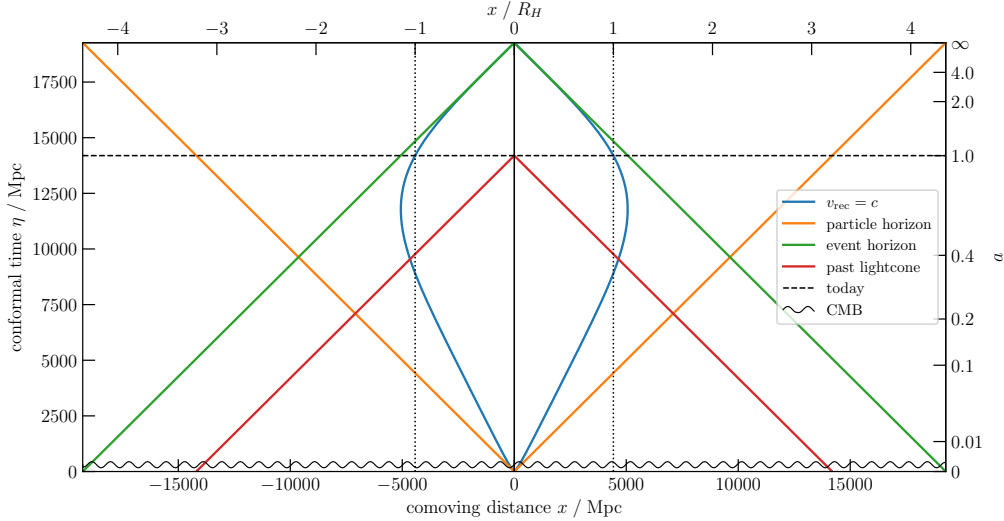


Figure 1.7: Causal structure of the Λ CDM model in a quantitative conformal diagram.

that light has travelled since the big bang. Clearly this is given by the line

$$\chi_\gamma = \eta \quad (1.76)$$

shown as the orange line in Figure 1.7.

Definition 1.29 — Past lightcone. The light that reaches us *right now* from a comoving distance $\chi_{lc}(a)$ with a redshift $z = 1/a - 1$ originates from the past lightcone given by

$$\chi_{lc} = \eta(a = 1) - \eta(a) \quad (1.77)$$

shown as the red line in Figure 1.7.

Clearly due to the Hubble law, there will be a distance R_∞ beyond which the recession velocity will exceed the speed of light. It is given by

$$v_{rec} = \dot{a}R_\infty \stackrel{!}{=} c \quad \Leftrightarrow \quad R_\infty(a) = \frac{c}{a^2 H(a)} \quad (1.78)$$

Its value *today*, is called the **Hubble radius** $R_H := R_\infty(a = 1)$ (which can be used to non-dimensionalise all distances). In fact, the existence of a finite R_∞ does not imply an event horizon since light from distances greater than R_∞ is able to reach us. The causal limit is given by the **event horizon**.

Definition 1.30 — Event horizon. All light rays that are able to reach us from a comoving distance χ_∞ over the entire age of the Universe are contained in the event horizon, defined as

$$\chi_\infty = \eta(a \rightarrow \infty) - \eta(a) \quad (1.79)$$

shown as the green line in Figure 1.7.

The causal structure of the Λ CDM model is shown in Figure 1.7. The blue line

marks the comoving distance at which the recession velocity $v_{\text{rec}} = \dot{a}x$ equals the speed of light, called the Hubble radius. This does *not* represent the event horizon however. The horizontal dotted line at $a = 1$ marks today, the vertical dotted line the comoving Hubble radius $R_H = c/H_0$ today. The red line marks our past lightcone, all astronomical observations lie on the red line. Only the region below it is causally connected to us. In contrast, the event horizon (green) marks all points (those below the green line) that are in principle observable over the entire lifetime of the Universe, i.e. the region below the green line is the maximal causally connected region of the Universe. Finally, the orange line represents the particle horizon, the comoving distance that light has travelled since the big bang. The last-scattering surface of the CMB is represented by the wiggly line. One of the main challenges of the big bang model is plainly obvious here: the past lightcone of any point on the last-scattering surface is tiny. Hence, most points on it have never been causally connected.

Exercise 1.11 — Existence of an event horizon. Show that cosmologies with $\Omega_\Lambda > 0$ have an event horizon. Determine $\eta(a \rightarrow \infty)$ for the Λ CDM model. ■

Exercise 1.12 — Causal disconnectedness of the CMB. Show that points separated by more than a relatively small comoving distance d_C at the time of the CMB ($a_{\text{CMB}} \approx 10^{-3}$) are not in each other's particle horizon (or alternatively: have no overlap of their past lightcones) and thus have never been in causal contact in the standard big bang model. ■

Newtonian cosmology

It is interesting to notice that the expanding Universe is not a consequence of relativistic physics, but is already part of Newtonian mechanics.

Definition 1.31 — Newtonian mechanics. Newtonian, or ‘non-relativistic’, mechanics is defined by Newton’s famous axioms. For our purposes in this section, we mainly need the second: acceleration equals force. If the force can be written as a gradient of a scalar function, we have that particle trajectories $x_{\text{phys}}(t)$ in physical coordinates obey

$$\ddot{x}_{\text{phys}} = -\nabla_{\text{phys}}\phi \quad (1.80)$$

where all coordinates are physical. In particular, we call \ddot{x}_{phys} **inertial motion**. This ODE is invariant under transformations $x \mapsto x + v_r t + x_r$ for arbitrary (but constant) v_r and x_r . Including also spatial rotations, this is the group of Galilean transformations that connects all inertial frames.

If we start from Poisson’s equation for the gravitational potential ϕ in a universe with uniform matter density $\bar{\rho}$ and cosmological constant Λ (Peebles, 1993), then Newton’s law of gravity reads

$$\nabla^2\phi = 4\pi G\bar{\rho} - \Lambda c^2. \quad (1.81)$$

Integrating once with suitable boundary conditions, it is trivial to see that it is consistent with a gravitational acceleration of the form

$$-\nabla\phi = \left[-\frac{4\pi G}{3}\bar{\rho} + \frac{\Lambda c^2}{3} \right] (\mathbf{r} - \mathbf{r}_0), \quad (1.82)$$

with arbitrary constant \mathbf{r}_0 . Evidently the freedom in choosing \mathbf{r}_0 allows one to fix an inertial frame at any point in space. At the same time, a point at distance $\mathbf{d} := \mathbf{r} - \mathbf{r}_0$ experiences an apparent acceleration $\ddot{\mathbf{d}} = -\nabla\phi$, so that one has

$$\ddot{\mathbf{d}} = \left[-\frac{4\pi G}{3}\bar{\rho} + \frac{\Lambda c^2}{3} \right] \mathbf{d} \quad (1.83)$$

which, for $\mathbf{d} = a(t)\chi$ with χ being a constant, precisely reduces to the second Friedmann equation (1.53b) in the absence of pressure. Furthermore, upon integrating once in time (for non-relativistic matter $\bar{\rho} \propto a^{-3}$, $p = 0$), one finds

$$\dot{a}^2 = \left[\frac{8\pi G}{3}\bar{\rho} + \frac{\Lambda c^2}{3} \right] a^2 + C, \quad (1.84)$$

where C is an integration constant which, if we rewrite it as $C = -kc^2$, turns eq. (1.84) into the first Friedmann equation (1.53a). In Newtonian gravity, the expansion of the Universe is thus the result of an isotropic tidal force acting on non-relativistic matter.

Chapter 2

The inhomogeneous universe

In the previous chapter we already introduced the notion of the universe as a maximally symmetric space. Clearly this is a highly idealized assumption and can only be approximately true – deviations, however small, must exist. In this chapter, we want to focus on such inhomogeneities and develop tools to describe them, as well as to create numerical realisations of Universes. A focus will be the development of tools in Fourier space, in which two-point correlators become diagonal, as we will see. As we have good reason to believe that the Universe is spatially flat, we will restrict ourselves to flat Euclidean space, i.e. we will from now on consider only random fields on \mathbb{E}^3 unless stated otherwise.

Random fields

In our study of the Universe, we will over and over encounter the notion of **random fields**. For our purposes, we can define them as stochastic processes taking values in three-dimensional Euclidean or Riemannian space (of constant curvature), or two- or three-dimensional tori \mathbb{T}^2 or \mathbb{T}^3 .

Definition 2.1 — Random fields as a stochastic process. A **stochastic process** f over a parameter space S is a collection of random variables

$$\{f(x) : x \in S\}. \quad (2.1)$$

If S is a space of dimension N , and the random variables $f(x)$ are vector-valued of dimension d , then we call the stochastic process f an (N, d) **random field** over S . If the random variables are tensor-valued of rank $n > 1$, we call the stochastic process a (N, d, n) random field over S .

The objects we will talk about are thus not the usual functions but random variables, parameterised by the space $x \in S$. The random variables $f(x)$ are usually real-valued, but can be complex-valued as well.

Fourier space: conventions and basic properties

We shall next introduce some aspects from harmonic analysis. Many (statistical) tools in cosmology are provided in Fourier space, where one works with a variable k (the ‘wave number’) that is the Fourier conjugate of a configuration-space variable x . Of course, Fourier transforms to other than spatial variables exist as

well (e.g., time \leftrightarrow frequency), but those will be of little concern in the present lecture, therefore we focus on Fourier transforms in the spatial domain in the following.

Definitions and key properties

Definition 2.2 — Fourier transform. We define the [Fourier transform](#) of a complex $(N, 1)$ random field f over \mathbb{R}^N analogously to that of a complex function $\mathbb{R}^N \rightarrow \mathbb{C}$. In the case of random fields, the Fourier transform yields another complex $(N, 1)$ random field \tilde{f} over \mathbb{R}^N . Hence for any complex $f \in L^1(\mathbb{R}^N)$ we define $\tilde{f}, \mathbb{R}^N \rightarrow \mathbb{C}$, as its Fourier transform

$$\tilde{f}(k) := \mathcal{F}[f](k) := \int_{\mathbb{R}^N} d^N x f(x) e^{-ik \cdot x}. \quad (2.2)$$

We say that \mathcal{F} maps f to [Fourier space](#). We caution that the precise sign and normalisation of the Fourier transform is a matter of definition. Here we adopt the convention that is consistent with what is adopted e.g. in `Numpy` to facilitate numerical implementations later.

From (2.2) it is trivial to show that the Fourier transform is linear, such that for $f_1, f_2 \in L^1(\mathbb{R}^N)$ with constants $a, b \in \mathbb{C}$ we have

$$\mathcal{F}[af_1 + bf_2] = a\mathcal{F}[f_1] + b\mathcal{F}[f_2]. \quad (2.3)$$

As it is linear, we can think of Fourier space simply as a representation of f in an alternative basis and of the Fourier transform as a *basis change*. One can demonstrate that the Fourier basis is in fact orthonormal and complete (in the sense that every $f \in L^1$ can be represented). In this new basis, several neat properties arise as we shall see in what follows.

We do not have to restrict ourselves to scalar functions or $(N, 1)$ random fields. Being linear, we simply define the Fourier transform component-wise for higher order objects.

Definition 2.3 — Fourier transform of vectors and tensors. We define the Fourier transform of vector or tensor valued fields and functions component-wise, i.e. for $f = (f_1, f_2, \dots)^\top$

$$\mathcal{F}[f] = (\mathcal{F}[f_1], \mathcal{F}[f_2], \dots)^\top \quad (2.4)$$

And equivalently for tensor objects $F = (f_{ijk})$, we define $(\mathcal{F}[F])_{ijk\dots} = \mathcal{F}[f_{ijk\dots}]$.

Theorem 2.1 — Shift theorem. Let T_y be the spatial translation operator, so that $(T_y f)(x) := f(x + y)$ for $y \in \mathbb{R}^N$, then

$$\mathcal{F}[T_y f](k) = \tilde{f}(k) e^{-ik \cdot y}. \quad (2.5)$$

The proof follows trivially from (2.2).

The implication is that translations can be represented by a simple multiplication with a k -dependent function in Fourier space. As we shall see below, this is just a special case of a convolution.

■ **Example 2.1** Consequently, any *multiplicatively separable* function \tilde{B} of multiple

variables in Fourier space

$$\tilde{B}(\mathbf{k}_1, \mathbf{k}_2, \dots, \mathbf{k}_n) := \tilde{f}_1(\mathbf{k}_1)\tilde{f}_2(\mathbf{k}_2) \cdots \tilde{f}_n(\mathbf{k}_n)$$

transforms under a spatial shift $T_y B = B(x_1 + y, x_2 + y, \dots, x_n + y)$ as

$$\mathcal{F}[T_y B] = \tilde{B}(\mathbf{k}_1, \mathbf{k}_2, \dots, \mathbf{k}_n) e^{ik_{12\dots n} \cdot y}, \quad (2.6)$$

where $\mathbf{k}_{12\dots n} := \mathbf{k}_1 + \mathbf{k}_2 + \dots + \mathbf{k}_n$. Thus, if \tilde{B} is invariant under translations for those values $\mathbf{k}_1, \dots, \mathbf{k}_n$ that fulfill the **closure condition** $\mathbf{k}_{12\dots n} = \sum_i \mathbf{k}_i \stackrel{!}{=} \mathbf{0}$. Note that geometrically it means that the vectors \mathbf{k}_i must form a closed loop (e.g. for three k 's a triangle). As a consequence, we have the following result. ■

Proposition 2.1 — Translation invariance. Translation invariant objects can be constructed out of multiplicatively separable functions with $n \geq 2$, obeying the **closure condition**, i.e. they must vanish for $\mathbf{k}_{12\dots n} \neq \mathbf{0}$.

Definition 2.4 — Parity transformations. We define the Hermitian conjugate of a function f as the parity transformation

$$(Pf)(\mathbf{x}) = f^*(-\mathbf{x}), \quad (2.7)$$

where the star denotes complex conjugation. We say that f is Hermitian, if $Pf = f$.

Lemma 2.1 The Fourier transform of a parity transformed field is given by

$$\mathcal{F}[Pf] = (\mathcal{F}[f])^* = \tilde{f}^*. \quad (2.8)$$

Proof.

$$\begin{aligned} \mathcal{F}[Pf](\mathbf{k}) &\stackrel{(2.2)}{=} \int_{\mathbb{R}^N} d^N x f^*(-\mathbf{x}) e^{-i\mathbf{k}\cdot\mathbf{x}} = \left(\int_{\mathbb{R}^N} d^N x f(-\mathbf{x}) e^{i\mathbf{k}\cdot\mathbf{x}} \right)^* \\ &\stackrel{\mathbf{y} := -\mathbf{x}}{=} \left(\int_{\mathbb{R}^N} d^N y f(\mathbf{y}) e^{-i\mathbf{k}\cdot\mathbf{y}} \right)^* = \mathcal{F}[f]^*(\mathbf{k}). \end{aligned}$$

■

In this book, we will mostly encounter real functions (as the fields/observables we are interested in are all real valued). While the Fourier transform of a real function is complex, it has the following important symmetry property.

Proposition 2.2 — Hermitian symmetry of real fields. If $f \in L^1(\mathbb{R}^N)$ is real valued, i.e. $\mathbb{R}^N \rightarrow \mathbb{R}$, then its Fourier transform \tilde{f} is complex $\mathbb{R}^n \rightarrow \mathbb{C}$ and *Hermitian*, i.e. it has the symmetry

$$P\tilde{f} = \tilde{f} \Leftrightarrow \tilde{f}(-\mathbf{k}) = \tilde{f}^*(\mathbf{k}) \quad \forall \mathbf{k}. \quad (2.9)$$

We leave the proof as an easy exercise.

Convolution products and the inverse Fourier transform

A key notion is that of the convolution product, which describes e.g. the processing of a signal by a filter.

Definition 2.5 — Convolution product. Let $f, g \in L^1(\mathbb{R}^N)$. We define the **convolution product** between f and g as

$$(f * g)(\mathbf{x}) := \int_{\mathbb{R}^N} d^N y f(\mathbf{x} - \mathbf{y}) g(\mathbf{y}). \quad (2.10)$$

The convolution product has most properties of the ordinary product. Let $f_1, f_2, f_3 \in L^1(\mathbb{R}^N)$, then the convolution product fulfills the following identities

$$f_1 * f_2 = f_2 * f_1 \quad \text{commutativity} \quad (2.11a)$$

$$f_1 * (f_2 + f_3) = f_1 * f_2 + f_1 * f_3 \quad \text{distributivity} \quad (2.11b)$$

$$f_1 * (f_2 * f_3) = (f_1 * f_2) * f_3 \quad \text{associativity} \quad (2.11c)$$

The straightforward proofs are left as an exercise. An important result of Fourier analysis is that convolution products become particularly simple in Fourier space.

Theorem 2.2 — Convolution theorem. Let $f, g \in L^1(\mathbb{R}^N)$, then the following property holds

$$\mathcal{F}[f * g] = \mathcal{F}[f] \mathcal{F}[g], \quad (2.12)$$

i.e. convolution products become ordinary products in Fourier space.

Proof.

$$\begin{aligned} \mathcal{F}[f * g](\mathbf{k}) &\stackrel{(2.10),(2.2)}{=} \int_{\mathbb{R}^N} d^N x \int_{\mathbb{R}^N} d^N y e^{-i\mathbf{k}\cdot\mathbf{x}} f(\mathbf{x} - \mathbf{y}) g(\mathbf{y}) \\ &\stackrel{\text{Fubini}, z:=x-y}{=} \int_{\mathbb{R}^N} d^N y \int_{\mathbb{R}^N} d^N z e^{-i\mathbf{k}\cdot(z+y)} f(z) g(y) \\ &= \int_{\mathbb{R}^N} d^N y \int_{\mathbb{R}^N} d^N z [f(z) e^{-i\mathbf{k}\cdot z}] [g(y) e^{-i\mathbf{k}\cdot y}] \\ &\stackrel{(2.2)}{=} \mathcal{F}[f](\mathbf{k}) \mathcal{F}[g](\mathbf{k}). \end{aligned}$$

■

The convolution theorem is a central result, we will use it over and over again. Its implications are particularly important also for numerical applications. Computing numerically the convolution product (2.10) for a vector of length n amounts to n^2 operations, so the algorithmic complexity is $\mathcal{O}(n^2)$. The Fast Fourier transform (FFT, cf. section 2) however has only a complexity of $\mathcal{O}(n \log n)$, and a simple product is $\mathcal{O}(n)$, so that convolutions become $\mathcal{O}(n \log n)$ with the FFT.

Definition 2.6 — Dirac- δ as multiplicative identity. The multiplicative unit $\mathbb{1}$ for the convolution product, defined as $f * \mathbb{1} = f$ defines the **Dirac- δ** distribution:

$$(f * \mathbb{1})(\mathbf{x}) = \int_{\mathbb{R}^N} d^N y f(\mathbf{x} - \mathbf{y}) \delta_D(\mathbf{y}) = f(\mathbf{x}) \quad (2.13)$$

By virtue of the existence of the multiplicative identity (2.13), (2.3), and (2.11), *the convolution product forms a commutative associative algebra*. Note that generally an inverse element however does not exist.

Proposition 2.3 — Fourier transform of Dirac- δ . The Dirac- δ distribution's Fourier transform follows from the convolution theorem as 1 (aka the 1 of \mathbb{C} under the standard product)

$$\mathcal{F}[\mathbf{1}] \equiv 1 \quad \text{since} \quad \mathcal{F}[f] = \mathcal{F}[f * \mathbf{1}] \stackrel{(2.12)}{=} \mathcal{F}[f] \mathcal{F}[\mathbf{1}]. \quad (2.14)$$

We therefore set $\delta_D \equiv \mathbf{1}$ (i.e. as the multiplicative one of the convolution product). It has the representation

$$\delta_D(\mathbf{x}) := \int_{\mathbb{R}^N} \frac{d^N k}{(2\pi)^N} e^{ik \cdot x}. \quad (2.15)$$

Proof. A formal proof would require us to dive into Schwartz space, and can be found in textbooks on distribution theory. To verify consistency of (2.15), we can however show that it $\mathcal{F}[\mathbf{1}] = 1$ is consistent with what we have said above. We have

$$\begin{aligned} \mathcal{F}[\mathbf{1}](\mathbf{l}) &\stackrel{(2.15), (2.2)}{=} \int_{\mathbb{R}^N} d^N x e^{-il \cdot x} \int_{\mathbb{R}^N} \frac{d^N k}{(2\pi)^N} e^{ik \cdot x} = \int_{\mathbb{R}^N} d^N x \int_{\mathbb{R}^N} \frac{d^N k}{(2\pi)^N} e^{i(k-l) \cdot x} \\ &\stackrel{m:=k-l}{=} \int_{\mathbb{R}^N} d^N x \int_{\mathbb{R}^N} \frac{d^N m}{(2\pi)^N} e^{im \cdot x} \stackrel{(2.15)}{=} \int_{\mathbb{R}^N} d^N x \delta_D(\mathbf{x}) \stackrel{(2.13)}{=} 1. \end{aligned}$$

■

Now that we have the multiplicative identity, we can use it to show that the Fourier transform has an inverse. In fact, having an inverse Fourier transform, there is a one-to-one mapping $f \leftrightarrow \tilde{f}$ between the two spaces.

Theorem 2.3 — Inverse Fourier transform. The inverse of the Fourier transform (2.2) is given by

$$\mathcal{F}^{-1}[\tilde{f}](\mathbf{x}) = \int_{\mathbb{R}^N} \frac{d^N k}{(2\pi)^N} \tilde{f}(\mathbf{k}) e^{ik \cdot x}, \quad (2.16)$$

so that $\mathcal{F}^{-1}[\mathcal{F}[f]] = f$.

Proof.

$$\begin{aligned} \mathcal{F}^{-1}[\mathcal{F}[f]](\mathbf{x}) &\stackrel{(2.2), (2.16)}{=} \int_{\mathbb{R}^N} \frac{d^N k}{(2\pi)^N} \left(\int_{\mathbb{R}^N} d^N y f(\mathbf{y}) e^{-ik \cdot y} \right) e^{ik \cdot x} \\ &\stackrel{\text{Fubini}}{=} \int_{\mathbb{R}^N} d^N y f(\mathbf{y}) \int_{\mathbb{R}^N} \frac{d^N k}{(2\pi)^N} e^{ik \cdot (x-y)} \\ &\stackrel{(2.15)}{=} \int_{\mathbb{R}^N} d^N y f(\mathbf{y}) \delta_D(x - \mathbf{y}) \stackrel{(2.13)}{=} f(x) \end{aligned}$$

■

Having found the inverse Fourier transform, we can prove the following important theorem.

Theorem 2.4 — Fourier transform of derivatives. One of the key features of working in Fourier space is that the Fourier basis is the eigenbasis of the

gradient ∇_x , whereby ∇_x turns into a simple product ik , specifically

$$\mathcal{F}[\nabla_x f](k) = ik \tilde{f}(k). \quad (2.17)$$

assuming that $ik\tilde{f} \in L^1$. The corresponding property holds for ∇_k derivatives in Fourier space, which become multiplication of f with $-ix$.

Proof.

$$\nabla_x f \stackrel{(2.16)}{=} \nabla_x \int_{\mathbb{R}^N} \frac{d^N k}{(2\pi)^N} \tilde{f}(k) e^{ik \cdot x} = \int_{\mathbb{R}^N} \frac{d^N k}{(2\pi)^N} (ik \tilde{f}(k)) e^{ik \cdot x} = \mathcal{F}^{-1}[ik \tilde{f}]$$

which is really just saying that

$$\nabla_x e^{ik \cdot x} = ik e^{ik \cdot x}$$

i.e. that $e^{\pm ik \cdot x}$ is an eigenvector of both ∇_x and ∇_k with eigenvalue $\pm ik$. ■

Correlations and their Fourier transform

We have seen in chapter 1 that the correlation structure of random fields is what characterizes them. The correlation function we used there is intimately connected to the following definition of a correlation product.

Definition 2.7 — Correlation product. Let $f, g \in L^1(\mathbb{R}^N)$. We define the correlation product of f and g by employing the “ \star ” symbol (not to be confused with the convolution denoted with the “ $*$ ” symbol)

$$(f \star g)(x) := \int_{\mathbb{R}^N} d^N y f^*(y) g(x + y). \quad (2.18)$$

Note the complex conjugated first field, as well as the reversed sign in the argument of g compared to the definition of the convolution product (2.10). Note that unlike the convolution product, we have $f \star g \neq g \star f$, unless both f and g are Hermitian.

As we will see next, there is a particularly simple relation between the correlation product and convolutions.

Lemma 2.2 — Relation between convolution and correlation. The following relation holds between convolution $(*)$ and correlation (\star) products

$$f \star g = (Pf) * g \quad (2.19)$$

and therefore follows from (2.8) also

$$\mathcal{F}[f \star g] = (\mathcal{F}[f])^* \mathcal{F}[g] \quad (2.20)$$

Proof.

$$\begin{aligned} (f \star g)(x) &\stackrel{(2.18)}{=} \int_{\mathbb{R}^N} d^N y f^*(y) g(x + y) \stackrel{(2.7)}{=} \int_{\mathbb{R}^N} d^N y (Pf)(-y) g(x + y) \\ &\stackrel{z:=x+y}{=} \int_{\mathbb{R}^N} d^N z (Pf)(x - z) g(z) \stackrel{(2.10)}{=} (Pf) * g \end{aligned}$$

■

Finally, the lemma above implies the following key theorem of harmonic analysis.

Theorem 2.5 — Wiener-Khinchin theorem. The Fourier transform of the auto-correlation product of f with itself is given by its power spectrum, defined as

$$\mathcal{F}[f * f](\mathbf{k}) = |\tilde{f}(\mathbf{k})|^2 =: P_{ff}(\mathbf{k}). \quad (2.21a)$$

The proof follows directly from (2.20) assuming that the Fourier transform and the autocorrelation function exist. It is also important to note that for a general correlation, we have

$$\mathcal{F}[f * g](\mathbf{k}) = \tilde{f}^*(\mathbf{k}) \tilde{g}(\mathbf{k}). \quad (2.21b)$$

Theorem 2.6 — Extension to periodic functions. The Fourier transform and all the properties we have discussed so far can be extended to periodic functions, i.e. functions defined on a torus \mathbb{T}^N . The only difference is that the Fourier transform is defined only for a set of discrete Fourier modes, and the inverse Fourier transform is a sum over these dual modes, i.e. we define in the periodic case the Fourier transform and its inverse as

$$\tilde{f}(\mathbf{m}) := \int_{\mathbb{T}^N} d^N x f(x) e^{-i 2\pi \mathbf{m} \cdot \mathbf{x}}, \quad \mathbf{m} \in \mathbb{Z}^N, \quad (2.22a)$$

and

$$f(\mathbf{x}) := \sum_{\mathbf{m} \in \mathbb{Z}^N} \tilde{f}(\mathbf{m}) \exp(i 2\pi \mathbf{m} \cdot \mathbf{x}) \quad (2.22b)$$

if the sum is convergent.

Random field statistics

We have already discussed random fields to some extent, but we haven't connected them yet to their underlying probability distributions. We shall do this next.

Basic statistical concepts

We begin with a few basic statistical concepts.

Definition 2.8 — Probability density. Consider a d -dimensional random variable $\mathbf{F} = (F_1, \dots, F_d) \in \Omega \subseteq \mathbb{R}^d$ drawn from some random process $\mathbf{F} \sim \mathcal{P}_F$. We define its **probability density** (PDF) $p : \Omega \rightarrow \mathbb{R}_{0+}$ in such a way that the probability that $\mathbf{F} \in B \subseteq \Omega$ is given by

$$\mathbb{P}[\mathbf{F} \in B] = \int_B d^N f p(f) \quad (2.23)$$

Naturally, p must be normalised so that $\mathbb{P}[\mathbf{F} \in \Omega] = 1$, and we want positive probabilities $\mathbb{P}[\mathbf{F} \in A] \geq 0$ for any subset $A \subseteq \Omega$ – this implies $p \geq 0$.

Definition 2.9 — Conditional probability. We define the **conditional probability**

for $F \in B$, given that also $F \in A$,

$$\mathbb{P}[F \in B \mid F \in A] = \frac{\mathbb{P}[F \in (B \cap A)]}{\mathbb{P}[F \in A]}. \quad (2.24)$$

With these definitions, the probability that a random variable takes on some range of values is connected to an integral over a domain of the probability density function.

Using the PDF, we can also calculate the expectation value of any (linear or non-linear) combination of random variables.

Definition 2.10 — Expectation value. The **expectation value** of a function $g : \mathbb{R}^N \rightarrow \mathbb{R}$ of a random variable $F \sim \mathcal{P}_F$ is defined as

$$\mathbb{E}[g(F)] := \int_{\mathbb{R}^N} d^N f g(f) p(f). \quad (2.25)$$

Generally, we can expand the probability distribution function in terms of monomials, that together will fully describe the PDF (in the sense that the monomials provide a basis).

Definition 2.11 — Moments. The expectation values of the monomials we call **moments of the distribution**. For the n -th moment, we set

$$m_F^{(n)} := \mathbb{E}[F^{\otimes n}] = \int_{\mathbb{R}^N} d^N f f^{\otimes n} p(f), \quad (2.26)$$

where the power is taken w.r.t. the outer product. This implies immediately that the zeroth moment (normalisation) is a scalar, the first (mean) a vector, the second a symmetric matrix (aka the ‘covariance matrix’, see below), and so on.

Alternatively to the probability density function, any random field can be described by its **characteristic function** $\tilde{p}(\kappa)$ which is the Fourier transform of its PDF (the characteristic function could also be defined through a Laplace transform).

Definition 2.12 — Characteristic function. Define the **characteristic function** $\tilde{p}(\kappa)$ of an N -variate distribution $p(f)$ with $f = (f_1, \dots, f_N)^\top$, $\kappa = (\kappa_1, \dots, \kappa_N)^\top$ as

$$\tilde{p}(\kappa) := \mathbb{E}[e^{-i\kappa \cdot F}] = \int d^N f p(f) e^{-i\kappa \cdot f}, \quad (2.27)$$

with inverse

$$p(f) = \int \frac{d^N \kappa}{(2\pi)^N} \tilde{p}(\kappa) e^{i\kappa \cdot f}. \quad (2.28)$$

Proposition 2.4 — Generating function for moments. The characteristic function acts as a **generating function** from which the moments of the probability distribution can be defined in terms of derivatives, i.e.,

$$\mathbb{E}[F_{j_1} \cdots F_{j_n}] = \lim_{\kappa \rightarrow 0} \left(i^n \frac{\partial}{\partial \kappa_{j_1}} \cdots \frac{\partial}{\partial \kappa_{j_n}} \tilde{p}(\kappa) \right). \quad (2.29)$$

The proof is analogous to that of (2.17).

We will come back to this property shortly.

Gaussian random variables

We begin with the probability density function for Gaussian fields, as well as state some basic properties for Gaussian random variables.

Definition 2.13 — Gaussian distribution. Let $f = [f_1, \dots, f_N]$ be an N -dimensional vector of random variables; f is called **Gaussian** if its joint **probability density** function p is a multivariate Gaussian, or, a normal distribution and henceforth dubbed \mathcal{N} , i.e., $F \sim \mathcal{N}(\mu, C)$ with PDF

$$p_{\mathcal{N}}(f | \mu, C) := \frac{1}{\sqrt{(2\pi)^N \det C}} \exp \left[-\frac{1}{2}(f - \mu)^\top C^{-1}(f - \mu) \right], \quad (2.30)$$

where C is the $N \times N$ positive definite and symmetric **covariance matrix** with real entries (thus C can be diagonalised), and μ is the vector of mean values. *A Gaussian distribution is fully specified by its mean and covariance matrix. An uncorrelated distribution has a diagonal covariance matrix, which allows it to be represented as a product of N univariate Gaussian PDFs.*

The pre-factor on the RHS of eq. (2.30) is to ensure that the probability density satisfies the appropriate normalisation condition such that it integrates to unity, i.e., $\int d^N f p_{\mathcal{N}}(f) = 1$ (cf. Eq. 2.26). More generally, the first three moments of a Gaussian distribution are

$$\mathbb{E}[1] = 1, \quad \mathbb{E}[F] = \mu, \quad \mathbb{E}[F \otimes F] = C + \mu \otimes \mu. \quad (2.31)$$

Proposition 2.5 — Characteristic function for Gaussian distribution. Furthermore, for a Gaussian field, using the PDF (2.30), the left integral in (2.27) can be explicitly calculated as it is a standard N -dimensional Gaussian integral with linear term, leading to

$$\tilde{p}_{\mathcal{N}}(\kappa | \mu, C) = \exp \left[-i\kappa^\top \mu - \frac{1}{2}\kappa^\top C \kappa \right], \quad (2.32)$$

which is an exponential with quadratic polynomial in κ . As a consequence, all moments are fully specified by products of μ and C . We leave the proof as an exercise.

Proposition 2.6 — Gaussianity of linear combinations of Gaussian random variables. A linear combination of uncorrelated Gaussian random variables $x_1, x_2, \dots \sim \mathcal{N}(0, 1)$

$$y := \beta + \alpha_1 x_1 + \alpha_2 x_2 + \dots \quad \beta, \alpha_1, \alpha_2, \dots \in \mathbb{R} \quad (2.33)$$

yields a Gaussian random variable

$$y \sim \mathcal{N}(\beta, \beta^2 + \alpha_1^2 + \alpha_2^2 + \dots). \quad (2.34)$$

More generally, consider a general $N \times N$ matrix A and an N -variate Gaussian random variable $x \sim \mathcal{N}(\mu, C)$, then

$$Ax \sim \mathcal{N}(A\mu, A C A^\top). \quad (2.35)$$

By contrast, any variable that is a non-linear combination of Gaussian variables, does not follow a Gaussian distribution. We say that it is *non-Gaussian*. Again, we leave the proof as a simple exercise.

Theorem 2.7 — Marcinkiewicz (1939) . Of particular importance here is **Marcinkiewicz' theorem** which states that the normal distribution (and as its limit also the Dirac δ -distribution) is the only distribution for which the characteristic function takes the form $\tilde{p}(k) = \exp[q_m(k)]$, where $q_m(k)$ is a polynomial of finite order m (with $m = 2$ in the case of the normal distribution and $m = 1$ in the case of the Dirac- δ -distribution).

By contrast, all *finite* higher-order polynomials in k are ruled out in the exponential of the characteristic function, as the positive definiteness of the corresponding probability distribution would be lost. The proof can be found in (Marcinkiewicz, 1939).

Random fields and their distributional properties

We are now in the position to connect the notion of a random field to its underlying distributional properties rather than just an abstract stochastic process. The following notion is of key importance: the distributional properties of a random field f are fully specified by forming a vector of its field values at $n \geq 1$ arbitrary points $(f(x_1), \dots, f(x_n))$ and specifying the joint n -variate probability distribution for these values. This is formalised in the following theorem.

Theorem 2.8 — Kolmogorov consistency theorem. The distributional properties of an (N, d) random field over S are determined by the entirety of its finite-dimensional probability distributions. Let $F_n := (f(x_1), \dots, f(x_n))$, then for all $n \geq 1$

$$\mathbb{P}[F_n \in B_1 \times \dots \times B_n] = \int_{B_1} d\mathfrak{f}_1 \dots \int_{B_n} d\mathfrak{f}_n p_n(\mathfrak{f}_1, \dots, \mathfrak{f}_n | x_1, \dots, x_n), \quad (2.36)$$

for all collections $\{x_j\}_{1 \leq j \leq n}$, and $B_{1\dots n} \subset \mathbb{R}^d$. Further, p_n is the joint probability density of field values $\mathfrak{f}_1, \dots, \mathfrak{f}_n$ given the n points x_1, \dots, x_n . This uniquely defines the stochastic process.

Proof. Proofs can be found in textbooks on stochastic processes or mathematical statistics; they go beyond what we need here in terms of mathematical rigour. ■

Gaussian random fields

A case of key importance in a variety of scientific disciplines is that of a **Gaussian random field** (GRF). Given any random field f over S , Theorem 2.8 states that we need to specify the finite dimensional distributions for $(f(x_1), \dots, f(x_n))$ with $1 \leq n < \infty$ and all $(x_1, \dots, x_n) \in S^n$. For a GRF, these will all be Gaussian.

Definition 2.14 — Gaussian random field. A GRF is defined as a random field for which the n -dimensional random variable $(f(x_1), \dots, f(x_n))$ with $1 \leq n < \infty$ are drawn from an n -variate Gaussian. Since Gaussians are determined by their mean vector and their covariance matrix, a GRF is fully determined by its mean

and covariance functions

$$\mu(\mathbf{x}) = \mathbb{E}[f(\mathbf{x})], \quad (2.37a)$$

$$C(\mathbf{x}_1, \mathbf{x}_2) = \mathbb{E}[(f(\mathbf{x}_1) - \mu(\mathbf{x}_1))(f(\mathbf{x}_2) - \mu(\mathbf{x}_2))]. \quad (2.37b)$$

Definition 2.15 — Gaussian random field of non-scalar variables. The definition above applies to $(N, 1)$ random fields. In the case of vectorial or tensorial fields \mathbf{f} , we define the correlator using the outer product. In the case of vectors, i.e. (N, d) fields, this renders the correlator a $d \times d$ matrix.

$$\mu(\mathbf{x}) = \mathbb{E}[\mathbf{f}(\mathbf{x})], \quad (2.38)$$

$$C(\mathbf{x}_1, \mathbf{x}_2) = \mathbb{E}[(\mathbf{f}(\mathbf{x}_1) - \mu(\mathbf{x}_1)) \otimes (\mathbf{f}(\mathbf{x}_2) - \mu(\mathbf{x}_2))]. \quad (2.39)$$

As in the scalar case, for Gaussian \mathbf{f} , these two functions determine all of its statistical properties.

We employ the shorthand notation $f_i := f(\mathbf{x}_i)$, $\mathbf{f} = (f_1, \dots, f_n)^\top$ and thus, the formula (2.30), valid for an n -variate Gaussian, applies also in the present case.

Homogeneous and isotropic GRFs

For a centered [homogeneous and isotropic](#) Gaussian random field, we write

$$\mu(\mathbf{x}) = 0, \quad (2.40a)$$

$$C(\mathbf{x}_1, \mathbf{x}_2) =: \xi(\|\mathbf{x}_1 - \mathbf{x}_2\|) =: \begin{cases} \xi_{12} & \text{if } \mathbf{x}_1 \neq \mathbf{x}_2 \\ \sigma^2 & \text{if } \mathbf{x}_1 = \mathbf{x}_2 \end{cases}. \quad (2.40b)$$

The one and two-point PDFs of a homogeneous, isotropic, and centered Gaussian random field are therefore given by

$$p_1(f \mid \mathbf{x}) = p(f) = \frac{1}{\sqrt{2\pi\sigma^2}} \exp\left(-\frac{1}{2}\frac{f^2}{\sigma^2}\right), \quad (2.41a)$$

$$p_2(f_1, f_2 \mid \mathbf{x}_1, \mathbf{x}_2) = p(f_1, f_2 \mid \|\mathbf{x}_1 - \mathbf{x}_2\|) = \frac{1}{\sqrt{(2\pi)^2 \det C_{12}}} \exp\left(-\frac{1}{2}\mathbf{f}^\top C_{12}^{-1} \mathbf{f}\right), \quad (2.41b)$$

where the covariance matrix and its inverse are respectively

$$C_{12} = \begin{pmatrix} \sigma^2 & \xi_{12} \\ \xi_{12} & \sigma^2 \end{pmatrix}, \quad C_{12}^{-1} = \frac{1}{\sigma^4 - \xi_{12}^2} \begin{pmatrix} \sigma^2 & -\xi_{12} \\ \xi_{12} & \sigma^2 \end{pmatrix}. \quad (2.42)$$

In the Gaussian case, all higher-order PDFs are expressible in terms of these two. We have e.g. the three-point PDF (for a general GRF, not necessarily centered, isotropic, or homogeneous)

$$\begin{aligned} p_3(f_1, f_2, f_3 \mid \mathbf{x}_1, \mathbf{x}_2, \mathbf{x}_3) &= p_2(f_1, f_2 \mid \mathbf{x}_1, \mathbf{x}_2) p_1(f_1 \mid \mathbf{x}_3) \\ &\quad + p_2(f_2, f_3 \mid \mathbf{x}_2, \mathbf{x}_3) p_1(f_2 \mid \mathbf{x}_1) \\ &\quad + p_2(f_3, f_1 \mid \mathbf{x}_3, \mathbf{x}_1) p_1(f_3 \mid \mathbf{x}_2), \end{aligned} \quad (2.43)$$

whose expectation value vanishes for a centered distribution. Of course, for a homogeneous and isotropic field, it only depends on $x_{12} := \|\mathbf{x}_1 - \mathbf{x}_2\|$, $x_{23} := \|\mathbf{x}_2 - \mathbf{x}_3\|$, and $x_{31} := \|\mathbf{x}_3 - \mathbf{x}_1\|$.

Exercise 2.1 Use eq. (2.29) to show that $\mathbb{E}[FF^\top] = C$ in the Gaussian case and thus, that the components of the covariance matrix are given by the correlation function. ■

Higher-order statistics

We have already seen from (2.43) that higher-order statistics for Gaussian random fields must be constructed out of the mean and covariance functions. This is formalised in the following theorem.

Theorem 2.9 — Isserlis' / Wick's theorem. Let $(f_1, \dots, f_n) := (f(x_1), \dots, f(x_n))$ be an n -variate Gaussian random variable with zero mean (i.e. centered), then

$$\mathbb{E}[f_1 f_2 \dots f_n] = \begin{cases} \sum_{p \in P_n^2} \prod_{\{i,j\} \in p} \underbrace{\mathbb{E}[f_i f_j]}_{=C(x_i, x_j)} & \text{if } n \text{ is even} \\ 0 & \text{if } n \text{ is odd} \end{cases} \quad (2.44)$$

where the sum is over all distinct partitions p of $\{1, \dots, n\}$ into pairs $\{i, j\}$, and the product is over the pairs in p . The proof can be found in all textbooks on statistics. In the physics literature, Isserlis' theorem is commonly called [Wick's theorem](#).

■ **Example 2.2** For $n = 4$, we have for Gaussian random variables

$$\mathbb{E}[f_1 f_2 f_3 f_4] = \mathbb{E}[f_1 f_2] \mathbb{E}[f_3 f_4] + \mathbb{E}[f_1 f_3] \mathbb{E}[f_2 f_4] + \mathbb{E}[f_1 f_4] \mathbb{E}[f_2 f_3]$$

As a direct consequence of Isserlis' theorem, for any Gaussian field with vanishing mean, any n -point correlator (or its Fourier counterpart) with $n > 2$ must either vanish or be representable in terms of (products of) two-point correlators. By contrast, due to Marcinkiewicz' theorem, any field with non-Gaussian distribution must excite an infinite hierarchy of (intrinsic/connected) n -point correlators that are not representable in terms of m -point correlators with $m < n$ alone. We shall come back to this in section 2 when discussing cumulants which are the intrinsic correlations in the moments of the probability distribution.

GRFs in Fourier space

Theorem 2.10 — Basis change for Gaussian random fields. By virtue of Proposition 2.6, a linear combination of independent Gaussian random variables is again a Gaussian random variable. As a consequence, a Gaussian random field remains a Gaussian random field under any basis change – in particular when going to and from Fourier space. This is obvious in the finite dimensional case, we leave the infinite dimensional case as a conjecture.

Therefore, also in Fourier space, a Gaussian random field is fully determined by its mean function and its two-point function. We have proven the Wiener-Khinchin theorem stating that the Fourier transform of the correlation product is the power spectrum.

We can form the Fourier-space two-point correlator

$$\tilde{C}_{ff}(\mathbf{k}_1, \mathbf{k}_2) := \mathbb{E}[\tilde{f}(\mathbf{k}_1) \tilde{f}(\mathbf{k}_2)]. \quad (2.45)$$

For real fields, and requiring translation invariance (i.e. homogeneity, cf. Proposition 2.1), we then have

$$\tilde{C}_{ff}(\mathbf{k}_1, \mathbf{k}_2) = \delta_D(\mathbf{k}_1 + \mathbf{k}_2) P_{\text{hom}}(\mathbf{k}_1), \quad (2.46)$$

where $P_{\text{hom}}(\mathbf{k})$ is the homogeneous power spectrum. This implies that for stationary (homogeneous) processes, the correlator in Fourier space is diagonal. If we further require isotropy, then we have to eliminate directional information, and we have

$$\tilde{C}_{ff}(\mathbf{k}_1, \mathbf{k}_2) = \delta_D(\mathbf{k}_1 + \mathbf{k}_2) P_{\text{hom iso}}(\|\mathbf{k}_1\|). \quad (2.47)$$

Generating a Gaussian random field

When generating Gaussian random fields, we will always use white noise as a starting point for our numerical investigation, on which we will impose a desired form of correlations in a later step.

Definition 2.16 — White noise. A so-called *white* Gaussian random field $w(\mathbf{x})$ is a field with no correlations whatsoever, i.e. its correlator is diagonal

$$\mathbb{E}[w(\mathbf{x})w(\mathbf{y})] = \sigma^2 \delta_D(\mathbf{x} - \mathbf{y}), \quad (2.48)$$

where $\sigma^2 \geq 0$ is a constant reflecting the variance. It follows that the power spectrum of a white noise field is constant, i.e. $P(k) \propto \sigma^2$.

Exercise 2.2 Prove that the power spectrum of a white Gaussian field is constant.

Our three-dimensional Gaussian random field realisation shall be described as a discrete field, i.e. we consider random fields over S^d where $S \subseteq \mathbb{N}$ instead of \mathbb{R}^d . We can imagine that we know the value at equally spaced discrete locations, i.e. let $h \in \mathbb{R}$ be the ‘grid spacing’ and $N_g \in \mathbb{N}$ the linear lattice size, then the discretised field can be written as

$$\mathbf{x}[\mathbf{n}] := nh \in \mathbb{R}^N \quad \text{where} \quad \mathbf{n} \in \{0, \dots, N_g - 1\}^N \subset \mathbb{Z}^N, \quad (2.49a)$$

$$f[\mathbf{n}] := f(nh) \quad (2.49b)$$

so that

$$f[\mathbf{n}] = f(\mathbf{x}[\mathbf{n}]) = f(nh). \quad (2.49c)$$

and consists of $M := N_g^N$ sites, and we think of the discrete f approaching the continuous as $h \rightarrow 0$.

For numerical applications, it is often useful to ‘linearise’ the index through any bijective map, e.g. $(i, j, k) \mapsto I$ with $I = (iN_g + j)N_g + k$. A discrete white Gaussian random field can be generated by sampling each site $f_I = f[\mathbf{n}]$ independently from a normal distribution $f_I \sim \mathcal{N}$. Since it is an uncorrelated ‘white’ field, the covariance matrix of the joint distribution is exactly diagonal, i.e., $C = I_M$, and the joint probability distribution functions factorises into the product

$$p(f_0, f_1, \dots, f_{M-1}) = \frac{\exp\left[-\frac{1}{2}\mathbf{f}^\top C^{-1}\mathbf{f}\right]}{\sqrt{(2\pi)^M \det C}} = \prod_{i=0}^{M-1} p_{\mathcal{N}}(f_i). \quad (2.50)$$

In this case, the Gaussian random field can be trivially generated by drawing a vector of M statistically independent Gaussian random numbers. The vector $\mathbf{f} = (f_0, \dots, f_{M-1})^T$ can be produced using a Gaussian random number generator, as e.g. provided by the Box-Muller transform.

Generating uncorrelated Gaussian random numbers

If we want to draw a random number from a normal distribution, we face the problem that often on computers we only have access to a random number generator for uniform distributions. Let us assume we have such a random number generator at hand, which is able to generate uncorrelated pseudo random numbers from the uniform distribution $u \sim \mathcal{U}(0, 1]$. We aim to turn this number into a number from the normal distribution $X \sim \mathcal{N}(0, 1)$.

Proposition 2.7 — Box-Muller Gaussian generator. Given two random variables $u, v \sim \mathcal{U}(0, 1)$ drawn from the uniform distribution over $(0, 1]$, the transformed variables x, y where

$$x = r \cos(2\pi v) \quad \text{and} \quad y = r \sin(2\pi v) \quad \text{with} \quad r := \sqrt{-2 \log u} \quad (2.51)$$

are normally distributed, i.e. $x, y \sim \mathcal{N}(0, 1)$.

Proof. Recall the Gaussian PDF

$$p_{\mathcal{N}}(x) = \frac{1}{\sqrt{2\pi}} \exp\left(-\frac{1}{2}x^2\right) \quad (2.52)$$

with cumulative distribution function (CDF)

$$F_{\mathcal{N}}(x) := \int_{-\infty}^x dx p_{\mathcal{N}}(x) = \frac{1}{2} \left[1 + \operatorname{erf}\left(\frac{x}{\sqrt{2}}\right) \right]. \quad (2.53)$$

The probability that X is less than a given value x is

$$\mathbb{P}[X < x] = F_{\mathcal{N}}(x). \quad (2.54)$$

This implies that a normally distributed random number can be generated by inverting \mathcal{C} , i.e. for a uniform random number $u \in (0, 1]$, $x = \mathcal{C}^{-1}(u)$ is normally distributed. Unfortunately this method is not practical as no closed form expression for \mathcal{C}^{-1} exists, so that it needs to be approximated. A more simple and also exact method is the ‘Box-Muller’ transform method. If one realises that by going to two dimensions, instead of drawing a pair (x, y) from a normal distribution, one can also draw a squared radius $q = r^2$ from a χ^2 distribution with 2 degrees of freedom, and an angle $\alpha \in (0, 2\pi]$ uniformly, then $x = r \cos \alpha$ and $y = r \sin \alpha$ are normally distributed. The CDF of the 2 d.o.f. χ^2 distribution is $F(q; 2) = 1 - \exp(-q/2)$. Applying again the inversion trick for a uniform $u \in (0, 1]$ so that $u = F(q; 2)$ yields $q = -2 \log(1 - u)$ or, since $1 - u$ is also uniform $r = \sqrt{-2 \log u}$. With a second uniform $v \in (0, 1]$ one then finds two normally distributed numbers $x = r \cos(2\pi v)$ and $y = r \sin(2\pi v)$. ■

Now that we know how to generate uncorrelated numbers $\mathbf{n} = (n_0, n_1, \dots, n_{M-1})$ with $n_i \sim \mathcal{N}(0, 1)$, we need to find a way to impose a desired correlation structure. We shall discuss this next.

Correlated noise – Method 1: Eigendecomposition. If we want to generate a field with correlations, then the covariance matrix \mathbf{C} will not be diagonal, and we have to follow a more involved approach. First, we note that the linear combination of any number of Gaussian random variables is a Gaussian random variable (cf. Proposition 2.6). Thus, we can simply diagonalise the covariance matrix with $\Lambda = \mathbf{S}^\top \mathbf{C} \mathbf{S}$, where $\Lambda := \text{diag}(\lambda_0, \dots, \lambda_{M-1})$ and let $\mathbf{v}_0, \dots, \mathbf{v}_{M-1}$ be the *normalised* eigenvectors of \mathbf{C} . Then,

$$f_i = \mathbf{v}_i^\top \Lambda^{1/2} \mathbf{n}, \quad \Lambda^{1/2} := \text{diag}(\sqrt{\lambda_0}, \dots, \sqrt{\lambda_{M-1}}) \quad (2.55)$$

yield samples from the M -variate target distribution with covariance matrix \mathbf{C} .

This eigendecomposition of a stochastic process is also called a [Karhunen-Loève decomposition](#). According to the Kosambi-Karhunen-Loève theorem, a stochastic process can be represented by an (infinite) linear combination of orthogonal functions

$$f(\mathbf{x}) = \sum_{i=0}^{\infty} \sqrt{\lambda_i} v_i(\mathbf{x}) n_i, \quad (2.56a)$$

We leave the proof that a Karhunen-Loève decomposition yields the correct distribution as an exercise for the interested reader. The coefficients n_i are uncorrelated Gaussian random numbers with unit variance, and the functions $v_i(\mathbf{x})$ are the eigenfunctions of the covariance operator, i.e. they fulfill the following operator eigenvalue equation

$$\int d^N x \mathbf{C}(\mathbf{x}, \mathbf{y}) v_i(\mathbf{y}) = \lambda_i v_i(\mathbf{x}). \quad (2.56b)$$

An explicit diagonalisation of the covariance matrix is however only feasible for small matrices, as the computational effort scales with the cube of the number of points.

Correlated noise – Method 2: Cholesky Factorization. Computationally it is much simpler to obtain however the Cholesky factorization of \mathbf{C} rather than the eigendecomposition. The [Cholesky factorization](#) is defined for positive definite Hermitian matrices, a condition fulfilled by the positive definite symmetric covariance matrix. It can therefore be written in terms of a lower triangular matrix \mathbf{L} as

$\mathbf{C} =: \mathbf{L} \mathbf{L}^\top$ from which follows $f = \mathbf{L} \mathbf{n}$

(2.57)

 Important algorithm to generate multi-variate Gaussian random numbers with given covariance matrix.

(This factorization also holds for complex matrices, if the “ \top ” is replaced with the conjugate transpose).

Proof. It is easy to prove that this works. We have $\mathbb{E}[\mathbf{n} \mathbf{n}^\top] = \mathbf{I}_M$ for the uncorrelated Gaussian random numbers. Then

$$\mathbb{E}[f f^\top] = \mathbb{E}[(\mathbf{L} \mathbf{n})(\mathbf{L} \mathbf{n})^\top] = \mathbb{E}[\mathbf{L} \mathbf{n} \mathbf{n}^\top \mathbf{L}^\top] = \mathbf{L} \mathbb{E}[\mathbf{n} \mathbf{n}^\top] \mathbf{L}^\top = \mathbf{L} \mathbf{L}^\top = \mathbf{C},$$

which is the required covariance. Note that the mean can be shifted by simply adding the desired mean function. ■

Correlated noise – Method 3: Fourier Transformation. The approaches discussed above are practicable only when the covariance matrix is small. For a spatial field, the covariance matrix is quadratic in the number of points at which we want to sample the field – a huge number for a two- or three-dimensional field. The approaches above work of course for any multivariate normal distribution with given (sufficiently well behaved) correlation structure. For spatial fields, it is more efficient however to notice that in Fourier space the covariance between modes is already diagonal for a stationary field, as expressed by the definition of the power spectrum (2.47). Assume now that we consider a discrete set of distinct wave numbers k_i . Then we can rewrite the definition of the power spectrum as the diagonal covariance matrix

$$\tilde{C}_{ij} := \mathbb{E}[\tilde{\delta}(k_i) \tilde{\delta}(k_j)] =: (2\pi)^3 P(k_i) \delta_D(k_i + k_j). \quad (2.58)$$

If we define $k'_j := -k_j$, then the covariance matrix is diagonal in Fourier space, i.e.

$$\tilde{C}_{ij} = \mathbb{E}[\tilde{\delta}(k_i) \tilde{\delta}(-k'_j)] \stackrel{\text{real}}{=} \mathbb{E}[\tilde{\delta}(k_i) \tilde{\delta}^*(k'_j)] = (2\pi)^3 P(k_i) \delta_{ij}. \quad (2.59)$$

TBD there should be a linear relation from Hermitian -> real covariance matrix. Since the covariance is diagonal, the Fourier basis is the eigenbasis in the Kosambi-Karhunen-Loëve theorem. We can therefore generate a Gaussian random field by first generating uncorrelated Gaussian random numbers in Fourier space, and then transforming back to real space. The eigenvalues (or Fourier coefficients) are given by

$$\tilde{f}_i = (2\pi)^{3/2} \sqrt{P(k_i)} n_i \quad n_i \sim \mathcal{N}(0, 1). \quad (2.60)$$

with eigenvectors given by the Fourier basis $\tilde{v}_i(x) = e^{ik_i \cdot x}$ and the Hermitian constraint enforced. The field is then obtained by inverse Fourier transformation (see below). In the context of a finite basis, the Fourier transform is a discrete Fourier transform (DFT) which we shall discuss in more detail next.

The Discrete Fourier Transform (DFT): basics

In practice, it is more convenient to work with uniformly discretized fields with a compact support. We thus assume from now on that our random fields are defined on a torus \mathbb{T}^d . The DFT is most efficiently performed numerically by a fast Fourier transform (FFT), which assumes that both the x and k are arranged on a regular grid. With the [grid spacing](#) h from above and $N_g \in \mathbb{N}$ discretisation points, we get the respective discrete Fourier modes

$$k[m] = m k_0, \quad (2.61)$$

$$\text{where } k_0 = \frac{2\pi}{n_g h}, \quad \text{and } m \in (-N_g/2, \dots, N_g/2]^d \subset \mathbb{Z}^d.$$

Definition 2.17 — Discrete Fourier Transform (DFT). Consider a function or field $f[n]$ sampled at N_g discrete locations. The one-dimensional discrete Fourier transform and its inverse can then be defined as

$$\tilde{f}[m] := \sum_{n=0}^{N_g-1} f[n] e^{-i2\pi mn/N_g} \quad f[n] = \frac{1}{N_g} \sum_{m=0}^{N_g-1} \tilde{f}[m] e^{i2\pi mn/N_g}. \quad (2.62)$$

Observe that the modes $\exp(\pm i2\pi mn)$ form an orthogonal basis

$$\sum_{l=0}^{N_g-1} e^{i2\pi ml} e^{-i2\pi ln} = N_g \delta_{mn}, \quad (2.63)$$

where δ_{mn} is the Kronecker delta. Relation (2.63) is essentially the discrete counterpart of equation (2.15) which defines the Dirac delta in the continuous case. Multi-dimensional transforms are trivially constructed by outer products.

Aliasing. It is important to recognise the intrinsic cyclic character of the discrete Fourier transform when evaluated on a limited amount of grid points N : the wave modes $\exp(i2\pi mn/N_g)$ and $\exp(i2\pi m(n + N_g)/N_g)$, $\exp(i2\pi m(n + 2N_g)/N_g)$, etc., are indistinguishable due to cyclic rotations, implying that if “accidentally” a mode beyond the largest sampled frequency $k_{n=N/2} = \pi/h \equiv k_{Ny}$ is excited, then a mode k_n may not appear at the correct frequency, but at its “alias” $k_{n \bmod N_g}$. Here, k_{Ny} is the [Nyquist frequency](#).

Python implementation of Gaussian random field generation

Exercise 2.3 — Numerically sampling a GRF. Familiarize yourself with the technique how to generate Gaussian random fields with a given correlation structure using the discrete Fourier transform in PYTHON described below. Try to reproduce first the plots shown there. Then, consider power law spectra of the form $P(k) \propto k^{-\alpha}$. Make different realisations of a cosmic density contrast field $\delta(x)$ as a Gaussian random fields with the given power spectrum $P(k)$ for different values of α and resolutions. Document and describe qualitatively your findings. ■

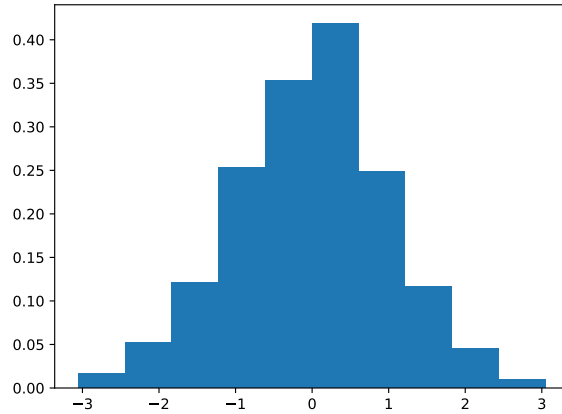
Uncorrelated fields. We can readily produce vectors or fields of normal distributed random numbers in python using the `random.normal` function from the `numpy` library.

```
1 nvals = np.random.normal(size=1000)
```

produces a vector `nvals` of 100 normal distributed random number of zero mean und unit variance. We can plot their distribution using the `hist` plotting command from the `matplotlib` library.

```
1 fig1 = plt.figure()
2 plt.hist(nvals, bins = 10, density = True)
```

this yields the following diagram:



The `bins` argument indicates the number of bins we want, the `density=True` argument automatically normalises the distribution, so that we obtain an empirically estimated probability density rather than a raw histogram.

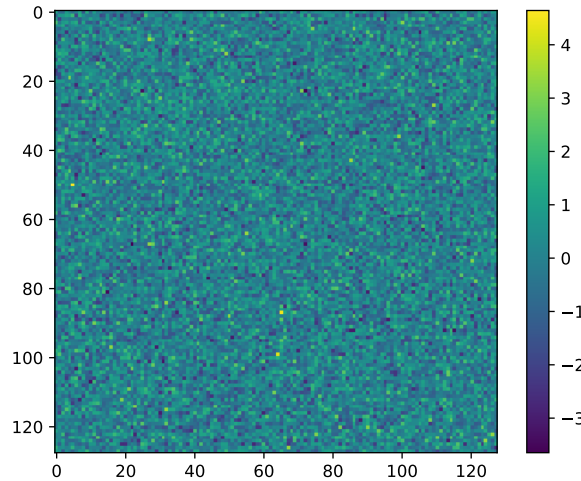
Instead of a one-dimensional vector, we can also directly generate a three-dimensional discrete field of size 128^3 and display a slice of it as a pseudocolor plot using

```

1 N = 128
2 f = np.random.normal(size=(N,N,N))
3 plt.imshow(f[:, :, 32])
4 plt.colorbar()

```

Here `imshow` shows a pseudocolor image of size 128^2 taken from the 33rd plane of values in the z -direction:



We also added a colorbar to understand how values map to colors. If we wanted to look at the histogram, we would need to ‘flatten’ the three-dimensional field into a one-dimensional vector first, using e.g.

```

1 plt.hist(f.flatten(), density=True, bins=100)

```

Correlated fields. Routines for discrete Fourier transforms using the FFT are included with numpy. In order to make a realisation of a correlated field using the Fourier transform technique, we have to first understand how wave numbers are associated with three-dimensional arrays in numpy. In the FFT, wave number indices for a transform of resolution N are re-arranged from

$$(-N/2, -N/2 + 1, \dots, 0, \dots, N/2 - 2, N/2 - 1)$$

to

$$(0, 1, \dots, N/2 - 1, \pm N/2, -N/2 + 1, \dots, -1)$$

for algorithmic reasons. The $k = 0$ (DC) mode is located in the first entry. The highest possible wave number is the Nyquist wave number associated with $\pm N/2$ and located in the very center of the array. In order to get the wave numbers for any resolution N , one can use the `fft.freq` command from numpy to obtain an array with the values:

```
1 print( np.fft.freq(8) )
```

yields

```
[ 0.  0.125  0.25  0.375 -0.5 -0.375 -0.25 -0.125 ]
```

These values are always between 0 and 0.5 and can be converted to ‘physical’ wave numbers using the `d` argument to `freq`. Finally, one can turn the one-dimensional vector of wave numbers into three-dimensional arrays that hold the correct wave number $k = (k_x, k_y, k_z)$ for each grid point (l, m, n) using the `meshgrid` command of numpy so that

```
1 L = 1.0          # the 'physical' box size, sets units of the fundamental mode
2 kmin = 2.0*np.pi/L # the fundamental mode of the box
3 kmax = kmin * N/2 # the Nyquist mode of each linear dimension
4 k1d = np.fft.freq(N,d=1.0/kmin/N)      # get FFT mode vector
5 kv = np.meshgrid(k1d,k1d,k1d)           # get k vector, k = (kx,ky,kz)
```

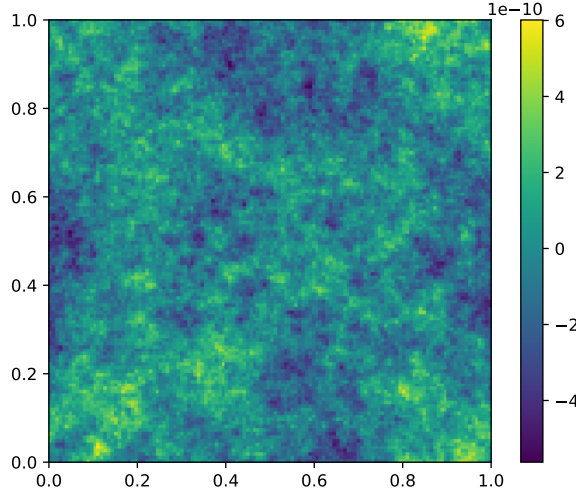
Finally, we want to create a realisation of a field with a power spectrum $P(k) = k^{-\alpha}$. For this, we need to create the complex white noise field, multiply it with the correct k -dependent amplitude and perform an inverse transformation using the `ifftn` multidimensional inverse FFT. The whole procedure can be achieved as follows

```
1 alpha = 3.0
2 norm = 1.0/(2*np.pi)**(-1.5)
3 kmod = np.sqrt(kv[0]**2 + kv[1]**2 + kv[2]**2)    # modulus of k = (kx,ky,kz)
4 fk = np.random.normal(size=(N,N,N)) + 1j * np.random.normal(size=(N,N,N))
5 fk = fk * kmod ** -(alpha/2)    # multiply with amplitude
6 fk[0,0,0] = 0.0                # zero f(k=0), to enforce zero mean
7 f = np.fft.ifftn(fk)           # inverse transform
8 f = norm * np.real(f)          # take real part and normalise
```

We can then display the result using the same pseudocolor plotting routine as above, now specifying the extent of the image

```
1 plt.imshow(f[:, :, 32], extent=[0, L, 0, L])
```

to get:



which clearly is a field with correlations. In order to get a feeling for such fields, investigate the impact of the exponent α on the structures you are seeing.

One-point statistics and coarse-grained fields

While we have so far discussed much the role of two-point correlators, a lot can be learned from their evaluation at “zero lag”, i.e., in the limit of the two points become one. In addition, we will introduce the notion of coarse-grained fields in this section.

One-point covariance

Beware the different star! It's not a convolution.

From (2.21b) and the definition of the inverse Fourier transform, we find that we can write the correlation function between two fields f and g as

$$(f \star g)(x) = \int_{\mathbb{R}^N} \frac{d^N k}{(2\pi)^N} \tilde{f}^*(k) \tilde{g}(k) e^{ik \cdot x}. \quad (2.64)$$

Definition 2.18 — One point covariance. We define the one-point covariance as

$$\langle f g \rangle_{1pt} := \lim_{x \rightarrow 0} (f \star g)(x) = \int_{\mathbb{R}^N} \frac{d^N k}{(2\pi)^N} \tilde{f}^*(k) \tilde{g}(k). \quad (2.65)$$

■ **Example 2.3 — Results in three dimensions ($N = 3$).** If f and g are isotropic fields, then their Fourier transforms do not depend on the direction of the k vectors and we can write for $N = 3$

$$(f \star g)(r) = \frac{1}{(2\pi)^3} \int_0^{2\pi} d\phi \int_{-1}^1 d\cos\theta \int_0^\infty dk k^2 \tilde{f}^*(k) \tilde{g}(k) e^{ikr \cos\theta}$$

where we use that $\int_{-1}^1 d\cos\theta e^{ikr \cos\theta} = 2 \frac{\sin kr}{kr}$ to find

$$= \frac{1}{2\pi^2} \int_0^\infty dk k^2 \tilde{f}^*(k) \tilde{g}(k) \frac{\sin kr}{kr}. \quad (2.66)$$

We find the 1-point covariance of isotropic fields to be

$$\langle f g \rangle_{1\text{pt}} = \mathbb{E} \left[\frac{1}{2\pi^2} \int_0^\infty dk k^2 \tilde{f}^*(k) \tilde{g}(k) \right], \quad (2.67)$$

if the limit exists. The [variance](#) of an isotropic field follows then as

$$\sigma^2 := \langle f^2 \rangle_{1\text{pt}} = \mathbb{E} \left[\frac{1}{(2\pi)^3} \int d^3k |\tilde{f}(\mathbf{k})|^2 \right] = \frac{1}{2\pi^2} \int dk k^2 P(k). \quad (2.68)$$

■

Coarse-grained fields

There may be many reasons to consider not a random field itself, but a filtered, smoothed version of it. A mathematical one might be that integrals like the one defining the variance, (2.68), might not converge for a given $P(k)$. Another reason is that one typically wishes to consider a certain scale in the field thereby ignoring all smaller scales.

Definition 2.19 — Coarse-grained field. Let f be a $(N, 1)$ random field. We define its coarse graining on scale R as a $(N, 1)$ random field obtained by convolving f with a [smoothing kernel](#) $W(\mathbf{x})$. The scaling of the kernel is parameterised by a length-scale $R > 0$, so that

$$f_R(\mathbf{x}) := (f * W_R)(\mathbf{x}) := \frac{1}{R^N} \int d^N y f(\mathbf{y}) W((\mathbf{x} - \mathbf{y})/R), \quad (2.69)$$

where we demand that W is normalised, i.e. $\int d^N x W(\mathbf{x}) = 1$. By virtue of the convolution theorem and the scaling property, we then also have that

$$\tilde{f}_R(\mathbf{k}) = \tilde{f}(\mathbf{k}) \tilde{W}(kR). \quad (2.70)$$

Using the expression for the variance and the Fourier transformed kernels, we can now express the variance of the filtered field in terms of the power spectrum. For example, in three space dimensions one has

$$\sigma^2(R) := \langle f_R^2 \rangle_{1\text{pt}} = \frac{1}{2\pi^2} \int_0^\infty dk k^2 \tilde{W}^2(kR) P(k), \quad (2.71)$$

which is a measure of the variance of fluctuations on the scale R .

■ **Example 2.4 — Gaussian filter.** A generic choice is a [Gaussian filter](#), which is defined as

$$W_G(\mathbf{x}) := (2\pi)^{-N/2} \exp(-\frac{1}{2}\|\mathbf{x}\|^2) \quad (2.72a)$$

with Fourier transform

$$\tilde{W}_G(\mathbf{k}) = \exp(-\frac{1}{2}\|\mathbf{k}\|^2) \quad (2.72b)$$

for all N , which is also a Gaussian filter in Fourier space. A disadvantage of Gaussian filters is that they are not compact in either space, i.e., the clear concept of the involved physical scales is diluted.

Assume a power-law spectrum for $P(k) = A k^\alpha$, then we have in three dimensions

$$\sigma^2(R) = \frac{A}{2\pi^2} \int_0^\infty dk k^{2+\alpha} \exp(-(kR)^2) \quad (2.72c)$$

$$= \frac{A}{4\pi^2 R^{3+\alpha}} \Gamma\left(\frac{3+\alpha}{2}\right) \quad \text{iff } \alpha > -3, \quad (2.72d)$$

where the integral converges for $\alpha > -3$ and Γ is the gamma function. ■

■ **Example 2.5 — Top-hat filter.** Another common choice is the [top-hat filter](#) (the name obviously is due to their visual resemblance to the old-style hats), which is defined as

$$W_{\text{TH}}(\mathbf{x}) := \frac{1}{\omega_N} \mathbf{1}_{\|\mathbf{x}\| \leq 1} \quad (2.73a)$$

where ω_N is the volume of the N -dimensional unit ball, i.e. $\omega_0 = 1$, $\omega_1 = 2$, $\omega_2 = \pi$, $\omega_3 = 4\pi/3$, $\omega_4 = \pi^2/2$, It has *compact support* by definition. Its Fourier transform is

$$\tilde{W}_{\text{TH}}(\mathbf{k}) = \begin{cases} j_0(k) & = \frac{\sin k}{k} \\ 2 J_1(k)/k & : N = 1 \\ 3 j_1(k)/k & : N = 2 \\ \vdots & : N = 3 \end{cases} \quad (2.73b)$$

where $k := \|\mathbf{k}\|$, J_n is the Bessel function of the first kind, and j_n is the spherical Bessel function. Evidently it has no longer compact support in Fourier space. Assume as above a power-law spectrum for $P(k) = A k^\alpha$, then we have in three dimensions

$$\sigma^2(R) = \frac{9}{2\pi^2 R^2} \int_0^\infty dk k^\alpha j_1^2(kR) \quad (2.73c)$$

$$= \frac{9A}{2\pi^{3/2} R^{3+\alpha}} \frac{1}{(\alpha-1)(\alpha-3)} \frac{\Gamma((3+\alpha)/2)}{\Gamma((2-\alpha)/2)} \quad \text{iff } 1 > \alpha > -3 \quad (2.73d)$$

where the integral only converges for $-3 < \alpha < 1$, which is a stronger condition than for the Gaussian filter. Note that this expression has no poles in any of the Γ -functions in this range so that it is directly suitable for numerical evaluation (Garrison, 2019). ■

■ **Example 2.6 — "UV cutoff".** A more drastic taming of integrals like (2.71) can be achieved by simply halting the integration at some maximum $\|\mathbf{k}\|$. This is achieved by choosing a top-hat filter in Fourier space, i.e., by adopting

$$\tilde{W}_{\text{UVcut}}(\mathbf{k}) := \mathbf{1}_{\|\mathbf{k}\| \leq 1}. \quad (2.74)$$

In the cosmology literature this choice is typically called a ‘sharp- k filter’, high-energy physicists would call it a ‘UV cutoff’ (since large $\|\mathbf{k}\|$ can be thought of as ‘short wavelength’). The corresponding W_{UVcut} is similar in form to \tilde{W}_{TH} . The effect on a power-law spectrum $P(k) = Ak^\alpha$ is that the variance converges for all $\alpha > -3$ to

$$\sigma^2(R) = \frac{A}{2\pi^2} \int_0^{1/R} dk k^{2+\alpha} = \frac{A}{2\pi^2 (3+\alpha) R^{3+\alpha}}. \quad (2.75)$$

Finally, we note that the dependence of the variance on the filtering scale is for all considered filters applied to fields with $P(k) \propto k^\alpha$ given by $\sigma^2(R) \propto R^{-(3+\alpha)}$.

Exercise 2.4 — Coarse graining of realisations. Modify your PYTHON code from Exercise 2.3 to provide a field coarse grained with one (or more) of the filters discussed above. Can you verify that the variance scales as predicted when increasing R ? If not, what are reasons that might prevent it? ■

One-point statistics of derivatives of random fields

One finds particularly simple relations for the covariance of derivatives of a random field. In general, random fields might be too ‘rough’ to be differentiable, so we should worry about differentiability. We shall however adopt a pragmatic stance and show shortly that the coarse-grained fields introduced above bring with them differentiability. We remark that such coarse-graining procedures play an important role in physics, especially within the wide context of renormalization (we will make some contact with renormalization in the following chapter).

Proposition 2.8 — Covariance of derivatives. The covariance between derivatives of a $(N, 1)$ random field are given by the general formula

$$\begin{aligned} \left\langle \frac{\partial^{\alpha+\beta} f}{\partial x_i^\alpha \partial x_j^\beta} \frac{\partial^{\kappa+\lambda} f}{\partial x_l^\kappa \partial x_m^\lambda} \right\rangle_{1pt} &= \int \frac{d^N k}{(2\pi)^N} (-ik_i)^\alpha (-ik_j)^\beta (ik_l)^\kappa (ik_m)^\lambda P(k) \\ &= (-1)^{\alpha+\beta} i^{\alpha+\beta+\kappa+\lambda} \int \frac{d^N k}{(2\pi)^N} k_i^\alpha k_j^\beta k_l^\kappa k_m^\lambda P(k). \end{aligned} \quad (2.76)$$

The proof is straightforward: the result follows directly from an application of Theorem 2.4, see also Adler (1981).

Definition 2.20 — Spectral moments. The covariance of derivatives of the field turn out to be simply moments of the power spectrum in Fourier space. Let us consider specifically the relevant case for cosmology here: isotropic centered fields in $N = 3$ dimensions. It will be convenient to define these moments as

$$\sigma_n^2 := \frac{1}{(2\pi)^3} \int d^3 k k^{2n} P(k) = \frac{1}{2\pi^2} \int_0^\infty dk k^{2n+2} P(k). \quad (2.77)$$

We call them **spectral moments** and see that the variance is the zeroeth moment, i.e. $\sigma^2 = \sigma_0^2$. We see from the integrand that higher moments have boosted power at large k , we say that the spectra of derivatives of a field are becoming ‘bluer’, again in analogy with light. In general, differentiability C^n of a field is determined by the convergence of the integral for σ_n^2 .

■ **Example 2.7 — Covariances up to 2nd derivatives.** Let us consider the isotropic $N = 3$ case. From eq. (2.76) follow specifically the variance of the field (with $\alpha = \beta = \kappa = \lambda = 0$) – cf. (2.68) – as

$$\langle f f \rangle_{1pt} = \frac{1}{2\pi^2} \int dk k^2 P(k) = \sigma_0^2, \quad (2.78a)$$

the variance of the gradient field ($\alpha = \kappa = 1, \beta = \lambda = 0$)

$$\langle \nabla f \cdot \nabla f \rangle_{1pt} = \frac{1}{2\pi^2} \int dk k^4 P(k) = \sigma_1^2, \quad (2.78b)$$

Note that for the σ_n^2 to be finite, we have to impose severe restrictions on $P(k)$. Things are usually fine for coarse-grained fields.

and the variance of the Hessian field ($\alpha = \beta = \kappa = \lambda = 1$)

$$\left\langle \frac{\partial^2 f}{\partial x_i \partial x_j} \frac{\partial^2 f}{\partial x_i \partial x_j} \right\rangle_{1pt} = \frac{1}{2\pi^2} \int dk k^6 P(k) = \sigma_2^2, \quad (2.78c)$$

Generally, correlations between 'incompatible' fields vanish, i.e. scalar with vector, vector with tensor, ...

and further that the field and its gradient are uncorrelated ($\alpha = 1, \beta = \kappa = \lambda = 0$)

$$\langle f \nabla f \rangle_{1pt} = \frac{1}{(2\pi)^3} \int d^3k (ik) P(k) = 0, \quad (2.78d)$$

that the gradient and the Hessian are uncorrelated ($\alpha = 1, \beta = 0, \kappa = \lambda = 1$)

$$\left\langle \frac{\partial f}{\partial x_i} \frac{\partial^2 f}{\partial x_l \partial x_m} \right\rangle_{1pt} = \frac{i}{(2\pi)^3} \int d^3k k_i k_l k_m P(k) = 0, \quad (2.78e)$$

and that the field and its Laplacian are anti-correlated ($\alpha = \beta = 0, \kappa = \lambda = 1$)

$$\langle f \nabla^2 f \rangle_{1pt} = -\frac{1}{2\pi^2} \int dk k^4 P(k) = -\sigma_1^2. \quad (2.78f)$$

For $N \neq 3$ the combinations of Kroneckers are the same, just the prefactor changes. Feel free to prove the general result...

Exercise 2.5 Show that the following relations hold for $N = 3$

$$\left\langle \frac{\partial f}{\partial x_i} \frac{\partial f}{\partial x_j} \right\rangle_{1pt} = \frac{\sigma_1^2}{3} \delta_{ij} \quad (2.78g)$$

$$\left\langle f \frac{\partial^2 f}{\partial x_i \partial x_j} \right\rangle_{1pt} = -\frac{\sigma_1^2}{3} \delta_{ij} \quad (2.78h)$$

$$\left\langle \frac{\partial^2 f}{\partial x_i \partial x_j} \frac{\partial^2 f}{\partial x_k \partial x_l} \right\rangle_{1pt} = \frac{\sigma_2^2}{15} (\delta_{ij} \delta_{kl} + \delta_{ik} \delta_{jl} + \delta_{il} \delta_{jk}) \quad (2.78i)$$

Beware that in index notation we always adopt Einstein's summation convention, i.e. doubly appearing indices (on the same side of an equation) are implicitly summed over.

■ **Example 2.8 — Spectral moments for smoothed fields.** We can directly write down the spectral moments for Gaussian and UV cutoff filtered fields in three dimensions with a power-law spectrum $P(k) = Ak^\alpha$ — we simply replace $\alpha \rightarrow \alpha + 2n$ in eqs. (2.72d) and (2.75) — to find

$$\sigma_n^2(R) = \frac{A \Gamma(\frac{3+\alpha+2n}{2})}{4\pi^2 R^{3+\alpha+2n}} \quad \text{Gaussian filtered} \quad (2.79a)$$

$$\sigma_n^2(R) = \frac{A}{2\pi^2 (3 + \alpha + 2n) R^{3+\alpha+2n}} \quad \text{UV cutoff} \quad (2.79b)$$

The differentiability of GRFs is determined by the finiteness of its spectral moments.

which both converge for all n iff $\alpha > -3$. This is in fact the proof that a GRF with power law spectrum with $\alpha > -3$ filtered with a Gaussian or with a UV cutoff is *infinitely differentiable*. The situation is quite different in the case of top-hat filtering! Here, even for the smallest $\alpha = -3 + \epsilon$, only σ_0^2 and σ_1^2 are finite. ■

The eigenvalue distributions of Hessians of Gaussian fields

Joint distributions of GRFs and its derivatives

In order to compute the expectation value $\mathbb{E}[n_{\text{crit}}]$, we have to write down the joint probability distribution for the gradient and the Hessian. Due to (2.78e), we know that they are uncorrelated, and we further see that they are all independent of x , so

$$p(\mathbf{G}, \mathbf{H} | \mathbf{x}) = p(\mathbf{G} | \mathbf{x}) p(\mathbf{H} | \mathbf{x}), \quad (2.80)$$

where, here and in the following, we drop the sub-index f of \mathbf{G} and \mathbf{H} for notational simplicity. Moreover, due to (2.78g) all three components of the gradient are uncorrelated. Let us form now a vector \mathbf{h} of random variables representing the matrix entries, i.e. $\mathbf{h} := (\mathbf{H}_{11}, \mathbf{H}_{22}, \mathbf{H}_{33}, \mathbf{H}_{12}, \mathbf{H}_{23}, \mathbf{H}_{31})^\top$. For the Hessian, we know from (2.78i) that the off-diagonal elements are uncorrelated, so that the following correlation structure holds

$$\Sigma_h := \begin{bmatrix} \langle \mathbf{H}_{11}^2 \rangle & \langle \mathbf{H}_{11}\mathbf{H}_{22} \rangle & \cdots & \langle \mathbf{H}_{11}\mathbf{H}_{31} \rangle \\ \langle \mathbf{H}_{22}\mathbf{H}_{11} \rangle & \langle \mathbf{H}_{22}^2 \rangle & \cdots & \langle \mathbf{H}_{22}\mathbf{H}_{31} \rangle \\ \vdots & \vdots & \ddots & \vdots \\ \langle \mathbf{H}_{31}\mathbf{H}_{11} \rangle & \langle \mathbf{H}_{31}\mathbf{H}_{22} \rangle & \cdots & \langle \mathbf{H}_{31}^2 \rangle \end{bmatrix} = \frac{\sigma_2^2}{15} \begin{bmatrix} 3 & 1 & 1 & 0 & 0 & 0 \\ 1 & 3 & 1 & 0 & 0 & 0 \\ 1 & 1 & 3 & 0 & 0 & 0 \\ 0 & 0 & 0 & 1 & 0 & 0 \\ 0 & 0 & 0 & 0 & 1 & 0 \\ 0 & 0 & 0 & 0 & 0 & 1 \end{bmatrix}.$$

We're forming a vector \mathbf{h} of independent matrix entries H_{ij} and then specify the covariance matrix $\Sigma_h = \mathbb{E}[\mathbf{h} \otimes \mathbf{h}]$.

Clearly the matrix has block-diagonal form. Let $\mathbf{s} := (\mathbf{H}_{11}, \mathbf{H}_{22}, \mathbf{H}_{33})^\top$, and $\mathbf{t} := (\mathbf{H}_{12}, \mathbf{H}_{13}, \mathbf{H}_{23})^\top$, then we can perform the following split $\Sigma_h =: \Sigma_s \oplus \Sigma_t$ so that

$$\Sigma_s := \langle \mathbf{s} \otimes \mathbf{s} \rangle_{1\text{pt}} = \frac{\sigma_2^2}{15} \begin{bmatrix} 3 & 1 & 1 \\ 1 & 3 & 1 \\ 1 & 1 & 3 \end{bmatrix}, \quad \Sigma_s^{-1} = \frac{3}{2\sigma_2^2} \begin{bmatrix} 4 & -1 & -1 \\ -1 & 4 & -1 \\ -1 & -1 & 4 \end{bmatrix} \quad (2.81)$$

with $\det \Sigma_s = 4\sigma_2^6/675$. For the off-diagonal elements, we have the covariance

$$\Sigma_t := \langle \mathbf{t} \otimes \mathbf{t} \rangle_{1\text{pt}} = l_3 \sigma_2^2 / 15, \quad \det \Sigma_t = \sigma_2^6 / 3375. \quad (2.82)$$

Therefore the probability measure for the entries of the Hessian is in terms of the six (coordinate-dependent) components given by

$$d\mu(\mathbf{h}) = \frac{d^6 h}{(2\pi)^3 \sqrt{\det \Sigma_s \det \Sigma_t}} \exp \left[-\frac{1}{2} \left(\mathbf{s}^\top \Sigma_s^{-1} \mathbf{s} + \frac{15}{\sigma_2^2} \mathbf{t}^\top \mathbf{t} \right) \right]. \quad (2.83)$$

The same can be done for the values of the gradient, with $\mathbf{g} := (G_1, G_2, G_3)^\top$ one has $\Sigma_g := l_3 \sigma_1^2 / 3$ and $\det \Sigma_g = \sigma_1^6 / 27$. Therefore, we can finally write the joint PDF as

$$\begin{aligned} p(\mathbf{G}, \mathbf{H} | \mathbf{x}) &= p(\mathbf{g}) p(\mathbf{s}) p(\mathbf{t}) \\ &= \frac{2025\sqrt{15}}{2(2\pi)^{9/2} \sigma_1^3 \sigma_2^6} \exp \left[-\frac{1}{2} \left(\mathbf{g}^\top \Sigma_g^{-1} \mathbf{g} + \mathbf{s}^\top \Sigma_s^{-1} \mathbf{s} + \mathbf{t}^\top \Sigma_t^{-1} \mathbf{t} \right) \right]. \end{aligned} \quad (2.84)$$

The coordinate invariant probability measure

We will now show that the probability measure $d\mu(\mathbf{h})$ from (2.83) is invariant under rotations, specifically under the group $SO(3)$. We have

$$d\mu(\mathbf{h}) = \frac{d^6 h}{(2\pi)^3 \sqrt{\det \Sigma_s \det \Sigma_t}} \exp \left[-\frac{1}{2\sigma_2^2} (6(H_{11}^2 + H_{22}^2 + H_{33}^2) + 15(H_{12}^2 + H_{23}^2 + H_{31}^2) - 3(H_{11}H_{22} + H_{22}H_{33} + H_{11}H_{33})) \right] \quad (2.85)$$

$$=: \frac{d^6 h}{(2\pi)^3 \sqrt{\det \Sigma_s \det \Sigma_t}} \exp \left[-\frac{1}{2\sigma_2^2} (6I_1^2 - 15I_2) \right] \quad (2.86)$$

where in the last equality, we made use of two of the well known invariants of 3×3 matrices¹

$$I_1 = \text{tr } \mathbf{H} = \lambda_1 + \lambda_2 + \lambda_3, \quad (2.88a)$$

$$I_2 = \frac{1}{2} ((\text{tr } \mathbf{H})^2 - \text{tr } (\mathbf{H}^2)) = \lambda_1\lambda_2 + \lambda_2\lambda_3 + \lambda_3\lambda_1, \quad (2.88b)$$

$$I_3 = \det \mathbf{H} = \lambda_1\lambda_2\lambda_3, \quad (2.88c)$$

which are composed of the eigenvalues λ_i and are therefore invariant under all similarity transformations.

We have to transform the integral measure from $d\mu(\mathbf{h})$ to $d\mu(\mathbf{I})$ which implies that we must marginalise (integrate) over all rotations of the eigenbasis (i.e. three degrees of freedom). This integral is closely related to the Haar measure for $SO(3)$. Since the integrand is independent of such rotations, this calculation is luckily simple.

Consider first the Haar measure in terms of Euler angles θ, ϕ_1, ϕ_2

$$\int_{SO(3)} d\mu(\gamma) = \int_0^\pi d\theta \sin \theta \int_0^{2\pi} d\phi_1 \int_0^{2\pi} d\phi_2 = 2\pi 4\pi = 8\pi^2. \quad (2.89)$$

We can understand this result as 4π coming from choosing the first basis vector to be anywhere on the unit sphere, and another 2π coming from the remaining degree of freedom of rotating the second basis vector around the first on a unit circle. For eigenvectors the measure must be different since they have no direction, specifically if \mathbf{v} is a normalised eigenvector, so is $-\mathbf{v}$. Therefore our measure is composed of only half the unit sphere, i.e. $4\pi/2$, and only half of the unit circle, i.e. $2\pi/2$, yielding the measure $2\pi^2$. We have therefore

$$d\mu(\mathbf{I}) = 2\pi^2 d\mu(\mathbf{h}) \quad (2.90)$$

¹These invariants (also called ‘principal invariants’) are related to the characteristic polynomial of the matrix \mathbf{H} through the Cayley–Hamilton theorem as (in 3D in our case given by)

$$\mathbf{H}^3 - I_1 \mathbf{H}^2 + I_2 \mathbf{H} - I_3 \mathbf{I} = 0. \quad (2.87)$$

where the d invariants I_j turn out to be the elementary symmetric polynomials in terms of the d eigenvalues λ_i (here in $d = 3$ dimensions). Specifically, we have in our case

$$I_1 = H_{11} + H_{22} + H_{33} = \lambda_1 + \lambda_2 + \lambda_3, \quad \text{and}$$

$$I_2 = H_{11}H_{22} + H_{22}H_{33} + H_{11}H_{33} - H_{12}^2 - H_{23}^2 - H_{31}^2 = \lambda_1\lambda_2 + \lambda_2\lambda_3 + \lambda_3\lambda_1$$

as the result of integrating out directional degrees of freedom of the eigensystem. We therefore have the rotationally invariant measure

$$d\mu(I) = \frac{675\sqrt{5}}{8\pi\sigma_2^6} \exp\left[-\frac{1}{2\sigma_2^2}(6I_1^2 - 15I_2)\right] d^3I. \quad (2.91)$$

Eigenvalue distributions

Joint distribution Finally, in order to express the distribution in terms of the eigenvalues themselves, we have to transform the measure once more from invariants to eigenvalues, i.e.

$$d^3I = \left| \frac{\partial(I_1, I_2, I_3)}{\partial(\lambda_1, \lambda_2, \lambda_3)} \right| d^3\lambda \quad (2.92)$$

where the Jacobian turns out to be a Vandermonde determinant: assume $\lambda_1 \geq \lambda_2 \geq \lambda_3$, then

$$\left| \frac{\partial(I_1, I_2, I_3)}{\partial(\lambda_1, \lambda_2, \lambda_3)} \right| = (\lambda_1 - \lambda_2)(\lambda_2 - \lambda_3)(\lambda_1 - \lambda_3) = \prod_{i < j} (\lambda_i - \lambda_j). \quad (2.93)$$

From this, we finally obtain the measure for the ordered eigenvalues as²

$$d\mu(\lambda) = \frac{675\sqrt{5}}{8\pi\sigma_2^6} \prod_{i < j} (\lambda_i - \lambda_j) \exp\left[-\frac{1}{2\sigma_2^2}(6I_1^2 - 15I_2)\right] d^3\lambda, \quad (2.94a)$$

$$=: p(\lambda) d^3\lambda \quad (2.94b)$$

a result first derived (to my knowledge) by Doroshkevich (1970).

Signature probabilities An immediate question we can answer with the help of the JPDF (2.94a) is what fraction of the volume occupies a given signature of the Hessian eigenvalues. We find

$$\begin{aligned} \mathbb{P}[+++] &:= \mathbb{P}[\lambda_1 > 0, \lambda_2 > 0, \lambda_3 > 0] = \int_0^\infty d\lambda_1 \int_0^{\lambda_1} d\lambda_2 \int_0^{\lambda_2} d\lambda_3 p(\lambda) \\ &= \frac{1}{2\pi} \left(\pi - \frac{2}{3}\sqrt{5} - \tan^{-1}\sqrt{5} \right) \approx 0.0796759, \end{aligned} \quad (2.95a)$$

$$\begin{aligned} \mathbb{P}[++-] &:= \mathbb{P}(\lambda_1 > 0, \lambda_2 > 0, \lambda_3 < 0) = \int_0^\infty d\lambda_1 \int_0^{\lambda_1} d\lambda_2 \int_{-\infty}^0 d\lambda_3 p(\lambda) \\ &= \frac{1}{2\pi} \left(\frac{2}{3}\sqrt{5} + \tan^{-1}\sqrt{5} \right) \approx 0.420324, \end{aligned} \quad (2.95b)$$

and by symmetry $\mathbb{P}[+--] = \mathbb{P}[++-]$ and $\mathbb{P}[---] = \mathbb{P}[+++]$. Note that this is an answer that is completely *independent* of the power spectrum! As

²The structure of random matrices is a fascinating topic in itself. The distribution for the Hessian eigenvalues has, as we have seen, intrinsic correlations. This sets it apart from Wigner matrices, which have an uncorrelated structure. The (ordered) eigenvalue distribution for $N \times N$ Wigner matrices has however the very similar form

$$p(\lambda_1, \dots, \lambda_N) \propto \exp\left[-\sum_i \lambda_i^2/2\sigma^2\right] \prod_{i < j} (\lambda_i - \lambda_j).$$

See for example Livan et al. (2017) for a very didactic introduction.

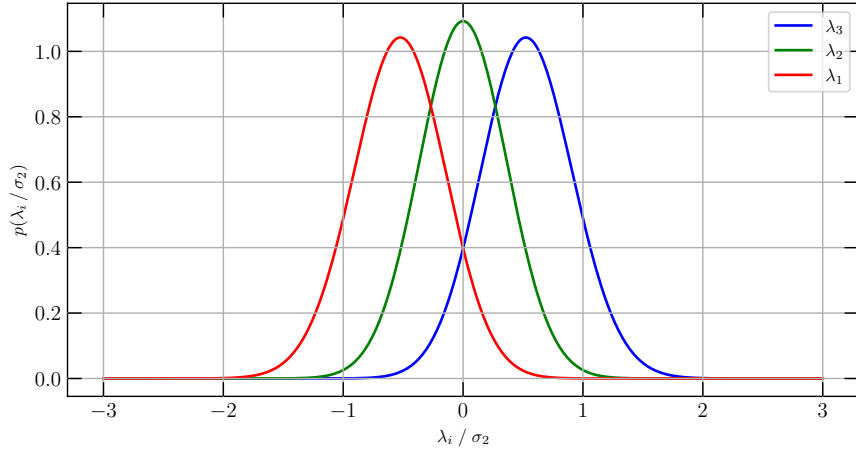


Figure 2.1: The three marginal distributions $p(\lambda_i)$ of the (sorted) eigenvalues $\lambda_1 > \lambda_2 > \lambda_3$ of the Hessian $f_{,ij}$ of a Gaussian random field f . The normalisation of the eigenvalues depends on the second spectral moment σ_2^2 but the distributions are otherwise completely independent of any other properties of the Gaussian random field.

long as the one-point variance σ_2^2 is finite, the random field decomposes with these fractions of 42% (+ + -, + --) and 8% (+ + +, --) into the different signatures, respectively. This is of course also true if we had filtered the field as it is a fundamental property of a real three-dimensional Gaussian random field with finite second spectral moment. It does not generally hold however for a non-Gaussian field.

Marginal distributions The marginal distributions $p(\lambda_i)$ can be given in (lengthy but) closed form (thanks to computer algebra systems) as

$$p(\lambda_1) = \int_{-\infty}^{\lambda_1} d\lambda_2 \int_{-\infty}^{\lambda_2} d\lambda_3 p(\lambda) \quad (2.96)$$

$$\begin{aligned} &= \sqrt{\frac{5}{72\pi}} \frac{20\lambda_1^2 - \sigma_2^2}{\sigma_2^3} \left(\operatorname{erf} \left[\frac{\sqrt{2}\lambda_1}{\sigma_2} \right] + 1 \right) \exp \left[-\frac{5\lambda_1^2}{2\sigma_2^2} \right] \\ &+ \sqrt{\frac{15}{16\pi\sigma_2^2}} \left(\operatorname{erf} \left[\frac{\sqrt{3}\lambda_1}{2\sigma_2} \right] + 1 \right) \exp \left[-\frac{15\lambda_1^2}{4\sigma_2^2} \right] + \frac{5\sqrt{5}}{3\pi\sigma_2^2} \lambda_1 \exp \left[-\frac{9\lambda_1^2}{2\sigma_2^2} \right] \end{aligned} \quad (2.97)$$

which implies that it is non-Gaussian, with a mean and centered variance of

$$\bar{\lambda}_1 := \mathbb{E}[\lambda_1] = \frac{3\sigma_2}{\sqrt{10\pi}} \approx 0.535237\sigma_2 \quad \mathbb{E}[(\lambda_1 - \bar{\lambda}_1)^2] = \frac{13\pi - 27}{30\pi} \sigma_2^2 \approx 0.146854\sigma_2^2 \quad (2.98)$$

In contrast, the distribution for λ_2 remains Gaussian

$$p(\lambda_2) = \int_{\lambda_2}^{\infty} d\lambda_1 \int_{-\infty}^{\lambda_2} d\lambda_3 p(\lambda) = \sqrt{\frac{15}{4\pi\sigma_2^2}} \exp \left[-\frac{15}{4\sigma_2^2} \lambda_2^2 \right] \quad (2.99)$$

with mean and variance of

$$\bar{\lambda}_2 := \mathbb{E}[\lambda_2] = 0 \quad \mathbb{E}[(\lambda_2 - \bar{\lambda}_2)^2] = \frac{2}{15}\sigma_2^2 \approx 0.133333\sigma_2^2 \quad (2.100)$$

The distribution $p(\lambda_3)$ is symmetric to that of λ_1 , obtained by multiplying with -1 . We also see that it would have been clever to rescale all eigenvalues with σ_2 . You find these expressions also in the `PYTHON` script accompanying the book.

Statistics of critical points of GRFs

With the tools that we have developed, we can ask the question how many extrema we can expect in a Gaussian random field. Let us calculate it.

Definition 2.21 — Critical point. We define a (non-degenerate) critical point \mathbf{x}_* of a $(N, 1)$ random field f as a point where the first gradient vanishes, while the Hessian does not, i.e. the set of critical points is defined as

$$\{ \mathbf{x}_* \mid \mathbf{G}_f(\mathbf{x}_*) = 0 \text{ and } \det \mathbf{H}_f(\mathbf{x}_*) \neq 0 \} \quad (2.101)$$

where we defined the gradient field $\mathbf{G}_f := \nabla f$ and the Hessian field $\mathbf{H}_f := \nabla \otimes \nabla f$. As a consequence, the field f can be approximated near a critical point in a Taylor series given by

$$f(\mathbf{x}) = f(\mathbf{x}_*) + \frac{1}{2}(\mathbf{x} - \mathbf{x}_*)^\top \mathbf{H}_f(\mathbf{x}_*) (\mathbf{x} - \mathbf{x}_*) + \text{h.o.t.} \quad (2.102)$$

We remark that a critical point whose Hessian determinant does not vanish is called degenerate. In the Taylor expansion, its properties are determined by the third or higher derivatives. For *non-degenerate critical points*, we call a critical point a

maximum if $\mathbf{H}_f(\mathbf{x}_*)$ is negative definite (i.e. all eigenvalues are negative)

minimum if $\mathbf{H}_f(\mathbf{x}_*)$ is positive definite (i.e. all eigenvalues are positive)

k -saddle if $\mathbf{H}_f(\mathbf{x}_*)$ has k negative eigenvalues - and therefore $N - k$ positive.

Can we calculate the expected number of critical points for a Gaussian random field? The following result will be useful.

Proposition 2.9 — Kac-Rice formula. We formulate an extension to multiple dimensions of an original (one-dimensional) result by Kac (1943) and Rice (1944, 1945). Assume $g(\mathbf{x}) \in C^1, \mathbb{R}^N \rightarrow \mathbb{R}^N$, to have only a finite number of zero points in any finite domain. Let $\mathbf{1}_X$ be the usual indicator function (1 if $\mathbf{x} \in X$ and 0 otherwise). Not counting multiple roots, the number Z of zeros of $g(\mathbf{x})$ inside of a domain V is

$$\begin{aligned} Z &= \lim_{\epsilon \rightarrow 0^+} \frac{1}{\omega_N \epsilon^N} \int_V d^N x \mid \det \mathbf{H}(\mathbf{x}) \mid \mathbf{1}_{\|g(\mathbf{x})\| < \epsilon} \\ &=: \int_V d^N x \mid \det \mathbf{H}(\mathbf{x}) \mid \delta_D(g(\mathbf{x})) \quad \text{where } \mathbf{H}(\mathbf{x}) := (\nabla \otimes g)(\mathbf{x}), \end{aligned} \quad (2.103)$$

and ω_d is the volume of the d -dimensional unit ball, i.e. $\omega_0 = 1, \omega_1 = 2, \omega_2 = \pi, \omega_3 = 4\pi/3, \omega_4 = \pi^2/2, \dots$ The Kac-Rice formula then states that if

we let \mathbf{h} be a vector of length $N(N+1)/2$ holding the entries of $\mathbf{J}(\mathbf{x})$, then for a stationary field

$$\mathbb{E}[Z] = \int d^{N(N+1)/2} h \int d^N g |\det H(\mathbf{h})| \delta_D(g) p(g, \mathbf{h}), \quad (2.104)$$

where $H(\mathbf{h})$ indicates that in the stationary case, H is independent of \mathbf{x} but can be computed from \mathbf{h} .

Proof. We only sketch the plausibility, for rigorous proofs, we refer to the literature. Since the zeros are isolated and countable, the set where $\mathbf{1}_{\|g(x)\|<\epsilon} = 1$ is the sum of disjoint open subsets $I_1, I_2, \dots, I_r \subset V$ containing one root each. It is easy to see that for small enough ϵ

$$\int_{I_i} d^N x |\det J(x)| \stackrel{y:=g(x)}{\equiv} \int d^N y \mathbf{1}_{\|y\|<\epsilon} = \omega_N \epsilon^N \quad i = 1, \dots, r$$

and therefore

$$\frac{1}{\omega_N \epsilon^N} \int_V d^N x |\det J(x)| \mathbf{1}_{\|g(x)\|<\epsilon} = \frac{1}{\omega_N \epsilon^N} \sum_{i=1}^r \int_{I_i} d^N x |\det J(x)| = r. \quad \blacksquare$$

As a consequence of Proposition 2.9, for any given realisation, the number density of critical points of f in some finite $V \subset \mathbb{R}^N$ is therefore given by

$$n_{\text{crit}} = \frac{1}{|V|} \int_V d^N x |\det H_f(x)| \delta_D(G_f(x)). \quad (2.105)$$

Using this distribution, we can now compute the expectation value of the number density of critical points as

$$\mathbb{E}[n_{\text{crit}}] = \int d^6 h \int d^3 g |\det H(\mathbf{h})| \delta_D(g) p(g) p(\mathbf{h}) \quad (2.106)$$

integrating out g

$$= \frac{\sqrt{27}}{(2\pi)^{3/2} \sigma_1^3} \int d^6 h |\det H(\mathbf{h})| p(\mathbf{h}) \quad (2.107)$$

where the determinant of the Hessian is best given in terms of the eigenvalues components is

$$\det H(\mathbf{h}) = \lambda_1 \lambda_2 \lambda_3 = I_3. \quad (2.108)$$

indicating that it is preferable to solve this integral in invariant space. Using the joint distribution of eigenvalues (2.94a), we find

$$\mathbb{E}[n_{\text{crit}}] = \frac{2025\sqrt{15}}{4(2\pi)^{5/2} \sigma_1^3 \sigma_2^6} \int d^3 \lambda |I_3| \prod_{i<j} (\lambda_i - \lambda_j) \exp \left[-\frac{1}{2\sigma_2^2} (6I_1^2 - 15I_2) \right]. \quad (2.109)$$

The integral can be (quite tediously even using a computer algebra system) solved in closed form to yield the number density of critical points as

$$\mathbb{E}[n_{\text{crit}}] = \frac{29}{30\sqrt{15}\pi^2} \frac{\sigma_2^3}{\sigma_1^3} \approx 0.025289 \left(\frac{\sigma_2}{\sigma_1} \right)^3. \quad (2.110)$$

Program Code 2.1 — Monte Carlo sampling of expectation values. As we have just seen, the calculation of an expectation value requires the solving of high-dimensional, usually non-trivial integrals. At the same time, obtaining the covariance matrices is relatively trivial in comparison, and computing the determinant for a given realisation of H is trivial. Since the integral is Gaussian, Monte-Carlo integration in fact becomes trivial in this case. All we have to do is make many realisations of the stochastic process. Assume we will do N_r realisations. Then in the i -th realisation, we compute

1. Draw $s \sim \mathcal{N}(0, \Sigma_s)$ using Cholesky decomposition
2. Draw $t_1, t_2, t_3 \sim \mathcal{N}(0, \sigma_2^2/15)$ directly since independent
3. Compute $h_i := |s_1 s_2 s_3 + 2t_1 t_2 t_3 - s_1 t_3^2 - s_2 t_2^2 - s_3 t_1^2|$

The Cholesky method is ideal to sample from the multivariate normal distributions since the covariance matrix is small. We have $\Sigma_s =: L_s L_s^\top$ with the lower triangular matrix

$$L_s = \frac{\sigma_2}{\sqrt{5}} \begin{bmatrix} 1 & 0 & 0 \\ 1/3 & \sqrt{8}/3 & 0 \\ 1/3 & 1/\sqrt{18} & \sqrt{5}/6 \end{bmatrix}. \quad (2.111)$$

and find from (2.57) that $s = L_s n_3$ has the expected covariance, if $n_3 \sim \mathcal{N}(0, I_3)$ is drawn from a three-dimensional uncorrelated normal distribution.

Having many realisations of the matrix elements $\{s_{1,2,3}, t_{1,2,3}\}$, we can then approximate

$$\mathbb{E}[n_{\text{crit}}] = \frac{1}{\sqrt{(2\pi)^3 \det \Sigma_g}} \lim_{N_r \rightarrow \infty} \frac{1}{N_r} \sum_{i=1}^{N_r} h_i = \frac{\sqrt{27}}{(2\pi)^{3/2} \sigma_1^3} \lim_{N_r \rightarrow \infty} \frac{1}{N_r} \sum_{i=1}^{N_r} h_i \quad (2.112)$$

where the prefactor is left over from integrating $\int d^3g \delta_D(g) p(g)$. We can code this in `PYTHON` code as follows – assume `sigma1 = sigma1` and `sigma2 = sigma2` are given, and `nsamples` is the number of Monte Carlo samples, then

```

1      sigma_t = np.sqrt(sigma2**2/15)
2
3      # Upper triangular matrix from Cholesky decomposition
4      # of covariance matrix  $\Sigma_s$ 
5      Ls = sigma2/np.sqrt(5) * np.array([[1, 0, 0], \
6                                         [1/3, np.sqrt(8)/3, 0], \
7                                         [1/3, 1/np.sqrt(18), np.sqrt(5/6)]])
8
9      # draw  $t=(H12, H13, H23)$  from uncorrelated Gaussian
10     t = np.random.normal(0, sigma_t, size=(nsamples, 3))
11
12     # draw  $s=(H11, H22, H33)$  from correlated Gaussian using Cholesky sampling
13     s = Ls @ np.random.normal(0, 1, size=(nsamples, 3))
14
15     # assemble Hessian matrix from components
16     H = np.zeros((nsamples, 3, 3))
17     H[:, 0, 0] = s[:, 0]
18     H[:, 1, 1] = s[:, 1]
19     H[:, 2, 2] = s[:, 2]
20     H[:, 0, 1] = t[:, 0]; H[:, 1, 0] = t[:, 0]
21     H[:, 0, 2] = t[:, 1]; H[:, 2, 0] = t[:, 1]
22     H[:, 2, 1] = t[:, 2]; H[:, 1, 2] = t[:, 2]
23
24     # get absolute value of the determinant
25     h = np.linalg(np.abs(H))
26
27     # compute the expectation value
28     exp_ncrit = np.sqrt(27)/((2*np.pi)**1.5*sigma1**3) * np.mean(h)

```

Starting from this code snippet, it is easy to compute also the density of maxima, minima, or k -saddles. We leave this as the following exercise.

Exercise 2.6 — Cholesky sampler and empirical covariance. Verify that the Cholesky sampler yields the correct covariance matrix, i.e. that indeed $\langle s \otimes s \rangle \approx \Sigma_s$. In **NUMPY**, a covariance matrix is estimated as follows

```
1 Cs_empirical = np.cov(s, rowvar=False)
```

we added `rowvar=False` since the dimensions of `s` are `nsamples × 3` in our case, i.e. the variables are along the second dimension. ■

Exercise 2.7 — Maxima, minima, and saddles. Modify the program above to compute the number density of maxima, minima, 1-saddles, and 2-saddles, in the $(3, 1)$ case, with an additional constraint that you require also that field exceeds a threshold value, i.e. that $f \geq \gamma \sigma_0$. For a vector of random symmetric (real) 2×3 matrices, i.e. of dimensions `nsamples × 3 × 3`, all eigenvalues can be computed in one go using **NUMPY**, i.e.

```
1 eigvals = np.linalg.eigvalsh(H)
```

Beware that when you add a sampler for f , you need to take into account its covariance with H . What do you expect for the relative numbers as a function of increasing ν ? Does the result agree with your expectations? ■

Excursion sets, geometric and topological properties of GRFs

So far, we have characterised Gaussian random fields in terms of their n -point correlation structure (which in the Gaussian case was fully determined in terms of

the 1- and 2-point correlations). In this section, we will instead focus on the geometric properties of such fields by employing notions from [integral geometry](#).

Definition 2.22 — Excursion and Level Set. We define the [excursion set](#) S_ν of a given (3,1) random field $f(x)$ on a three-dimensional domain $\mathcal{D} \subset \mathbb{R}^3$ as the set of points where f exceeds a given threshold parameter ν , i.e.

$$S_\nu := \{x \in \mathcal{D} \mid f(x) \geq \nu\} \quad \text{with boundary} \quad \partial S_\nu = \{x \in \mathcal{D} \mid f(x) = \nu\}. \quad (2.113)$$

The boundary set is often called a '[level set](#)'.

We are looking now for motion invariants (under translations and rotations in \mathbb{R}^3) characterising such excursion sets. Such questions have been addressed in the domain of integral geometry. Specifically, Hadwiger's theorem states that in three dimensions, there are precisely four distinct invariants (that are further additive). We are concerned only about its application to three-dimensional space, which we formulate as follows.

Proposition 2.10 — Hadwiger 3D. There are four measures of size (invariant valuations) for convex subsets of \mathbb{R}^3 . These are

1. volume measure
2. surface area measure
3. mean curvature
4. Gauss curvature / Euler characteristic

They are the $d+1$ [Minkowski functionals](#) in d -dimensions.

We sketch out here only those aspects of integral geometry that are relevant for our particular case; an excellent monograph that presents all aspects of the geometry of random fields in mathematical rigour is the book by Adler and Taylor (2009).

In Figure 2.2, we show the appearance of the level set as the threshold parameter scans through the range of values of the random field. The complex nature of this surface can be described in terms of its invariants.

The zeroth Minkowski functional is the volume functional. It is the volume fraction occupied by the set S_ν , and is given by an integral over the indicator function denoting S_ν

$$v_0(\nu) := \frac{\text{vol}(S_\nu)}{\text{vol}(\mathcal{D})} = \frac{1}{\text{vol}(\mathcal{D})} \int_{\mathcal{D}} d^3x \mathbf{1}_{S_\nu} . \quad (2.114)$$

Since we are evaluating this integral point by point, we can write

$$\mathbb{E}[v_0(\nu)] = \langle \mathbf{1}_{f \geq \nu} \rangle_{\text{1pt}} = \int_{-\infty}^{\infty} df p(f) \stackrel{\text{for GRFs}}{=} \frac{1}{2} \operatorname{erfc} \left[\frac{\nu}{\sqrt{2}\sigma_0} \right]. \quad (2.115)$$

In the cosmological literature, the dimensionless quantity ν/σ_0 is typically called the 'peak height' in the cosmological literature.

The first Minkowski functional is the area functional. It is up to a multiplicative constant the area density of the set ∂S_ν , which is given by

$$6 v_1(\nu) := \frac{\text{vol}(\partial S_\nu)}{\text{vol}(\mathcal{D})} = \frac{1}{\text{vol}(\mathcal{D})} \int_{\mathcal{D}} d^3x \mathbf{1}_{\partial S_\nu} \quad (2.116a)$$

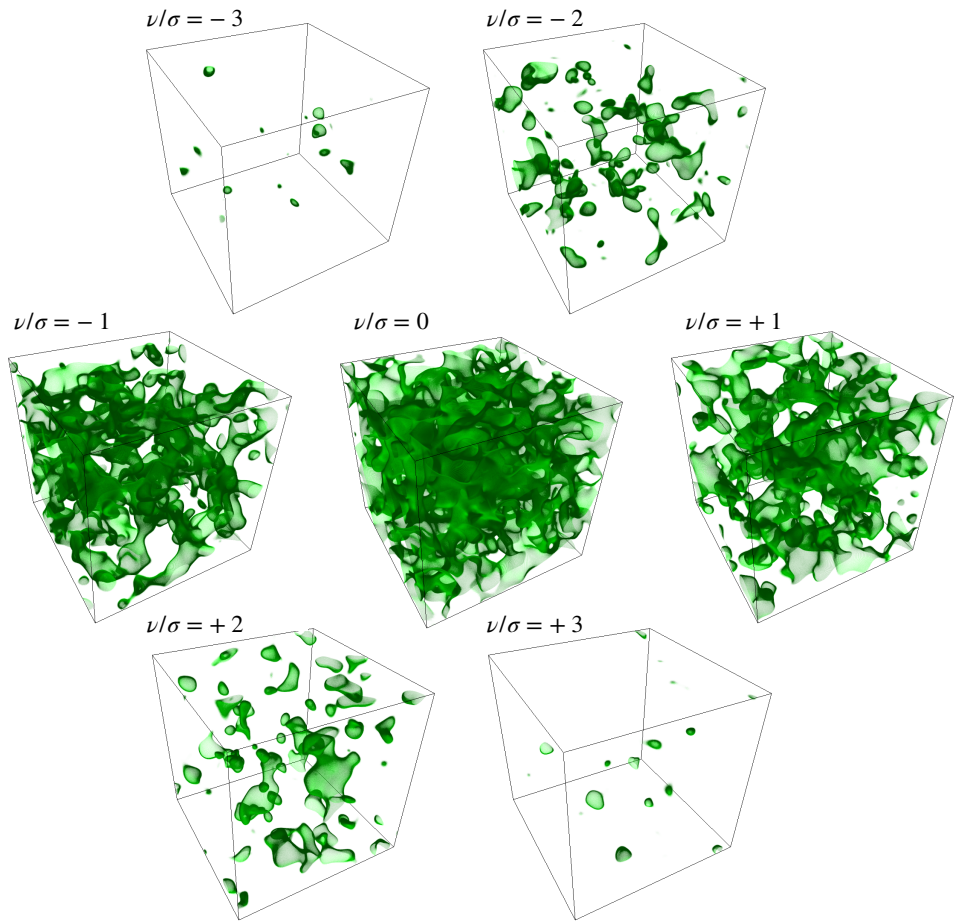


Figure 2.2: The boundary ∂S_ν of an excursion set for different values of the threshold parameter ν for a smoothed three-dimensional Gaussian random field. For the highest and lowest thresholds $\nu = \pm 3\sigma_0$, the boundary consists of isolated spheres enclosing the most extreme maxima and minima of the field. As $\nu \rightarrow 0$, more spheres appear around local extreme and the boundaries expand, eventually merging and forming a percolating set. The area density is maximal for $\nu = 0$. For small $|\nu|$, the boundary is predominantly hyperbolic (negative Gauss curvature), while for large $|\nu|$ it is predominantly elliptic (positive curvature).

i.e. the indicator function picks out only those points where $f(\mathbf{x}) = \nu$. They coincide with the roots of $f(\mathbf{x}) - \nu$ so that we will be able to apply the Kac-Rice formula (2.103) again to compute expectation values, this time for a scalar field, and we have

$$v_1(\nu) = \frac{1}{6\text{vol}(\mathcal{D})} \int_{\mathcal{D}} d^3x \|\nabla f\| \delta_D(f(\mathbf{x}) - \nu). \quad (2.116b)$$

In order to obtain the expectation value of this integral, we need to integrate over the joint distribution of values of f and gradients ∇f . We remember the statistical independence between ∇f and f , cf. (2.78d), and also the diagonal covariance matrix of the gradient, cf. (2.78g). Setting $\mathbf{g} := (\nabla f)(\mathbf{x})$, we therefore have $p(f, \mathbf{g}) = p(f)p(\mathbf{g})$, and

$$\begin{aligned} \mathbb{E}[v_1(\nu)] &= \langle \mathbf{1}_{f=\nu} \rangle_{\text{1pt}} = \int df \int d^3g \|\mathbf{g}\| \delta_D(f - \nu) p(f) p(g) \\ &\stackrel{\text{for GRFs}}{=} \frac{3^{3/2}}{(2\pi)^2 \sigma_0 \sigma_1^3} \int df \int d^3g \|\mathbf{g}\| \delta_D(f - \nu) \exp \left[-\frac{f^2}{2\sigma_0^2} - \frac{\|\mathbf{g}\|^2}{2\sigma_1^2/3} \right] \\ &= \frac{2}{6\pi} \frac{\sigma_1}{\sigma_0} \exp \left[-\frac{\nu^2}{2\sigma_0^2} \right]. \end{aligned} \quad (2.117)$$

This is the first Minkowski functional for a Gaussian random field. It quantifies the area density of the level set, and we see immediately that the area is maximal for $\nu = 0$. We also see that the excursion set area density diverges whenever σ_1 diverges, which imposes a significant constraint on the behaviour of the underlying power spectrum at large k .

The remaining two Minkowski functionals in three-dimensional space correspond to integrals of the mean curvature, and the Gaussian curvature over the boundary of the excursion set. We shall not evaluate these expressions here by hand. Instead, we shall make use of a general result, which holds in arbitrary dimensions.

Theorem 2.11 — Tomita (1986). For Gaussian random fields in d dimensions, the expectation value of the Minkowski functional of order k , ($d \geq k > 0$) is given by

$$\mathbb{E}[v_k^{(d)}(\nu)] = \frac{1}{(2\pi)^{k/2}} \frac{\omega_d}{\omega_{d-k} \omega_k} \left(\frac{\sigma_1}{\sigma_0} \right)^k H_{k-1}(\nu/\sigma_0), \quad \text{with } H_n(x) := (-1)^n \frac{d^n}{dx^n} \mathcal{N}(x) \quad (2.118)$$

where \mathcal{N} is the normal distribution, and ω_k is again the volume of the k -dimensional unit ball, i.e. $\omega_0 = 1$, $\omega_1 = 2$, $\omega_2 = \pi$, $\omega_3 = 4\pi/3$, $\omega_4 = \pi^2/2$, The proof can be found in Tomita (1986). Note that the H_n for $n \geq 1$ are Hermite polynomials multiplying $\exp[-\nu^2/2\sigma_0^2]$. For $k = 0$ an anti-derivative appears.

We list the expectation values for GRFs of the four Minkowski functionals in

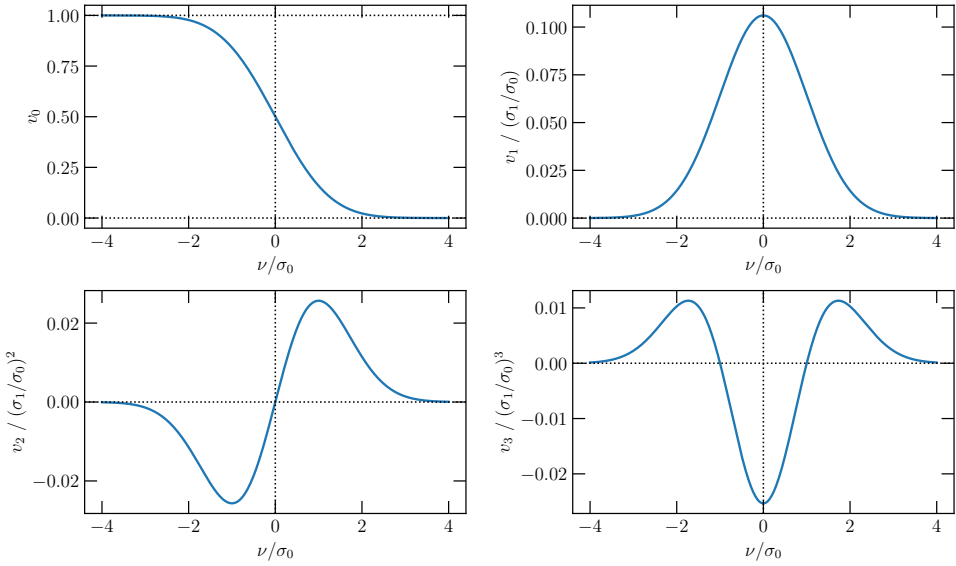


Figure 2.3: The four Minkowski functionals $v_{0\dots 3}$ characterising surfaces in three-dimensional space as applied to excursion sets S_ν of Gaussian random fields. They describe, in increasing order, the volume occupied by the excursion set, the area density of the boundary of the excursion set, its integrated mean curvature, as well as the integrated Gauss curvature. The latter is the negative of the Euler characteristic by virtue of the Gauss-Bonnet theorem.

$N = 3$ -dimensional space as for reference

$$\mathbb{E}[v_0(\nu)] = \frac{1}{2} \operatorname{erfc} \left[\frac{\nu}{\sqrt{2}\sigma_0} \right] \quad (2.119a)$$

$$\mathbb{E}[v_1(\nu)] = \frac{2}{6\pi} \frac{\sigma_1}{\sigma_0} \exp \left[-\frac{\nu^2}{2\sigma_0^2} \right] \quad (2.119b)$$

$$\mathbb{E}[v_2(\nu)] = \frac{2}{3(2\pi)^{3/2}} \frac{\sigma_1^2 \nu}{\sigma_0^3} \exp \left[-\frac{\nu^2}{2\sigma_0^2} \right], \quad (2.119c)$$

$$\mathbb{E}[v_3(\nu)] = \frac{1}{(2\pi)^2} \frac{\sigma_1^3}{\sigma_0^3} \left(\frac{\nu^2}{\sigma_0^2} - 1 \right) \exp \left[-\frac{\nu^2}{2\sigma_0^2} \right]. \quad (2.119d)$$

These are related to the two- and the three-dimensional genus of the boundary surface of the excursion set, i.e., they carry topological information. That the integral over the Gaussian curvature yields the Euler characteristic, or the genus, of the surface follows from the [Gauss-Bonnet theorem](#). In a nutshell it states that the integral Gauss curvature specifies the topology, i.e. by summing up the curvature, we know how many spheres vs. holes exist in the level set. Specifically the genus of the boundary surface is $g = -v_3(\nu) \operatorname{vol}(\mathcal{D})$, with Euler characteristic $\chi = 2 - 2g$. From the shape of $g(\nu)$, we can see that the excursion set boundary is sphere-like for large $\pm\nu$, while for $\nu \simeq 0$ the surface has a maximal number of holes. The four Minkowski functionals $v_k(\nu)$ are graphically represented in Figure 2.3.

Exercise 2.8 — Rendering of level sets. Use a 3D rendering toolkit and create visualisations of level sets. I recommend either PYVISTA or K3D. ■

Higher-order correlators

Moments and cumulants

In the earlier sections we have already extensively discussed the two-point correlation function, as well as its counterpart in Fourier space, the power spectrum (see e.g. eq. 2.47 and surrounding discussion). The two-point functions can be generalized to n -point correlation functions (or simply “ n -point correlators”) for any integer $n > 2$, which is in particular relevant when a given random variable is not Gaussian. Indeed, as we have learnt from Marcinkiewicz’ theorem, any field that is non-Gaussian excites an infinite hierarchy of n -point correlators (cf. also Isserlis/Wick’s theorem in section 2 which only applies to Gaussian fields).

As a natural extension of Isserlis/Wick’s theorem for Gaussian fields, one may decompose any non-Gaussian fields in combinations of lower-order correlations, as well as in *intrinsic* (*i.e.*, *not reducible*) correlations which are called cumulants. The latter are defined as follows.

Definition 2.23 — Cumulants. Let $\mathbf{X} = [X_1, \dots, X_N]$ be an N -dimensional vector of random variables or random functions with non-vanishing mean, and assume homogeneity (cf. Proposition 2.1; this allows us to use the previously mentioned angle notation for denoting moments instead of the expectation values). Furthermore let X_i, X_j, \dots denote mutually different variables (or functions) from this vector, with $i, j, \dots = 1, 2, \dots, N$. Then, the first n -point **moments** decompose into the following irreducible parts

$$\begin{aligned}\langle X_i \rangle &= \langle X_i \rangle_c, \\ \langle X_i X_j \rangle &= \langle X_i \rangle \langle X_j \rangle + \langle X_i X_j \rangle_c, \\ \langle X_i X_j X_k \rangle &= \langle X_i \rangle \langle X_j \rangle \langle X_k \rangle + \langle X_i X_j \rangle_c \langle X_k \rangle + \langle X_i X_k \rangle_c \langle X_j \rangle \\ &\quad + \langle X_j X_k \rangle_c \langle X_i \rangle + \langle X_i X_j X_k \rangle_c,\end{aligned}\tag{2.120}$$

and so forth, where “c” stands for connected parts or **cumulants**, which can be thought of intrinsic or “pure” parts of the correlations. In Fig. 2.4 we provide for $n = 1, 2, 3, 4$ these relations between n -point moments and cumulants in terms of an intuitive diagrammatic representation.

As a special case of the relationship (2.120), we remind the reader that a Gaussian field is entirely determined by its two-point-correlation function. As a direct consequence, the relation (2.120) between n -point moments and cumulants simplifies significantly for Gaussian fields, reducing n th-order moments into sums of products of two-point-correlation functions, if the random variable has vanishing mean. This reduction leads to significant simplifications in analytical computations which we will also discuss in detail further below.

Cumulant expansion

Theorem 2.12 — Cumulant expansion theorem. Alternatively to the diagrammatic representation, one can define the cumulants employing the **cumulant expansion**

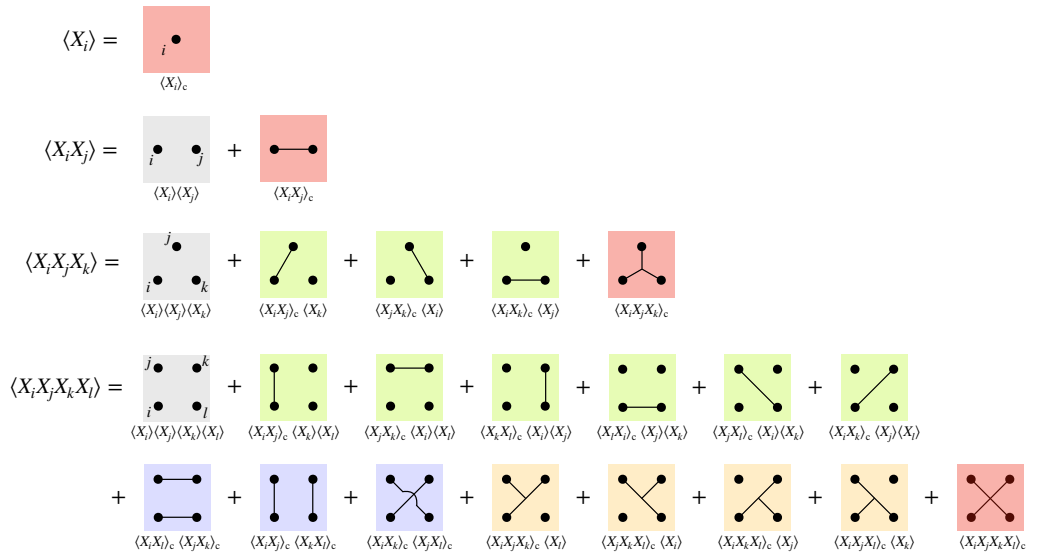


Figure 2.4: Expansion of moments into cumulants from first to fourth order and their representation as undirected graphs (physicists may think of possible “particle interactions” in the spirit of Feynman graphs). Red shaded components are the (fully) connected components of each order, all other diagrams of a given order can be composed out of products of lower order connected components. Note that if the variables have vanishing mean, i.e., $\langle X_i \rangle = 0$ etc., then the number of non-zero diagrams is dramatically reduced, i.e., all grey, green and orange contributions vanish. If furthermore X_i is Gaussian then all connected cumulants vanish except those that are powers of $\langle X_i X_j \rangle_c$ (e.g., the only non-zero terms in the 4th-order moment stems from the blue contributions).

[theorem](#), as well as the previously introduced characteristic (generating) function $\tilde{p}(k) = \langle e^{-ik \cdot X} \rangle$ for the random fields collected in the N -dimensional vector X . The [cumulant expansion theorem](#) states that

$$\langle e^{-ik \cdot X} \rangle = \exp \left[\sum_{n=1}^{\infty} \frac{(-i)^n}{n!} \langle (k \cdot X)^n \rangle_c \right]. \quad (2.121)$$

See e.g. Ma (1985) for a proof of this theorem.

Exercise 2.9 : Re-derive equations (2.120) up to order $n = 3$, starting from (2.121)

Let us denote LHS := $\langle \exp\{-ik_i X_i\} \rangle$ and RHS := $\exp \left[\sum_{n=1}^{\infty} \frac{(-i)^n}{n!} \langle (k_i X_i)^n \rangle_c \right]$ in the following, and, summation over repeated indices is assumed (mind the compact notation which involves a sum over independent variables!). The RHS is for $n = 3$

$$\begin{aligned} \text{RHS} &= \exp \left[-i \langle k_i X_i \rangle_c - \frac{1}{2} \langle k_i X_i k_j X_j \rangle_c + \frac{i}{6} \langle k_i X_i k_j X_j k_k X_k \rangle_c \right] \\ &= 1 - i \langle k_i X_i \rangle_c - \frac{1}{2} \langle k_i X_i k_j X_j \rangle_c - \frac{1}{2} \langle k_i X_i \rangle_c \langle k_j X_j \rangle_c \\ &\quad + \frac{i}{2 \cdot 3} \left[\langle k_i X_i \rangle_c \langle k_j X_j k_k X_k \rangle_c + 2 \text{ perms.} \right] + \frac{i}{6} \langle k_i X_i \rangle_c \langle k_j X_j \rangle_c \langle k_k X_k \rangle_c \\ &\quad + \frac{i}{6} \langle k_i X_i k_j X_j k_l X_l \rangle_c + O(X^4), \end{aligned} \quad (2.122)$$

where “2 perms.” stands for 2 cyclic permutations in i, j, k . At the same time, Taylor expanding the LHS of (2.121) yields

$$\text{LHS} = 1 - i \langle k_i X_i \rangle - \frac{1}{2} \langle k_i X_i k_j X_j \rangle + \frac{i}{6} \langle k_i X_i k_j X_j k_k X_k \rangle + O(X^4). \quad (2.123)$$

Pulling out the various k_i, k_j etc. from the above relations, as well as equating LHS and RHS and identifying the involved correlators to fixed orders, one re derives the three relations given in (2.120).

■

Lemma 2.3 — Relation between moments and cumulants for autocorrelations.. If $X_i = X_j = X_k =: X$ then eqs. (2.120) reduce to

$$\begin{aligned} \langle X \rangle &= \langle X \rangle_c, \\ \langle X^2 \rangle &= \langle X \rangle^2 + \langle X^2 \rangle_c, \\ \langle X^3 \rangle &= \langle X \rangle^3 + 3 \langle X^2 \rangle_c \langle X \rangle + \langle X^3 \rangle_c. \end{aligned} \quad (2.124)$$

This special case is particularly relevant within the context of one-point statistics (section 2), which we will also apply within a cosmological context in chapter 3.

Chapter 3

Dynamical Equations

The present chapter is devoted to the generally accepted theory for the cosmic large-scale structure of the Universe.

Section 3 discusses the cosmological Vlasov–Poisson equations, while in section 3 we show under which circumstances these equations can be reduced to the fluid equations. Traditional perturbative techniques for the fluid equations will be already introduced in the following section, while we devote sections 3–3 for a step-by-step description on contemporary formulations of perturbation theory (which essentially amounts to employing Taylor-series representations for the dark-matter fluid variables).

Vlasov–Poisson equations

How do we describe the gravitational evolution of matter in the Universe? The answer to this question is given by the Vlasov–Poisson equations, which for physicists are often presented as “the collisionless limit of the Boltzmann–Poisson equations”. These equations are of utmost importance for both the theoretical (this chapter) as well as the numerical description (the following chapter) of cosmic structures.

In the cosmological literature it is standard to start directly with the equations in comoving coordinates and comoving momenta; here we follow a more pedagogical view and exploit first the equations in non-comoving (i.e., physical) coordinates, where both the current positions and momentum include the “shifts” due to the overall Hubble expansion of the Universe. Afterwards, in section 3 we show how the physical Vlasov–Poisson equations can be equivalently formulated in terms of an infinite chain of coupled fluid-type equations. Then, in section 3, we show how the physical Vlasov–Poisson equations related to the more commonly known cosmological Vlasov–Poisson equations in comoving coordinates.

Vlasov–Poisson and phase-space distributions in physical coordinates

Our starting point is the [physical distribution function](#) $F(\mathbf{r}, \mathbf{P}, t)$, with $\mathbf{r} \in \mathcal{V}_r \subset \mathbb{R}^3$ the space of (physical) spatial coordinates, and $\mathbf{P} \in \mathcal{V}_P \subset \mathbb{R}^3$ the space of the (conjugate) momentum coordinates, while t is the temporal parameter. The distribution function is defined such that

$$dN = F(\mathbf{r}, \mathbf{P}, t) d^3r d^3P \quad (3.1)$$

is the number of matter elements which, at time t , have momenta within an infinitesimal momentum-space volume d^3P around \mathbf{P} and have positions within an infinitesimal configuration-space volume d^3r around \mathbf{r} (in a Hamiltonian formulation, \mathbf{r} and \mathbf{P} are canonically conjugate variables). If the number of particles is conserved by physical processes (i.e., particles are neither produced nor annihilated), which is what we typically assume for dark matter, then

$$N = \int_{\mathcal{V}_r} \int_{\mathcal{V}_P} F(\mathbf{r}, \mathbf{P}, t) d^3r d^3P = \text{const.} \quad (3.2)$$

Definition 3.1 — Physical Vlasov-Poisson system. Therefore, the [physical Vlasov–Poisson equations](#) states how the distribution of dark matter, in the presence of (long-range) gravitational (self-)interactions only, evolves in time,

$$\frac{dF}{dt} = \frac{\partial F}{\partial t} + \frac{\mathbf{P}}{m} \cdot \nabla_r F - m \nabla_r \phi \cdot \nabla_P F = 0, \quad (3.3a)$$

$$\nabla_r^2 \phi(\mathbf{r}, t) = 4\pi G \varrho - \Lambda c^2. \quad (3.3b)$$

The density occurring in the physical Poisson equation is determined via

$$\varrho(\mathbf{r}, t) := m \langle 1 \rangle_{\mathcal{V}_P} := m \int_{\mathcal{V}_P} F(\mathbf{r}, \mathbf{P}, t) d^3P. \quad (3.4)$$

It is worth noting that $F(\mathbf{r}, \mathbf{P}, t)$ is a one-parameter family of probability distribution functions over $3 + 3$ -dimensional phase-space coordinates. The density $\varrho(\mathbf{r}, t)$ is thus the [marginal of the phase-space distribution](#) over momentum space.

Vlasov-Poisson (VP) can be rigorously derived by simply requiring that particles are moving purely geodesically and are conserved. VP is then essentially the continuum limit of Hamiltonian mechanics, with characteristic (one-particle) Hamiltonian

$$H = \frac{|\mathbf{P}|^2}{2m} + m \phi(\mathbf{r}, t), \quad (3.5)$$

and Hamiltonian equations of motion

$$\dot{\mathbf{r}} = \nabla_P H = \mathbf{P}/m, \quad \dot{\mathbf{P}} = -\nabla_r H = -m \nabla_r \phi. \quad (3.6)$$

To gain some intuition into the evolution of phase-space distributions, we show in Fig. 3.1, without gravity and in 1+1-dimensional phase space with coordinates r and P , the evolution of a circular distribution of particles in phase-space in a non-expanding universe without gravitational interactions. In this case, the evolution in phase space is just a shearing motion, since different momentum coordinates move at different velocities. Hamiltonian (symplectic) dynamics guarantees that volume forms in phase space ($dr \wedge dP$, where “ \wedge ” stands for the wedge product) are conserved and thus that the phase-space area occupied by the particles is constant. In the example shown in Fig. 3.1, periodic boundary conditions are applied, so that the sheared and stretched distribution is folded back onto the same finite space, leading to ‘[multi-streaming](#)’, where different particles occupy the same spatial position at a given time, which generates velocity dispersion. We remark that the sketch in that figure is essentially V.I. Arnold’s ‘cat

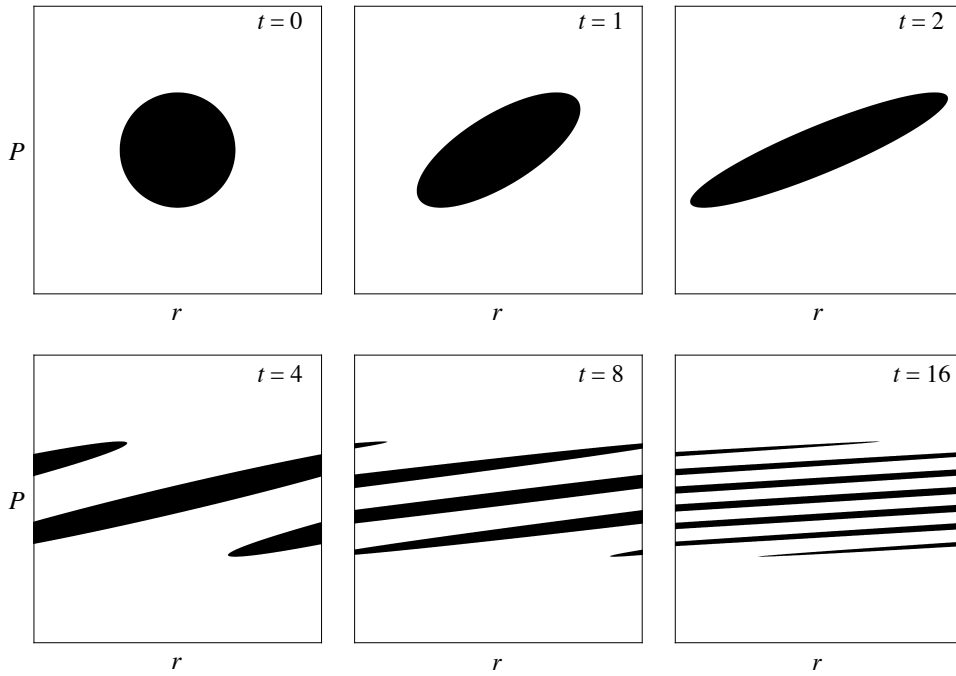


Figure 3.1: Schematic evolution (without gravity) of an initial particle distribution in the continuum limit (in arbitrary units), occupying a disk in phase space at $t = 0$. Without acceleration, the particles at different momenta have relative velocities, leading to a shearing motion over time. Symplectic dynamics guarantees that the phase-space volume occupied by the particles (the black area) is constant. Due to the absence of gravitational acceleration, particles move never vertically. Here periodic boundary conditions are employed on a torus geometry (i.e., particles exiting on the left side of the period of the torus enter on the right; and vice versa) so that ‘multi-streaming’ appears.

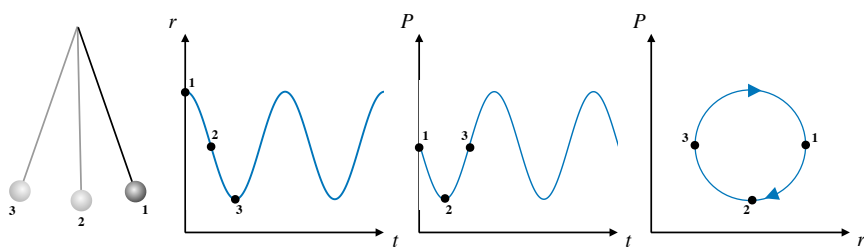


Figure 3.2: Phase space intuition 2: Evolution of a mathematical pendulum in phase space (an evolution with a constant potential $\phi = \frac{1}{2}r^2$). This corresponds to a harmonic oscillator. The evolution is simply governed by a global rotation of the entire phase space. The radius of the circle of the actual trajectory is determined by the energy.

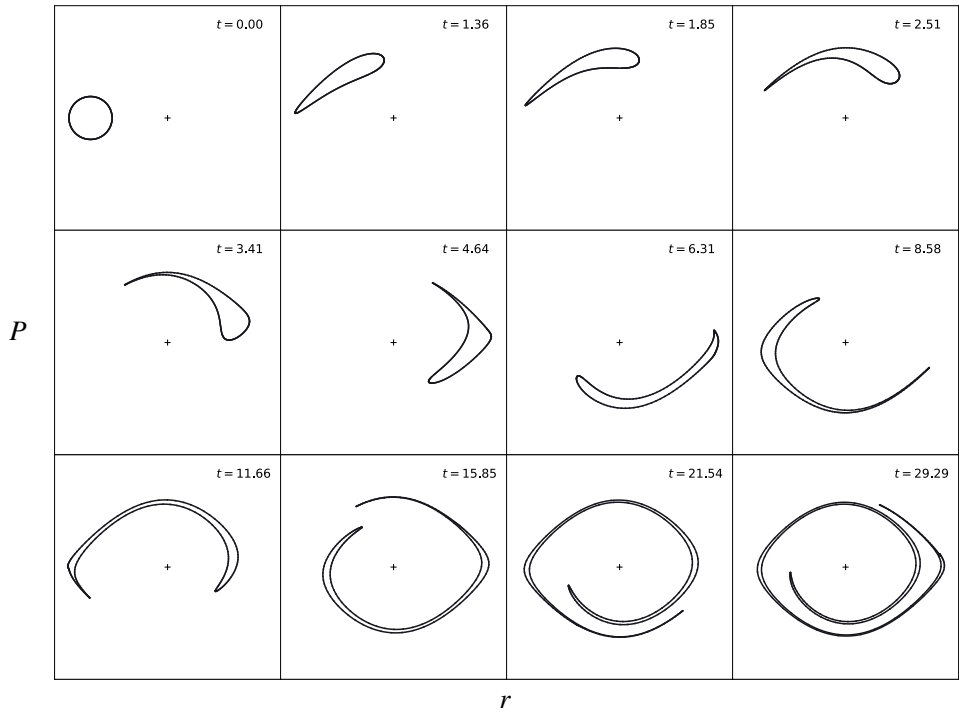


Figure 3.3: Phase space intuition 3: Schematic evolution of a particle distribution in phase space orbiting in a fixed inharmonic potential $\phi = \cos(r)$ in the continuum limit. The minimum energy point ($r = \pi, P = 0$) is indicated by the cross. Initially the particles occupy a circle in phase space at $t = 0$, which is then accelerated towards the minimum of the potential. For a harmonic potential the circle would simply rotate uniformly around the center point over time. In the inharmonic case, one however observes [phase mixing](#), where the circle is deformed and for infinite time the entire space between the points of lowest and highest energy is ‘filled’. Again, because of the underlying symplectic structure, the area enclosed by the contour remains constant for all times.

map' (since he used an image of a cat rather than a circle to illustrate the same dynamics).

In the presence of a potential, the simple shearing motion is modified and can become periodic if the potential has a local minimum. The simplest case of a constant harmonic potential corresponds to a harmonic oscillator (cf. Fig.3.2) which corresponds to a global rotation of the entire phase space. The case of a fixed inharmonic potential is shown in Figure 3.3. Here we use $\phi = \cos(r)$. In the presence of any inharmonic perturbation $\partial^3\phi/\partial r^3 \neq 0$, one observes phase mixing. While the particles oscillate in the potential, they also 'wind up' in phase space, occupying the entire space allowed by their energies. Hamiltonian dynamics guarantees that contours such as those shown in the figure remain regular and the enclosed area remains constant.

Marginal/kinetic moments and the Vlasov hierarchy

In important physical cases it is preferable to work with [marginals](#), which are functions of the physical coordinate with the momentum dependence being integrated out.

The evolution equation for $\varrho(\mathbf{r}, t)$ is readily obtained by computing the marginal of the Vlasov equation itself (i.e., integrating out the momentum dependence in $dF/dt = 0$), yielding

$$\int_{\mathcal{V}_P} \frac{dF}{dt} d^3P \stackrel{\text{eq. (3.3a)}}{=} \left[\frac{\partial \varrho}{\partial t} + \nabla_r \cdot \boldsymbol{\pi} = 0, \right] \quad (3.7)$$

which is a continuity equation stating mass conservation, where

$$\boldsymbol{\pi}(\mathbf{r}, t) := \langle \mathbf{P} \rangle_{\mathcal{V}_P} := \int_{\mathcal{V}_P} \mathbf{P} F(\mathbf{r}, \mathbf{P}, t) d^3P \quad (3.8)$$

is the first marginal moment (analogous to $\varrho = \langle 1 \rangle_{\mathcal{V}_P}$ being the zeroth moment), the momentum density. These marginal moments w.r.t. momentum space are usually called '[kinetic moments](#)'. One has

$$\mathbf{V} := \boldsymbol{\pi}/\varrho, \quad (3.9)$$

where \mathbf{V} is the physical velocity or, more precisely, a (phase space-)density weighted average of the velocities of all particles within the control volume d^3r .

The evolution equation for the zeroth kinetic moment ϱ depends on the knowledge of the first kinetic moment $\boldsymbol{\pi}$, and one can already guess that this will recursively unfold in a generally infinite hierarchy, the so-called [Vlasov hierarchy](#) (or Boltzmann hierarchy). Indeed one finds the first marginal moment of the Vlasov equation to be (for the Cartesian spatial component P_i of the vector \mathbf{P})

$$\int_{\mathcal{V}_P} P_i \frac{dF}{dt} d^3P \stackrel{\text{eq. (3.3a)}}{=} \left[\frac{\partial \pi_i}{\partial t} + \frac{1}{m} \frac{\partial \Pi_{ij}}{\partial r_j} + \varrho \frac{\partial \phi}{\partial r_i} = 0, \right] \quad (3.10)$$

which involves the second kinetic moment

$$\Pi_{ij}(\mathbf{r}, t) := \langle P_i P_j \rangle_{\mathcal{V}_P} := \int_{\mathcal{V}_P} P_i P_j F(\mathbf{r}, \mathbf{P}, t) d^3P. \quad (3.11)$$

Repeating this exercise one very last time, one finds the evolution equation for the second kinetic moment to be given by

$$\int_{\mathcal{V}_P} P_i P_j \frac{dF}{dt} d^3 P \stackrel{\text{eq. (3.3a)}}{=} \left[\frac{\partial \Pi_{ij}}{\partial t} + \frac{1}{m} \frac{\partial Y_{ijk}}{\partial r_k} + m \pi_i \frac{\partial \phi}{\partial r_j} + m \pi_j \frac{\partial \phi}{\partial r_i} \right] = 0, \quad (3.12)$$

and the third kinetic moment

$$Y_{ijk}(\mathbf{r}, t) := \langle P_i P_j P_k \rangle_{\mathcal{V}_P} := \int_{\mathcal{V}_P} P_i P_j P_k F(\mathbf{r}, \mathbf{P}, t) d^3 P. \quad (3.13)$$

As expected, this hierarchy continues ad infinitum and, in general, we do not end up with a closed system of equations. Instead of one equation on 3+3-dimensional space, we have now infinitely many equations on 3-dimensional space. Obviously, working with the moment equation is only constructive if some sort of (exact or approximative) closure condition is employed; we will come back to this shortly.

Apart from using the raw marginal/kinetic moments, we can also employ the intrinsic parts in the moments of the distributions a.k.a. the [cumulants](#), which we have discussed in the previous chapter in their general statistical context. Specifically, we have the second cumulant

$$\begin{aligned} \varrho \sigma_{ij} &:= \frac{1}{m} \langle P_i P_j \rangle_{\mathcal{V}_P} - \frac{1}{\varrho} \langle P_i \rangle_{\mathcal{V}_P} \langle P_j \rangle_{\mathcal{V}_P} \\ &= \frac{\Pi_{ij}}{m} - \frac{\pi_i \pi_j}{\varrho}, \end{aligned} \quad (3.14)$$

whose trace, $\frac{1}{2} \text{tr } \varrho \sigma_{ij}$ is known to physicists as the internal energy density, and σ_{ij} is called the [velocity dispersion tensor](#). The second moment corresponds to the total energy density, while the conversion of energy from the unconnected part of the moment to the connected part is related to entropy production in thermodynamic systems. Indeed, for the third cumulant we obtain a term that is related to an entropy flux and is given by (omitting the subscript ' \mathcal{V}_P ' for brevity)

$$\begin{aligned} \varrho \gamma_{ijk} &:= \frac{1}{m} \langle P_i P_j P_k \rangle - \frac{1}{\varrho} (\langle P_i P_j \rangle \langle P_k \rangle + \langle P_i P_k \rangle \langle P_j \rangle + \langle P_j P_k \rangle \langle P_i \rangle) - \frac{1}{\varrho^2} \langle P_i \rangle \langle P_j \rangle \langle P_k \rangle \\ &= \frac{1}{m} Y_{ijk} - \frac{1}{\varrho} (\Pi_{ij} \pi_k + \Pi_{ik} \pi_j + \Pi_{jk} \pi_i) - \frac{1}{\varrho^2} \pi_i \pi_j \pi_k. \end{aligned} \quad (3.15)$$

If we remember Marcinkiewicz' theorem from the previous chapter (see page 48), then we know immediately that progress can be made if we can assume that the distribution function is either Dirac- δ ($m = 1$) or Gaussian ($m = 2$) at all times (note that the width of the Gaussian and the mean of Dirac and Gauss are allowed to change however). In that case all higher cumulants $> m$ vanish and the Boltzmann hierarchy is truncated. This behaviour can be guaranteed only in two cases: (1) in the Dirac- δ case, while the velocity field remains single-valued (which is not at all guaranteed during the later gravitational evolution!), then

$$\sigma_{ij} \text{ and all higher cumulants} = 0 \Leftrightarrow \text{infinitely cold limit}, \quad (3.16)$$

where the latter implies no multi-streaming; and (2) in the Gaussian case if there is an additional collision process (which is inconsistent with the Vlasov equation and only applies for the Boltzmann equation), which on short time-scales maximises the entropy locally thus suppressing the third cumulant (the entropy flux), then

$$\gamma_{ijk} \text{ and all higher cumulants} = 0 \Leftrightarrow \text{maximum entropy limit}. \quad (3.17)$$

This last aspect is often discussed in the context of ‘molecular chaos’ and Boltzmann’s H-theorem, and one assumes that entropy is maximised locally on timescales much shorter than the mean field dynamics, which is usually termed ‘local thermodynamic equilibrium’ (LTE) – it is local, because globally the system need not be in thermodynamic equilibrium. We will only acknowledge this here and assume that we can happily work with the truncated hierarchies in the two limiting cases of the cold-collisionless (Vlasov) limit and the strongly collisional (Boltzmann) limit.

It is important to note that we can a priori guarantee these limits only for specific initial data, i.e., we can set up a fluid with an initial distribution function F that has the right properties. We can however not guarantee that they remain in this state for any amount of time under Vlasov evolution. The reason is that there are smooth solution of Vlasov dynamics that have singular behaviour in the fluid equations, where the solutions can have infinities or discontinuities. These singularities are usually connected with entropy production in the fluid system in order to guarantee a conservation of energy. We will discuss such singularities later in Section TBD.

The Vlasov–Poisson equations in comoving coordinates

Above we have discussed the Vlasov–Poisson equations in physical coordinates, where the overall expansion of the Universe is not yet optimally encapsulated in the equations. To do so it is useful to (re-)introduce comoving variables and coordinates, which we have actually already discussed in the previous chapter.

For this note that the physical distribution function contains also a background part due to the overall Hubble flow. To see this we impose the *Ansatz* that F is at the background level

$$F(\mathbf{r}, \mathbf{P}, t) = \bar{F}(\mathbf{r}, \mathbf{P}, t) := \bar{\rho} \delta_D^{(3)}(\mathbf{P} - mH(t)\mathbf{r}), \quad (3.18)$$

where $H = \dot{a}/a$, and $\delta_D^{(3)}$ denotes the three-dimensional Dirac-delta distribution. Indeed, plugging (3.18) into (3.3) and noting that at the background level the Poisson equation reduces to (1.81), it is straightforward to derive the second Friedmann equation (1.53b), as well as $\bar{\rho} \sim a^{-3}$ as established in section 1. In a forthcoming exercise (section 3) we will perform analogous manipulations, however not in phase-space but at the fluid level, where calculations are more tractable.

Next we consider fluctuations to the Vlasov–Poisson equations for which we employ the comoving phase-space variables \mathbf{x} and \mathbf{p} , which are related to the physical variables as follows,

$$\mathbf{r} = a(t)\mathbf{x}, \quad \mathbf{P} = \frac{\mathbf{p}}{a(t)} + m\dot{a}(t)\mathbf{x}. \quad (3.19)$$

This transformation is actually canonical as can be seen by expressing the Lagrangian L corresponding to the physical Hamiltonian $H(\mathbf{r}, \mathbf{P}, t)$, given in Eq. (3.5), in the new variables:

$$L := \dot{\mathbf{r}} \cdot \mathbf{P} - H(\mathbf{r}, \mathbf{P}, t) = \dot{\mathbf{x}} \cdot \mathbf{p} - \mathcal{H}(\mathbf{x}, \mathbf{p}, t) + \frac{d}{dt} \left(\frac{ma\dot{a}}{2} |\mathbf{x}|^2 \right), \quad (3.20)$$

where the “peculiar” (one-particle) Hamiltonian expressed in the new phase-space variables is

$$\mathcal{H}(\mathbf{x}, \mathbf{p}, t) := \frac{|\mathbf{p}|^2}{2ma^2} + m\varphi(\mathbf{x}, t), \quad \varphi(\mathbf{x}, t) := \phi(t, a\mathbf{x}) + \frac{a\ddot{a}}{2}|\mathbf{x}|^2, \quad (3.21)$$

with corresponding Hamiltonian equations of motion

$$\dot{\mathbf{x}} = \nabla_{\mathbf{p}} \mathcal{H} = \frac{1}{ma^2} \mathbf{p}, \quad \dot{\mathbf{p}} = -\nabla_{\mathbf{x}} \mathcal{H} = -m\nabla_{\mathbf{x}} \varphi. \quad (3.22)$$

Furthermore, we can define the [peculiar distribution function](#) $f(\mathbf{x}, \mathbf{p}, t)$ as

$$f(\mathbf{x}, \mathbf{p}, t) := F(a\mathbf{x}, \mathbf{p}/a + m\dot{\mathbf{x}}, t) \quad (3.23)$$

which, using (3.3), implies the [peculiar Vlasov–Poisson equations](#)

$$\frac{df}{dt} = \frac{\partial f}{\partial t} + \frac{\mathbf{p}}{ma^2} \cdot \nabla_{\mathbf{x}} f - m\nabla_{\mathbf{x}} \varphi \cdot \nabla_{\mathbf{p}} f = 0, \quad \nabla_{\mathbf{x}}^2 \varphi(\mathbf{x}, t) = 4\pi G \bar{\rho} a^2 \delta(\mathbf{x}, t), \quad (3.24)$$

where $\delta(\mathbf{x}, t) = [\rho(\mathbf{x}, t) - \bar{\rho}(t)]/\bar{\rho}(t)$ is the aforementioned [density contrast](#) while in comoving variables $\rho(\mathbf{x}, t) := m \int f(\mathbf{x}, \mathbf{p}, t) d^3 p = a^3 \rho(t, a\mathbf{x})$. Note the distinguished appearance of the Poisson equation in peculiar coordinates, as opposed to the physical one (eq. 3.3); now a background part $\sim \ddot{a}/a$ has been subtracted out (using eq. 3.18). Again, similar but more tractable calculations will be performed as an exercise in a subsequent section.

Continuity equations

Let us connect Vlasov to the notion of a continuity equation by means of [Gauss' theorem](#) and thereby neglect for the moment the expansion of the Universe. Let us consider the number of particles in some volume V of the $2d$ -dimensional phase space and let us use $\boldsymbol{\mu} := (\mathbf{x}, \mathbf{p})$ as a combined coordinate in this space. Then we have

$$N_V(t) = \int_V f(\boldsymbol{\mu}, t) dV \quad (3.25)$$

as the number of particles occupying the phase space volume V . This number will change as particles enter or leave the volume element. Let us denote by $\boldsymbol{\omega}$ the $2d$ -dimensional flow field in phase-space, associated with the Hamiltonian \mathcal{H} . This might seem abstract, but it is really just the rate at which particles move (i.e. the velocity) in the first d coordinates, and the rate at which particle change their momentum (i.e. mass times acceleration) in the second d coordinates. The rate at which particles enter or leave the volume V is of course proportional to the density of particles at the boundary of the volume times the component of $\boldsymbol{\omega}$ normal to the surface of the boundary, i.e. we can write

$$\frac{\partial}{\partial t} \int_V f(\boldsymbol{\mu}, t) dV = - \oint_{\partial V} f(\boldsymbol{\mu}, t) \boldsymbol{\omega} \cdot d\mathbf{S}, \quad (3.26)$$

where the integral on the right-hand-side is over the closed boundary ∂V of V and where $d\mathbf{S}$ is the outward-pointing normal vector at each point of the volume surface boundary.

We can now apply Gauss' theorem (also sometimes called Ostrogradsky's theorem, or divergence theorem) to this surface integral in order to turn it into a volume integral. Indeed we find

$$\frac{\partial}{\partial t} \int_V f(\mu, t) dV = - \oint_{\partial V} f(\mu, t) \omega \cdot dS = - \int_V \nabla_\mu \cdot (f(\mu, t) \omega) dV. \quad (3.27)$$

Note that we have added an index μ to the ∇ operator. This means that it is not the usual 3-dimensional operator but contains $2d$ -derivatives with respect to all components of x and p .

If we fix the volume V in time, we can pull the time derivative into the integral and since we have made no further assumptions about the volume V , the equation has to hold also directly for the integrand, i.e.

$$\frac{\partial}{\partial t} f(\mu, t) + \nabla_\mu \cdot (f(\mu, t) \omega) = 0. \quad (3.28)$$

This equation will always hold as long as the number of particles in the system is conserved, i.e., as long as no particles are created in the system or disappear from it. This is a continuity equation in 6-dimensional phase space, and it agrees with the Vlasov equation iff $\nabla_\mu \cdot \omega = 0$, i.e., if the phase space flow is incompressible (Liouville's theorem). For a Hamiltonian system, we have $\omega = (\nabla_p \mathcal{H}, -\nabla_x \mathcal{H})$ so that indeed $\nabla_\mu \cdot \omega = 0$ and we recover Vlasov as

$$\frac{\partial}{\partial t} f(\mu, t) + \omega \cdot \nabla_\mu f(\mu, t) = 0. \quad (3.29)$$

Formulated this way, the Vlasov equation can be interpreted as an advection equation along the Hamiltonian vector field ω .

Fluid equations

Fluid in physical coordinates

As we have discussed in section 3, the 3+3+1-dimensional formulation in phase space through the Vlasov-Poisson equations can be formulated in a 3+1-dimensional description by taking marginal moments w.r.t. momentum space. Formulated in the fluid variables, the resulting fluid-type equations are the [continuity equation](#)

$$\partial_t \varrho + \nabla_r \cdot (\varrho \mathbf{V}) = 0 \quad (3.30a)$$

and the [Euler equation](#)

$$\partial_t \mathbf{V} + (\mathbf{V} \cdot \nabla_r) \mathbf{V} = -\nabla_r \phi - \frac{1}{\varrho} \nabla_r \cdot (\varrho \boldsymbol{\sigma}), \quad (3.30b)$$

which are supplemented with the physical Poisson equation,

$$\nabla_r^2 \phi(r, t) = 4\pi G \varrho - \Lambda c^2. \quad (3.30c)$$

So far these equations are an exact representation of the VP equations, however with the important difference that, in general, for the n th marginal moment, one needs knowledge of the $(n+1)$ th marginal moment. Thus, as mentioned before, the 3+3+1-dimensional formulation is replaced by an infinite set of

momentum-integrated equations in 3+1 dimensions, the Vlasov hierarchy. Needless to say, an infinite set of fluid-type equations is unbearably complex, and thus the whole strategy of performing kinetic moments from Vlasov might appear to be not very constructive.

However, for various physical scenarios, such as the early gravitational evolution of cold dark matter after recombination, σ_{ij} is effectively zero on sufficiently large scales and thus perfectly cold. Indeed, any initial small velocity dispersion would decay away with the expansion of the Universe (i.e., the expansion effectively cools the particle distribution). If $\sigma_{ij} = 0$, the infinite Vlasov hierarchy is exactly terminated at the first marginal and, as a consequence, for such scenarios, the fluid equations (3.30) with $\sigma_{ij} = 0$ are an exact reduction of the full VP equations. At the same time, the physical momentum of particles does not decay as its temporal evolution is driven by the gradient of the gravitational potential. We note however that $\sigma_{ij} = 0$ is not justified anymore during the final stages of structure formation (especially in dark-matter halos where typically $\varrho\sigma_{ij}$ is of the same magnitude as $\pi_i\pi_j/\varrho$).

Fluid in comoving coordinates

The fluid equations can also be formulated in comoving coordinates $x = \mathbf{r}/a(t)$, i.e. coordinates that are at rest with respect to the expanding background (note that they are not fully ‘Lagrangian’ coordinates, as they are not comoving with the fluid itself, only the background). As we will see shortly, such reformulations are in particular crucial for analytical avenues. As before, for this one splits up all fluid variables in background and fluctuation parts,

$$\varrho = \bar{\varrho}(t)[1 + \delta], \quad \mathbf{V} = H(t)\mathbf{r} + a\mathbf{u}, \quad \phi = \bar{\phi}(t) + \varphi_p, \quad \sigma_{ij} = \bar{\sigma}(t)\delta_{ij}, \quad (3.31)$$

where δ_{ij} is the [Kronecker-delta](#) which is unity if $i = j$ and zero otherwise, and we note that, for simplicity, from here on we keep σ_{ij} only as a *scalar background* component. Plugging these definitions into the fluid equations (3.30) one obtains at the background level (again) the Friedmann equations (??), and at the fluctuation level the following set of [peculiar fluid equations](#) coupled to a peculiar Poisson equation.

Definition 3.2 — Cosmological Euler–Poisson equations. Let $\delta(x, t) : \Omega \subseteq \mathbb{R}^n \times [0, T] \rightarrow \mathbb{R}$ denote the density contrast, $\mathbf{u}(x, t) : \Omega \subseteq \mathbb{R}^n \times [0, T] \rightarrow \mathbb{R}^n$, and $\varphi_p(x) : \Omega \subseteq \mathbb{R}^n \rightarrow \mathbb{R}$ the peculiar gravitational potential. Assume further that $a(t)$ solves the Friedmann equation (??) for $t \in [0, T]$ with a matter density parameter Ω_m , and $\bar{\sigma} : [0, T] \rightarrow \mathbb{R}_0^+$ is a non-negative function representing a background “velocity dispersion”. The following set of PDEs

$$\partial_t \delta + \nabla_x \cdot [(1 + \delta)\mathbf{u}] = 0, \quad (3.32a)$$

$$\partial_t \mathbf{u} + (\mathbf{u} \cdot \nabla_x) \mathbf{u} + 2\frac{\dot{a}}{a} \mathbf{u} = \frac{1}{a^2} \left(-\nabla_x \varphi_p - \bar{\sigma} \frac{\nabla_x \delta}{1 + \delta} \right), \quad (3.32b)$$

$$\nabla_x^2 \varphi_p = \frac{3H_0^2 \Omega_m}{2} a^{-1} \delta, \quad (3.32c)$$

govern the evolution of the cosmic matter fluid, given suitable initial and boundary conditions. Note that $T > 0$ is bounded from above by the emergence

of the shell-crossing singularity (about which we will learn later).

Exercise 3.1 — Derivation of the peculiar fluid equations. Starting from the physical fluid equations (3.30), derive the peculiar fluid equations (3.32) in the absence of anisotropic stress. For this one first needs to extract the background part of (3.30), which can be done by keeping only the purely temporal part in the decomposition (3.31), i.e., $\rho = \bar{\rho}(t)$, $\mathbf{V} = H(t) \mathbf{r}$, $\phi = \bar{\phi}(t)$ and $\sigma_{ij} = \bar{\sigma}(t) \delta_{ij}$. This leads to the second Friedmann equation with vanishing pressure. Then we can solve for the fluctuation part by plugging the full decomposition (3.31) into (3.30).

Hints for this exercise: To arrive at eq. (3.32b), some terms can be vastly simplified by using the second Friedmann equation. Also, for an arbitrary function $f(\mathbf{r}, t) = f(a(t) \mathbf{x}, t)$ we know that

$$\partial_t f|_{\mathbf{x} \text{ fixed}} = \partial_t f|_{\mathbf{r} \text{ fixed}} + \dot{a} (\mathbf{x} \cdot \nabla_{\mathbf{r}}) f|_{t \text{ fixed}}. \quad (3.33)$$

Finally, one also needs to convert the spatial derivatives according to $\nabla_{\mathbf{r}} = (1/a) \nabla_{\mathbf{x}}$. ■

Linear analysis of fluid equations

The fluid equations are of non-linear nature and thus difficult (but not impossible) to solve analytically. However, during the very early stages of cosmic structure formation, fluctuations in the fluid variables w.r.t. their background values are tiny and thus, the *linearised* fluid equations are fully meaningful, which surely simplifies the analysis. In fact such considerations are essential when we motivate suitable boundary conditions below, which enables us to solve the non-linear fluid equations by analytical means.

Formally linearising the fluid equations (3.32) around the steady state, all terms that are multiple combinations of the peculiar fluid variables δ and \mathbf{u} can be ignored. Then, the fluid equations can be combined into a single differential equation for the linearised density contrast, denoted with $\delta = \delta_1$,

$$\ddot{\delta}_1 + 2H(t) \dot{\delta}_1 - (4\pi G \bar{\rho} + a^{-2} \bar{\sigma} \nabla_x^2) \delta_1 = 0. \quad (3.34)$$

We see immediately that in the $\bar{\sigma} \rightarrow 0$ limit, the only term that contains spatial derivatives drops out and we obtain

$$\ddot{\delta}_1 + 2H(t) \dot{\delta}_1 - 4\pi G \bar{\rho} \delta_1 = 0. \quad (3.35)$$

Observe that this is an *ordinary* differential equation in time, which might be surprising given that the fluid equations involve *partial* differential equations. In fact, this separation of temporal and spatial scales persists for most background cosmologies of practical purposes¹. The important observation is that Newtonian gravity for a single and pressure-less fluid is free of any spatial scale, and for precisely this reason we are able to decouple the spatial and the temporal part here, turning the PDE into an ODE without further ado. Note that this scale-free behaviour is broken when $\bar{\sigma}$ is finite [and/or if additional fluids are

¹This is slightly more complicated at the nonlinear level: There, perturbative solutions at a given order are a superposition of terms that each factorise in purely time- and space-dependent parts (Ehlers and Buchert, 1997).

present], which does *not* allow us to decouple time and space at this level [under certain simplifying assumptions, the equations for multiple cold fluids can be decoupled (Rampf et al., 2021b)].

Let us discuss the most important solutions of the second-order differential equation (3.35), which, due to the appearance of $H(t)$, depend explicitly on the chosen background cosmology.

Finite temperatures: the Jeans scale

Let us first discuss the case of $\bar{\sigma} > 0$ which in physical models typically occurs when the considered fluid has a finite temperature (that comes with a thermal component in the velocity distribution). In this case, we can turn the linear PDE (3.34) – as any linear PDE – into an ODE by Fourier transformation. We know already that under a Fourier transform $\nabla \rightarrow ik$ and hence $\nabla^2 \rightarrow -k^2$. The Fourier transform of (3.34) is thus

$$\ddot{\tilde{\delta}}_1 + 2H(t)\dot{\tilde{\delta}}_1 - (4\pi G\bar{\rho} - a^{-2}\bar{\sigma}k^2)\tilde{\delta}_1 = 0. \quad (3.36)$$

We shall not attempt here yet to solve this equation, which is complicated by the appearance of the Hubble friction term $H(t)\dot{\tilde{\delta}}_1$ comprising a product of two time-dependent functions, which cannot be simply handled by another Fourier transform into frequency space (since the product turns into a convolution in Fourier space). Instead, we note that for finite $\bar{\sigma}$, the source term flips its sign at a characteristic scale k_J , the '[Jeans scale](#)', going back to a pioneering analysis (carried out for a non-expanding Newtonian universe) by James Jeans in 1902 ([Jeans 1902](#)) (see also the beautiful modern discussion by Kiessling [2003](#)). It is defined by

$$4\pi G\bar{\rho} - a^{-2}\bar{\sigma}k_J^2 = 0 \quad \Rightarrow \quad k_J = \pm a\sqrt{\frac{4\pi G\bar{\rho}}{\bar{\sigma}}}. \quad (3.37)$$

Ignoring the Hubble friction term for the moment, one immediately sees that modes $|k| > |k_J|$ correspond to oscillating solutions, while modes $|k| < |k_J|$ correspond to growing/decaying solutions. The scale k_J itself is time-dependent, shifting over time to larger wave numbers, i.e., smaller spatial scales. Finite temperature effects thus prevent small scales from collapsing under their own gravity. Note that even for initially perfectly cold flow, finite temperature arises at late times due to shell-crossing singularities (see Section TBD). We shall not pursue the finite temperature regime further for the moment (we will come back armed with a computer), and instead consider the simpler and analytically tractable cold limit.

Cold solutions

As discussed above, in the cold limit with $\sigma = 0$ in (3.32), the early-time evolution of the collisionless fluid is free of spatial scales, leading to the ODE (3.35) for the linear density fluctuations. The cold case is the most important limiting case for cosmology, and thus will be thoroughly discussed in the following sections. In a purely matter dominated universe with zero curvature and vanishing cosmological constant, i.e., the [Einstein-de Sitter \(EdS\) universe](#), the linear solution to (3.35) is

$$\delta_1(\mathbf{x}, t) = C_1(\mathbf{x})a(t) + C_2(\mathbf{x})a^{-3/2}(t) \quad (\text{linear EdS solution}) \quad (3.38)$$

where $C_{1,2}$ are spatial constants that should be fixed using appropriate boundary conditions (see below). Of course, apart from the spatial dependence which is now three-dimensional, this result coincides with the one from the 1D analysis in ???. Solutions for an EdS universe play an important role in analytical studies for the Euler–Poisson equations (3.32), mainly since those equations are believed to provide meaningful results for sufficiently early stages during cosmic structure formation, where the impact of Λ and/or, potentially of nonzero σ , are vanishingly small.

Another important example is when not only matter but also a cosmological constant Λ is included in the cosmological model, i.e., the Λ CDM Universe, for which the two solutions of the second-order ODE (3.35) are

$$\delta_1(\mathbf{x}, t) = C_1(\mathbf{x}) D_+(t) + C_2(\mathbf{x}) D_-(t), \quad (\text{linear } \Lambda\text{CDM solution}) \quad (3.39a)$$

with

$$D_+(t) = a(t) \sqrt{1 + \lambda_0 a^3(t)} {}_2F_1\left(\frac{3}{2}, \frac{5}{6}, \frac{11}{6}, -\lambda_0 a^3(t)\right), \quad (3.39b)$$

$$D_-(t) = a^{-3/2}(t) \sqrt{1 + \lambda_0 a^3(t)}, \quad (3.39c)$$

where ${}_2F_1$ is the Gauss hypergeometric function, and $\lambda_0 := \Omega_\Lambda / \Omega_{m,0}$.² The solutions are plotted for both EdS and Λ CDM in Figure 3.4.

Program Code 3.1 — Λ CDM linear growth via special functions in Scipy. Gauss' hypergeometric function is part of the `scipy` PYTHON package. Let $\lambda_0 := \Omega_\Lambda / \Omega_{m,0}$. The growing mode solution is e.g. easily computed via

```

1 import scipy.special as sf
2 import numpy as np
3
4 def Dplus( lambda0, a ):
5     return a * np.sqrt(1.0+lambda0*a**3) * \
6             sf.hyp2f1(3.0/2.0, 5.0/6.0, 11.0/6.0, -lambda0 * a**3 )
7 def Dminus( lambda0, a ):
8     return a**(-3.0/2.0) * np.sqrt(1.0+lambda0*a**3)

```

These routines were used to produce Figure 3.4.

For further analytic solutions with scanning for various cosmological set-ups, see e.g. Demianski et al. (2005). Also note that, for any cosmology, once the linear density is determined, the linear velocity divergence $\nabla \cdot \mathbf{u}_1$, follows from the linearised continuity equation (eq. 3.32a),

$$\nabla_{\mathbf{x}} \cdot \mathbf{u}_1 = -\partial_t \delta_1(\mathbf{x}, t). \quad (3.40)$$

Furthermore, note that provided $\nabla_{\mathbf{x}} \times \mathbf{u} = 0$ initially, which is typically assumed in structure formation (see also discussion below around eq. 3.41), then one can retrieve from $\nabla \cdot \mathbf{u}_1$ also the velocity field (taking the boundary conditions into account).

But what if $\nabla_{\mathbf{x}} \times \mathbf{u} \neq 0$ initially or generally at early times? To see what happens let us define the vorticity

$$\mathbf{w} := \nabla_{\mathbf{x}} \times \mathbf{u}, \quad (3.41)$$

²Note that the linear growing mode in Λ CDM has the analytic expansion around $a = 0$: $D_+ = a - (2/11)\lambda_0 a^4 + \mathcal{O}(a^7)$. Thus, for short times, $D_+ \propto a$, as is also apparent from the asymptotic behaviour in Fig. 3.4.

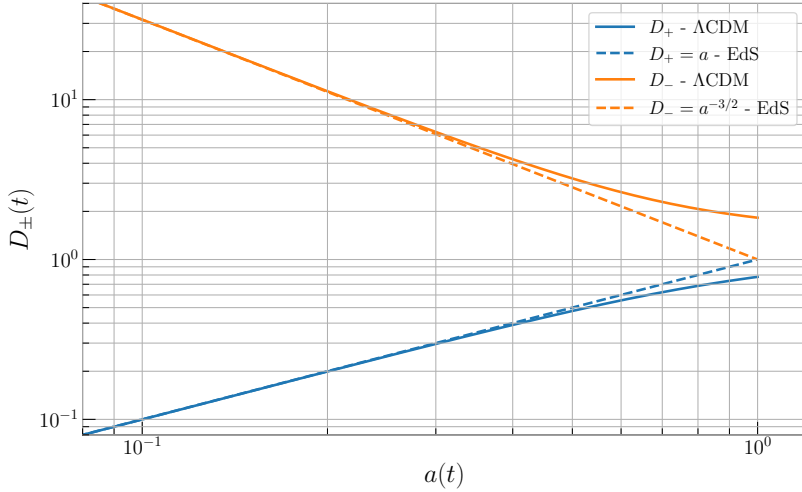


Figure 3.4: The growth of perturbations of the linearised Euler-Poisson equations in ΛCDM (solid lines, $\Omega_\Lambda \simeq 0.7$, $\Omega_m \simeq 0.3$) and EdS (dashed lines) as a function of the scale-factor of the universe. The growing modes are shown in blue, the decaying modes in orange. Note that here the D_\pm for ΛCDM are not normalised to unity today (as is commonly done) but to the EdS asymptotics to highlight physical differences.

and take the curl of the linearised Euler equation (3.32b) and ignore for the moment velocity dispersion. Then one obtains for the linear vorticity the equation

$$\partial_t \mathbf{w}_1 + 2H(t)\mathbf{w}_1 = 0, \quad (3.42)$$

which has the solution $\mathbf{w}_1 \propto a^{-1}$, implying that for sufficiently early times, any nonzero vorticity decays as the Universe expands. This argument is typically employed when justifying to ignore initial vorticity to begin with.

The above solutions $\propto C_+$ and $\propto C_-$ are called [growing-mode](#) and [decaying-mode](#) solutions since their temporal amplitudes, D_+ and D_- , respectively grow and decay in the course of cosmic time; see Fig. 3.4. The impact of decaying modes – if not excited e.g. due to iso-curvature modes or due to (late-time) energy injections – are usually negligible in comparison to the growing-mode, especially at sufficiently late times. To see this, suppose that we provide at time $a = a_{\text{ini}}$ the initial data $\delta_{\text{ini}} := \delta(a_{\text{ini}})$ and $\theta_{\text{ini}} := \nabla_x \cdot \mathbf{u}(a_{\text{ini}})/\dot{a}_{\text{ini}}$ in an EdS universe; evaluating (3.39a) and (3.40) at a_{ini} and using the intial data, one then finds that $C_- \propto \delta_{\text{ini}} + a_{\text{ini}}\theta_{\text{ini}}$. However, the nature of gravitational collapse of a single fluid enforces the parallelism between gravitational acceleration and infalling velocities and, as a consequence $\delta_{\text{ini}} + a_{\text{ini}}\theta_{\text{ini}} \simeq 0$ unless external forces (e.g., through the presence of other fluids) distort this parallelism. Therefore, for many cosmological applications, it is customary and justified to effectively ignore the decaying modes.

Zel'dovich approximation from early-time asymptotics

Early-time asymptotic behaviour

For simplicity, we consider an EdS model (i.e. only matter with $\Omega_m = 1$, so that $\dot{a}/a = a^{-3/2}$). Additionally, we define the rescaled peculiar velocity

$v(x, a) := \partial x / \partial a$ which relates to the “old” peculiar velocity as follows,

$$\mathbf{u}(x, t) = \dot{a} \mathbf{v}. \quad (3.43)$$

Definition 3.3 — EdS fluid equations for cold cosmic matter in a -time. With these definitions, and using the first Friedmann equation to get an expression for \dot{a} , the peculiar fluid equations (3.32) become for an EdS universe

$$\partial_a \delta + \nabla_x \cdot [(1 + \delta) \mathbf{v}] = 0, \quad (3.44a)$$

$$\partial_a \mathbf{v} + (\mathbf{v} \cdot \nabla_x) \mathbf{v} = -\frac{3}{2a} (\mathbf{v} + \nabla_x \varphi), \quad (3.44b)$$

$$\nabla_x^2 \varphi = \frac{\delta}{a}, \quad (3.44c)$$

where all involved functions depend now on the scale-factor time, and we note that, for convenience, the cosmological potential has been rescaled by a factor of $2/(3\dot{a}^2 a)$.

Proposition 3.1 — Early-time asymptotics. Multiplying the Euler (3.44b) and Poisson equations (3.44c) by a and subsequently taking the limit $a \rightarrow 0$ yields the following early-time asymptotic solutions for the linearised Euler–Poisson equations (3.44). At $a \rightarrow 0$ we have

$$\mathbf{v} = -\nabla_x \varphi \quad \delta = 0. \quad (3.45a)$$

Definition 3.4 — Method of characteristics. Solutions to the Euler equation can be expressed in terms of characteristics. We define a characteristics as the family of curves $X(\mathbf{q}, a)$ starting from the initial position $X(\mathbf{q}, 0) = \mathbf{q}$ and parameterised by a . The equations for the characteristics are given by ordinary differential equations.

■ **Example 3.1 — Euler equation.** Define the ODE

$$\frac{dX}{da} = \mathbf{v}(X, a). \quad (3.46)$$

Then

$$\frac{d^2X}{da^2} = \frac{\partial}{\partial a} \mathbf{v}(X, a) + \left(\frac{dX}{da} \cdot \nabla_x \right) \mathbf{v}(X, a) = [\partial_a \mathbf{v} + (\mathbf{v} \cdot \nabla_x) \mathbf{v}]_{x=X(q,a)}. \quad (3.47)$$

Therefore, the Euler equation (3.44b) can be rewritten in terms of the characteristics as a second order ODE of the form

$$\frac{d^2X}{da^2} = -\frac{3}{2a} \left(\frac{dX}{da} + (\nabla_x \varphi)(X) \right). \quad (3.48)$$

supplemented with the initial data $X(\mathbf{q}, 0) = \mathbf{q}$ and $\frac{dX}{da}(\mathbf{q}, 0) = \mathbf{v}(\mathbf{q}, 0)$. ■

The Zel'dovich map

Definition 3.5 — Zel'dovich map. The early-time asymptotics defines the [Zel'dovich map](#) as

$$X(\mathbf{q}, a) = \mathbf{q} + a v^{\text{ini}}(\mathbf{q}), \quad (3.49)$$

where trivially $X(\mathbf{q}, 0) = \mathbf{q}$ is fulfilled, and the initial velocity field is given by

$$\frac{dX}{da} = v^{\text{ini}}(\mathbf{q}) = -\nabla_{\mathbf{q}} \varphi^{\text{ini}}(\mathbf{q}). \quad (3.50)$$

which, in the given spatio-temporal coordinates, has the extremely simple physical interpretation of ballistic motion, i.e. $\frac{d^2X}{da^2} = 0$ – fluid particles just follow their initially prescribed velocity. Of course, this solution trivially holds also for a Λ CDM Universe upon the replacement $a \rightarrow D_+$, where the latter is the corresponding linear growth rate (see Eq. 3.39b and/or Fig. 3.4).

Definition 3.6 — Lagrangian map. The Zel'dovich map is a special case of the [Lagrangian map](#), which is defined as the mapping from the initial (Lagrangian) position \mathbf{q} to the current (Eulerian) position \mathbf{X} , i.e.,

$$\mathbf{X}(\mathbf{q}, a) := \mathbf{q} + \Psi(\mathbf{q}, a). \quad (3.51)$$

The Zel'dovich map (and most Lagrangian maps) is measure preserving, i.e. it expresses mass conservation in the most general form as the equality of measures in Lagrangian and Eulerian space through an induced density $1 + \delta$,

$$[1 + \delta(\mathbf{X}, a)] d^3X = d^3q.$$

Be aware that in general the map may be not one-to-one, i.e. there may exist multiple \mathbf{q}_i for which $\mathbf{X}(\mathbf{q}_i, a) = \mathbf{x}$. This implies that the general expression for the density contrast in terms of the Lagrangian map is

$$1 + \delta(\mathbf{x}, a) = \int \delta_D(\mathbf{x} - \mathbf{X}(\mathbf{q}, a)) d^3q, \quad (3.52)$$

Proposition 3.2 Let $f : \Omega \subseteq \mathbb{R}^n \rightarrow \mathbb{R}^n$ be a differentiable function with isolated zeros. Then the n -dimensional generalization of the substitution formula for Dirac- δ functions reads

$$\delta_D(f(\mathbf{q})) = \sum_i \frac{\delta_D(\mathbf{q} - \mathbf{q}_i^*)}{|\det Df(\mathbf{q}_i^*)|}, \quad (3.53)$$

where the sum runs over all roots \mathbf{x}_i^* of $f(\mathbf{x})$, i.e. $f(\mathbf{x}_i^*) = 0$, and Df is the Jacobian of f .

As long as the Lagrangian mapping is bijective, i.e., at any position in \mathbf{x} -space there is only one fluid particle with label \mathbf{q} , then the argument of the Dirac-delta in (3.52) has only one root \mathbf{q} for which $\mathbf{x} = \mathbf{X}(\mathbf{q}, a)$, implying that mass conservation simplifies to

$$1 + \delta(\mathbf{q}, a) = \frac{1}{J(\mathbf{q}, a)}, \quad J(\mathbf{q}, a) := \left| \det \left(\frac{\partial \mathbf{X}}{\partial \mathbf{q}} \right) \right|, \quad (3.54)$$

where J is the said Jacobian. From that equation it is evident that the density becomes infinite if the Jacobian vanishes (which in the left panel of Fig. 3.5 may be

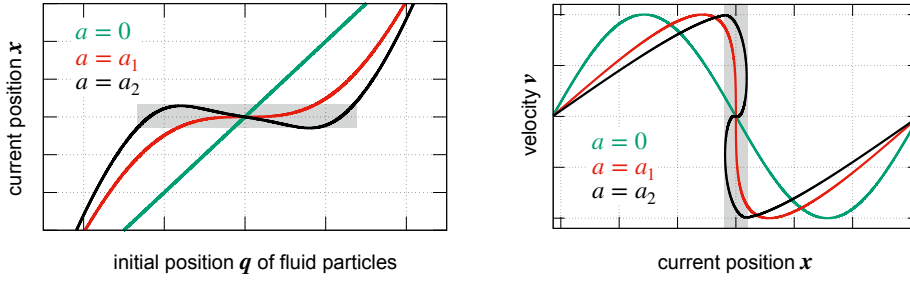


Figure 3.5: **Left:** Sketch of the Lagrangian map $q \mapsto X(q, a)$ at initial time (green) for which $x(q, a = 0) = q$, and at subsequent later times a_1 (red) and a_2 (black). Note the critical time $a = a_1$ called **shell-crossing**, which is accompanied with an infinite density (here: at the center). Shortly after, say at time $a = a_2$, there are regions where different fluid streams occupy the same current position (grey shading), the so-called **multi-streaming regime** which is accompanied with a non-zero velocity dispersion. **Right:** Same but shown is the phase space.

viewed as the location where the Lagrangian space derivative of the map is zero). The first instant when this happens is commonly denoted with **shell-crossing**, and amounts to an important phase transition of the matter fluid: From here on there are locations with non-zero velocity dispersion, resulting from the presence of multiple fluid streams at some current positions. From a physical point of view, bound cosmological structures are seeded by the first shell-crossings.

Definition 3.7 — Shell crossing. The locations of shell-crossing at a given time a_* are defined as the positions q_* where the Jacobian J vanishes. These locations are where the density contrast δ becomes infinite.

Theorem 3.1 — Odd number of roots at shell-crossing. For a differentiable Lagrangian map, the number of roots of the Lagrangian map $X(q, a)$ is odd at all locations that are not shell-crossing points. In shell-crossing points, the number of roots is even.

Proof. This is quite non-trivial to prove, I haven't found an easy proof for more than one dimension yet. ■

One of the immediate features of the ZA is that it predicts qualitatively the first shell-crossing, i.e., when the density becomes formally infinite due to the first crossing of particle trajectories. Indeed, plugging (3.49) into the mass conservation law (3.54) yields the (parametric) solution

$$\delta(X, a) + 1 = \frac{1}{\det[\delta_{ij} - a\varphi_{,ij}^{\text{ini}}(q)]} = \frac{1}{[1 + a\lambda_1(q)][1 + a\lambda_2(q)][1 + a\lambda_3(q)]'} \quad (3.55)$$

where $\lambda_{1,2,3}$ are the real eigenvalues of the symmetric tensor $-\varphi_{,ij}^{\text{ini}}$. From the last equality it is clear that $\delta \rightarrow \infty$ locally, if at least one of the three square-bracketed terms vanishes.

From the above it can be already 'guessed' that ZA has more predictive power as compared to the first-order counterpart in Eulerian perturbation theory. Indeed, the latter dictates $\delta \simeq a\nabla_x^2\varphi$ at first order in perturbation theory, which predicts

an infinite density (i.e., shell-crossing) only for $a \rightarrow \infty$, which is physically not very meaningful. By contrast, from numerical experiments using random field initial conditions (Rampf and Hahn, 2021), we know that the ZA predicts the actual time of first shell-crossing to an accuracy of about 20% – a truly stunning performance for a first-order description!

In this context, we remind the reader of section 2 where we determined the eigenvalue distributions of Hessians of Gaussian fields. These derivations are also valid for the present case of the Zel'dovich approximation; see in particular Figure 2.1 where show the three marginal distributions of the three eigenvalues $\lambda_{1,2,3}$.

Proposition 3.3 — Zel'dovich solution. The Zel'dovich map (3.49)

$$\mathbf{X}(\mathbf{q}, a) = \mathbf{q} - D_+ \nabla_{\mathbf{q}} \varphi_{\text{ini}}(\mathbf{q}) \quad (3.56)$$

is the *exact solution* to the non-linear Euler–Poisson equations for one-dimensional initial data prior to shell-crossing. It is therefore not only the asymptotic solution for early times in this case, and we call it the **Zel'dovich solution** in this case.

Proof. For one dimensional planar initial data, i.e. varying only along one Cartesian direction, the solution to the Euler–Poisson system possesses the same symmetry. Therefore it suffices to show that the Zel'dovich map is a solution to the non-linear Euler–Poisson equations in one Cartesian dimension. We can therefore evaluate the characteristic equation (3.46) in one dimension, which reads

$$\frac{d^2 X}{da^2} = -\frac{3}{2a} \left(\frac{dX}{da} + \frac{\partial \varphi}{\partial x}(X) \right). \quad (3.57)$$

It suffices to show that the Zel'dovich map is a solution to this equation. We have at $a = 0$ that $\frac{dX}{da} = -\frac{\partial \varphi_{\text{ini}}}{\partial x}$. The Poisson equation in one dimension reads $\frac{\partial^2 \varphi}{\partial x^2} = \frac{\delta}{a}$ with source term $1 + \delta(X, a) = \left(\frac{\partial X}{\partial q} \right)^{-1} = J^{-1}$. The solution to this equation is for a fluid element q_* prior to shell-crossing (so that the map $q_* \mapsto X(q_*)$ is one-to-one)

$$\frac{\partial \varphi}{\partial x} = \frac{1}{a} \int_{-\infty}^{X(q_*)} \delta(x, a) dx = \frac{1}{a} \int_{-\infty}^{q_*} \delta(X, a) \frac{\partial X}{\partial q} dq = \frac{1}{a} \int_{-\infty}^{q_*} (1 - J) dq \quad (3.58)$$

For the Zel'dovich map we have $J = 1 + a \frac{\partial^2 \varphi_{\text{ini}}}{\partial q^2}$, and thus

$$\frac{\partial \varphi}{\partial x} = \int_{-\infty}^{q_*} \frac{\partial^2 \varphi_{\text{ini}}}{\partial q^2} dq = \left. \frac{\partial \varphi_{\text{ini}}}{\partial q} \right|_{q_*} + C(a) \quad (3.59)$$

where $C(a)$ is a function of a only, called the **Heckmann-Schücking boost**. Therefore, if initially $\frac{dX}{da} = -\frac{\partial \varphi_{\text{ini}}}{\partial x}$ at $a = 0$, then this will always hold. The Heckmann-Schücking boost gives an additional global freedom to add a global time-dependent motion $X \rightarrow X + C(a)$. ■

The ZA has many important applications in cosmology, and has been the starting point of many other influential investigations; see e.g. Buchert (1992); Valageas (2011); McQuinn and White (2016), and White (2014); Rampf (2021) for recent reviews.

Non-gaussianity and non-linear structure

Calculations from perturbation theory can be straightforwardly used for predicting the statistics of the cosmic large-scale structure. In the following we focus on two examples how this can be done.

Two-point correlation function in the ZA

In the previous chapters we have discussed the two-point correlation function ξ for a statistically isotropic and homogeneous (stationary) Universe described by a density contrast function δ which we abbreviate in the following with

$$\mathbb{E}[\delta(\mathbf{x}_1)\delta(\mathbf{x}_2)] = \xi(x) := \langle \delta(\mathbf{x}_1)\delta(\mathbf{x}_2) \rangle \quad (3.60)$$

for $x = \mathbf{x}_2 - \mathbf{x}_1$, $x = |\mathbf{x}|$; here and in the following we will suppress some obvious dependences of functions.

In the exercise below we show how the ZA can be used to obtain the semi-analytic prediction for the two-point correlation function, denoted with ξ_{ZA} ,

$$\xi_{\text{ZA}}(x) + 1 = \int \frac{d^3q}{(2\pi)^{3/2}} (\det A_{ij})^{-1/2} \exp \left\{ -\frac{1}{2} (\mathbf{x} - \mathbf{q})^T \mathbf{A}^{-1} (\mathbf{x} - \mathbf{q}) \right\}, \quad (3.61)$$

where \mathbf{A} is a second-order cumulant with components $A_{ij}(\mathbf{q}) := \langle \Delta_i \Delta_j \rangle_c$ with $\Delta_i(\mathbf{q}) := \psi_i^{\text{ZA}}(\mathbf{q}_1) - \psi_i^{\text{ZA}}(\mathbf{q}_2)$ and $\mathbf{q} := \mathbf{q}_2 - \mathbf{q}_1$. Here, the ZA displacement is $\psi^{\text{ZA}} = D(a) \nabla_{\mathbf{q}} \varphi^{\text{ini}}(\mathbf{q})$, where $D(t)$ is the growing mode solution in a Λ CDM Universe given in eq. (3.39b), and φ^{ini} the initial gravitational potential that is assumed to be Gaussian.

Exercise 3.2 — Derivation of eq.(3.61). From the previous section we have learnt that the Eulerian density can be expressed in terms of the Lagrangian displacement field ψ (cf. eq. 3.52)

$$\delta(\mathbf{x}) + 1 = \int d^3q \delta_D[\mathbf{x} - \mathbf{q} - \psi(\mathbf{q})] = \int d^3q \int \frac{d^3k}{(2\pi)^3} e^{-ik \cdot [\mathbf{x} - \mathbf{q} - \psi(\mathbf{q})]}, \quad (3.62)$$

where in the last step we have employed the Fourier transform of the Dirac delta. Using (3.62) to get an expression for the right-hand side of (3.60), one finds

$$\xi(x) + 1 = \int d^3q_{12} \int \frac{d^3k_{12}}{(2\pi)^6} e^{-ik_1 \cdot (\mathbf{x}_2 - \mathbf{x} - \mathbf{q}_1) - ik_2 \cdot (\mathbf{x}_2 - \mathbf{q}_2)} \left\langle e^{-ik_1 \cdot \psi(\mathbf{q}_1) - ik_2 \cdot \psi(\mathbf{q}_2)} \right\rangle, \quad (3.63)$$

where $\int d^3q_{12} := \int d^3q_1 \int d^3q_2$, we set $\mathbf{x} = \mathbf{x}_2 - \mathbf{x}_1$, and we used that $\langle \delta(\mathbf{x}) \rangle = 0$. By statistical homogeneity, the correlator on the RHS of (3.63) can only depend on the difference $\mathbf{q} := \mathbf{q}_2 - \mathbf{q}_1$; to exploit this we perform a change of variables into the difference \mathbf{q} and center-of-mass coordinates $\mathbf{Q} = (\mathbf{q}_1 + \mathbf{q}_2)/2$. This leads to

$$\xi(x) + 1 = \int d^3q \int d^3Q \int \frac{d^3k_{12}}{(2\pi)^6} e^{iQ \cdot (k_1 + k_2) - ik_1 \cdot (\mathbf{x}_2 - \mathbf{x} + \mathbf{q}/2) - ik_2 \cdot (\mathbf{x}_2 - \mathbf{q}/2)} \left\langle \dots \right\rangle, \quad (3.64)$$

where the ellipsis “ $\langle \dots \rangle$ ” means that the respective correlator on the RHS of (3.63) has not changed. Since that correlator $\langle \dots \rangle$ is independent of Q , the integration $\int d^3Q$ can be performed, yielding a $(2\pi)^3 \delta_D(\mathbf{k}_1 + \mathbf{k}_2)$; that Dirac-delta can be used to trivially evaluate $\int d^3k_2$ (or $\int d^3k_1$). Then one gets

$$\xi(x) + 1 = \int d^3q \int \frac{d^3k}{(2\pi)^3} e^{ik \cdot (x-q)} \left\langle e^{-ik \cdot (\psi(q_1) - \psi(q_2))} \right\rangle. \quad (3.65)$$

So far all manipulations are exact and hold for any (non-linear) displacement. To evaluate the involved expectation value one can employ the [cumulant expansion theorem](#) (eq. 2.121) which states for any random variable X that

$$\left\langle e^{-iX} \right\rangle = \exp \left[\sum_{n=1}^{\infty} \frac{(-i)^n}{n!} \langle X^n \rangle_c \right]. \quad (3.66)$$

Let us briefly discuss the importance of this theorem in the present context of simplifying “ $\langle \dots \rangle$ ” in Eq. (3.65). Suppose that X is a non-Gaussian field (induced by non-linear gravitational evolution), then (3.66) tells us that an infinite hierarchy of n -point cumulants is generated. In the present case, one could truncate this hierarchy by Taylor expanding the exponential with the cumulants to certain orders in perturbation theory, which then leads to standard loop calculations which are discussed in the following section (see also Matsubara 2008). If we however assume that the displacement fields in (3.65) are Gaussian fields that furthermore have vanishing means, then only the second-order cumulant survives in the cumulant expansion. Precisely this is the case if we set $\psi(\mathbf{q}) \simeq \psi^{ZA}(\mathbf{q}) = D(a) \nabla_q \varphi^{ini}(\mathbf{q})$ in eq. (3.65), since we have assumed that φ^{ini} is a Gaussian random field. We then obtain the ZA correlator

$$\xi_{ZA}(x) + 1 = \int d^3q \int \frac{d^3k}{(2\pi)^3} e^{ik \cdot (x-q)} e^{-(1/2) k_i k_j A_{ij}(\mathbf{q})}, \quad (3.67)$$

with

$$A_{ij}(\mathbf{q}) := \left\langle \left[\psi_i^{ZA}(\mathbf{q}_1) - \psi_i^{ZA}(\mathbf{q}_2) \right] \left[\psi_j^{ZA}(\mathbf{q}_1) - \psi_j^{ZA}(\mathbf{q}_2) \right] \right\rangle_c. \quad (3.68)$$

Finally, the integration over d^3k in (3.67) can be evaluated analytically (if A is a symmetric positive-definite matrix that has an inverse), as it is a standard three-dimensional Gaussian integral with linear term, leading to (3.61). ■

It is straightforward to integrate eq. (3.61) numerically (see Carlson et al. 2013 for details), and the result is shown on the left side of fig. 3.6. Recall that the present theoretical model is just based on first-order perturbation theory, but executed in Lagrangian coordinates—and it performs extremely well when compared against non-linear simulations! If instead one would apply the same analysis using Eulerian/standard perturbation theory, the resulting prediction for the correlation function would be extremely poor, which is due to bad convergence behaviour of SPT in *configuration space*.

By contrast, however, if one uses SPT in *Fourier space* as done in the following, the performance of SPT is actually not bad.

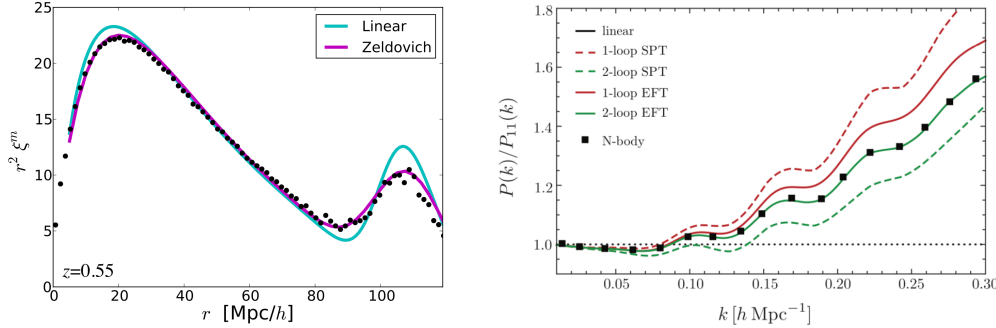


Figure 3.6: **Left:** Real-space two-point correlator as determined by the ZA (pink line, as determined through eq. 3.61), compared against simulation (black dots) and linear standard perturbation theory (cyan solid line); figure credit: Martin White. **Right:** The matter power spectrum as predicted from numerical simulations (black squares), one-loop SPT (red dashed), two-loop SPT (green dashed), as well as their improvements within the effective field theory (EFT; solid lines); figure credit Daniel Baumann.

Eulerian (standard) perturbation theory

Let us return back to a single-fluid description, i.e., as discussed in the beginning of this chapter but now applied to a matter fluid in three space dimensions.

Of course, even in 3D, the considered single-fluid description is just a reduced model of what we believe is required for the theoretical modelling. Nonetheless, this simple model already quite accurately describes the gravitational evolution of cosmic structures. Furthermore, generalisations to multiple, even including finite (baryonic) pressure, exist.

Assuming decaying modes (and thus vorticity) to be negligible we will no consider how to solve the fluid equations perturbatively to higher order. Indeed, the simplest of such techniques aim to represent the growing modes of the unknown fields in terms of a power (Taylor) series expanded around $a = 0$ for an EdS universe (or in Λ CDM: around the growing mode D_+). That is, one imposes the *Ansatz*

$$\delta(\mathbf{x}, a) = \sum_{n=1}^{\infty} \delta_n(\mathbf{x}) a^n, \quad \theta(\mathbf{x}, a) = \sum_{n=1}^{\infty} \theta_n(\mathbf{x}) a^{n-1} \quad (3.69)$$

for solving (3.44), where $\theta(\mathbf{x}, a) := \nabla_{\mathbf{x}} \cdot \mathbf{v}(\mathbf{x}, a)$ is the **velocity divergence**, while δ_n and θ_n are purely spatial functions that need to be determined – order by order (it is actually not as tedious as it may sound), all the way up to infinity (well that would be tedious). Note again that the used boundary conditions assume vanishing initial vorticity such that the fluid velocity can be exactly reconstructed from $\mathbf{v} = \nabla_{\mathbf{x}}^{-2} \nabla_{\mathbf{x}} \theta$, where $\nabla_{\mathbf{x}}^{-2}$ (taking the spatial boundary conditions into account; one typically assumes a torus geometry).

We remark that the *Ansatz* (3.69) assumes that analytic solutions can be written in separable form, i.e., where the temporal and spatial dependences factorise out. This turns out to be a valid assumption, and holds even for a Λ CDM Universe (see Ehlers and Buchert 1997 for the proof). The *Ansatz* becomes however invalid as soon as velocity dispersion is generated post shell-crossing Pietroni (2018); Rampf et al. (2021a), but then the fluid equations need to be revisited too.

Such perturbative techniques applied to a cosmological setup are usually called Eulerian perturbation theory, or [standard perturbation theory \(SPT\)](#). Before solving the underlying fluid equations (3.44) in the present choice of coordinates, it is useful to take the divergence of the Euler equation such that Poisson's equation can be used to get an expression for $\nabla_x^2 \varphi$, as well as to separate all terms with one field from quadratic combinations of fields. One obtains directly

$$\partial_a \begin{pmatrix} \delta \\ \theta \end{pmatrix} + \begin{pmatrix} 0 & 1 \\ 3/(2a^2) & 3/(2a) \end{pmatrix} \begin{pmatrix} \delta \\ \theta \end{pmatrix} = -\nabla_x \left((\mathbf{v} \cdot \nabla_x) \mathbf{v} \right). \quad (3.70)$$

Let us begin solving these equations in an EdS universe using the *Ansatz* (3.69) at the first (i.e., linear) order for which we thus set $\delta(\mathbf{x}, a) = \delta_1(\mathbf{x})a$ and $\theta(\mathbf{x}, a) = \theta_1(\mathbf{x})$. Using the boundary conditions (??), one finds that

$$\delta_1(\mathbf{x}) = \nabla_x^2 \varphi^{\text{ini}}(\mathbf{x}) = -\theta_1(\mathbf{x}), \quad (3.71)$$

where the first equality can also be read off from the Poisson equation (3.44c) with the replacement $\delta \rightarrow \delta_1(\mathbf{x})a$. Thus, with the present choice of boundary conditions, by construction only the initial gravitational potential needs to be specified; see e.g. Michaux et al. (2021) for further details.

To proceed to arbitrarily high orders, we plug the *Ansatz* (3.69) into (3.70); identifying the various powers of a^n , one obtains the following [all-order recursion relations](#) for $n \geq 2$

$$\begin{pmatrix} \delta_n(\mathbf{x}) \\ \theta_n(\mathbf{x}) \end{pmatrix} = \frac{1}{(n+3/2)(1-n)} \begin{pmatrix} n+1/2 & -1 \\ -3/2 & n \end{pmatrix} \sum_{p+q=n} \nabla_x \left(\left(\nabla_x^{-1} \theta_p \cdot \nabla_x \right) \nabla_x^{-1} \theta_q \right), \quad (3.72)$$

where we have defined the operator $\nabla_x^{-1} := \nabla_x^{-2} \nabla_x$ such that $\nabla_x^{-1} \theta = \mathbf{v}$ (this operator exploits the fact that $\nabla_x \times \mathbf{v} = \mathbf{0}$ and thus \mathbf{v} can be written in terms of a scalar potential). Observe that these equations have the expected recursive form, i.e., that the present order of the fluid variables are retrieved from combinations of lower-order but known solutions. Thus, once the boundary conditions are provided, perturbative solutions for the density and velocity can be easily obtained at arbitrary high orders. In practice, one can exploit these analytical results by determining loop corrections to matter poly spectra (power, bispectrum, etc.); see section 3 for details. Alternatively, one can also sample these analytical results on a numerical grid, from which the poly-spectra can be determined as well Taruya et al. (2018, 2022).

Exercise 3.3 — Determine second-order solutions. As a simple example of the above recursive relations, use the recursive relations (3.72) together with the first-order solutions (3.71) to determine

$$\delta_2(\mathbf{x}) = \frac{5}{7} \varphi_{,ll}^{\text{ini}} \varphi_{,mm}^{\text{ini}} + \varphi_{,l}^{\text{ini}} \varphi_{,lm}^{\text{ini}} + \frac{2}{7} \varphi_{,lm}^{\text{ini}} \varphi_{,lm}^{\text{ini}}, \quad (3.73)$$

$$\theta_2(\mathbf{x}) = -\frac{3}{7} \varphi_{,ll}^{\text{ini}} \varphi_{,mm}^{\text{ini}} - \varphi_{,l}^{\text{ini}} \varphi_{,lm}^{\text{ini}} - \frac{4}{7} \varphi_{,lm}^{\text{ini}} \varphi_{,lm}^{\text{ini}}, \quad (3.74)$$

where we apply the Schwarzian notation to denote partial derivatives, i.e., $\varphi_{,l}^{\text{ini}} := \partial_{x_l} \varphi^{\text{ini}}$, and summation over repeated indices is assumed. ■

For practical applications (section 3) it is often convenient to represent the recursive solutions for δ_n and θ_n in Fourier space (Goroff et al., 1986; Bernardeau et al., 2002):

$$\tilde{\delta}_n(\mathbf{k}) = \int \frac{d^3 k_{12\dots n}}{(2\pi)^{3n-3}} \delta_D(\mathbf{k} - \mathbf{k}_{12\dots n}) F_n(\mathbf{k}_1, \mathbf{k}_2, \dots, \mathbf{k}_n) \tilde{\delta}_1(\mathbf{k}_1) \tilde{\delta}_1(\mathbf{k}_2) \cdots \tilde{\delta}_1(\mathbf{k}_n), \quad (3.75a)$$

$$\tilde{\theta}_n(\mathbf{k}) = \int \frac{d^3 k_{12\dots n}}{(2\pi)^{3n-3}} \delta_D(\mathbf{k} - \mathbf{k}_{12\dots n}) G_n(\mathbf{k}_1, \mathbf{k}_2, \dots, \mathbf{k}_n) \tilde{\delta}_1(\mathbf{k}_1) \tilde{\delta}_1(\mathbf{k}_2) \cdots \tilde{\delta}_1(\mathbf{k}_n), \quad (3.75b)$$

where we use the simplified notations $\int d^3 k_{12\dots n} := \int d^3 k_1 \cdots \int d^3 k_n$ and $\mathbf{k}_{12\dots n} := \mathbf{k}_1 + \mathbf{k}_2 + \cdots + \mathbf{k}_n$, while F_n and G_n denote the Fourier space kernel functions. We note that these kernel functions have been symmetrised in their dependences, obtained by a weighted sum over all possible permutations in the variables. For convenience we show here the first few solutions in Fourier space. At $n = 1$ we have $F_1 = 1 = -G_1$, while at second and third order we have for the density kernels

$$F_2(\mathbf{k}_1, \mathbf{k}_2) = \frac{5}{7} + \frac{1}{2} \frac{\mathbf{k}_1 \cdot \mathbf{k}_1}{k_1 k_2} \left(\frac{k_1}{k_2} + \frac{k_2}{k_1} \right) + \frac{2}{7} \frac{(\mathbf{k}_1 \cdot \mathbf{k}_2)^2}{k_1^2 k_2^2}, \quad (3.76)$$

$$F_3(\mathbf{k}_1, \mathbf{k}_2, \mathbf{k}_3) = \left[\frac{7}{54} \frac{\mathbf{k}_{123} \cdot \mathbf{k}_{12}}{k_{12}^2} + \frac{1}{27} k_{123}^2 \frac{\mathbf{k}_{12} \cdot \mathbf{k}_3}{k_{12}^2 k_3^2} \right] G_2(\mathbf{k}_1, \mathbf{k}_2) \\ + \frac{7}{54} \frac{\mathbf{k}_{123} \cdot \mathbf{k}_3}{k_3^2} F_2(\mathbf{k}_1, \mathbf{k}_2) + 2 \text{ cyclic permutations.} \quad (3.77)$$

For explicit solutions up to fourth order in symmetrised form, see Rampf and Wong (2012). This is the [standard perturbation theory \(SPT\)](#), which provides reasonably well approximations to cosmic structure formation at sufficiently early times ($z \gtrsim 5$), as well as at sufficiently large spatial scales ($l \gtrsim 10$ Mpc). Indeed, at later times, the generation of velocity dispersion limits the predictive power of SPT, while SPT has never been designed to model the small-scale physics to begin with, where baryonic effects can become important.

There are several ways to circumvent both of these shortcomings of SPT. One way is considering the [effective field theory of cosmic large-scale structure \(EFTofLSS\)](#) (e.g., Carrasco et al. 2012; Lewandowski et al. 2015), which still requires SPT as theory input but is able to rigorously incorporate the late-time and small-scale physics through various counter terms. This seemingly elegant way however comes at a price, namely that there is currently no method available that can predict those counter terms from theoretical considerations solely; instead it is customary to estimate them from numerical simulations. Therefore, the predictive power of EFTofLSS is somewhat limited. Nonetheless, there are several groups who employ EFTofLSS for extracting cosmological parameters from cosmological observations (e.g. Philcox et al. 2020; Nishimichi et al. 2020).

SPT is also vastly inefficient in resolving convective (advective) fluid motion, since the chosen coordinate system is not optimal. Another shortcoming of SPT is that, so far, we do not know the *precise conditions* for its mathematical convergence.

Matter power spectrum at one loop

Here we will show how Standard Perturbation theory (SPT; section 3) can be used to retrieve non-Gaussian statistical predictions, specifically, to the [matter power](#)

spectrum $P(k, t)$ which is the two-point correlator of the density contrast in Fourier space,

$$\mathbb{E} [\tilde{\delta}(\mathbf{k}_1, t) \tilde{\delta}(\mathbf{k}_2, t)] = (2\pi)^3 \delta_D(\mathbf{k}_{12}) P(\|\mathbf{k}_1\|, t), \quad (3.78)$$

where $\mathbf{k}_{12\dots n} = \mathbf{k}_1 + \mathbf{k}_2 + \dots + \mathbf{k}_n$. While the computations in section 3 are exact only for an EdS universe, the derived results hold also to a good approximation for a Λ CDM Universe, where the Fourier-space density can be represented (until some finite time) as the following power series

$$\tilde{\delta}(\mathbf{k}, t) = \sum_{n=1}^{\infty} \tilde{\delta}_n(\mathbf{k}) D_+^n(t) =: \sum_{n=1}^{\infty} \tilde{\delta}_n(\mathbf{k}, t). \quad (3.79)$$

Here $D_+(t)$ is the linear growth time in Λ CDM defined in eq. (3.39b), and the $\tilde{\delta}_n$'s are determined through the recursive relations (3.75a).

In the below exercise we derive, for Gaussian initial conditions, the matter power spectrum up to one loop accuracy, i.e.,

$$P(k, t) = P_{11}(k, t) + P_{\text{loop}}(k, t), \quad P_{\text{loop}}(k, t) := P_{22}(k, t) + P_{13}(k, t), \quad (3.80)$$

with the perturbative correlators ($1 \leq i, j \leq 3$)

$$\langle \tilde{\delta}_i(\mathbf{k}_1, t) \tilde{\delta}_j(\mathbf{k}_2, t) \rangle := (2\pi)^3 \delta_D(\mathbf{k}_{12}) P_{ij}(k_1, t), \quad (3.81)$$

where specifically P_{11} is the linear matter power spectrum that can be determined from numerical codes such as CLASS³, and

$$P_{22}(k, t) = 2 \int \frac{d^3 p}{(2\pi)^3} [F_2(\mathbf{k} - \mathbf{p}, \mathbf{p})]^2 P_{11}(|\mathbf{k} - \mathbf{p}|, t) P_{11}(p, t), \quad (3.82)$$

$$P_{13}(k, t) = 6 P_{11}(k, t) \int \frac{d^3 p}{(2\pi)^3} F_3(\mathbf{k}, \mathbf{p}, -\mathbf{p}) P_{11}(p, t), \quad (3.83)$$

are the first non-vanishing loop integrals for Gaussian initial conditions.

Exercise 3.4 Derivation of eq. (3.80) To keep the calculations concise, we suppress in the following some obvious (temporal) dependences. We begin by plugging in the power series expansion in the left-hand side of (3.78), which leads to

$$\langle \tilde{\delta}(\mathbf{k}_1) \tilde{\delta}(\mathbf{k}_2) \rangle = \left\langle \left(\sum_{i=1}^{\infty} \tilde{\delta}_i(\mathbf{k}_1) \right) \left(\sum_{j=1}^{\infty} \tilde{\delta}_j(\mathbf{k}_2) \right) \right\rangle. \quad (3.84)$$

Terms in the summations to very large orders i, j are suppressed since D_+ is assumed to be a small expansion parameter; for our purpose we can truncate the right-hand-side to the maximal orders $i, j = 3$. Splitting up the terms in the sum we can generally write

$$\langle \tilde{\delta}(\mathbf{k}_1) \tilde{\delta}(\mathbf{k}_2) \rangle = C_{11} + C_{22} + 2C_{12} + 2C_{13} + \dots, \quad (3.85)$$

where $C_{ij} := \langle \tilde{\delta}_i(\mathbf{k}_1) \tilde{\delta}_j(\mathbf{k}_2) \rangle$, and we note that $C_{ij} = C_{ji}$. Let us show how those four terms in (3.85) are derived; the first one is trivial since, using (3.75a) with $F_1 = 1$ for $n = 1$, one obtains directly $C_{11} = (2\pi)^3 \delta_D(\mathbf{k}_{12}) P_{11}(k_1)$; thus, this term comprises just the input that we retrieve from linear Einstein–Boltzmann

³See <http://class-code.net>.

codes. For the next term we have, using eq. (3.75a) for $n = 2$,

$$C_{22} = \langle \tilde{\delta}_2(\mathbf{k}_1) \tilde{\delta}_2(\mathbf{k}_2) \rangle = \int \frac{d^3 p_{1234}}{(2\pi)^6} \delta_D(\mathbf{p}_{12} - \mathbf{k}_1) \delta_D(\mathbf{p}_{34} - \mathbf{k}_2) \times \quad (3.86)$$

$$\times F_2(1, 2) F_2(3, 4) D_{22}(1, 2, 3, 4),$$

where $D_{22}(1, 2, 3, 4) := \langle \tilde{\delta}_1(\mathbf{p}_1) \tilde{\delta}_1(\mathbf{p}_2) \tilde{\delta}_1(\mathbf{p}_3) \tilde{\delta}_1(\mathbf{p}_4) \rangle$ is a four-point correlator, and we use the short-hand notation $F_2(i, j) := F_2(\mathbf{p}_i, \mathbf{p}_j)$. Since D_{22} is solely built from Gaussian fields, we can apply Wick's theorem to write it in terms of combinations of two-point correlators only, i.e.,

$$D_{22} = D_{11}(12) D_{11}(34) + D_{11}(13) D_{11}(24) + D_{11}(14) D_{11}(23), \quad (3.87)$$

where $D_{11}(ij) := \langle \tilde{\delta}(\mathbf{p}_i) \tilde{\delta}(\mathbf{p}_j) \rangle = (2\pi)^3 \delta_D(\mathbf{p}_{ij}) P_{11}(p_j)$. Now it boils down to evaluate the involved Dirac deltas on the RHS of (3.87): The first term does not contribute to the connected correlator since in that case the other Dirac delta's in (3.86) imply that $\mathbf{k}_1 = \mathbf{0} = \mathbf{k}_2$. By contrast, for the second and third term we get two identical contributions leading to

$$C_{22} = (2\pi)^3 \delta_D(\mathbf{k}_{12}) P_{22}(k_1), \quad (3.88)$$

with $P_{22}(k_1)$ given in (3.82). The derivation of C_{13} is completely analogous, leading to $2C_{13} = (2\pi)^3 \delta_D(\mathbf{k}_{12}) P_{13}(k_1)$. For C_{12} we note that only three-point correlators of the linear density are involved, i.e., $\langle \delta_1 \delta_1 \delta_1 \rangle$; these correlators however vanish since δ_1 is assumed to be Gaussian. Thus, $C_{12} = 0$. ■

It is straightforward to perform the loop integrations in eqs. (3.82)–(3.83) using publicly available libraries;⁴ See the following section for explicit instructions and a Python implementation. In the right panel of Fig. 3.6 we compare the loop results against numerical N-body simulations; there we also show the results from the effective field theory which requires the loop results from SPT as input (e.g., Carrasco et al. 2012; Lewandowski et al. 2015).

Numerical Evaluation of Loop Integrals

Observe that some of the angular integrations in (3.82)–(3.83) can be explicitly performed when changing to spherical coordinates, yielding (Suto and Sasaki, 1991)

$$P_{22}(k, t) = \frac{k^3}{98(2\pi)^2} \int_0^\infty dr P_{11}(kr, t) \times$$

$$\times \int_{-1}^{+1} dx P_{11}(k\sqrt{1+r^2-2rx}, t) \frac{(3r+7x-10rx^2)^2}{(1+r^2-2rx)^2}, \quad (3.89)$$

$$P_{13}(k, t) = \frac{k^3 P_{11}(k, t)}{252(2\pi)^2} \int_0^\infty dr P_{11}(kr, t) \left[\frac{12}{r^2} - 158 + 100r^2 + \right.$$

$$\left. - 42r^4 + \frac{3}{r^3} (r^2-1)^3 (7r^2+2) \ln \left| \frac{1+r}{1-r} \right| \right].$$

⁴See in particular the Cuba library (<http://www.feynarts.de/cuba/>), which provides several numerical integration techniques.

In the following we show how to numerically integrate these expressions.

Program Code 3.2 Loop integrals with cubature. As we have seen above, the loop integrals, already at 1-loop, contain multi-dimensional integrals which can be reduced to at most two integrations, leading to Eqs. (3.89). To numerically integrate such expressions it is recommended to employ dedicated python packages. For this, we use `cubature` which is a deterministic integration routine that is fairly accurate while computationally very fast (provided one exploits the vectorisation feature of sc Python!). To install the `cubature` library, simply run `pip install cubature` in your `PYTHON` environment. The `cubature` package is imported with

```
1 import cubature as cub
```

Another great option is the `CUBA` library along with its wrapper `PyCuba`, which allows you to swap easily between different integration methods; see <http://www.feynarts.de/cuba/>.

and we need to specify next the functions to be integrated. The P_{13} and P_{22} integrals can be computed, given the P_{11} tree level spectrum that we assume is already a predefined `PYTHON` function or lambda expression, using the integrand routines

```
1 # integrand for P_22 loop
2 def integrand_P22( x_array, *args, **kwargs ):
3     r = x_array[:,0]      # integration variables are stored in 'x_array' vector
4     x = x_array[:,1]
5     k = args[0]           # additional parameters are passed in 'args' vector
6     return k**3 / 98 / (2*np.pi)**2 * Ptree(k*r)
7         * Ptree(k*np.sqrt(1+r**2-2*r*x))
8         * (3*r+7*x-10*r*x**2)**2/(1+r**2-2*r*x)**2
9
10 #integrand for P_13 loop
11 def integrand_P13( x_array, *args, **kwargs ):
12     r = x_array[:,0]
13     k = args[0]
14     return Ptree(k) * k**3 / 252 / (2*np.pi)**2 * Ptree(k*r)
15         * (12/r**2-158+100*r**2-42*r**4+3/r**3*(r**2-1)**3*(7*r**2+2)
16         * np.log(np.abs((1+r)/(1-r))))
```

along with a driver main loop that calls the `cubature` integrator, integrating in the present case

$$P_{22}(k) = \int_{r_{\min}}^{r_{\max}} dr \int_{(\cos \theta)_{\min}}^{(\cos \theta)_{\max}} d \cos \theta \text{ integrand_P22}(r, \cos \theta ; k) \quad (3.90)$$

$$P_{13}(k) = \int_{r_{\min}}^{r_{\max}} dr \text{ integrand_P13}(r ; k) \quad (3.91)$$

for discrete values of k in the range $0.005h/\text{Mpc} \leq k \leq 10h/\text{Mpc}$, specifically here for `numpt=200` logarithmically spaced values:

```

1 # number of evaluation points
2 nump = 200
3
4 k = np.geomspace(0.005,10,nump)
5 P11 = Ptree(k)
6 P13 = np.zeros_like(P11)
7 P22 = np.zeros_like(P11)
8
9 # integration boundaries
10 rmin = 1e-4
11 rmax = 100
12 costhetamin = -1.0
13 costhetamax = +1.0
14
15 for ik,ak in enumerate(k):
16     val,err = cub.cubature(integrand_P22, 2, 1, \
17                             [rmin,costhetamin], [rmax,costhetamax], \
18                             args=(ak,), \
19                             relerr=1e-5, maxEval=10000000, vectorized=True)
20     P22[ik] = val
21
22     val,err = cub.cubature(integrand_P13, 1, 1, \
23                             [rmin], [rmax], \
24                             args=(ak,), \
25                             relerr=1e-5, maxEval=10000000, vectorized=True)
26     P13[ik] = val

```

The result of the integration, if for the tree-level power spectrum $P_{\text{tree}}(k)$ a tabulated realistic power spectrum is used is shown in Figure 3.7. It is highly instructive to observe the dependence of the end result on the integration boundaries. Since these are always finite in numerical settings, the independence of the loop-integration result from the specific choice needs to be always ensured. We strongly encourage the reader to modify the boundaries and develop some feeling for just how sensitive these results can be.

Beyond the one-loop matter power spectrum, it is generally impossible to simplify the three-dimensional integrands appearing in loop expansions, as it was done when arriving at (3.89). This however possesses no fundamental limitation especially when using cubature integration routines which are a good choice for integrations in less than about 10 dimensions.

One important step in numerical integrations is to actually identify potential problems for the algorithm in the integrand. For example, the term

$$c(r) := (r^2 - 1)^3 (7r^2 + 2) \ln \left| \frac{1+r}{1-r} \right| \quad (3.92)$$

appearing in Eq. (3.83) has actually a well-defined limit $\lim_{r \rightarrow 1} c(r) = 0$, but the numerical result might be unstable nonetheless due to the $1/(1-r)$ appearing in the log. In even worse, naive integration routines could accidentally evaluate the integrand at exactly $r = 1$ which clearly leads to a quasi blow-up of the numerical result. To circumvent any of such numerical problems, one introduces a tiny numerical cut-off parameter $\epsilon > 0$ and provide a safety routine that sets $c(r)$ to zero (or equal to some low-order Taylor approximation) if $|1-r| < \epsilon$. Of course, the final result must not depend on this artificial cut-off, thus one should let ϵ be allowed to be come arbitrarily small (limited by numerical precision).

For very high-dimensional integrals, one is typically forced to use Monte-Carlo integration routines which are however not very accurate.

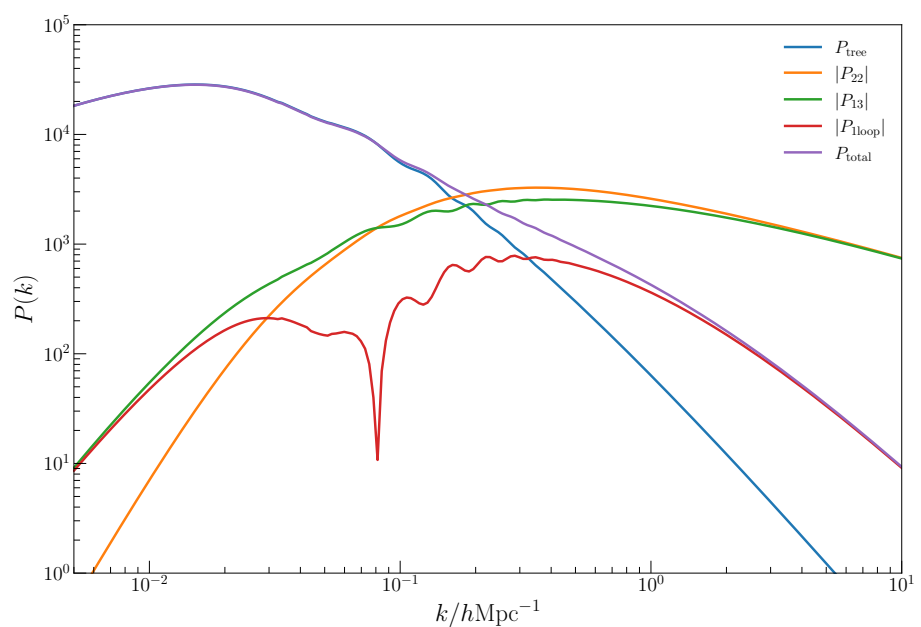


Figure 3.7: The 1-loop power spectrum along with its two contributions from $P_{13}(k)$ and $P_{22}(k)$ as integrated in **PYTHON** using the cubature multi-dimensional integration routines.

Chapter 4

N-body simulations

Discretising the Universe

The (in-)finite numerical Universe

Computers can store only finite amounts of information. When we want to simulate the Universe, we are thus facing the problem that we have to restrict ourselves to a finite d -dimensional spatial domain \mathcal{D} . For consistency with the [cosmological principle](#), we would like the domain to be invariant under spatial translations and rotations. This is impossible to fulfill in a numerical setting unfortunately, so that in practice one of them is violated.

Definition 4.1 — Compact toroidal spatial domain. Translation invariance is fulfilled, if we assume a domain

$$\mathcal{D} = [0, 1)^d \subset \mathbb{R}^d \quad \text{with topology} \quad \mathbb{T}^d = \mathbb{S}^1 \times \cdots \times \mathbb{S}^1, \quad (4.1)$$

i.e. for $d = 3$ with a [3-torus topology](#) (a 3-torus is the Cartesian product of three circles). This yields a d -dimensional compact manifold without boundary. It is however not rotation invariant.

Alternatively, it is possible to map d -dimensional Euclidean space to a d -sphere \mathbb{S}^d and thus compactify it, see e.g. Rácz et al. (2018) and Figure 4.2. This results in a rotationally invariant finite universe, violating however translation invariance, as the origin is special. We will not consider such approaches further here, and instead focus on the flat torus topology.

Exercise 4.1 — Distance of points on the d -torus. Determine the distance r of two points $x \in \mathcal{D}$ and $y \in \mathcal{D}$ by suitably redefining the Cartesian L_2 vector norm on the d -torus \mathbb{T}^d . ■

Definition 4.2 — Periodic boundaries. One can also think of this domain as an infinite repetition of $[0, 1)^d$, as shown in Figure 4.1 for $d = 3$, equivalent to [periodic boundary conditions](#): a point $x \in \mathcal{D}$ is invariant under all translations with nL with $n \in \mathbb{Z}^d$. In particular, a particle i sees another particle j located at x_j along with infinitely many copies at $x_j + n$.

In what follows, We will use fields that are one-parameter families (the time dimension) of functions on \mathcal{D} , i.e. we split the time from the spatial dimension (relativists would say we use a $d + 1$ split and consider a foliation).

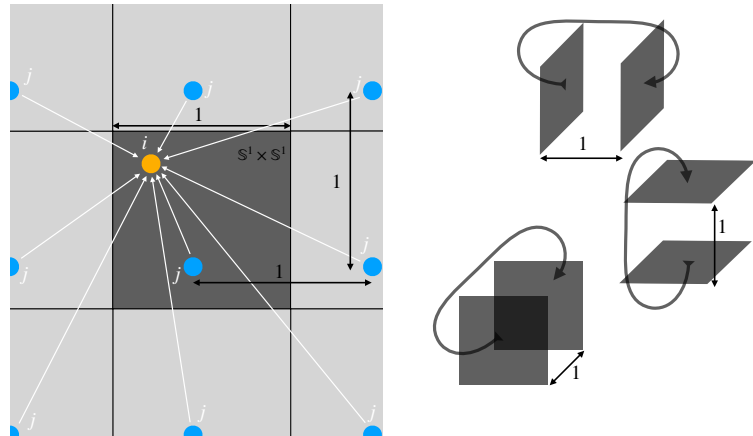


Figure 4.1: The infinite but bounded N -body universe. Standard cosmological N -body simulation evolve the matter distribution in a finite box of co-moving length L . In order to avoid boundary effects, *periodic boundary conditions* are employed, i.e. (Left:) a particle i interacts with infinitely many periodic copies of another particle j . (Right:) The periodic boundary conditions effectively endow the cubic box with a 3-torus topological structure, where a particle that leaves through one face, re-enters through the opposite face of the cube.

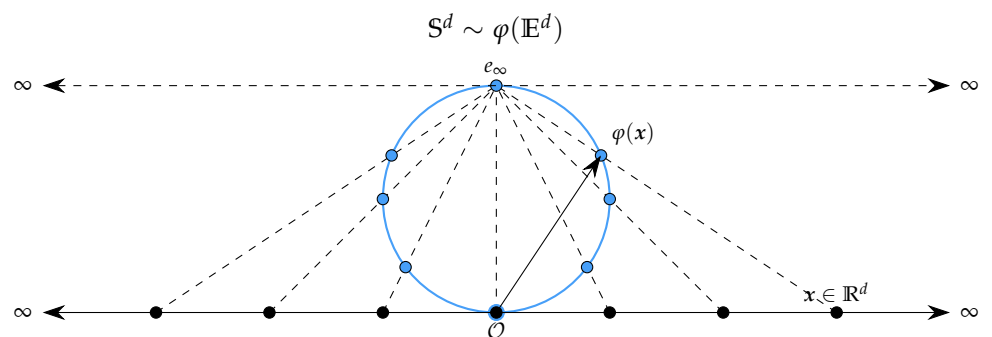


Figure 4.2: One-point compactification of d -dimensional Euclidean space \mathbb{E}^d to the d -sphere S^d by a stereographic projection embedded in \mathbb{R}^{d+1} (extending vertically from the solid line representing \mathbb{E}^d to add the sphere). The compactification requires adding a point at infinity e_∞ which is the limit of all points on \mathbb{R}^d that are infinitely distant from the origin \mathcal{O} .

The N -body universe: discretising mass

The governing equations.

As discussed in some detail in the previous chapter, the evolution of cosmic matter is for our purposes fully described by the Vlasov-Poisson system of partial differential equations for an expanding universe. For reference, we restate it here in co-moving form. Let $f(\mathbf{x}, \mathbf{v}, t) : \mathcal{D} \times \mathbb{R}^d \times \mathbb{R} \rightarrow \mathbb{R}^+$ be the 1-parameter family of the phase-space density of particles, then

$$\frac{\partial f}{\partial t} + \frac{\mathbf{v}}{a^2} \cdot \nabla_{\mathbf{x}} f - \nabla_{\mathbf{x}} \phi \cdot \nabla_{\mathbf{v}} f = 0 \quad (4.2a)$$

$$\nabla^2 \phi = \frac{3\Omega_m}{2a} \left(\frac{n}{\bar{n}} - 1 \right) \quad (4.2b)$$

where $a(t)$ obeys the Friedmann equation, and Ω_m is a constant (the matter density parameter). We also defined

$$n(\mathbf{x}, t) := \int_{\mathbb{R}^d} d^d v f \quad \text{and} \quad \bar{n} := \int_{\mathcal{D}} d^d x n. \quad (4.2c)$$

We specify initial data $f_0(\mathbf{x}, \mathbf{v}) \geq 0$ at $t = t_0$.

Exercise 4.2 Show that $\bar{n} = \int_{\mathbb{R}^d} d^d v \int_{\mathcal{D}} d^d x f = \text{const.}$ under (4.2a). We may therefore assume $\bar{n} = 1$ without loss of generality by redefining $f \rightarrow f/\bar{n}$. ■

The method of characteristics.

We will now introduce a key technique to turn hyperbolic PDEs into ODEs. We shall introduce it for the linear advection equation, before we apply it to the non-linear Vlasov equation.

Application to the linear advection equation Let us introduce the method of characteristics by applying it to the linear [advection equation](#). Let $f(\mathbf{x}, t) : \mathbb{S}^1 \times \mathbb{R} \rightarrow \mathbb{R}_0^+$, then the linear advection equation is given by

$$\frac{\partial f}{\partial t} + v \frac{\partial f}{\partial x} = 0 \quad (4.3)$$

where $v \in \mathbb{R}$ is a constant, and we specify initial data $f_0(\mathbf{x}) := f(\mathbf{x}, t = t_0)$ at t_0 .

Definition 4.3 — Method of characteristics. The solution to this Cauchy problem is easily obtained by the method of characteristics. Let $X(t) : \mathbb{R} \rightarrow \mathbb{S}^1$ be a yet undetermined differentiable function (the [characteristic curve](#)) with $X(t = t_0) =: X_0$. Then

$$\frac{df(X(t), t)}{dt} = \left[\frac{\partial f}{\partial t} + \frac{dX}{dt} \frac{\partial f}{\partial x} \right]_{x=X(t)} = 0 \quad (4.4)$$

i.e. f is constant along the curve $X(t)$ with

$$\frac{dX}{dt} = v, \quad \text{which describes curves with} \quad X(t) = X_0 + (t - t_0)v. \quad (4.5)$$

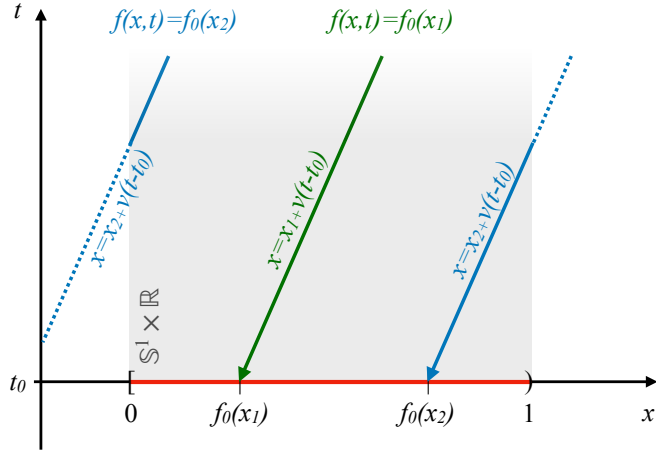


Figure 4.3: Method of characteristics applied to the linear advection equation (4.3) where the characteristics are straight parallel lines. The value of the solution is given by $f(x, t) = f_0(x - v(t - t_0))$, found by tracing the characteristic $X(t) = x - v(t - t_0)$ back to the initial data at t_0 . Due to the periodic boundaries (the S^1 topology), characteristics leaving the domain (gray) on the right re-enter on the left (and vice versa).

The solutions can thus be written as

$$f(x, t) = f_0(x_0(x, t)) \quad \text{where} \quad x_0(x, t) := x - v(t - t_0) \quad (4.6)$$

is the function that traces each point x back to its origin x_0 at t_0 . The linear advection equation thus simply shifts over time the initial data f_0 through space. We say v is its (here constant) characteristic speed.

Definition 4.4 — Galilean transformation. The linear advection equation corresponds to a Galilean transformation from a frame (i.e. a time-dependent labeling of coordinates) x_0 to a frame $x = x_0 + (t - t_0)v$. The two frames x_0 and x move with a (global and constant) relative velocity v .

Application to the Vlasov equation. In contrast to the linear advection equation (4.3), the Vlasov equation (4.2a) is non-linear, and lives on a higher-dimensional domain. Nonetheless, we can apply the same steps. Instead of solving directly for the unknown function $f(\mathbf{x}, \mathbf{v}, t)$ for $t > t_0$, consider two 1-parameter curves (the characteristics)

$$X(t) : \mathbb{R} \rightarrow \mathcal{D} \quad \text{and} \quad V(t) : \mathbb{R} \rightarrow \mathbb{R}^d. \quad (4.7)$$

We want to study the evolution of f along these curves, i.e.

$$f_c : t \mapsto f(X(t), V(t), t) \quad \text{given} \quad X(t = t_0) =: X_0, \quad V(t = t_0) =: V_0 \quad (4.8)$$

Applying the chain rule, we find

$$\frac{df_c}{dt} = \frac{\partial f_c}{\partial t} + \nabla_x f_c|_{x=X(t)} \cdot \frac{dX}{dt} + \nabla_v f_c|_{v=V(t)} \cdot \frac{dV}{dt}. \quad (4.9)$$

Evidently, by comparing the terms with the Vlasov equation (4.2a), we find that

$$\frac{df_c}{dt} = 0 \quad \text{iff} \quad \begin{cases} \dot{\mathbf{X}}(t) &= a^{-2} \mathbf{V}(t) \\ \dot{\mathbf{V}}(t) &= -\nabla_x \phi|_{x=\mathbf{X}(t)} \end{cases} \quad (4.10)$$

i.e. that the phase space density is conserved along the characteristics obeying the ODEs (4.10) with initial data $\mathbf{X}(t_0) = \mathbf{X}_0$ and $\mathbf{V}(t_0) = \mathbf{V}_0$. Since $f_c = \text{const.}$, we can identify it as before with the value in the initial data, i.e. we trace each characteristic to t_0

$$f_c(t) = f(\mathbf{X}(t_0), \mathbf{V}(t_0), t_0) = f(\mathbf{X}_0, \mathbf{V}_0, t_0) \quad \forall t. \quad (4.11)$$

If the field $\phi(x, t)$ were specified, we would have a working numerical method by simply integrating the ODEs (4.10) for any characteristic of our choice. In particular, we can define a large collection of characteristics as the following set.

Definition 4.5 — N -body system. We define the N -body system at time t as the set of N characteristics

$$\mathcal{X}_t := \left\{ (\mathbf{X}_i(t), \mathbf{V}_i(t)) \in \mathcal{D} \times \mathbb{R}^d \mid i = 1, \dots, N \right\}. \quad (4.12)$$

To avoid having to write double indices, let us specify the initial data for the N -body system as

$$\mathcal{X}_0 := \left\{ (\mathbf{Q}_i, \mathbf{W}_i) \in \mathcal{D} \times \mathbb{R}^d \mid i = 1, \dots, N \right\}, \quad (4.13)$$

so that $\mathbf{X}_i(t_0) =: \mathbf{Q}_i$ and $\mathbf{V}_i(t_0) =: \mathbf{W}_i$.

Connection with Lagrangian coordinates approach.

The method of characteristics is in fact identical to the Lagrangian coordinates approach discussed in ?? with the only difference, that there we did not think about a finite discrete number of characteristics but instead considered the general Lagrangian map of the \mathbb{R}^{2d} phase space onto itself, i.e.

$$\mathbb{R}^{2d} \rightarrow \mathbb{R}^{2d} : (\mathbf{q}, \mathbf{w}) \mapsto (\mathbf{x}(\mathbf{q}, \mathbf{w}; t), \mathbf{v}(\mathbf{q}, \mathbf{w}; t)). \quad (4.14)$$

Characteristics (aka ‘particles’) are effectively a discrete subset of Lagrangian coordinates

In fact, there we considered only cold systems, i.e. systems restricted to the Lagrangian submanifold, where $\mathbf{w} = \nabla_{\mathbf{q}} S(\mathbf{q})$ can be expressed through the [Lagrangian coordinate \$\mathbf{q}\$](#) alone, given a differentiable $S(\mathbf{q})$.

In contrast, in the N -body approach, we consider the discrete mapping followed by a set of N characteristics

$$\mathbb{R}^{N2d} \rightarrow \mathbb{R}^{N2d} : (\mathbf{Q}_i, \mathbf{W}_i) \mapsto (\mathbf{X}_i(t), \mathbf{V}_i(t)), \quad i = 1, \dots, N \quad (4.15)$$

as sketched in Figure 4.4. If the initial data is unique, i.e. if $\mathbf{Q}_i \neq \mathbf{Q}_j$ and $\mathbf{W}_i \neq \mathbf{W}_j$ for $i \neq j$, then the index i can be used itself as a Lagrangian coordinate since it uniquely identifies both trajectories and initial data. This is a nontrivial fact and actually requires further that particle trajectories never cross in phase space, i.e. that also for all later times $t > 0$ that $\mathbf{X}_i(t) \neq \mathbf{X}_j(t)$ and $\mathbf{P}_i(t) \neq \mathbf{P}_j(t)$ if $i \neq j$.

Characteristics sample a discrete subset of Lagrangian space – but note that by doing so, its manifold structure is lost

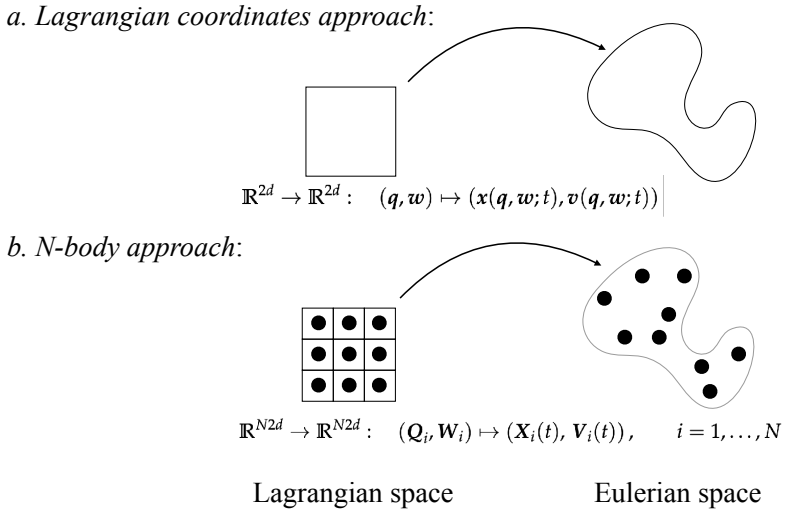


Figure 4.4: The essence of the N -body discretisation: The general Lagrangian map $(q, w) \mapsto (x(q, w; t), v(q, w; t))$ between Lagrangian space and Eulerian space is sampled by discrete characteristics (particles) $i = 1, \dots, N$, here shown for two spatial dimensions (momentum space not shown). Particles are initially located at positions Q_i and have velocities W_i , e.g. approximating an initially isotropic and homogeneous state. They then evolve self-consistently under the N -body Hamiltonian following trajectories $(X_i(t), V_i(t))$ over time.

Connection with Hamiltonian mechanics

The characteristic equations (4.10) have an underlying Hamiltonian structure (which is not surprising, since we already established this for the Lagrangian coordinates approach, cf. (3.5)). For the N -body system, we find equivalence of the equations of motion with the N -particle Hamiltonian of the form

$$\mathcal{H}_N := \sum_{i=1}^N \left[\frac{V_i^2}{2a^2} + \sum_{j \neq i} I(X_i; X_j; a) \right], \quad (4.16)$$

where $I(X_i, X_j; a)$ is a (yet to be specified) interaction term between particle i and j . It is straightforward to verify that

$$\dot{X}_i = \frac{\partial \mathcal{H}_N}{\partial V_i} = \frac{V_i}{q^2} \quad (4.17)$$

$$\dot{V}_i = -\frac{\partial \mathcal{H}_N}{\partial X_i} = -\sum_{j \neq i} \frac{\partial I(X_i, X_j; a)}{\partial X_i} =: A_i. \quad (4.18)$$

so that we can later exploit the rich theory of such Hamiltonian systems when integrating the characteristic curves.

Gravity and the approximative character of N -body systems.

Sourcing gravity with the characteristics. What remains to be solved is the Poisson equation (4.2b), for which we need to first determine its source (4.2c), i.e. the expression

$$n(\mathbf{x}, t) = \int_{\mathbb{R}^d} d^d v f(\mathbf{x}, \mathbf{v}, t). \quad (4.19)$$

All we have to inform us about the distribution of mass are the characteristics. Let us next therefore define the ***N*-body distribution function** as (cf. also Klimontovich, 1967)

$$f_N(\mathbf{x}, \mathbf{v}, t) = \sum_{i=1}^N f_{i,0} \delta_D(\mathbf{x} - \mathbf{X}_i(t)) \delta_D(\mathbf{v} - \mathbf{V}_i(t)), \quad (4.20)$$

where $f_{i,0}$ is the value of the distribution function in the initial data (to which the characteristics trace back), i.e.

$$f_{i,0} := f(\mathbf{Q}_i, \mathbf{W}_i, t_0). \quad (4.21)$$

We assume an initially homogeneous and isotropic Universe, so that we set

$$f_{i,0} = \text{const.} = \frac{1}{N} \quad \text{to also have} \quad \int_{\mathcal{D}} d^d x \int_{\mathbb{R}^d} d^d v f_N(\mathbf{x}, \mathbf{v}, t) = 1. \quad (4.22)$$

Assumption — Convergence of f_N to the true f . Clearly, replacing f with f_N is a crude approximation of the true underlying continuous distribution function and we are free to control the discretisation scale through N , i.e. an N -body particle is *not* a microscopic particle. The hope is that the simulation converges for large N , i.e.

$$f_N \rightarrow f \quad \text{as} \quad N \rightarrow \infty, \quad (4.23)$$

Unfortunately for all realistic cases, we have no rigorous proofs of convergence to the true solutions – only convincing ‘empirical’ evidence.

but this convergence can almost never be proven rigorously and usually reliability of the results in the deeply non-linear regime has to be demonstrated empirically. For formal proofs (and also for numerical convergence) it is better to replace the Dirac- δ ‘particles’ with Gaussian particles (i.e. replace $\delta_D(\mathbf{x} - \mathbf{X}(t))$ with some Kernel $K(\mathbf{x} - \mathbf{X}(t), \sigma)$ of finite extent σ , see section 4).

Replacing $\delta_D(\mathbf{r})$ with $K(\mathbf{r}, \sigma)$ is called ‘**force softening**’.

Remark In the method of characteristics, no approximations have been made: we simply selected a set of phase space points, along which the evolution of the full continuous Vlasov system is followed. The approximative character arises when we introduce the coupling between the Vlasov and the Poisson equation, i.e. when we close the system by approximating its source term

$$n(\mathbf{x}, t) \simeq \hat{n}(\mathbf{x}, t) := \int_{\mathbb{R}^d} d^d v f_N(\mathbf{x}, \mathbf{v}, t) = \frac{1}{N} \sum_{i=1}^N \delta_D(\mathbf{x} - \mathbf{X}_i(t)). \quad (4.24)$$

Discreteness errors:
Errors due to the
particle discretisation
causing
 $|f - f_N|_{\mathbf{x}=\mathbf{X}_i(t)} \neq 0$.

Errors related to this approximation are called **discreteness errors**.

Solving Poisson’s equation. We can now attempt to solve the cosmological Poisson equation for the N -body source

$$\nabla_x^2 \phi = \frac{3\Omega_m}{2a} (n - 1) \quad \text{subject to periodic BCs} \quad (4.25)$$

using the **Green’s function** function approach.

Definition 4.6 — Green’s function. The function $\mathcal{G} : (\mathbf{x}, \mathbf{s}) \in \mathcal{D} \times \mathcal{D} \rightarrow \mathbb{R}$ is called the Green’s function associated with the d -dimensional Laplacian operator ∇_x^2 if it fulfills the equation

$$\nabla_x^2 \mathcal{G}(\mathbf{x}, \mathbf{s}) = \delta_D(\mathbf{x} - \mathbf{s}). \quad (4.26)$$

Using the Green’s function approach,
solving Poisson’s equation becomes
computing the interaction of every
particle with all the other $N - 1$ particles...

It represents the ‘impulse response’ of the operator to a Dirac pulse – i.e. here the gravitational potential produced by a point mass. Note that we define it for $\mathbf{x}, \mathbf{s} \in \mathbb{R}^d$ with no boundary conditions specified.

Having found the Green’s function, solutions to $\nabla_{\mathbf{x}}^2 f = g$ with well-enough behaved g (e.g. compact support) can be written as

$$f(\mathbf{x}) = \int_{\mathcal{D}} d^d s \, g(\mathbf{s}) \mathcal{G}(\mathbf{x}, \mathbf{s}) = g * \mathcal{G}. \quad (4.27)$$

These are convolutions if the Green’s function is [translation invariant](#) i.e. iff $\mathcal{G}(\mathbf{x}, \mathbf{s}) = \mathcal{G}(\mathbf{x} - \mathbf{s})$, then

$$f(\mathbf{x}) = \int_{\mathcal{D}} d^d s \, g(\mathbf{s}) \mathcal{G}(\mathbf{x} - \mathbf{s}) = g * \mathcal{G}. \quad (4.28)$$

If we want to apply periodic boundaries on \mathbb{T}^d , then we can just use the \mathbb{R}^d Green’s functions and replicate the source term accordingly. Then the formal solution of the Poisson equation for the N -body system is given by integrating \mathcal{G} over the replicated source, i.e.

$$\phi(\mathbf{x}) = \frac{3\Omega_m}{2a} \int_{\mathcal{D}} d^d s \, \mathcal{G}(\mathbf{x}, \mathbf{s}) \sum_{\mathbf{m} \in \mathbb{Z}^d} (n(\mathbf{s} - \mathbf{m}) - 1). \quad (4.29)$$

Proposition 4.1 — Green’s functions for the Laplacian on \mathbb{R}^d . Green’s functions of the Laplacian, i.e. solutions of (4.26), on \mathbb{R}^d in one, two, and three dimensions are respectively found to be

$$\mathcal{G}(\mathbf{x}, \mathbf{s}) = \begin{cases} \frac{1}{2}r & \text{if } d = 1 \\ \frac{1}{2\pi} \log r & \text{if } d = 2 \\ -\frac{1}{4\pi r} & \text{if } d = 3 \end{cases} \quad \text{where } r := \|\mathbf{x} - \mathbf{s}\| \quad (4.30)$$

Note that we have not specified boundary conditions for these Green’s functions – in particular we have not specified the periodic boundary conditions^a.

^aTherefore, these Green’s functions’ behaviour on the boundary (at infinity) might not be well defined. In particular, physicists like to assume that $\phi \rightarrow 0$ (or at least a constant) at ‘infinity’. Clearly this does not hold in $d = 1$ or 2 . On the other hand, in cosmology, we are lucky to be able to assume that δ is centered, and therefore $\int_{\mathcal{D}} d^d x \delta = 0$, and therefore the potential cannot diverge. We omit any detailed discussion of such aspects here however, even though they are not at all uninteresting.

Remark We replaced here the periodic boundary conditions on \mathbb{T}^3 by assuming a periodic replication of the source term of Poisson’s equation. This way, we can replace the Green’s function computed on the torus (i.e. with periodic boundary conditions), with the Green’s function on \mathbb{R}^d , but we have to include the extra sum over periodic sources.

Inserting the N -body distribution function (4.20), the formal solution for the gravitational potential at location $\mathbf{x} \in \mathcal{D}$ is then given by the sum over the contribution of all particles in the system along with all periodic replicas of the

finite box, i.e. in three dimensions

$$\phi(\mathbf{x}) = -\frac{3\Omega_m}{8\pi a} \sum_{\mathbf{n} \in \mathbb{Z}^3} \left[\frac{1}{N} \sum_{\substack{j=1 \\ \mathbf{X}_j \neq \mathbf{x}}}^N \frac{1}{\|\mathbf{x} - \mathbf{X}_j(t) - \mathbf{n}\|} + \varphi_{\text{box}}(\mathbf{x} - \mathbf{n}) \right]. \quad (4.31)$$

Note that we have taken the obvious singularity $\mathbf{x} = \mathbf{X}_j$ when evaluating on top of a particle out. Here φ_{box} is the potential due to mean density,

$$\varphi_{\text{box}}(\mathbf{x}) = - \int_{\mathcal{D}} d^d s \mathcal{G}(\mathbf{x}, \mathbf{s}). \quad (4.32)$$

As it stands, we do not know whether this sum converges, and if so, how fast. As it turns out, it is under general assumptions only conditionally convergent, and usually converges extraordinarily slowly even if it does. We will come back to this aspect shortly.

The cosmological N -body problem.

Note that at this stage, we have a closed set of equations which define the cosmological N -body problem

Definition 4.7 — Cosmological N -body problem. Written in cosmic time, the set of equations to solve for cosmological simulations of (collisionless) structure formation is

$$\dot{a} = a H(a) \quad (4.33a)$$

$$\dot{\mathbf{X}}_i = \frac{\mathbf{V}_i}{a^2}, \quad \dot{\mathbf{V}}_i = -\nabla_{\mathbf{x}}\phi|_{\mathbf{x}=\mathbf{X}_i}, \quad (4.33b)$$

$$\nabla_{\mathbf{x}}\phi(\mathbf{x}) = \frac{3\Omega_m}{2a} \left(\frac{1}{N} \sum_{\mathbf{n} \in \mathbb{Z}^d} \sum_{i=1}^N \delta_D(\mathbf{x} - \mathbf{X}_i(t) - \mathbf{n}) \right) * (\nabla_{\mathbf{x}}\mathcal{G}). \quad (4.33c)$$

These are the equations (apart from details) solved by *all* cosmological simulation codes.

All cosmological N -body simulation codes solve this set of equations (possibly using different time coordinates). Physically, it corresponds to the non-relativistic limit of the purely gravitational interaction of N massive bodies in an expanding universe. This is valid whenever the underlying dynamics is governed by Vlasov-Poisson and is therefore applicable whenever collisional and relativistic effects are negligible.

Exercise 4.3 Determine the interaction term $I(\mathbf{X}_i, \mathbf{X}_j; a)$ explicitly that appears in (4.16). ■

Symplectic integration of Hamiltonian systems

We see that the Hamiltonian (4.16) is separable, and therefore can be integrated using standard numerical theory for Hamiltonian systems. A minor complication is that obviously the cosmic time t is an unfortunate choice as it leaves both the kinetic and the potential piece time-dependent. A simple change to so-called **superconformal time** $d\tilde{t} := a^{-2}dt$ resolves this, and we find the superconformal Hamiltonian with a time-independent kinetic part to be

$$\tilde{\mathcal{H}} = \sum_{i=1}^N \frac{\|\mathbf{V}_i\|^2}{2} + a^2 \sum_i \sum_{j \neq i} I(\mathbf{X}_i, \mathbf{X}_j; a) =: T(\{\mathbf{V}\}) + U(\{\mathbf{X}\}, a). \quad (4.34)$$

For Hamiltonians of the form (4.34), standard symplectic techniques can be employed, as they can be written in [extended phase space](#), where the time coordinate appears on equal grounds with the spatial coordinates, as an autonomous separable Hamiltonian system.

How do we integrate Hamiltonian systems, such as those given in eq. (4.34)? Let us first re-write the canonical equations for such a Hamiltonian for N particles in the form

$$\frac{d}{dt}(X_i, V_i) = \begin{bmatrix} 0 & \mathbb{I} \\ -\mathbb{I} & 0 \end{bmatrix} \cdot \begin{pmatrix} \partial \tilde{\mathcal{H}} / \partial X_i \\ \partial \tilde{\mathcal{H}} / \partial V_i \end{pmatrix} \quad i = 1, \dots, 3N. \quad (4.35a)$$

Definition 4.8 — Symplectic integrator. A time-integrator is a map advancing the state vector $\xi := (X, V)$ of any pair of a coordinate X and its canonically conjugate momentum V from time t to time $t + \epsilon$, i.e.

$$F_\epsilon : \xi_t \mapsto \xi_{t+\epsilon}. \quad (4.36)$$

A *symplectic* time-integrator is the sub-class of integrators for which

$$\det \frac{\partial F}{\partial \xi} = 1. \quad (4.37)$$

which guarantees conservation of $dX \wedge dV$.

■ **Example 4.1 — Forward Euler.** Let us first consider the forward Euler method as the simplest integrator imaginable. It can be written as using $A := a \partial V / \partial x|_{x=X_i}$ as

$$F_\epsilon = \begin{pmatrix} X + \epsilon V \\ V - \epsilon A(X) \end{pmatrix} \quad \text{so that} \quad \det \frac{\partial F_\epsilon}{\partial \xi} = 1 + \epsilon^2 \frac{\partial A}{\partial X}$$

which therefore is not symplectic unless U is at most a linear function of the X . ■

Proposition 4.2 — Symplectic Leapfrog integrator. Given a separable Hamiltonian as the one above, i.e. $\tilde{\mathcal{H}} = T(\{V\}) + a(\tilde{t}) U(\{X\})$, a second order accurate symplectic integration scheme that is very commonly used is the [leapfrog integrator](#). It is given in DDK form as

$$X_j(\tilde{t} + \epsilon/2) = X_j(\tilde{t}) + \frac{\epsilon}{2} V_j(\tilde{t}) \quad (4.38a)$$

$$V_j(\tilde{t} + \epsilon) = V_j(\tilde{t}) - \epsilon \frac{\partial U(\tilde{t} + \epsilon/2)}{\partial X_j} \quad (4.38b)$$

$$X_j(\tilde{t} + \epsilon) = X_j(\tilde{t} + \epsilon/2) + \frac{\epsilon}{2} V_j(\tilde{t} + \epsilon). \quad (4.38c)$$

In the alternative KDK form, first the momentum is updated by a half-step. Since this is a symplectic integration scheme, it will conserve the energy associated with the Hamiltonian $\tilde{\mathcal{H}}$. They also have the nice property that they are time-symmetric (i.e. they give back the same result if one integrates one step forward and then one backward in time). It is a consequence of [Noether's theorem](#) that such symmetries always relate to conservation properties.

Proof. In contrast to forward Euler, the DDK leapfrog integrator reads with

$$\hat{X} := X + \epsilon V/2$$

$$F_\epsilon = \begin{pmatrix} X + \epsilon V - \frac{\epsilon^2}{2} A(\hat{X}) \\ V - \epsilon A(\hat{X}) \end{pmatrix} \quad \text{for which} \quad \det \frac{\partial F_\epsilon}{\partial \xi} = 1.$$

■

Time integration for Λ CDM. In addition one has the supplementary equation $da/d\tilde{t} = a^3 H(a)$, which can be integrated inexpensively to arbitrarily high precision in general cases, for EdS one has $\tilde{t} = -2/(H_0 \sqrt{a})$ and in Λ CDM

$$\tilde{t} = -\frac{2}{H_0 \sqrt{\Omega_m a}} {}_2F_1(-1/6, 1/2, 5/6; -f_\Lambda(a)), \quad (4.39)$$

where $f_\Lambda := \Omega_\Lambda / (\Omega_m a^{-3})$, which has to be inverted numerically to yield $a(\tilde{t})$.

Perturbation theory inspired integrators

Definition 4.9 — Zeldovich consistency. A time integrator is Zel'dovich consistent, if it reproduces the Zel'dovich solution (3.56) exactly.

Let us formulate the cosmological N-body problem in growth-factor time D_+ , then with $F := a^2 \dot{D}_+$, the equations of motion are

$$\mathcal{V}_i := \frac{dX_i}{dD_+} = \frac{1}{F} V_i \xrightarrow{\text{EdS}} \frac{dX_i}{da} = \mathcal{V}_i = \frac{V_i}{a^{3/2}}, \quad (4.40a)$$

$$\frac{dV_i}{dD_+} = -\frac{1}{\dot{D}_+} \nabla_x \phi|_{x=X_i} \xrightarrow{\text{EdS}} \frac{dV_i}{da} = -a^{1/2} \nabla_x \phi|_{x=X_i}, \quad (4.40b)$$

or respectively in terms of \mathcal{V}

$$\frac{d\mathcal{V}_i}{dD_+} = -\frac{a^2}{F^2} [\dot{F} \mathcal{V}_i - \nabla_x \phi|_{x=X_i}] \xrightarrow{\text{EdS}} \frac{d\mathcal{V}_i}{da} = -\frac{3}{2a} \mathcal{V}_i - \frac{1}{a} \nabla_x \phi|_{x=X_i} \quad (4.40c)$$

where we used that in EdS $D_+ = a$, $F = a^{3/2}$ and $\dot{F} = \frac{3}{2}$. We can write a more general leapfrog-like integrator of the form

$$X_j(D + \epsilon/2) = X_j(D) + \frac{\epsilon}{2} \mathcal{V}_j(D) \quad (4.41a)$$

$$\mathcal{V}_j(D + \epsilon) = G(\epsilon, D) \mathcal{V}_j(D) - H(\epsilon, D) \frac{\partial U(D + \epsilon/2)}{\partial X_j} \quad (4.41b)$$

$$X_j(D + \epsilon) = X_j(D + \epsilon/2) + \frac{\epsilon}{2} \mathcal{V}_j(D + \epsilon). \quad (4.41c)$$

Proposition 4.3 — Zel'dovich consistent time integrator. The integrator (4.41) is Zel'dovich consistent if the functions G and H are chosen such that

$$\frac{1 - G(\epsilon, D)}{H(\epsilon, D)} = \frac{3\Omega_m}{2} (D + \epsilon/2) \xrightarrow{\text{EdS}} \frac{3}{2} (a + \epsilon/2). \quad (4.42)$$

For the integrator to be symplectic, the function G must be chosen to recover the

'canonical momentum' V_i at the end of the time step, i.e.

$$G(\epsilon, D) = \frac{F(D)}{F(D + \epsilon)} \underset{\text{EdS}}{\asymp} \left(\frac{a}{a + \epsilon} \right)^{3/2}. \quad (4.43)$$

To have an integrator that is both symplectic and Zel'dovich consistent, these two conditions must be satisfied simultaneously, which determines both G and H .

Proof. The proof is straightforward and can be found in List & Hahn (2024). ■

N-body experiments in 1+1 dimensions

The simplest case, in which one can best see the peculiar properties of dark matter, is given by a 1+1 dimensional phase space, meaning we only have a one dimensional configuration space and a one dimensional velocity space. The beauty of it is that we can visualise all of phase space easily, since it is only two-dimensional (for 2+2 it is already 4 dimensional and impossible to plot without making projections).

Solving Poisson's equation in 1D

Another significant simplification in 1+1 dimensions is that we can trivially solve Poisson's equation, since now

$$\frac{\partial^2 \phi}{\partial x^2} = \frac{3\Omega_m}{2a} (n - 1), \quad \text{subject to periodic BCs.} \quad (4.44)$$

The N -body density contains of course the infinite sum over repeated copies. In 1D, it is possible to simplify the sum considerably. Let us consider the formal integral over the coordinate x , we find at the position of particle i

$$\begin{aligned} \left. \frac{\partial \phi}{\partial x} \right|_{x=X_i} &= \frac{3\Omega_m}{2a} \left[C + \int_0^{X_i} dx (n(x) - 1) \right] \\ &= \frac{3\Omega_m}{2a} \left[C + \int_0^{X_i} dx \left(\frac{1}{N} \sum_{j \neq i} \delta_D(x - X_j) - 1 \right) \right] \\ &= \frac{3\Omega_m}{2a} \left[C + \frac{1}{N} \left(\sum_{j \neq i} \Theta(X_i - X_j) - X_i N \right) \right] \end{aligned}$$

In one dimension,
Poisson eq. is just an
ODE.

where C is a yet undetermined integration constant (taking into account the boundary condition) and $\Theta(x)$ is the Heaviside step function. The Heaviside step function simply counts the number of particles j to the left of particle i . If we sort the particles so that $X_j < X_i$ if $j < i$, then the number of particles to the left of particle i is $i - 1$. For sorted particles therefore the acceleration can be written

$$\left. \frac{\partial \phi}{\partial x} \right|_{x=X_i} = \frac{3\Omega_m}{2a} \left(C + \frac{i - 1}{N} - X_i \right) \quad \text{iff } X_j < X_i \text{ for } j < i, \quad (4.45)$$

where C is determined by requiring that the acceleration vanishes when integrated over one interval, $\int_0^1 dx (\partial_x \phi) = 0$, which guarantees momentum conservation and

that $\phi(0) = \phi(L)$. This implies that

$$0 = \sum_{i=1}^N \left[C + \frac{i-1}{N} - X_i \right] = CN + \frac{N(N-1)}{2N} - \bar{X}N \quad \text{with} \quad \bar{X} := \frac{1}{N} \sum_{i=1}^N X_i$$

and thus

$$C = \left(\bar{X} - \frac{N-1}{2N} \right)$$

We therefore find for $i = 1, \dots, N$

$$\frac{\partial \phi}{\partial x} \Big|_{x=X_i} = \frac{3\Omega_m}{2a} \left(\frac{i-1/2}{N} - (X_i - \bar{X}) - \frac{1}{2} \right) \quad \text{iff} \quad X_j < X_i \text{ for } j < i, \quad (4.46)$$

In one dimension,
Poisson can be solved
by sorting particles.

Note that the subtraction of \bar{X} needs to be included explicitly. It evolves due to the periodic boundary conditions, even if the mean momentum vanishes at all times. This can be easily seen since $(X_i \bmod 1)$ changes discontinuously as a particle moves from $1 - \epsilon$ to $1 + \epsilon$.

Time integration, cosmological parameters and units

For the time integration, we shall use the leapfrog integrator in both superconformal time and the Zel'dovich consistent integrator as described above. In order to make our life easier, we shall assume an Einstein-de Sitter cosmology (i.e. $\Omega_m = 1$, $\Omega_\Lambda = \Omega_r = 0$) which is valid during matter domination. The Friedmann equation in superconformal time reads then

$$\frac{da}{d\tilde{t}} = a^{3/2} \quad \Leftrightarrow \quad \frac{da}{d\hat{t}} = a^{3/2} \quad \text{with} \quad d\hat{t} := d\tilde{t}, \quad (4.47)$$

so that we can use the dimensionless superconformal time \hat{t} which obeys $\hat{t} = 2 - 2/\sqrt{a}$ (where we have chosen the integration constant so that $a = 1$ corresponds to $\hat{t} = 0$) or $a = (1 - \hat{t}/2)^{-2}$. Note that $a \rightarrow 0$ corresponds to $\hat{t} \rightarrow -\infty$ and $a \rightarrow \infty$ corresponds to $\hat{t} \rightarrow 1$.

We remark once again that in the case of an Einstein-de Sitter cosmology, the linear growth function is just the scale factor, i.e. $D_+(\hat{t}) = a(\hat{t})$. We have furthermore already non-dimensionalised (since the domain is $[0, 1]^d$). Since time is dimensionless, the only remaining free parameter in the system is the particle number N , which is of course only of numerical and not of physical significance. Therefore, in the EdS case, there are no cosmological physical scales.

Plane Wave Initial Conditions

Let us consider a simple plane wave which shell-crosses at $a = 1$ as initial conditions. Since the Zel'dovich solution is exact in 1D, we can use it to obtain the discrete Lagrangian map for the particles $i = 1, \dots, N$

$$X_i(\hat{t}_0) = Q_i + \frac{a(\hat{t}_0)}{2\pi} \sin(2\pi Q_i) \quad \text{with} \quad Q_i := \frac{i-1}{N}. \quad (4.48)$$

The initial particle velocities must be given in the corresponding canonically conjugate momentum in superconformal time. We have $dX_i/d\hat{t} = V_i$ and therefore with $da/d\hat{t} = a^{3/2}$

$$V_i(\hat{t}_0) = \frac{a(\hat{t}_0)^{3/2}}{2\pi} \sin(2\pi Q_i). \quad (4.49)$$

The non-linear evolution of the trajectories for such single mode initial conditions is shown both in phase space and as a space-time diagram in Figure 4.5.

Program Code 4.1 One-dimensional N -body code.

We now want to implement the one-dimensional gravity solver based on particle sorting in `PYTHON` next. Let us assume we store particle positions in some numpy array `X` and particle coordinates are in ‘box units’, i.e. $0 \leq X < 1$. Let us further assume there exists other particle data, e.g. a vector of momenta `P`, so that we cannot actually scramble the particle coordinates. The numpy routing `argsort` solves this problem – it allows to obtain the indices to an array such that they sort the array according to some criterion. Based on this, the implementation of that calculation of the particle acceleration according to eq. (4.46) is straightforward:

```

1 def calc_acc( X ):
2     acc = np.zeros_like(X)      # init to zero
3     rank = np.arange(len(X))   # create rank indices 0,...,N-1
4     Xs = np.fmod(1.0+X,1.0)   # periodically wrap X to be inside [0,1)
5     Xm = np.mean(Xs)          # determine  $\bar{X}$ 
6     # determine the sorting order:
7     sorted_ind = np.argsort(Xs)
8     # implement eq. (4.46) with 1 added to rank (i=1,...):
9     acc[sorted_ind] = (rank+0.5)/len(X)-(Xs[sorted_ind]-Xm)-0.5
10    return acc

```

At the same time, we wish to use the particle acceleration in a symplectic time-integrator. An implementation of the second-order accurate leapfrog integrator in DKD form is easily written in superconformal time as

```

1 def step( X, V, a, da, aend ):
2     tbegin = 2-2/np.sqrt(a)
3     tend = 2-2/np.sqrt(aend)
4     amid = 1/(1-(tbegin+tend)/4)**2
5     dt = tend-tbegin
6     X = X + 0.5*dt * V
7     V = V - dt * 3.0/2.0 * amid * calc_acc( X )
8     X = X + 0.5*dt * V
9     a = a + da
10    return (X,V,a)

```

What remains to be coded up is a driver routine which sets up the initial conditions and calls the `step` routine until the target time is reached. This can be done along the lines of

```

1 X      = ... # the initial conditions for X
2 V      = ... # the initial conditions for V
3 da     = ... # choose some appropriate time step
4 a      = a0  # set a to a0 where ICs are specified
5 amax   = ... # the end time of the simulation
6 istep  = 0   # step counter
7
8 while a<amax:
9     anext = np.minimum(a+da,amax)
10    (X,V,a) = step( X, V, a, da, anext )
11    istep += 1

```

Where we left out the initial conditions and the choice of appropriate time step

Exercise 4.4 Implement the code above and run it for a single-mode plane wave initial condition. Plot the phase space portrait of the particle distribution at three different times: at $a = 1/10$, at shell-crossing $a = 1$ and at a much later time $a = 10$. ■

Exercise 4.5 Rewrite the code above to use the Zel'dovich consistent integrator. Compare the results of the two integrators by plotting the error as a function of the step size ϵ before shell-crossing w.r.t. the exact Zel'dovich solution. You should find that the leapfrog integrator is second order accurate, while the Zel'dovich consistent integrator is indeed exact to machine precision. ■

Hierarchical structure formation

Even with this simple one-dimensional simulation set-up one can study some dynamical implications of [hierarchical structure formation](#) in collisionless cold dark matter. In Figure 4.6, the evolution of multiple perturbations on different scales – this is not yet a full perturbation spectrum, simply four modes with different amplitudes and phases. The space-time trajectories of selected Lagrangian coordinates have been distinctly coloured. It is clearly evident how small perturbations collapse first and merge into a larger structure subsequently. Due to the collisionless nature, these [substructures](#) retain their identity and can pass through each other, interacting only through long-range interactions. It is further very noticeable that individual clumps, follow a straight line ‘Zel'dovich’ trajectory themselves after they shell-crossed until they fall (merge) into a larger structure.

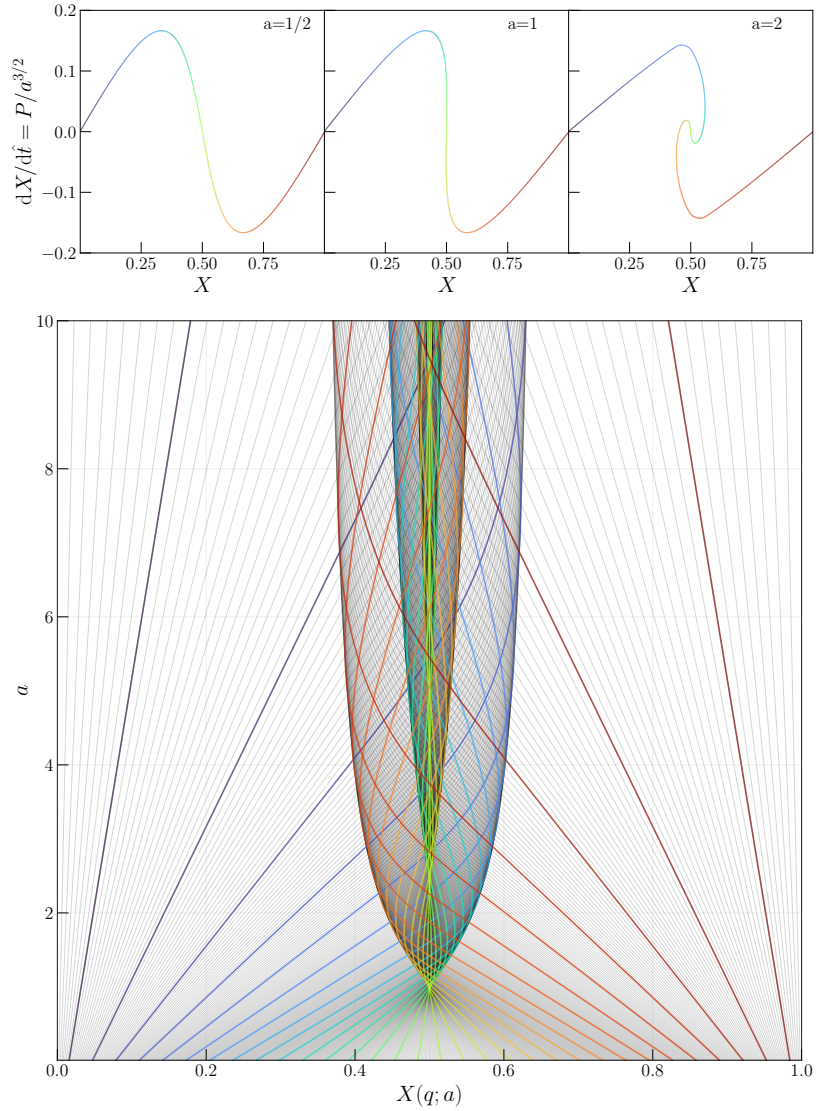


Figure 4.5: (Top:) Phase space diagrams for the single-mode plane wave initial conditions, prior (left, at $a = 1/2$), at (middle, at $a = 1$), and after shell-crossing (right, at $a = 2$). (Bottom:) Trajectories of Lagrangian fluid elements in a single-mode plane wave collapse. Shell-crossing occurs here at $a = 1$, trajectories for selected Lagrangian coordinates q are coloured distinctly thus revealing how caustics are formed as the envelope of turning points of individual trajectories.

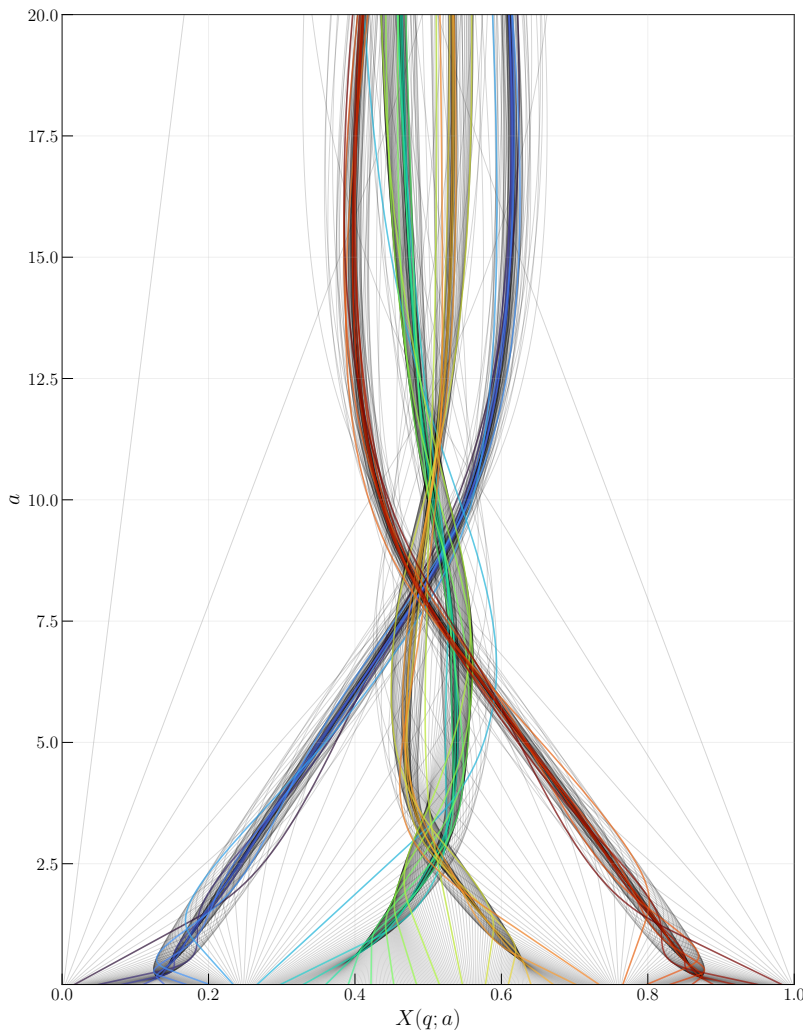


Figure 4.6: Same as Fig. 4.5 but for multiple modes (here four: $\{1, 3, 4, 5\} \times k_0$ with shifted relative phases). In this case one can already see some features of hierarchical structure formation: smaller structures collapse first and merge to form larger structures (a first merger occurs at $a \sim 3$, a second at $a \sim 7$) but retain some of their identity as bound structures even at late times as revealed by the coloured trajectories which encodes the Lagrangian coordinate q . Even in this more complicated scenario, trajectories that have not crossed into a multi-stream region, correspond to straight lines.

Poisson solvers beyond 1D

The simple particle sorting algorithm discussed above unfortunately cannot – at least to our knowledge – be extended to higher dimensions, where the Poisson equation is a proper partial differential equation. For this reason one has to resort to other methods.

Taming the infinite sum: Direct Ewald summation

When trying to solve a related question to eq. (4.33c) in solid-state physics, Paul Peter Ewald developed an extremely efficient mathematical trick in 1921. Let us re-state

$$\phi = -\frac{3\Omega_m}{2a} \sum_{n \in \mathbb{Z}^3} \left(1 - \frac{1}{N} \sum_{i=1}^N \delta_D(\mathbf{x} - \mathbf{X}_i - \mathbf{n}) \right) * \mathcal{G}.$$

This sum converges extremely slowly because the Green's function decays only like $1/r$ (for $d = 3$, even slower for $d = 2$). Ewald's ingenious insight was to split the Green's function into two contributions with a splitting kernel $f(r)$ with $f(r) \rightarrow 1$ for $r \rightarrow 0$ and which decays exponentially for $r \rightarrow \infty$, then

$$\mathcal{G} =: S_\epsilon(r)\mathcal{G} + (1 - S_\epsilon(r))\mathcal{G} =: \mathcal{G}_{sr} + \mathcal{G}_{lr} \quad (4.50)$$

Ewald's original choice was

$$S_\epsilon(r) = \text{erfc}(r/\sqrt{2}\epsilon) \quad \text{where} \quad \text{erfc } r = 1 - \text{erf } r, \quad (4.51)$$

and erf is the error function (i.e. the integral over the normal distribution $\text{erf } r := \frac{2}{\sqrt{\pi}} \int_0^r dx \exp[-x^2]$). The resulting short-range and long-range Green's function and their comparison with the Newtonian Green's function is shown in Figure 4.7. Let us for simplicity consider a single particle. The split of the Green's function also splits the potential into two contributions

$$\phi_{i,sr} := \sum_{n \in \mathbb{Z}^3} \delta_D(\mathbf{x} - \mathbf{X}_i - \mathbf{n}) * \mathcal{G}_{sr} \quad \text{and} \quad \phi_{i,lr} := \sum_{n \in \mathbb{Z}^3} \delta_D(\mathbf{x} - \mathbf{X}_i - \mathbf{n}) * \mathcal{G}_{lr} \quad (4.52)$$

The short-range interaction. For the short-range sum, the Green's function for the potential and the force are then respectively in three dimensions ($d = 3$) given by

$$\mathcal{G}_{sr,3D}(\mathbf{x}) = -\frac{1}{4\pi\|\mathbf{x}\|} \text{erfc} \left[\frac{\|\mathbf{x}\|}{\sqrt{2}\epsilon} \right], \quad (4.53a)$$

$$-\nabla \mathcal{G}_{sr,3D}(\mathbf{x}) = \frac{\mathbf{x}}{\|\mathbf{x}\|^2} \frac{1}{(2\pi)^{3/2}\epsilon} \exp \left[-\frac{\|\mathbf{x}\|^2}{2\epsilon^2} \right] + \frac{\mathbf{x}}{4\pi\|\mathbf{x}\|^3} \text{erfc} \left[\frac{\|\mathbf{x}\|}{\sqrt{2}\epsilon} \right] \quad (4.53b)$$

while in two dimensions ($d = 2$), we have¹

$$\mathcal{G}_{sr,2D}(\mathbf{x}) = -\frac{2 \log \|\mathbf{x}\| - \text{Ei} \left[\frac{\|\mathbf{x}\|}{\sqrt{2}\epsilon} \right]}{4\pi}. \quad (4.53c)$$

$$-\nabla \mathcal{G}_{sr,2D}(\mathbf{x}) = \frac{\mathbf{x}}{2\pi\|\mathbf{x}\|^2} \left(1 - \exp \left[-\frac{\|\mathbf{x}\|^2}{2\epsilon^2} \right] \right) \quad (4.53d)$$

and due to the exponential decay of \mathcal{G}_{sr} , only few, if any, $\|\mathbf{n}\| > 0$ need to be considered since they are strongly suppressed if $\epsilon \ll 1$.

¹where the exponential integral is $\text{Ei}(x) := \int_{-\infty}^x \frac{\exp(t)}{t} dt$.

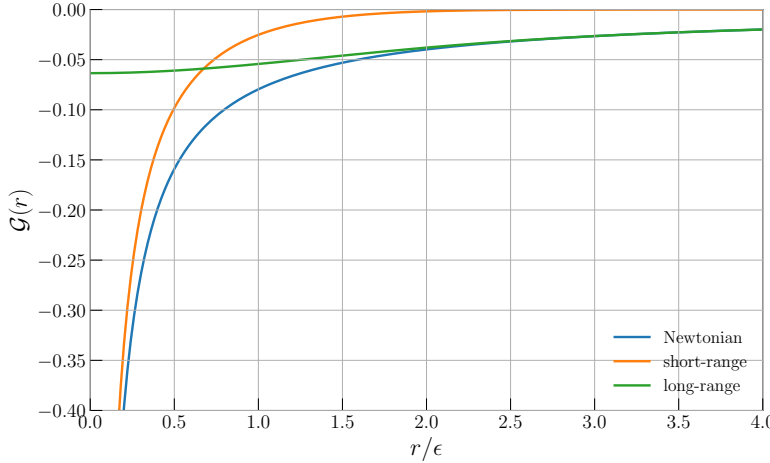


Figure 4.7: In Ewald summation, the interaction kernels are split into a long-range and short-range contribution that together add to the Newtonian Green's function $-1/(4\pi r)$ (in 3D), with $r = \|\mathbf{x}\|$.

The long-range interaction. This is of course not true for the long-range sum. Let us however consider its Fourier transform. The Fourier transform of the long-range Green's function is given by

$$\tilde{\mathcal{G}}_{\text{lr}}(\mathbf{k}) = \begin{cases} 0 & \text{if } k = 0 \\ -\frac{1}{k^2} \exp\left[-\frac{1}{2}k^2\epsilon^2\right] & \text{otherwise.} \end{cases} \quad (4.54\text{a})$$

$$-\widehat{\nabla \mathcal{G}}_{\text{lr}}(\mathbf{k}) = \begin{cases} 0 & \text{if } k = 0 \\ \frac{i\mathbf{k}}{k^2} \exp\left[-\frac{1}{2}k^2\epsilon^2\right] & \text{otherwise.} \end{cases} \quad (4.54\text{b})$$

At the same time, the Fourier transform of the Dirac comb is

$$\begin{aligned} \tilde{\rho}_i(\mathbf{k}) &= \int d^d x \exp(i\mathbf{k} \cdot \mathbf{x}) \sum_{\mathbf{n} \in \mathbb{Z}^d} \delta_D(\mathbf{x} - \mathbf{X}_i - \mathbf{n}) \\ &= \sum_{\mathbf{n} \in \mathbb{Z}^d} \exp[i\mathbf{k} \cdot (\mathbf{X}_i + \mathbf{n})] = \exp[i\mathbf{k} \cdot \mathbf{X}_i] \sum_{\mathbf{n} \in \mathbb{Z}^d} \exp[i\mathbf{k} \cdot \mathbf{n}] \\ &= \exp[i\mathbf{k} \cdot \mathbf{X}_i] (2\pi)^d \sum_{\mathbf{n} \in \mathbb{Z}^d} \delta_D(\mathbf{k} - 2\pi\mathbf{n}) \end{aligned} \quad (4.55)$$

where we have applied the [Poisson summation formula](#)

$$\sum_{\mathbf{n} \in \mathbb{Z}^d} f(\mathbf{n}) = \sum_{\mathbf{k} \in \mathbb{Z}^d} \tilde{f}(\mathbf{k}) \quad (4.56)$$

in the last equality. This is of course the well-known result that the Fourier transform of a Dirac comb is a Dirac comb. If we now transform back to real space, we find for the potential

$$\begin{aligned} \phi_{i,\text{lr}}(\mathbf{x}) &= \frac{1}{(2\pi)^d} \int d^d k \exp(-i\mathbf{k} \cdot \mathbf{x}) \overbrace{\tilde{\rho}_i(\mathbf{k}) \mathcal{G}_{\text{lr}}(\mathbf{k})}^{\tilde{\phi}_{i,\text{lr}}(\mathbf{k})} \\ &= \frac{1}{(2\pi)^d} \int d^d k \exp(-i\mathbf{k} \cdot \mathbf{x}) \exp[i\mathbf{k} \cdot \mathbf{X}_i] (2\pi)^d \sum_{\mathbf{n} \in \mathbb{Z}^d} \delta_D(\mathbf{k} - 2\pi\mathbf{n}) \mathcal{G}_{\text{lr}}(\mathbf{k}) \\ &= \sum_{\mathbf{n} \in \mathbb{Z}^d} \exp[-i2\pi\mathbf{n} \cdot (\mathbf{x} - \mathbf{X}_i)] \tilde{\mathcal{G}}_{\text{lr}}(2\pi\mathbf{n}) \end{aligned} \quad (4.57)$$

This sum can be evaluated by direct summation and is well-behaved – the contributions decay as $\exp(-\|\mathbf{n}\|^2)/\|\mathbf{n}\|$ – and given a maximum error bound can be truncated at some finite $\|\mathbf{n}\| < n_{\max}$. This method is in principle practical, the infinite sum has been tamed. However, its computational complexity is quadratic in the number of particles, i.e. $\mathcal{O}(N^2)$. This is worse than our sorting approach in 1D, which had a complexity of $\mathcal{O}(N \log N)$ if an optimal sorting algorithm is used.

If the masses were given themselves on a Dirac comb (aka grid) and we were to evaluate the sum at those positions, then this expression is just the inverse discrete Fourier transform (iDFT) of $\tilde{\mathcal{G}}_{lr}(\mathbf{k})$.

Particle mesh methods

An extremely powerful approach, and one of the first ones used for cosmological N -body simulations is the [particle-mesh \(PM\) method](#), which in the context of plasma simulations is also known as the [particle-in-cell \(PIC\) method](#). It consists of three steps: (1) a projection step, where the particles are projected onto a ‘mesh’, (2) the solving of Poisson’s equation on the mesh, and (3) the interpolation step, where the acceleration, which is now known on the mesh, is interpolated back to the particle.

Fourier Poisson solvers

If the mass distribution $\delta := n - 1$ is known on a regular periodic grid, then it can be represented in terms of a discrete Fourier transform. Consider all fields represented on a regular grid of linear dimension n_g , with $\Delta := 1/n_g$ the linear grid spacing. Then with $\mathcal{Z}_g^d := [-n_g/2, n_g/2]^d \subset \mathbb{Z}^d$ we can represent the field in terms of its discrete Fourier decomposition, cf. (2.62),

$$\delta[\mathbf{m}] = \frac{1}{n_g^d} \sum_{\mathbf{n} \in \mathcal{Z}_g^d} \tilde{\delta}[\mathbf{n}] \exp \left[-i \frac{2\pi}{n_g} \mathbf{n} \cdot \mathbf{m} \right] \quad \forall \mathbf{m} \in \mathcal{Z}_g^d. \quad (4.58)$$

Such discrete Fourier transforms can be very efficiently computed using the [Fast Fourier Transform \(FFT\)](#) which exploits symmetries of the Fourier transform to execute a transform in d -dimensions with a complexity of $\mathcal{O}(n_g^d \log n_g)$. Since forward and backward transforms have to be made at every time step, it is critical to have the most efficient algorithm possible. A further important optimisation is the use of real-valued transforms (see box below).

The Poisson equation can consequentially be written in discrete Fourier space as

$$-(2\pi)^2 \|\mathbf{n}\|^2 \tilde{\varphi}[\mathbf{n}] = \frac{3\Omega_m}{2a} \tilde{\delta}[\mathbf{n}] \quad \forall \mathbf{n} \in \mathcal{Z}_g^d. \quad (4.59)$$

This equation takes the periodicity directly into account by summing contributions in Fourier space. It is an algebraic equation for which we can straightforwardly write down the solution as

$$\tilde{\varphi}[\mathbf{n}] = \begin{cases} C & \text{if } \|\mathbf{n}\| = 0 \\ -\frac{3\Omega_m}{2a} \frac{\tilde{\delta}[\mathbf{n}]}{(2\pi)^2 \|\mathbf{n}\|^2} & \text{otherwise} \end{cases} \quad (4.60)$$

where C is an arbitrary integration constant, that can be set to zero without loss of generality, which enforces that φ has a vanishing spatial mean. This is only correct

because δ also has vanishing spatial mean. In order to compute accelerations, the gradient of the potential must be computed, it is obtained as $A = -\nabla_x \varphi$, and therefore

$$\tilde{A}[\mathbf{n}] = -i2\pi\mathbf{n} \cdot \tilde{\varphi}[\mathbf{n}] \quad \forall \mathbf{n} \in \mathcal{Z}_g^d. \quad (4.61)$$

In order to exploit this approach for an N -body code, we are still however missing two ingredients:

1. a method to project the particle distribution onto the grid in order to obtain δ_n , and
2. a method to interpolate the accelerations a_n to the particle positions.

Real FFTs – memory economic transforms

We had already encountered the discrete Fourier transform when we discussed how to make realisations of Gaussian random fields with a prescribed power spectrum as described in the box on page 54. Since we are exclusively dealing with real fields, in fact half of the Fourier transformed coefficients is redundant. The reason is that for real fields $f \in \mathbb{R}$, the Fourier coefficients obey the following two relations:

$$\tilde{f}[j] = \tilde{f}^*[-j] \quad \tilde{f}[-j] = \tilde{f}[n_g - j] \quad \forall n \in [-n_g/2, n_g/2) \quad (4.62)$$

– the first is the Hermiticity property. This implies that the negative coefficients do not need to be stored for a one-dimensional real transform. Instead of n_g complex coefficients $\tilde{f}_k \in \mathbb{C}$, $-\frac{n_g}{2} \leq k \leq \frac{n_g}{2} - 1$ only the $n_g/2 + 1$ coefficients $0 \leq k \leq \frac{n_g}{2}$ need to be stored. This effectively reduces the memory requirements by a factor of two and allows optimisations that speed up the calculation. Note further that the Nyquist mode $j = -n_g/2$ has the property

$$\tilde{f}[-n_g/2] = \tilde{f}^*[n_g/2] \Rightarrow \tilde{f}[\pm n_g/2] \in \mathbb{R}. \quad (4.63)$$

This optimization is implemented when instead of `numpy.fft.fft` and `numpy.fft.ifft` the *real* routines `numpy.fft.rfft` and `numpy.fft.irfft` are used. The associated memory layout is shown in panel a) of Figure 4.8.

Naturally such an optimisation is also possible in higher dimensions. E.g. in two dimensions, the space of negative modes in the y -direction can be dropped. I.e. for a two-dimensional sampled field the Fourier coefficients are

$$\tilde{f}[k, l] = \sum_{i \in \mathcal{Z}_g} \sum_{j \in \mathcal{Z}_g} f[i, j] \exp [i2\pi(ik + kl)/n_g] \quad (4.64)$$

and they obey the symmetry

$$\tilde{f}[-k, -l] = \sum_{i \in \mathcal{Z}_g} \sum_{j \in \mathcal{Z}_g} f[i, j] \exp [-i2\pi(ik + kl)/n_g] = \tilde{f}^*[k, l] \quad \text{if } f[i, j] \in \mathbb{R}. \quad (4.65)$$

It therefore suffices to store e.g. only the coefficients $[-\frac{n_g}{2}, \frac{n_g}{2} - 1] \times [0, \frac{n_g}{2}] \subset \mathcal{Z}_g^2$. Since the DFT coefficients are periodic, their representation can of course be periodically shifted. In the FFT algorithm, the $\tilde{f}[0, 0]$ coefficient is always stored at

a) one-dimensional *real* DFT

f_0	f_1	f_2	f_3	f_4	f_5	\dots	f_{N-2}	f_{N-1}
-------	-------	-------	-------	-------	-------	---------	-----------	-----------

sampled field, length N

$$f_j = f(j h)$$

only positive half-space needs to be stored since $\tilde{f}_{-k} = \overline{\tilde{f}_k}$

$\Re \tilde{f}_0$	$\Im \tilde{f}_0$	$\Re \tilde{f}_1$	$\Im \tilde{f}_1$	$\Re \tilde{f}_2$	$\Im \tilde{f}_2$	\dots	$\Re \tilde{f}_{\frac{N}{2}-1}$	$\Im \tilde{f}_{\frac{N}{2}-1}$	$\Re \tilde{f}_{\frac{N}{2}}$	$\Im \tilde{f}_{\frac{N}{2}}$
-------------------	-------------------	-------------------	-------------------	-------------------	-------------------	---------	---------------------------------	---------------------------------	-------------------------------	-------------------------------

DC mode

Nyquist mode

DFT coefficients

$$\tilde{f}_k = \sum_{j=0}^{N-1} f_j \exp(i2\pi j k / N)$$

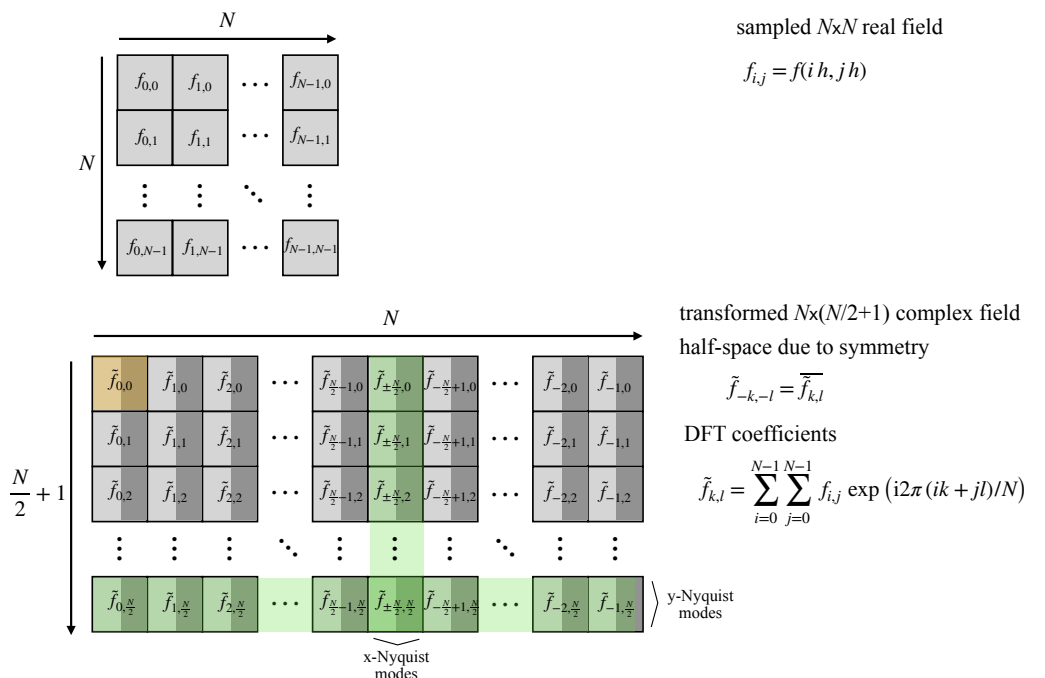
a) two-dimensional *real* DFT

Figure 4.8: The memory layout of one- and two-dimensional (panel a, and b, respectively) FFTs of real-valued functions as used by most FFT routines but especially also the `numpy.fft.rfft` routine for real one-dimensional (panel a) and the `numpy.fft.rfft2` routine for real two-dimensional data (panel b). The situation for higher dimensions is analogous, where the last dimension is always the one for which only the half-space is stored. Note that in the figure $N \equiv n_g$

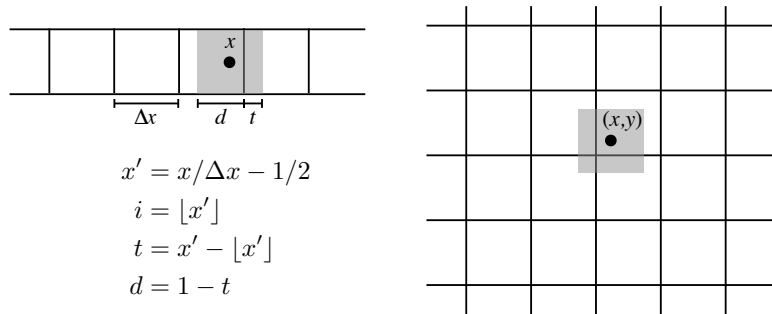


Figure 4.9: The Cloud-in-Cell (CIC) mass assignment scheme in one (left panel) and two (right panel) dimensions. For a particle at location x , one determines the left grid cell i as well as the overlap of the particle assuming a size $\Delta x = 1/n_g$ with cell i and the neighbour $i + 1$. In more than one dimension, one has to repeat this procedure for each dimension ending up with 2^d intersections.

the first memory location. This leads to a memory layout for the two-dimensional real FFT as shown in panel b) of Figure 4.8. This is the coefficient layout that the Python routines `numpy.fft.rfft2` and `numpy.fft.irfft2` operate on. In three (and higher) dimensions, one proceeds analogously, storing only the coefficients $[-\frac{n_g}{2}, \frac{n_g}{2} - 1]^{d-1} \times [0, \frac{n_g}{2}] \subset \mathcal{Z}_g^d$, as implemented by `numpy.fft.rfftn` and `numpy.fft.irfftn`.

Particle interpolation schemes

The simplest method to assign particle positions to grid cells is to associate a particle with the nearest cell centre. This method is called **Nearest-Grid-Point (NGP)**. It would be implemented as follows. For a grid spacing $\Delta x = 1/n_g$, if n_g the number of grid cells per dimension, then assign the mass of a particle with coordinates (x, y, z) entirely to the cell

$$(i, j, k) = \lfloor x/\Delta x, y/\Delta x, z/\Delta x \rfloor, \quad (4.66)$$

where $\lfloor \cdot \rfloor$ represents flooring to the nearest integer. Repeating this assignment for all particles yields an estimate of the density field.

Remark — Consistency of interpolation scheme. In order for a mass assignment scheme to be consistent, one has to use the same scheme for mass assignment and back-interpolation of the acceleration \mathbf{a} , i.e. once we have \mathbf{a} , we simply look up the value from cell (i, j, k) for the particle at (x, y, z) according to eq. 4.66. We say that the back-interpolation has to be adjoint to the mass assignment.

Note that the force changes discontinuously for NGP assignment as a particle moves through the grid.

At the next higher order, one can use multi-linear interpolation, which is called **Cloud-in-Cell (CIC)** interpolation in the context of mass/charge interpolation methods. Instead of assigning all mass to a single cell, one calculates the overlap of a particle of hypothetical size h in each dimension with the 2^n cells it can intersect in n dimensions. The procedure is illustrated in Figure 4.9. The left intersection with cell i shall be called d , the one with the right neighbour $i + 1$ shall be called t . Let $m_N = 1/N$ be the mass carried by one particle. A fraction of the mass $m_N d$ is

assigned to cell i , and the remainder $m_N(1 - d)$ to cell $i + 1$. In three dimensions, the respective assignments become e.g.

$$\begin{aligned} (i, j, k) &\leftarrow m_N d_x d_y d_z \\ (i+1, j, k) &\leftarrow m_N (1 - d_x) d_y d_z \\ (i, j+1, k) &\leftarrow m_N d_x (1 - d_y) d_z \\ &\dots \\ (i+1, j+1, k+1) &\leftarrow m_N (1 - d_x)(1 - d_y)(1 - d_z) \end{aligned} \quad (4.67)$$

where the factor for the left cell is always the d and the one for the right the $1 - d$, in total contributing to eight cells. In the reverse interpolation, the values of the force in the eight cells are summed with weights given by the products of $(1 - d)$'s and d 's on the right hand side. For the CIC assignment, the force changes linearly as the particle moves through the grid. For periodic boundary conditions one has to change of course $i + 1$ to $(i + 1) \bmod n_g$.

In principle one can go to arbitrarily higher order interpolation. The next higher order is called Triangular-shaped-clouds (TSC) and it corresponds to quadratic multi-dimensional interpolation. It is rare that schemes with higher order than TSC are used in computational cosmology. The reason is that while higher order implies a smoother interpolation, it also increases the grid footprint, i.e. the number of grid cells that need to be accessed for a particle deposit or interpolation at any given order.

These three most important assignment functions can also be explicitly written out in kernel form as (following the book by Hockney & Eastwood 1981)

$$W_{\text{NGP}}(x | h) = \frac{1}{\Delta x} \times \begin{cases} 1 & |x| \leq \frac{\Delta x}{2} \\ 0 & \text{otherwise} \end{cases} \quad (4.68a)$$

$$W_{\text{CIC}}(x | h) = \frac{1}{\Delta x} \times \begin{cases} 1 - \frac{|x|}{h} & |x| < \Delta x \\ 0 & \text{otherwise} \end{cases} \quad (4.68b)$$

$$W_{\text{TSC}}(x | h) = \frac{1}{\Delta x} \times \begin{cases} \frac{3}{4} - \left(\frac{x}{h}\right)^2 & |x| \leq \frac{\Delta x}{2} \\ \frac{1}{2} \left(\frac{3}{2} - \frac{|x|}{h}\right)^2 & \frac{\Delta x}{2} < |x| \leq \frac{3\Delta x}{2} \\ 0 & \text{otherwise} \end{cases} \quad (4.68c)$$

The shapes of these functions are depicted in Figure 4.10. Higher-dimensional assignment functions can be composed by tensor product, e.g. $W(\mathbf{x}) = W(x_1) W(x_2) W(x_3)$.

These mass assignment schemes also have a softening effect on the mass distribution and facilitate to reach the *collisionless limit* when the ratio of particles/cell is sufficiently high. For the “naked” particle distribution that we had above in (4.24)

$$\hat{n}(\mathbf{x}) := \frac{1}{N} \sum_{i=1}^N \delta_D(\mathbf{x} - \mathbf{X}_i), \quad (4.69)$$

the density distribution after assigning the mass to the grid using an assignment function $W(\mathbf{x} | h)$ is given at grid point locations \mathbf{x}_g by the convolution

$$\rho[\mathbf{m}] = \frac{1}{N} \int d^d x' \hat{n}(\mathbf{x}') W(\mathbf{m} - \mathbf{x}' / h | h) = \frac{1}{N} \sum_{i=1}^N W(\mathbf{m} - \mathbf{X}_i / h | h) \quad (4.70)$$

where $h = 1/n_g$.

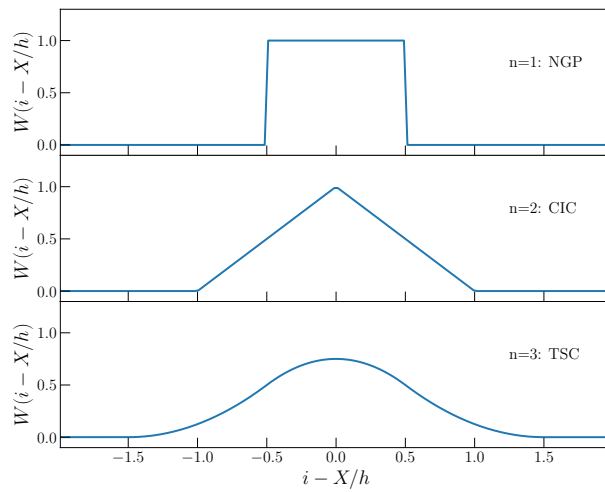


Figure 4.10: Shape of the particle projection/interpolation kernels from the lowest $n = 1$ order NGP (nearest grid point) method, over the $n = 2$ CIC (cloud-in-cell) method to the $n = 3$ TSC (triangular-shaped-cloud) method. For CIC the field value interpolated to a particle is continuous, for TSC it is once differentiable with respect to the motion across the grid.

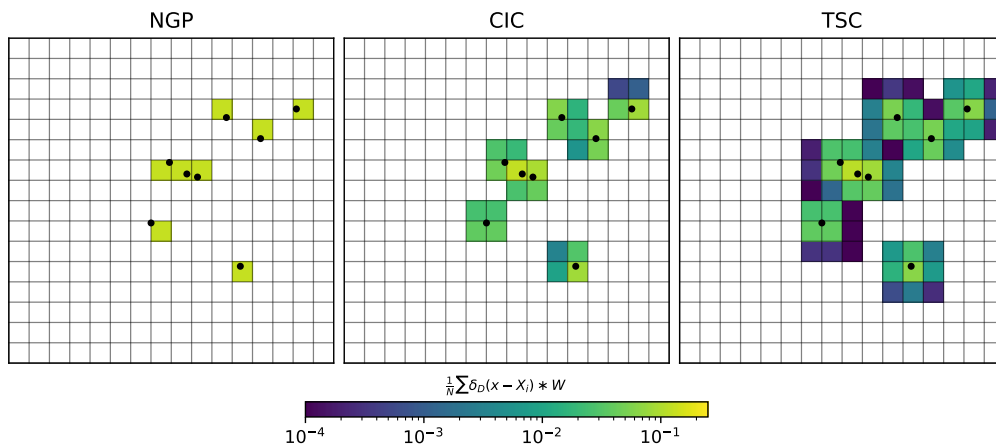


Figure 4.11: Effect of the interpolation kernels (4.68) on the resulting discretised density field $n[i, j]$: with increasing order, a particle contributes to more and more cells, and the resulting field becomes smoother. The images are for $N = 8$ particles and a 16×16 grid ($n_g = 16$).

The assignment kernel for the various schemes can be shown to be in Fourier space given by the simple formula

$$\tilde{W}[k] = n_g^{-3} \operatorname{sinc}^n(k/2\pi), \quad (4.71)$$

with $n = 1$ for NGP, $n = 2$ for CIC and $n = 3$ for TSC. Note that by the central limit theorem, the limit of $n \rightarrow \infty$ leads to a Gaussian. The resulting fields for increasing order of the scheme is shown for a random collection of particles in Figure 4.11.

Since the back interpolation of forces to particles utilizes the same scheme for consistency, the effective smoothing is \hat{W}^2 so that the higher order assignment schemes are increasingly smoother and thus effectively low-pass filtered. More details about mass assignment schemes can be found in the classic book by Hockney and Eastwood (1981).

The back-interpolation can be written, e.g. for the acceleration as

$$A_i = \sum_{n \in \mathbb{Z}^3} A_{PM,n} W(n - X_i / \Delta x), \quad (4.72)$$

Of course this sum can be dramatically simplified by evaluating only those n for which the contribution is non-zero, i.e. within the support of W centered on X_i . Again, in order to avoid self-forces, the same order n needs to be used for projection and interpolation.

Program Code 4.2 A 1D particle-mesh solver In order to speed up the execution of critical `PYTHON` code, we will employ [just in time \(JIT\) compilation](#) from the `NUMBA` package. If you haven't installed it yet, you can e.g. get a version via
`$ pip install numba`

By decorating functions with the `jit` decorator, one enables that this function is, behind the scenes, translated into optimized C code. This is advisable whenever expensive functions are used that cannot exploit the `numpy` vectorisation features, i.e. have to use loops rather than operate on full `numpy` arrays. Exploiting JIT, a one-dimensional particle projection using CIC interpolation can then be written as

```

1  from numba import jit
2
3  @jit(nopython=True)
4  def cic_deposit( X, ngrid ):
5      rho = np.zeros(ngrid)
6      for x in X:
7          x = np.fmod(1.0+x,1.0)
8          i = int(np.floor(x*ngrid))
9          d = 1 - (x*ngrid-float(i))
10         rho[i] += d
11         rho[(i+1)%ngrid] += 1-d
12
13  return rho/len(X)-1.0

```

The inverse operation, interpolating a field F to the particle positions X is written as

```

1  @jit(nopython=True)
2  def inverse_cic( X, F, ngrid ):
3      res = np.zeros_like(X)
4      for ip,x in enumerate(X):
5          x = np.fmod(1.0+x,1.0)
6          i = int(np.floor(x*ngrid))
7          d = 1.0 - (x*ngrid-float(i))
8          res[ip] = F[i] * d + F[(i+1)%ngrid] * (1-d)
9  return res

```

To complete the algorithm, we need to solve Poisson's equation and compute the acceleration. To this end, three steps are made

deposit particles, using e.g. CIC

2. compute the acceleration field using FFT based on eq. (4.61)
3. interpolate acceleration from field to particle positions, e.g. using inverse CIC.

These three steps then become in **PYTHON** the following piece of code:

```

1  def calc_acc_PM( X, ngrid ):
2      rho = cic_deposit( X, ngrid ) # deposit particles to grid
3      k = np.arange(ngrid//2+1) * 2*np.pi # get fourier modes for grid points
4      k[0] = 1.0 # to avoid division by zero
5      facc = -1j*np.fft.rfft(rho)/k # solve Poisson and take gradient
6      facc[0] = 0.0 # set to DC mode to zero
7      acc = np.fft.irfft(facc) # transform back
8      A = inverse_cic( X, acc, ngrid ) # interpolate back to particles
9  return A

```

The result of a one-dimensional single mode collapse is shown in Figure 4.12. A comparison with a simulation based on the exact N -body force from the sorting algorithm shows that, for low grid resolution, the solution deviates due to an effective gravitational force that is smoother than the exact force. In this figure, also the density on the PM grid (middle panel) and the particle acceleration field (bottom panel) is shown. In all cases, $N = 256$ particles were used. It is evident that sharper features in the acceleration are reproduced as the resolution is increased and the force approaches the exact (unsmoothed) N -body force. At the same time, the number of particles per cell naturally decreases thus increasing the [Poisson noise](#) in the density estimate. Particularly in multi-stream regions, this leads to visible particle noise in the acceleration. This reveals an important catch-22 of N -body simulations: the fine tuning of particle resolution and grid resolution in order to achieve the most accurate solution possible given the computational resources.

Anti-aliasing

So far, we have completely glanced over a very important limitation of discrete Fourier transforms.

Definition 4.10 — Aliasing of Fourier modes. Due to the finite bandwidth associated with the finite resolution – only modes $-N\pi \leq k \leq N\pi$ can be represented by a DFT. The maximum representable mode is called the [Nyquist mode](#) $k_{Ny} := N\pi$. Higher frequency modes $k' > k_{Ny}$ get aliased into this finite range of modes. This simply means that instead of appearing at the correct

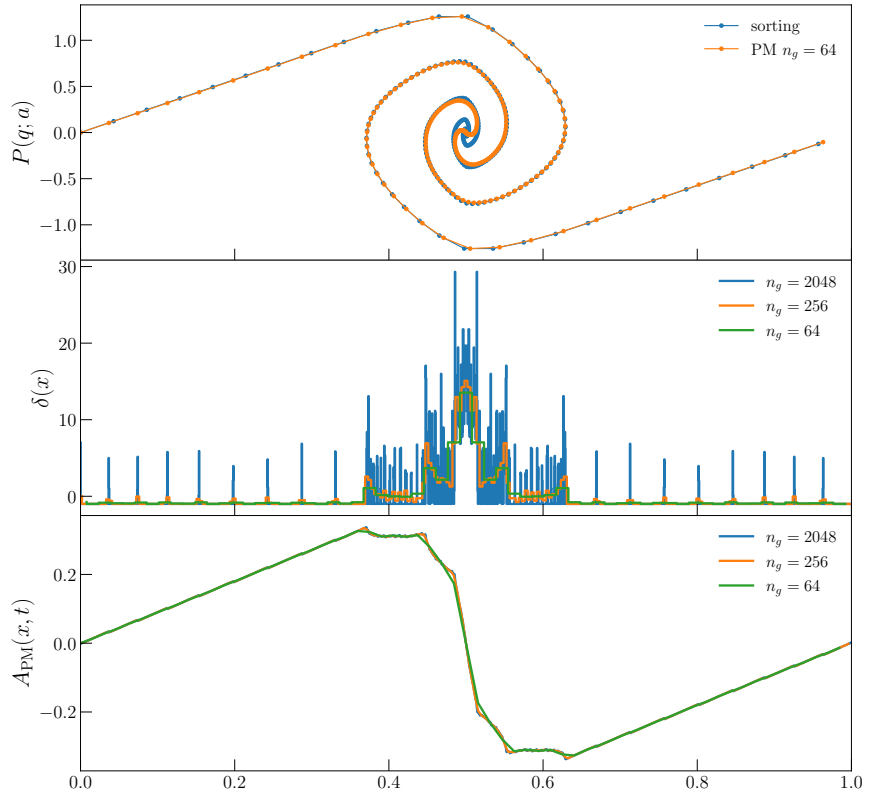


Figure 4.12: One-dimensional particle mesh (PM) simulation of the single mode plane wave collapse. $N = 256$ particles are used. The *top panel* shows the comparison of the solution obtained with the PM method and $n_g = 64$ grid cells (orange line) and the solution based on the sorting algorithm which yields the exact N -body force. The PM force with few grid cells leads to an effective smoothing, i.e. the PM force is smoother than Newtonian gravity on scales $\sim h = 1/n_g$. The *middle panel* shows the CIC density that is used in the Fourier calculation, and the *bottom panel* shows the acceleration obtained from eq. (4.61) on the PM grid. For high PM resolution, increasingly sharper features in the acceleration are resolved, but at the same time, the particle noise increases since the number of particles per cell, and therefore the Poisson noise, decreases.

mode $k' > k_{Ny}$, they are periodically wrapped into the representable range and appear at $k'_{\text{alias}} = k' - 2N\pi$ so that again $-N\pi \leq k'_{\text{alias}} \leq N\pi$. Even if a function is band-limited, aliasing can arise whenever functions are multiplied in real space. This phenomenon is graphically depicted in Figure 4.13.

In the case of the particle mesh method, however, the particle distribution is generally not bandwidth limited, and then projected onto the mesh (which is bandwidth limited). The resulting density field consequentially suffers from aliased modes. Essentially the same problem is also encountered in computer graphics, e.g. when a line is rasterised into pixels. There are essentially two solutions to the aliasing problem: filtering and anti-aliasing. We shall only discuss the latter as the first essentially works by filtering out the small-scale modes into which the aliased contributions are predominantly mapped.

More interesting perhaps than filtering is the [antialiasing](#) technique. It works by repeatedly mapping the particle distribution with sub-PM-cell ('sub-pixel') shifts and then averaging the resulting accelerations. Evidently, let $\{X_j\}_{j=1\dots N} \mapsto A_{\text{PM},i}$ represent the PM acceleration calculation for particle i , i.e. the full cycle of the projection of all N particles, spectral solution of the Poisson equation including differentiation, and back-interpolation to the position of particle i located at X_i .

One-fold anti-aliasing now works by computing two versions, one un-shifted, and one shifted by one cell diagonal, i.e. by the vector $d_{1/2} := \frac{1}{2n_g}\mathbf{1}$, where $\mathbf{1} = (1, \dots, 1)^\top$ is the one-vector, the one-fold dealiased acceleration can then be written

$$A_i^{1\times\text{AA}} = \frac{1}{2} [A_{\text{PM},i}(\{X_j\}_{j=1\dots N}) + A_{\text{PM},i}(\{X_j + d_{1/2}\}_{j=1\dots N})] \quad (4.73)$$

It is easy to show that this average cancels out the leading aliased modes. In principle this can be repeated further, but unfortunately at rapidly growing cost in higher dimensions. Without developing this further, higher order aliasing is achieved by inserting further finer sub-pixel shifts. E.g. in one dimension, in addition to the shift by $h/2$ one would include at the next order (' $2\times\text{AA}$ ') also the shifts by $h/4$ and $3h/4$, and at three-fold anti-aliasing (' $3\times\text{AA}$ ') further the shifts by $h/8, 3h/8, 5h/8$, and $7h/8$. Evidently the number of full force calculations is $2^{\ell n}$ for $\ell \times \text{AA}$ in n dimensions.

The effect of anti-aliasing on the acceleration calculation is shown in Figure 4.15. We use sawtooth initial conditions $\Psi = q$ with $-1/2 \leq q < 1/2$ and periodic repetition. The reason for this choice is that the sawtooth has no compact support in Fourier space, and it certainly also does not decay quickly towards the Nyquist wave number. It is not a completely academic exercise since prior to shell-crossing the map is essentially saw-tooth like. When computing the acceleration even while the perturbation is still negligibly small, one already sees clearly that significant aliased contributions are present in the acceleration as evidenced by the oscillations of the orange line. They essentially appear as a [Gibbs phenomenon](#), which often does not decrease in amplitude with resolution but remains constant. However, already averaging over one additional shift reduces the oscillations strongly, as seen for the red line. Further iterations reduce the oscillations further, but are rapidly increasing in computational cost in higher dimensions. It is clear that the de-aliased acceleration converges faster to the true acceleration as the grid resolution is increased so that the force approaches the Newtonian force.

A word of caution. We want to pause for a moment and emphasise the importance of reducing any source of noise in such N -body simulations. The

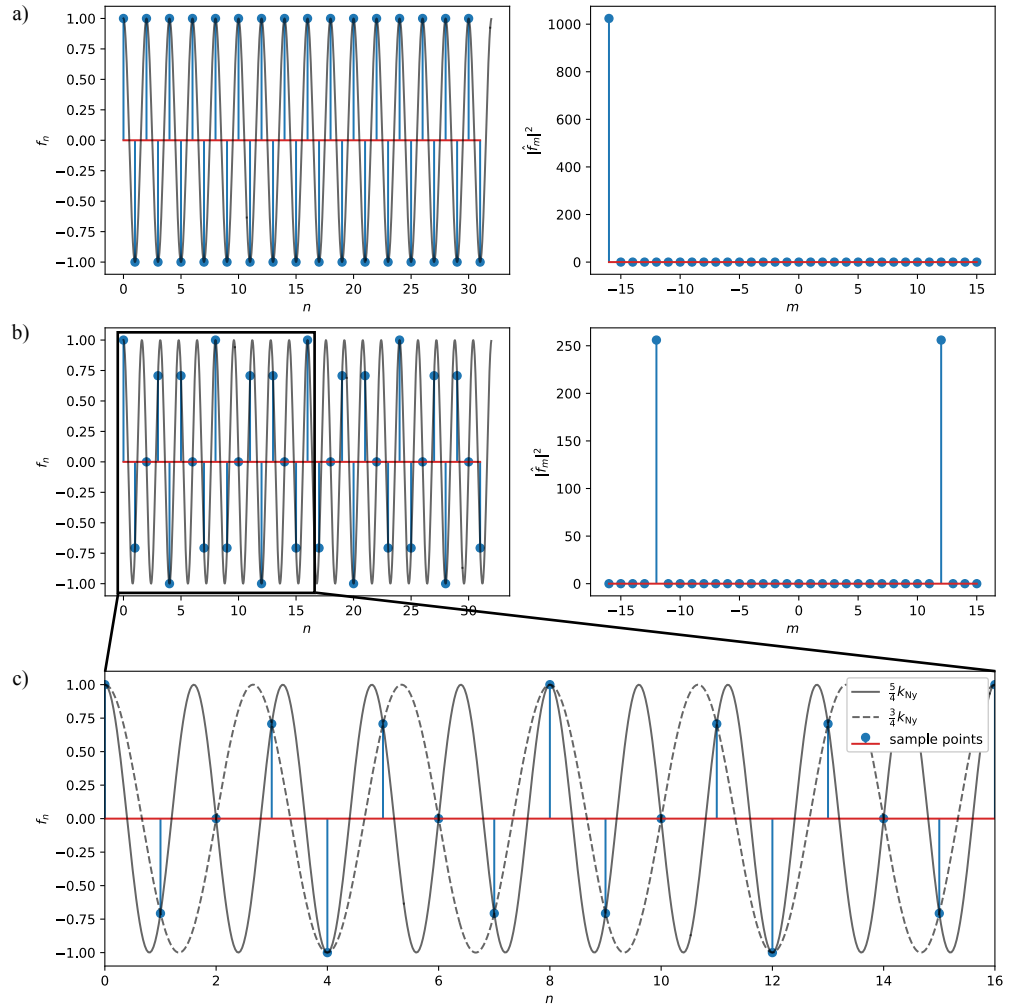


Figure 4.13: The Nyquist mode is the shortest wavelength (or equivalently, highest frequency) representable by discrete sampling. The top panels (a) demonstrate the sampling of a sinusoidal function with Nyquist wavelength (top left) and the associated power spectrum (top right), which has power only at the Nyquist mode. In contrast, the panels (b) demonstrate what happens if a function that has $k_{\text{true}} = \frac{5}{4}k_{\text{Ny}}$ is sampled: a beating frequency appears (bottom left), and the power spectrum (bottom right) shows corresponding aliased power not at the correct mode, but at a lower mode $k_{\text{aliased}} = \frac{3}{4}k_{\text{Ny}}$. In the enlargement (c) one can clearly see that with the given sampling h , k_{true} and k_{aliased} are indistinguishable.

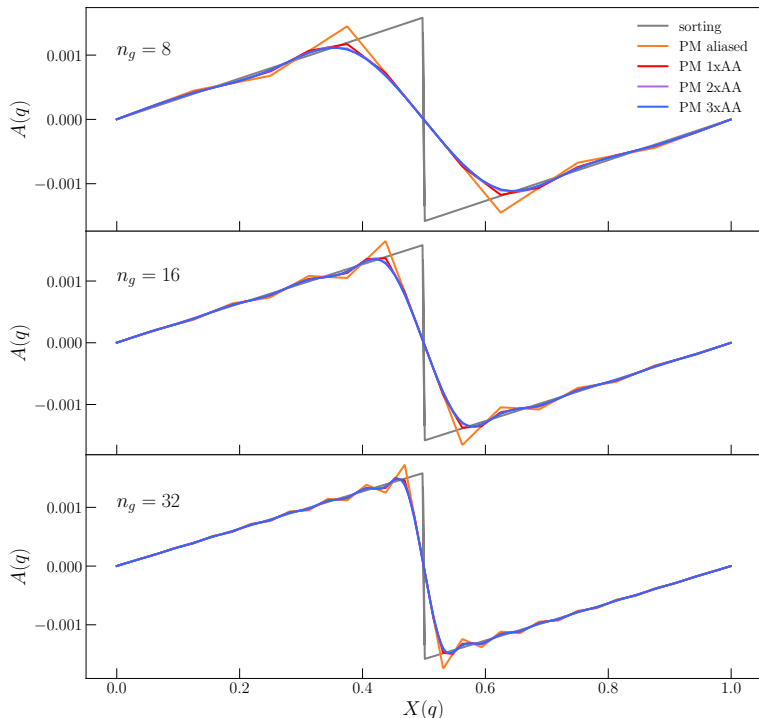


Figure 4.14: Effect of antialiasing on the acceleration calculation. Here we consider an initial displacement field which is a sawtooth function, i.e. $\Psi = q$ for $-1/2 \leq q < 1/2$ with periodic repetition. The acceleration in the first time step is shown in the graphs as computed using the sorting solver (gray lines), and using a single evaluation of the PM acceleration (orange lines) based on a grid with a resolution of $n_g = 8, 16$ and 32 (from top to bottom). It is clearly obvious that the acceleration is not only the true acceleration filtered by the CIC assignment kernel. In addition aliased contributions are visible as spurious oscillations. Already adding one-fold anti-aliasing, by averaging the PM acceleration with one obtained with a shifted version of the particles, strongly reduces these oscillations. In two-fold and three-fold one averages over four and eight shifted versions respectively.

reason is that the cold initial conditions that served us so well when performing Lagrangian perturbation theory are unforgiving to numerical errors. The reason is that there is no stabilising pressure that would counter-act small perturbations in the acceleration. If the errors are large enough, it is always possible that a density perturbation is produced that is large enough to collapse under its own gravity. Luckily one is saved to some degree by the large amounts of small scale structure in CDM (i.e. there are already significant perturbations on all scales of cosmological origin), but the lesson had to be learned the hard way when the first WDM (warm dark matter simulations) were carried out that produced copious amounts of spurious small-scale clumps of clearly numerical origin. While they were not the product of aliasing errors, in the era of precision cosmology, any source of systematic error in numerical simulations needs to be understood, tested and quantified.

Two-dimensional N -body simulations – a comparison with LPT

Program Code 4.3 A 2D PM gravity solver

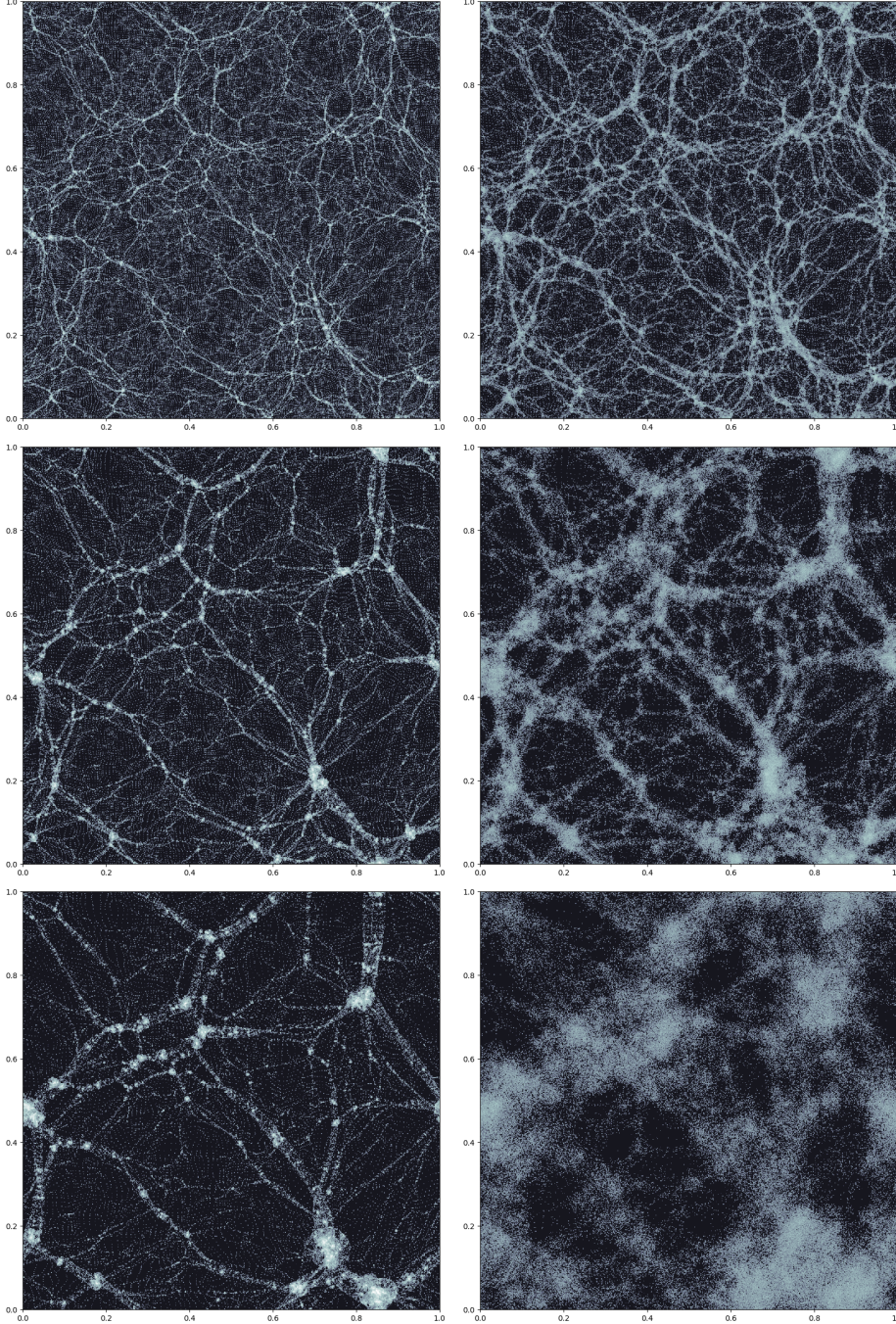


Figure 4.15: Cosmic structure evolution over time (top panels $a = 0.25$, middle panels $a = 0.5$, bottom panels $a = 1.0$). We show a comparison between a two-dimensional particle mesh N -body simulation (100 time steps to $a = 1$) in the left panels, and the one step LPT prediction (Zel'dovich approximation, 1 step). One can discern the perturbative and the non-perturbative regime of cosmic structure. While the Zel'dovich approximation is extraordinarily successful to predict the formation of non-shell-crossed structures, it has no post-shell-crossing interactions, so that structures that form disperse again. In contrast in the N -body simulation, structure keeps forming hierarchically and the increasingly larger clusters contain increasingly more substructure that has been accreted.

Non-uniform Fast Fourier transforms

Algorithmically, the PM method is relatively involved. Effectively, it can be seen as a way to perform a fast Fourier transform on a non-uniform grid. The reason is that the particle positions are not on a regular grid, while the density field required as input for the FFT is required on a regular grid.

Rather recently, a new class of algorithms has been developed that can perform a fast Fourier transform of non-uniformly sampled data, i.e. when

$$f(x) = \sum_{j=1}^M f_j \delta_D(x - x_j) \quad (4.74)$$

where the $x_j \in [0, 1]$ are M non-uniform sampling points. The most prominent of these is the [non-uniform fast Fourier transform \(NUFFT\)](#) algorithm. The NUFFT algorithm is based on the idea of performing the Fourier sum

$$\tilde{f}_n := \sum_{j=1}^M f_j e^{-i2\pi n x_j}, \quad n \in \mathbb{Z}, \quad \frac{n_g}{2} \leq n < \frac{n_g}{2} \quad (4.75)$$

with adjoint

$$f_j := \sum_{n=-n_g/2}^{n_g/2-1} \tilde{f}_n e^{i2\pi n x_j} \quad (4.76)$$

efficiently, where the $x_j \in [0, 1]$ are the M non-uniform grid points, while in Fourier space, the Fourier coefficients are on a regular grid (although NUFFT can also handle non-uniform grids in Fourier space). A naive evaluation of this sum would require $\mathcal{O}(Mn_g)$ operations, while the NUFFT algorithm can achieve this in $\mathcal{O}(n_g \log n_g + M)$ operations, similar to the FFT. This is achieved by effectively performing an algorithm comparable to the PM algorithm with optimized interpolation kernels.

A very fast implementation of the NUFFT algorithm is available in the [PYTHON](#) package `finufft` which can be installed via

```
$ pip install finufft
```

The method uses a special kernel function for which exponential convergence can be proven Barnett et al. (2019); Barnett (2020)² of the form

$$W_{\text{NUFFT}}(x) = \exp(\beta \sqrt{1 - x^2}) \quad (4.77)$$

where β is a kernel width parameter (in units of the regular grid to which one interpolates). These authors prove that the convergence is exponential with $\exp(-\beta C)$ with some C independent of β , i.e. the kernel width parameter can be chosen to control the accuracy of the NUFFT algorithm.

The `finufft` package is easy to use, e.g. for the 1D case, the following code snippet demonstrates how to use the NUFFT algorithm to compute the acceleration field. Using the NUFFT, we can directly Fourier transform the N -body density field

$$\rho_N(x) = \frac{1}{N} \sum_{j=1}^N \delta_D(x - X_j) \quad (4.78)$$

²<https://arxiv.org/abs/1808.06736>, <https://arxiv.org/abs/2001.09405>

i.e. each particle contributes a Dirac delta of weight $1/N$. If the particles were not all of the same weight, we could generalise to $\sum_j w_j \delta_D(x - X_j)$, where w_j is the weight of particle j .

```

1 import finufft
2
3 def calc_acc_nufft( x, ng = 256, eps = 1e-4 ):
4     """
5         Calculate acceleration using NUFFT
6     Parameters:
7         X (array) : particle positions
8         ng (int)   : number of grid points
9         eps (float): NUFFT accuracy
10    Returns:
11        acc (array): acceleration field
12    """
13    # weight for each particle = 1/N
14    w = np.ones_like(X, dtype=np.complex128) / len(X)
15    # call the 1D non-uniform->uniform FFT
16    f = finufft.nufft1d(X * 2*np.pi, w, ng, eps=eps)
17    # solve Poisson equation in Fourier space
18    k = 2 * np.pi * (np.arange(ng)-ng//2)
19    k[ng//2] = 1.0
20    f = f * (1j * k / k**2)
21    # adjoint transform, i.e. uniform->non-uniform iFFT
22    acc = finufft.nufft1d2( X * 2*np.pi, f, eps=eps)
23    return acc.real # finufft is complex, so return real part.
```

replacing the PM solver in the code snippet 4.2. In the two- and three-dimensional case, the NUFFT algorithm is also available in the `FINUFFT` package through the `nufft2d1/nufft2d2` and `nufft3d1/nufft3d2` functions, and the usage is analogous to the 1D case.

Trees for hierarchical multipole expansions

In the PM approach (also when using NUFFT), we have traded the exact evaluation of the particle-particle interaction with an approximation to speed up the calculation by introducing a mesh. In fact, it is a philosophical difference to give up on the exact (i.e. to machine precision) solution and require only a maximum bound on the error we are making. Without introducing a mesh, it is possible to circumvent the $\mathcal{O}(N^2)$ scaling of direct summation when accuracy can be sacrificed (as is almost always the case in practical applications).

A common approach is to employ a hierarchical tree structure to partition the mass distribution in space and compute the gravitational potential jointly exerted by groups of particles, whose potential is expanded to a given multipole order Barnes and Hut (1986). Thus, instead of particle-particle interactions, particle-node interactions are evaluated. Since the depth of such a tree is typically $\mathcal{O}(\log N)$, the complexity of the evaluation of all interactions can be reduced to $\mathcal{O}(N \log N)$. This can be further reduced to an ideal $\mathcal{O}(N)$ complexity with the fast multipole method (FMM, see below).

There are several alternatives for constructing tree structures. The most common choice is a regular octree (or quadtree in 2D) in which each tree level is subdivided in n dimensions into 2^n sub-cells of equal size. The tree subdivision continues until some prespecified number $M \geq 1$ of particles per node is reached. The main advantage brought by tree methods is that the pairwise interaction can be expanded perturbatively and grouped among particles at similar locations, thus reducing dramatically the number of calculations that needs to be carried out.

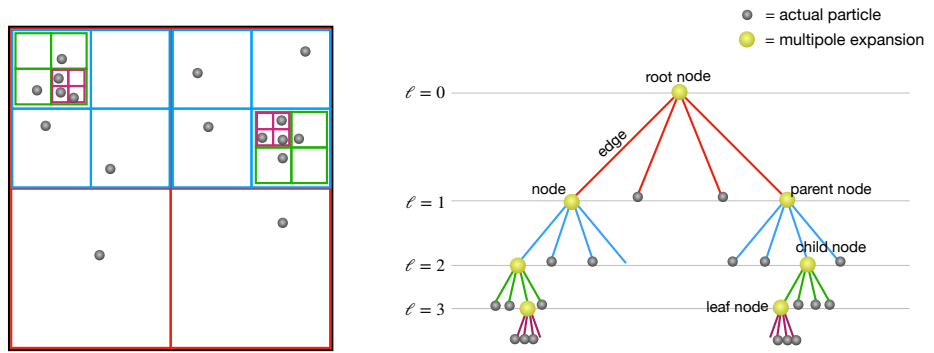


Figure 4.16: The Barnes& Hut tree algorithm. Instead of a direct summation, one organises particles in a hierarchical tree whose leaves partition the volume. Each tree node has a pivot point λ (e.g. the centre of mass of all particles in the node) and stores a multipole expansion of the particle mass distribution around the pivot point. Depending on the distance of the particle which wishes to compute the interaction, one can replace the entire tree branch with the multipole interaction to specifiable accuracy. The resulting algorithm ends up being $N \log N$ in the number of particles in typical cases instead of N^2 as for naive direct summation of pairwise particle interactions. In one spatial dimension one finds a binary tree, in two a ‘quadtree’ and in three an ‘octree’ structure.

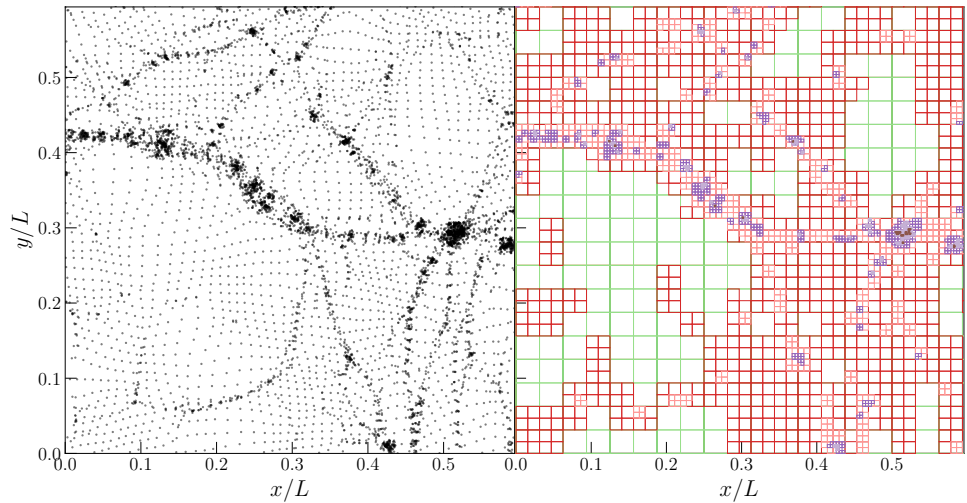


Figure 4.17: The quadtree structure (right) of a cosmological particle distribution (left). Here the maximum number of particles per node is set to 8 and empty tree nodes are not drawn. The bounding box of each tree node is colored by its refinement level ℓ with respect to the root node, which has $\ell = 0$. It is clearly evident how the tree structure is self-adaptive, i.e. in high density regions, the node size is reduced.

In the ‘Barnes & Hut tree’ algorithm Appel (1985); Barnes and Hut (1986), particle-node interactions are evaluated instead of particle-particle interactions. Let us consider a hierarchical octree decomposition of the simulation box volume $\mathcal{V} := [0, L_{\text{box}}]^3$ at level ℓ into cubical subvolumes, dubbed ‘nodes’, $\mathcal{S}_{i=1 \dots N_\ell}^\ell$ of side length $L_{\text{box}}/2^\ell$, where $N_\ell = 2^{3\ell}$, so that $\bigcup_i \mathcal{S}_i^\ell = \mathcal{V}$ and $\mathcal{S}_i^\ell \cap \mathcal{S}_{j \neq i}^\ell = \emptyset$ on each level gives a space partitioning. Let us consider the gravitational potential due to all particles contained in a node $X_j \in \mathcal{S}_i^\ell$. The partitioning is halted when only one (but typically a few) particle is left in a node. We shall assume isolated boundary conditions for clarity, i.e. we neglect the periodic sum in eq. (4.31). Thanks to the partitioning, the gravitational interaction can be effectively localised with respect to the ‘tree node’ pivot at location $\lambda \in \mathcal{S}_i^\ell$, so that the distance $\|X_j - \lambda\| \leq \sqrt{3}L_{\text{box}}/2^\ell =: r_\ell$ is by definition bounded by the ‘node size’ r_ℓ and can serve as an expansion parameter. To this end, one re-writes the potential due to the particles in the node subvolume \mathcal{S}_i^ℓ , which *in three dimensions* is given by

$$\phi_i^\ell(x) \propto \sum_{X_j \in \mathcal{S}_i^\ell} \frac{M_j}{\|x - X_j\|} = \sum_{X_j \in \mathcal{S}_i^\ell} \frac{M_j}{\|(x - \lambda) - (X_j - \lambda)\|} = \sum_{X_j \in \mathcal{S}_i^\ell} \frac{M_j}{\|\mathbf{d} + \lambda - X_j\|} \quad (4.79)$$

where $\mathbf{d} := x - \lambda$. While *in two dimensions*

$$\phi_i^\ell(x) \propto - \sum_{X_j \in \mathcal{S}_i^\ell} M_j \log \|\mathbf{d} + \lambda - X_j\| \quad (4.80)$$

This can be Taylor expanded to yield the ‘P2M’ (particle-to-multipole) interaction for the potential (note that the terms in square brackets are the multipole moments and are independent of \mathbf{d}). Let $\mathbf{r}_j := X_j - \lambda$ be the position of particle j relative to the node pivot, then for the Green’s function of the potential *in three dimensions*

$$\frac{1}{\|\mathbf{d} - \mathbf{r}_j\|} = \underbrace{\frac{1}{\|\mathbf{d}\|} \left[1 \right]}_{\text{monopole } \mathcal{O}(1/d)} + \underbrace{\frac{d_k}{\|\mathbf{d}\|^3} \left[r_{j,k} \right]}_{\text{dipole } \mathcal{O}(r_\ell/d^2)} + \underbrace{\frac{1}{2} \frac{d_k d_l}{\|\mathbf{d}\|^5} \left[3r_{j,k} r_{j,l} - \delta_{kl} \|\mathbf{r}_j\|^2 \right]}_{\text{quadrupole } \mathcal{O}(r_\ell^2/d^3)} + \dots \quad (4.81)$$

which converges quickly if $\|\mathbf{d}\| \gg r_\ell$. While *in two dimensions* one has

$$-\log \|\mathbf{d} - \mathbf{r}_j\| = \underbrace{-\log \|\mathbf{d}\| \left[1 \right]}_{\text{monopole } \mathcal{O}(\log d)} + \underbrace{\frac{d_k}{\|\mathbf{d}\|^2} \left[r_{j,k} \right]}_{\text{dipole } \mathcal{O}(r_\ell/d)} + \underbrace{\frac{1}{2} \frac{d_k d_l}{\|\mathbf{d}\|^4} \left[2r_{j,k} r_{j,l} - \delta_{kl} \|\mathbf{r}_j\|^2 \right]}_{\text{quadrupole } \mathcal{O}(r_\ell^2/d^2)} + \dots \quad (4.82)$$

The multipole moments depend only on the vectors $\mathbf{r}_j = (X_j - \lambda)$ and can be pre-computed up to a desired maximum order p during the tree construction and stored with each node. In doing this, one can exploit that multipole moments are best constructed bottom-up, as they can be translated in an upward-sweep to the parent pivot and then co-added – this yields an ‘upwards M2M’ (multipole-to-multipole) sweep through the tree. Note that if one sets λ to be the centre of mass of each tree node, then the dipole moment vanishes. Explicitly, the multipole moments of a node (say node i on level ℓ whose set of particles contained in the

node is \mathcal{S}_i^ℓ) are up to octupole order given in n_d dimensions by

$$\text{monopole} \quad M^{(\ell,i,0)} := \sum_{\mathbf{x}_j \in \mathcal{S}_i^\ell} 1 \quad (4.83a)$$

$$\text{dipole} \quad M_k^{(\ell,i,1)} := \sum_{\mathbf{x}_j \in \mathcal{S}_i^\ell} \mathbf{r}_{j,k} \quad (4.83b)$$

$$\text{quadrupole} \quad M_{kl}^{(\ell,i,2)} := \sum_{\mathbf{x}_j \in \mathcal{S}_i^\ell} \left[n_d \mathbf{r}_{j,k} \mathbf{r}_{j,l} - \delta_{kl} \|\mathbf{r}_j\|^2 \right] \quad (4.83c)$$

$$\text{octupole} \quad M_{klm}^{(\ell,i,3)} := n_d \sum_{\mathbf{x}_j \in \mathcal{S}_i^\ell} \left[(n_d + 2) \mathbf{r}_{j,k} \mathbf{r}_{j,l} \mathbf{r}_{j,m} - (\delta_{lm} \mathbf{r}_{j,k} + \delta_{km} \mathbf{r}_{j,l} + \delta_{kl} \mathbf{r}_{j,m}) \|\mathbf{r}_j\|^2 \right] \quad (4.83d)$$

It is easy to verify that moments beyond the dipole vanish in one dimension (for the same reason why LPT has no higher order terms in one dimension).

If one seeks the acceleration of a particle due to the node, the potential needs to be once more differentiated. This can of course also be expressed in terms of the multipole moments. One finds in three dimensions for a particle at distance \mathbf{d} from the node pivot the expansion

$$\begin{aligned} -\partial_a \sum_{\mathbf{x}_j \in \mathcal{S}_i^\ell} \frac{1}{\|\mathbf{d} - \mathbf{r}_j\|} &= \frac{d_a}{\|\mathbf{d}\|^3} M^{(\ell,i,0)} + \frac{3d_a d_k - \delta_{ak} \|\mathbf{d}\|^2}{\|\mathbf{d}\|^5} M_k^{(\ell,i,1)} + \\ &+ \frac{1}{2} \frac{5d_a d_k d_l - (\delta_{ak} d_l + \delta_{al} d_k) \|\mathbf{d}\|^2}{\|\mathbf{d}\|^7} M_{kl}^{(\ell,i,2)} + \dots \end{aligned} \quad (4.84)$$

and in two dimensions the expansion

$$\begin{aligned} \partial_a \sum_{\mathbf{x}_j \in \mathcal{S}_i^\ell} \log \|\mathbf{d} - \mathbf{r}_j\| &= \frac{d_a}{\|\mathbf{d}\|^2} M^{(\ell,i,0)} + \frac{2d_a d_k - \delta_{ak} \|\mathbf{d}\|^2}{\|\mathbf{d}\|^4} M_k^{(\ell,i,1)} + \\ &+ \frac{1}{2} \frac{4d_a d_k d_l - (\delta_{ak} d_l + \delta_{al} d_k) \|\mathbf{d}\|^2}{\|\mathbf{d}\|^6} M_{kl}^{(\ell,i,0)} + \dots \end{aligned} \quad (4.85)$$

When evaluating the potential $\varphi(\mathbf{x})$ or the acceleration $\mathbf{A}(\mathbf{x})$ one now proceeds top-down from the root node at $\ell = 0$ in a ‘tree walk’ and evaluates M2P (multipole-to-particle) interactions between the given particle and the node. Since one knows that the error in $\phi_i^\ell(\mathbf{x})$ is $\mathcal{O}((r_\ell/d)^p)$, one defines a maximum ‘opening angle’ θ_c and requires in order for the multipole expansion $\phi_i^\ell(\mathbf{x})$ to be an acceptable approximation for the potential due to the mass distribution in \mathcal{S}_i^ℓ that the respective opening angle obeys

$$\frac{r_\ell}{\|\mathbf{d}\|} < \theta_c. \quad (4.86)$$

Otherwise the procedure is recursively repeated with each of the eight child nodes. Since the depth of a (balanced) octree built from a distribution of N particles is typically $\mathcal{O}(\log N)$, a full potential or force calculation has an algorithmic complexity of $\mathcal{O}(N \log N)$ instead of the $\mathcal{O}(N^2)$ of the direct summation. The resulting relative error in a node-particle interaction is Dehnen (2002)

$$|\delta\phi_i^\ell| \lesssim \frac{\theta_c^{p+1}}{1 - \theta_c} \frac{M^{(\ell,i,0)}}{\|\mathbf{d}\|}, \quad (4.87)$$

where $M^{(\ell,i,0)}$ is the zeroeth multipole moment (i.e. the node mass, aka the sum of the masses of all particles in S_i^ℓ), and p is the order of the multipole expansion. This error estimate is not a rigorous estimate of the true error, but can serve as reasonable guidance. To control the accuracy of an evaluation, one has therefore two possibilities: (1) to reduce the threshold ‘opening angle’ θ_c , or (2) to increase the expansion order p . Both increase of course the computational cost: (1) by evaluating more nodes and traversing deeper down the tree, and (2) by requiring more complex computations to evaluate a single particle-node interaction. These two have different performance characteristics and depending on implementation and computer architecture, either may be favourable in different scenarios.

Program Code 4.4 Building a quadtree in PYTHON

To build a particle quadtree in PYTHON, we will use a method based on recursive subdivision and an [object oriented](#) implementation for the tree nodes. The fundamental unit is the `QuadTreeNode` class. Let us assume all particles are inside the bounding box $[0, 1]^2$. Given a call to the constructor of a node, it will compute the multipole moments from the passed particles and determine if it is passed a number of particles that crosses the threshold for further subdivision. If this is the case, then it sorts its particles into four subranges for four sub-quadrants. This means that it rearranges the particles so that in the array where the particle data is stored, the particles of the first quadrants (or ‘quad’) come first, then those of the second, and so on. Then it calls the constructor for a new node using the sub-range of particles. The ranges are managed here by simply given the first and end index in the numpy array. This algorithm can be cast into PYTHON code as follows:

```

1   # implements a quadtree node structure
2   class QuadtreeNode:
3       # constructor of a quadtree node
4       def __init__( self, points, imin, imax, corner, length, level=0 ):
5           # corner coordinates of this node
6           self.corner = corner
7           # edge length of this node
8           self.length = length
9           # geometric center of this node (used as split point)
10          self.center = self.corner + self.length/2
11          # number of particles in the node
12          self.size = imax-imin
13          # range of particle indices that are inside this node
14          self.range = (imin,imax)
15          # refinement level of this node
16          self.level = level
17          # dictionary of children
18          self.children = {}
19
20          # multipoles
21          self.multipoles = compute_multipoles( points, imin, imax, self.center )
22
23          # if more than 1 (could be more) particles in the node, then
24          # recursively split (partition) the node into children
25          if self.size > 1:
26              self.partition( points )
27
28          # member function that partitions the node particles and creates
29          # new children nodes
30          def partition( self, points ):
31              # sort into quads and store number in each of the quads in nquads and
32              # the offsets for each quad in nquadoff
33              nq,nqoff = partition_sort( points, self.range[0], \
34                                         self.range[1], self.center )
35
36              for i in range(2):
37                  for j in range(2):
38                      quad_id = j*2+i
39                      if nq[quad_id] > 0: # if particles in quad, create new node
40                          newlength = self.length/2
41                          newcorner = self.corner + np.array((i,j)) * newlength
42
43                          self.children[quad_id] = QuadtreeNode( points, \
44                                                 nqoff[quad_id], \
45                                                 nqoff[quad_id+1], \
46                                                 newcorner, \
47                                                 newlength, \
48                                                 self.level+1 )

```

We haven't specified yet the function that sorts particles into the quads and counts how many end up in each quad. Since this is a time critical functions during the tree construction, we shall speed it up with numba jit acceleration. An implementation is e.g. given by (but maybe you find a faster or shorter one yourself?)

```

1  @jit(nopython=True)
2  def partition_sort( points, imin, imax, center ):
3      # sort particles in range imin...imax into quads
4      nodepoints = pointsimin:imax]
5      partition_idx = (nodepoints[:,1] > center[1])*2 \
6                      + (nodepoints[:,0] > center[0])
7      partition_order = np.argsort(partition_idx)
8      pointsimin:imax,:] = nodepoints[partition_order,:]
9
10     # compute how many particles in each quad
11     points_in_quad = np.zeros(4,dtype=numba.int64)
12     for quad_id in partition_idx:
13         points_in_quad[quad_id] += 1
14
15     # compute offsets
16     points_in_quad_offsets = np.zeros(5,dtype=numba.int64)
17     points_in_quad_offsets[1:] = np.cumsum(points_in_quad)
18     points_in_quad_offsets += imin # get the offset in the global array
19
20     return points_in_quad, points_in_quad_offsets

```

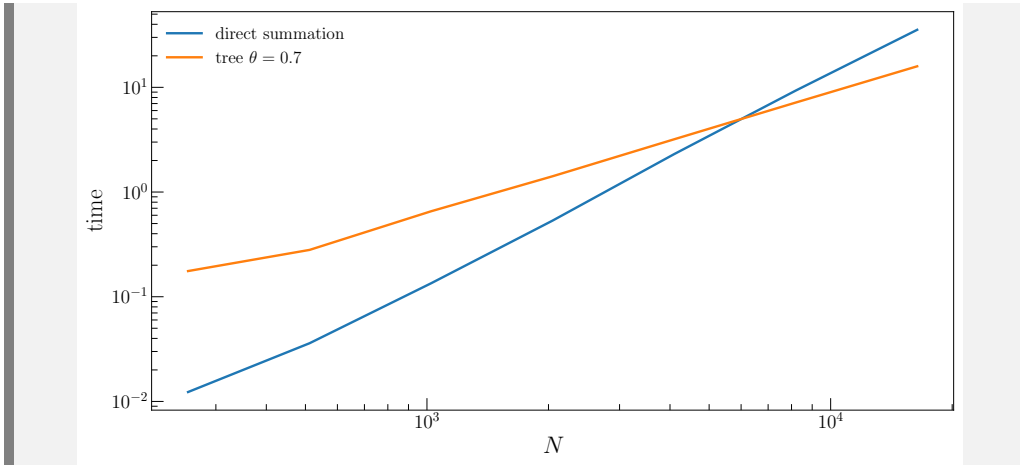
And finally, we have to write the member function that carries out the actual tree walk to compute the potential or acceleration, deciding whether a node is a good enough approximation, or whether its children nodes need to be used. If there are particles in the node but no children, then one can resort to direct summation.

```

1  # member of class QuadtreeNode
2  def potential( self, points, theta, i ):
3      # vector from evaluation to pivot
4      dvec = points[i,0:2]-self.center
5      # distance evaluation to pivot
6      d = np.linalg.norm(dvec)
7      # diagonal size of node
8      rl = 0.86602540378 * self.length # sqrt(3)/2 * edge length of node
9      if rl / d < theta: # node passes accuracy criterion
10          potential = evaluate_multipoles( self.multipoles, dvec, d )
11      else: # need to go to children nodes to reduce error
12          if len(self.children)>0 : # if there are any, do so
13              potential = 0.0
14              for c in self.children.values():
15                  potential += c.potential( points, theta, i )
16          else:
17              # if there aren't any, direct sum of particles in node
18              # i.e. compute the exact interaction of particles in self.range
19              # with particle i
20              potential = potential_directsum( points, i, \
21                                              self.range[0], self.range[1] )
22
23      return potential

```

We can measure the time needed to compute the potential or acceleration for each particle, and one typically finds a plot like this:



Despite the $\mathcal{O}(N^2)$ scaling, the direct summation is faster for small particle numbers. The break-even point is reached for 5000 particles for our implementation, at which point the tree is more efficient. The details depend on the exact implementation, but this behaviour is generic.

Space-partitioning and space-filling curves

Instead of the recursive sorting of sub-intervals of the particle range that we employed in our tree-building algorithm above, it is more efficient to exploit a relation between quadtrees/octrees and fractals, specifically the two- and three-dimensional Hilbert curve and the Morton curve (sometimes also called Z-order curve). These space-filling curves allow, given a discretisation scale, to map higher dimensional space onto a one-dimensional line. Due to their fractal (self-similar) character, they naturally have the hierarchical structure that also the quadtree and octree has. While classically (in the C programming language, e.g.) trees would be built with using memory pointers as edges between nodes, it is more efficient to rely on such ordering curves. If one sorts particles by the position on the one-dimensional space-filling curve, they automatically are in the right order for hierarchical trees. The space filling curve essentially gives, for each level ℓ of the hierarchical tree, a unique way to number (or traverse) all nodes on that level. For the Hilbert and Morton ordering what this looks like for $\ell = 1, 2, 3$ is shown in Figure 4.18

Now, given a space-filling curve at some sufficiently high order, each particle's location in the tree can be efficiently determined by its location on the curve. Assume the space-filling curve has a total length 1 and is given up to some level ℓ_{\max} , then we can assign particles to cells $i = \lfloor x/2^\ell \rfloor \subset \mathbb{Z}^d$. Knowing that there are $2^{\ell n}$ nodes on level ℓ in n dimensions, the part of the curve with q between $/2^{\ell d} \leq q < (j+1)/2^{\ell d}$ with $j = 0, \dots, 2^{\ell d} - 1$. What this looks like is shown in Figure 4.19.

Such space-filling curves are also used in the task of [domain decomposition](#) for parallel computing in order to achieve what is called [load balancing](#). Here, the space-filling curve is split into segments of equal computational cost and these segments assigned to distinct processors. Since processors that do not share memory have to communicate through slower interlinks, it is often beneficial to minimise further surface to volume ratios of such decompositions. Given the complexity of modern computer architectures, recent developments however often

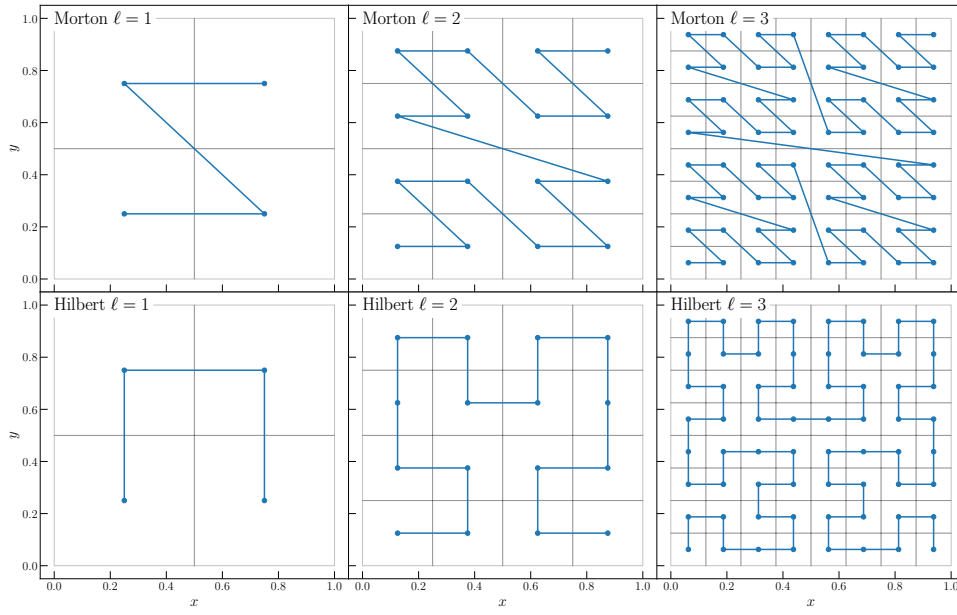


Figure 4.18: Hierarchical space partitioning due to quadtrees and octrees has an intimate connection with certain fractal space-filling curves. The space-filling curves permit a mapping between spatial regions ('nodes') and a one-dimensional number (the position on the curve). This works in two and higher dimensions.

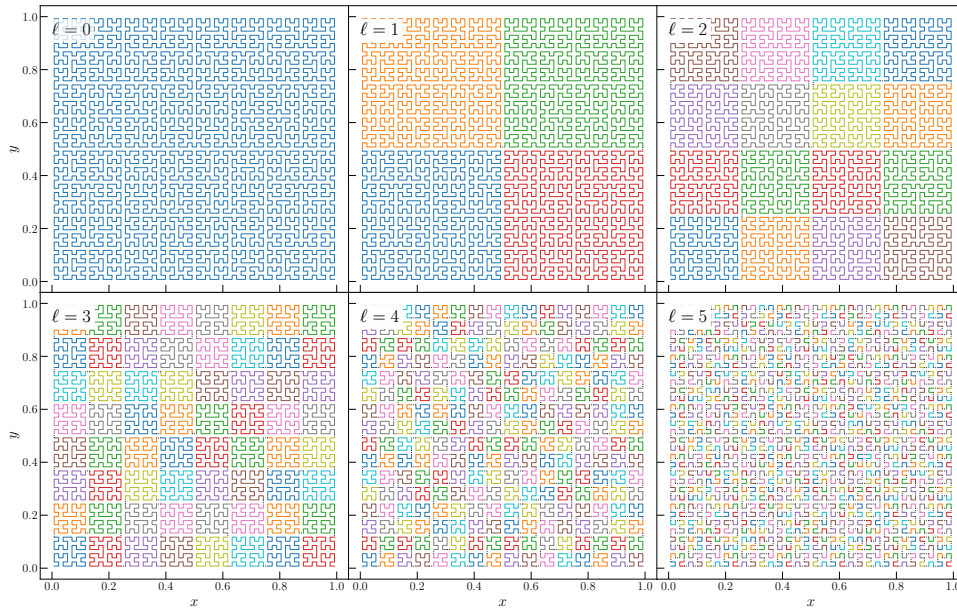


Figure 4.19: Given a space-filling curve at some sufficiently high order, each particle's location in the tree can be efficiently determined by its location on the curve. Cutting the curve into $2^{\ell n}$ pieces of equal length yields the individual subvolumes that belong to the nodes on level ℓ .

use more advanced domain decomposition techniques, that optimise dynamically the load balance.

Particle-Mesh-Ewald – the P³M and TreePM hybrid methods

When discussing the tree above, we haven't taken into account the periodic boundary conditions. While the tree accelerates the evaluations of interactions, it still requires Ewald summation to be applied in order to correctly compute accelerations in the periodic volume. A particularly efficient class of methods exploits the PM method to evaluate the long-range interactions, and then either direct summation – giving rise to the particle-particle - particle-mesh (P³M) methods – or a tree method – giving rise to the Tree-PM methods – to compute the short-range interactions.

For the PM part, one can re-use the exact algorithm and implementation that we have outlined in Section 4, but of course the Green's function has to be replaced with the long-range Ewald Green's function. This means that instead of the Fourier space solutions for the potential and accelerations given in eqs. (4.60) and (4.61). Defining the dimensionless force-splitting scale $\alpha^2 := (2\pi)^2 \epsilon^2$, the solution for the long-range Poisson equation reads

$$\tilde{\phi}_{\mathbf{n}} = \begin{cases} 0 & \text{if } \|\mathbf{n}\| = 0 \\ -\frac{4\pi G \bar{\rho}}{(2\pi)^2 a} \tilde{\delta}_{\mathbf{n}} \|\mathbf{n}\|^{-2} \exp[-\frac{1}{2}\alpha^2 \|\mathbf{n}\|^2] & \text{otherwise} \end{cases} \quad \forall \mathbf{n} \in \mathbb{Z}^{n_d} \quad (4.88)$$

which can again be conveniently computed using FFT techniques. The acceleration is obtained by additional differentiation, which can be either performed in Fourier space, so that one finds

$$\tilde{\mathbf{A}}_{\mathbf{n}} = \begin{cases} 0 & \text{if } \|\mathbf{n}\| = 0 \\ \frac{4\pi G \bar{\rho}}{2\pi a} \tilde{\delta}_{\mathbf{n}} \frac{\text{in}}{\|\mathbf{n}\|^2} \exp[-\frac{1}{2}\alpha^2 \|\mathbf{n}\|^2] & \text{otherwise} \end{cases} \quad \forall \mathbf{n} \in \mathbb{Z}^{n_d} \quad (4.89)$$

Alternatively, since the long-range contribution is very smooth, it is usually accurately enough but substantially faster to compute the long-range potential in Fourier space and then obtain the acceleration in real space by finite differencing the potential field at second or fourth order. This saves two backward FFTs as well as having to store a copy of the full acceleration field in memory. Otherwise, the steps are identical to the standard PM algorithm: deposit particles, solve for potential/acceleration, interpolate back to particle position. In addition, for these hybrid methods, the short-range contribution needs to be added on top.

For the P³M method, the short-range contribution is summed by direct summation, but due to the Ewald cutoff, the summation can be restricted to a region of a few PM grid cells only, which makes this a practical solution. Such methods have seen renewed interest, since GPUs can be used to very efficiently compute direct particle interactions as they do not rely on complicated data structures such as trees.

For the tree-PM method, the short-range contribution is evaluated using the particle tree (as outlined in the previous section). Due to the force cut-off, the multipole expansion has to be modified however. Starting with the short-range Green's function [OH: TBD]

$$\mathcal{G}_{\text{sr},3D}(r) = -\frac{1}{4\pi r} \text{erfc} \left[\frac{r}{\sqrt{2}\epsilon} \right], \quad \mathcal{G}_{\text{sr},2D}(r) = \quad (4.90)$$

and defining $\mathcal{G}'_{\text{sr}}(r)$ as the radial derivative $\partial \mathcal{G}_{\text{sr}} / \partial r$, the multipole expansion reads of course

$$\mathcal{G}_{\text{sr}}(\|\mathbf{d} - \mathbf{r}_j\|) = \mathcal{G}_{\text{sr}}(\|\mathbf{d}\|) - \mathcal{G}'_{\text{sr}}(\|\mathbf{d}\|) \frac{d_k}{\|\mathbf{d}\|} [r_{j,k}] + \frac{1}{2} \mathcal{G}''_{\text{sr}}(\|\mathbf{d}\|) \frac{d_k d_l}{\|\mathbf{d}\|^2} [r_{j,k} r_{j,l}] \dots \quad (4.91)$$

Again, if the node pivot points are set at the center of mass, then the dipole term vanishes since the dipole moment vanished then.

The frontier: fast-multipole methods

Despite the huge advantage with respect to direct summation, a particle-node interaction in the [Barnes & Hut tree](#) method is still computationally expensive as it has a $\mathcal{O}(\log N)$ complexity. Furthermore, trees as described above have other disadvantages, for instance, gravitational interactions are not strictly symmetric. This leads to a violation of momentum conservation.

A solution to these limitations is provided by the [fast multipole method \(FMM\)](#), originally proposed by Greengard and Rokhlin (1987). This algorithm takes optimizes hierarchical expansions even further by realising that significant parts of the particle-node interactions are redundantly executed for particles that are within the same node. In order to achieve a $\mathcal{O}(1)$ complexity per particle, the node-node interaction should be known and translated to the particle location. To achieve this, FMM exploits a double expansion of the interaction. Up to recently, FMM methods have not been widespread in cosmology. The advantages of FMM are becoming evident in the most modern N -body codes, which simulate extremely large numbers of particles. We kindly refer the reader to detailed reviews by, e.g., Kurzak and Pettitt (2006); Dehnen and Read (2011) for more information on the method.

The FMM method builds on the same hierarchical space decomposition as the Barnes&Hut tree above and shares some operators. For the FMM algorithm, three steps are missing from the tree algorithm outlined in the previous section: a ‘downward M2L’ (multipole-to-local) sweep, which propagates the interactions back down the tree after the upward M2M sweep, thereby computing a local field expansion in the node. This expansion is then shifted in ‘downward L2L’ (local-to-local) steps to the centers of the child nodes, and a final ‘L2P’ (local-to-particle) translation. As one has to rely on the quality of the local expansion in each node, FMM requires significantly higher order multipole expansions compared to standard Barnes & Hut trees to achieve low errors.

Force softening

We have mentioned before that it may be desirable to replace the [N-body distribution function](#)

$$f_N(\mathbf{x}, \mathbf{v}, t) = \frac{1}{N} \sum_{i=1}^N \delta_D(\mathbf{x} - \mathbf{X}_i(t)) \delta_D(\mathbf{v} - \mathbf{V}_i(t)) \quad (4.92)$$

with a Kernel smoothed version in order to prevent divergence when $\mathbf{X}_i(t) = \mathbf{X}_j(t)$ for $i \neq j$ at some point (remember that the Green’s functions in more than one dimension diverge for zero lag). Applying kernel smoothing to only the positional

part, we find with some softening parameter $\sigma \in \mathbb{R}^+$ the [softened distribution function](#)

$$f_N^\sigma(\mathbf{x}, \mathbf{v}, t) = \frac{1}{N} \sum_{i=1}^N K(\mathbf{x} - \mathbf{X}_i(t) \mid \sigma) \delta_D(\mathbf{v} - \mathbf{V}_i(t)). \quad (4.93)$$

This is of course equivalent to a convolution of the original N -body distribution with the softening kernel $K(\cdot \mid \sigma)$, so that

$$f_N^\sigma(\mathbf{x}, \mathbf{v}, t) = f_N * K_\sigma. \quad (4.94)$$

Importantly, due to transitivity of the convolution product, we can shift in gravity calculations the softening kernel to the [Green's function](#), i.e.

$$\phi_\sigma = (\rho * K_\sigma) * \mathcal{G} = \rho * (K_\sigma * \mathcal{G}) =: \rho * \mathcal{G}_\sigma. \quad (4.95)$$

■ **Example 4.2 — Plummer softening.** A (formerly) common choice for the Kernel function in the astrophysics literature (i.e. in $d = 3$ dimensions) is the Plummer function

$$K_{\text{Plummer}}(r \mid \sigma) := \frac{3}{4\pi} \frac{\sigma^2}{(r^2 + \sigma^2)^{5/2}} \quad r := \|\mathbf{x} - \mathbf{X}\| \quad (4.96)$$

for which it is easy to show that with $\mathcal{G}(r)$ from (4.30) one finds for $d = 3$ with $\mathcal{G} = -\frac{1}{4\pi r}$ that the softened Green's function then becomes

$$\mathcal{G}_\sigma(r) = -\frac{1}{4\pi \sqrt{r^2 + \sigma^2}}. \quad (4.97)$$

Unlike the unsoftened Green's function, this one is now bounded from below:

$$-\frac{1}{4\pi\sigma} \leq \mathcal{G}_\sigma < 0 \quad \forall \quad r \in \mathbb{R}_0^+. \quad (4.98)$$

A decided disadvantage of the Plummer softening is that it recovers the non-softened Green's function only asymptotically, which is often referred to as 'Plummer gravity not being Newtonian for large r' . ■

The 'softened gravity is not Newtonian' statement can be turned into a requirement for exact transition to Newtonian gravity.

Proposition 4.4 — Compact support softening. For the softened Green's function \mathcal{G}_σ to be equal to the unsoftened \mathcal{G} for $r > \sigma$, the softening kernel must have compact support, i.e. $K_\sigma(r) = 0$ for all $r > \sigma$.

Proof. The proof follows directly from the Gauss-Stokes theorem. Details are left as an exercise. ■

■ **Example 4.3 — Compact softening.** Simple compactly supported kernels can be easily constructed from polynomial functions. Consider for example the choice $K_\sigma(r) = \sigma^{-1} K(r/\sigma)$ with

$$K(r) = \begin{cases} \frac{15}{8\pi} (1 - r^2) & \text{if } r < 1 \\ 0 & \text{if } r \geq 1 \end{cases}, \quad (4.99)$$

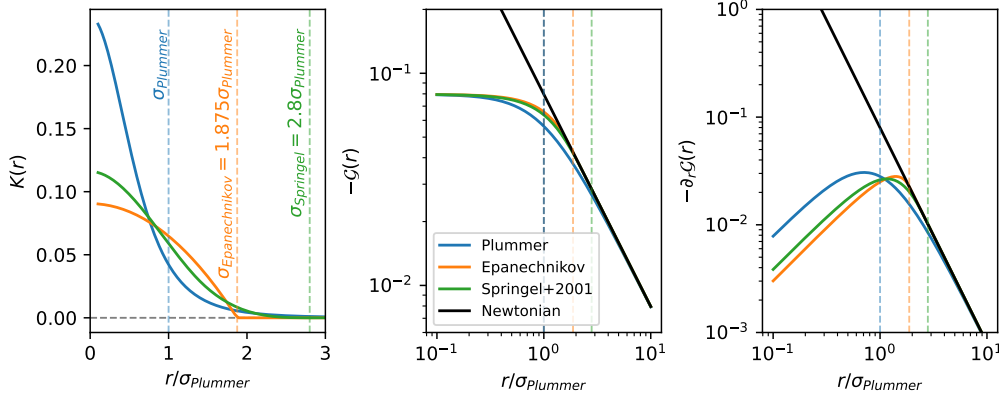


Figure 4.20: The effect of force softening: *Left panel*: the Delta-Diracs in the empirical N -body distribution function are replaced by Kernels of finite extent: the Plummer kernel (mymiddleblue, not compactly supported), the Epanechnikov kernel (orange), and the kernel from Springel et al. (2001) which approximates a Gaussian with compact support. *Middle Panel*: The resulting Green's function of the three-dimensional Laplacian. *Right Panel*: The resulting gradient Green's functions. The softening parameters have been tuned to recover the same asymptotic potential (middle panel), and therefore in some rough sense the same ‘energy scale’.

which is the Epanechnikov kernel for $d = 3$, and the lowest order polynomial that is differentiable at the origin and continuous at $r = 1$, then

$$\mathcal{G}(r) = \begin{cases} -\frac{3r^4 - 10r^2 + 15}{32\pi} & \text{if } r < 1 \\ -\frac{1}{4\pi r} & \text{if } r \geq 1 \end{cases} \quad \text{with } \mathcal{G}(r) \geq -\frac{15}{32\pi} \quad \forall r. \quad (4.100)$$

The Epanechnikov Green's function matches asymptotically for $r \rightarrow 0$ the Plummer Green's function if $\sigma_{\text{Epanechnikov}} = \frac{15}{8}\sigma_{\text{Plummer}}$. ■

Modern cosmological N -body codes typically adopt compactly supported approximations to a Gaussian kernel. In Figure 4.20, we show a comparison between different softening kernels and the impact on the Green's function and the gradient Green's function. We show also results for the ' W_2 ' kernel of Springel et al. (2001) (their eq. 71), which is e.g. adopted in the `GADGET4` code (Springel et al., 2021). See, e.g., Dehnen (2001); Barnes (2012) for further in-depth discussions regarding force softening in collisionless simulations. In particular, Dehnen (2001) demonstrate that the softening kernels above can introduce a bias in the interaction part of the Hamiltonian – and proposes improved kernel that might perform better (but this, to our knowledge, has never been tested for cosmological simulations).

Discreteness errors in cosmological simulations

We might wonder how well the discrete N -body system agrees with the continuous Lagrangian coordinates approach. The first is a particle system, the second is in the fluid limit. We have already computed the linear perturbation theory for the fluid system in section 3, *but what would be the corresponding result for the discrete N -body system?*

The respective calculation can be done, is however not entirely trivial based on the knowledge developed so far here. The perturbation theory of discrete particle

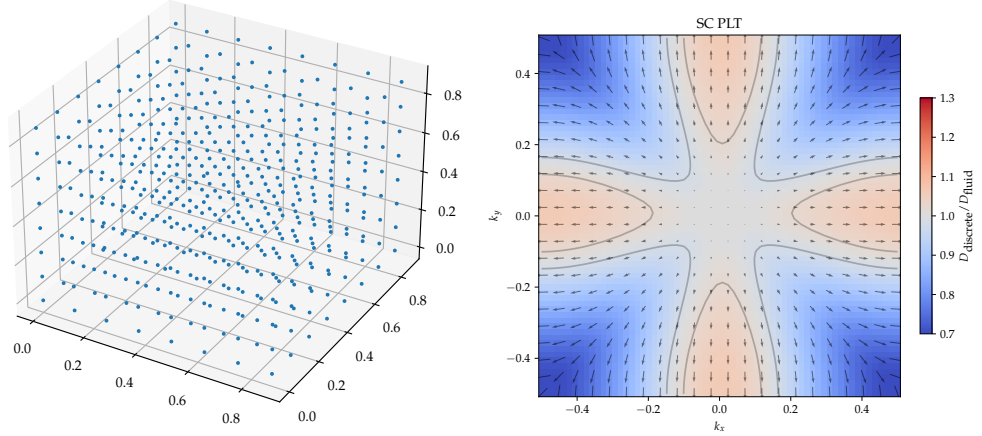


Figure 4.21: Discreteness error on the growth of cosmological perturbations. (*Left*): a simple cubic lattice (i.e. a regular grid) of 8^3 particles – an arrangement that is usually used for the unperturbed initial state of a cosmological simulation. (*Right*): For a simulation started from a simple cubic (SC) lattice PLT (particle linear theory) shows that growth of perturbations is faster along the Cartesian axes and slower along diagonals than in the continuous fluid limit. The contoured line indicates where deviations between growth in the fluid limit and for the particle system are below 2 per cent.

system has been developed in a series of papers (Joyce et al., 2005; Marcos et al., 2006; Marcos, 2008). The resulting [particle linear theory \(PLT\)](#) revealed that the growth of perturbations in discrete N -body universes significantly deviates from that in continuous fluid universes. In particular, what is a spatially independent growth factor $D_+(t)$ in the linear fluid perturbation theory, becomes an anisotropic function kernel $D_+(k, t)$ in PLT – see Figure 4.21. While the analysis was so far only carried out for N -body simulations that start from an initial equilibrium state described by a [Bravais lattice](#), the result is probably generic: modes close to the mean particle spacing are dominated by the particle distribution and do not grow consistently with perturbation theory. In the case of a [simple cubic lattice](#) (SC) – i.e. a regular grid – the interpretation is most clear: particles’ nearest neighbours (nearer than the mean particle separation) are along the Cartesian basis vectors and that is precisely where perturbations grow faster than in the [fluid limit](#), while they are further along space and planar diagonals (larger than the mean particle separation) and so they grow more slowly than in the fluid limit. This behavior is clearly visible in Figure 4.21. In that figure, a gray line indicates the region that deviates less than 2 per cent from the fluid growth – its isotropic part is limited to a region around the center – i.e. it involves averaging over multiple particles, as one might also intuitively expect. In principle this finding should imply that force softening (cf. above) should therefore involve a scale averaging over several particles. While an interesting and very relevant topic, we consider a more in depth discussion beyond the scope of the material presented here, since the question how to ‘get as close as possible to the fluid limit with as few particles as possible’ is one of the key directions in the development of new numerical techniques for large-scale cosmological simulations.

Initial conditions for cosmological N -body simulations

Initial conditions for cosmological N -body simulations can be generated by using the asymptotic solutions of the linear perturbation theory. The most common approach is to use the Zel'dovich approximation, which is a first-order Lagrangian perturbation theory. The Zel'dovich approximation is a simple and efficient way to generate initial conditions for cosmological N -body simulations. It is a good approximation for the large-scale structure of the Universe, but if higher accuracy is needed, one has to include second or even third order corrections.

Practically, one chooses a time a_i (well before shell-crossing) for which particle positions and velocities are computed using the perturbation theory. And then one can evolve the system using the N -body code.

Using Zel'dovich consistent integrators, it is possible to avoid the need for a separate initial condition generator. In practice however, it is difficult to fully control all discreteness errors.

Beyond N -body: tessellation and metric methods

By discretising simply mass, the N -body distribution function discards all information about the Lagrangian submanifold structure. Two approaches have been developed to circumvent this crucial limitation. We shall briefly discuss them next.

Metric methods

Evolution equations.

Let us consider general Hamiltonian mappings of phase space onto itself $(q, w) \mapsto (x, p)$ (but note that this definition is formally not valid as $a \rightarrow 0$ since in the canonical cosmological case the momentum space blows up). Before, we considered only the [Lagrangian submanifold](#) of full phase space, which is defined by $w = \nabla_q S(q)$ with some scalar function $S(q)$. The associated phase-space Jacobian matrix D , which reflects the effect in Eulerian space of infinitesimal changes to the Lagrangian coordinates, is

$$D := \frac{\partial(x, p)}{\partial(q, w)} = \begin{bmatrix} \frac{\partial x}{\partial q} & \frac{\partial x}{\partial w} \\ \frac{\partial p}{\partial q} & \frac{\partial p}{\partial w} \end{bmatrix}, \quad (4.101)$$

where the 6D tensor naturally splits into four blocks and the block $\partial x / \partial q$ corresponds to the Jacobian matrix of the Lagrangian map that we have considered before also in the context of LPT. The dynamics of D are fully determined by the canonical equations of motion Habib and Ryne (1995); Vogelsberger et al. (2008) and one finds, since e.g.

$$\begin{aligned} \frac{d}{dt} \frac{\partial x_i}{\partial q_j} &= \frac{\partial \dot{x}_i}{\partial q_j} = \frac{\partial^2 \mathcal{H}(x, p)}{\partial p_i \partial q_j} \\ &= \frac{\partial}{\partial p_i} \left(\frac{\partial \mathcal{H}}{\partial x_k} \frac{\partial x_k}{\partial q_j} + \frac{\partial \mathcal{H}}{\partial p_k} \frac{\partial p_k}{\partial q_j} \right) = \frac{\partial^2 \mathcal{H}}{\partial p_i \partial x_k} \frac{\partial x_k}{\partial q_j} + \frac{\partial^2 \mathcal{H}}{\partial p_i \partial p_k} \frac{\partial p_k}{\partial q_j} \end{aligned}$$

that the full evolution equation for D can be written as

$$\dot{D} = \frac{\partial(\dot{x}, \dot{p})}{\partial(q, w)} = \left(\begin{bmatrix} \nabla_x \otimes \nabla_p & \nabla_p \otimes \nabla_p \\ -\nabla_x \otimes \nabla_x & \nabla_p \otimes \nabla_x \end{bmatrix} \mathcal{H} \right) \cdot D =: H'' D. \quad (4.102)$$

This equation is called the “geodesic deviation equation” (GDE) in the literature and it quantifies the volume deformation in phase space along the Hamiltonian flow. For our cosmological Hamiltonian $\mathcal{H} = T(\mathbf{p}) + V(\mathbf{x}, a)$, the coupling matrix \mathbf{H}'' has an anti-diagonal form

$$\mathbf{H}'' = \begin{bmatrix} 0 & (\nabla_p \otimes \nabla_p)T \\ -(\nabla_x \otimes \nabla_x)V & 0 \end{bmatrix} = \begin{bmatrix} 0 & m^{-1}\delta_{ij} \\ -a^2\varphi_{,ij} & 0 \end{bmatrix}, \quad (4.103)$$

where the second equality holds for the *Hamiltonian in superconformal time*. This equation shows a coupling to the gravitational tidal tensor $\varphi_{,ij}$ Vogelsberger et al. (2008); Vogelsberger and White (2011) instead of the gravitational acceleration φ_i alone. Note also that the blocks with derivatives w.r.t. \mathbf{q} are decoupled from the two blocks with derivatives w.r.t. \mathbf{w} . The first describes the tangent space, the second is related to the normal space of the Lagrangian manifold. Multiplying out eq. (4.102) in this case, yields the explicit form

$$\begin{bmatrix} \frac{\partial \dot{x}_i}{\partial q_j} & \frac{\partial \dot{x}_i}{\partial w_j} \\ \frac{\partial \dot{p}_i}{\partial q_j} & \frac{\partial \dot{p}_i}{\partial w_j} \end{bmatrix} = \begin{bmatrix} m^{-1}\frac{\partial p_i}{\partial q_j} & m^{-1}\frac{\partial p_i}{\partial w_j} \\ -a^2\varphi_{,ik}\frac{\partial x_k}{\partial q_j} & -a^2\varphi_{,ik}\frac{\partial x_k}{\partial w_j} \end{bmatrix} \quad (4.104)$$

These equations can be rather easily integrated into our standard leapfrog integrator, all they require is a computation of the tidal field. In the one-dimensional case, the tidal field simply corresponds to the overdensity field, in multiple dimensions one has to explicitly compute the six components of $\frac{\partial_i \partial_j}{\nabla^2} \delta$, which is however easily achieved using Fourier methods.

The evolution of \mathbf{D} can be used to track the evolution of an infinitesimal environment in phase space around a trajectory $(\mathbf{x}(\mathbf{q}, \mathbf{w}; t), \mathbf{p}(\mathbf{q}, \mathbf{w}; t))$. In particular, as we already know, the zero-crossings of the determinant of the $\partial \mathbf{x} / \partial \mathbf{q}$ block correspond to caustics. Evolving $\partial \mathbf{x} / \partial \mathbf{q}$ therefore allows to estimate the local (single) stream density at each particle location and access to further statistics, such as counting the number of caustic crossings. Infinite density caustics would cause singular behaviour in the evolution of \mathbf{D} (singular kicks), so that its numerical evolution *has* to be carried out with sufficient softening Vogelsberger and White (2011); Stücker et al. (2020). Since it is sensitive to caustic crossings, the GDE can be used to quantify the distinct components of the cosmic web (Stücker et al. (2020), see also Section ??). The GDE has an intimate connection also to studies of the emergence of chaos in gravitationally collapsed structures since it quantifies the divergence of orbits in phase space and has an intimate connection to [Lyapunov exponents](#) Habib and Ryne (1995). Lyapunov exponents were introduced in the study of chaos in dynamical systems to quantify whether initially infinitesimally separated trajectories remain near each other or whether they exponentially diverge over time. The latter is the case in the case of chaotic systems (the famous butterfly effect), where $\delta \mathbf{x} \propto \exp(\lambda t) \delta \mathbf{x}_0$.

Initial conditions

Initial conditions for the tensor \mathbf{D} are readily obtained from Lagrangian perturbation theory. With the LPT expansion $\mathbf{x} = \mathbf{q} + \sum_{n=1}^{\infty} D_+^n \Psi^{(n)}(\mathbf{q})$, one finds in

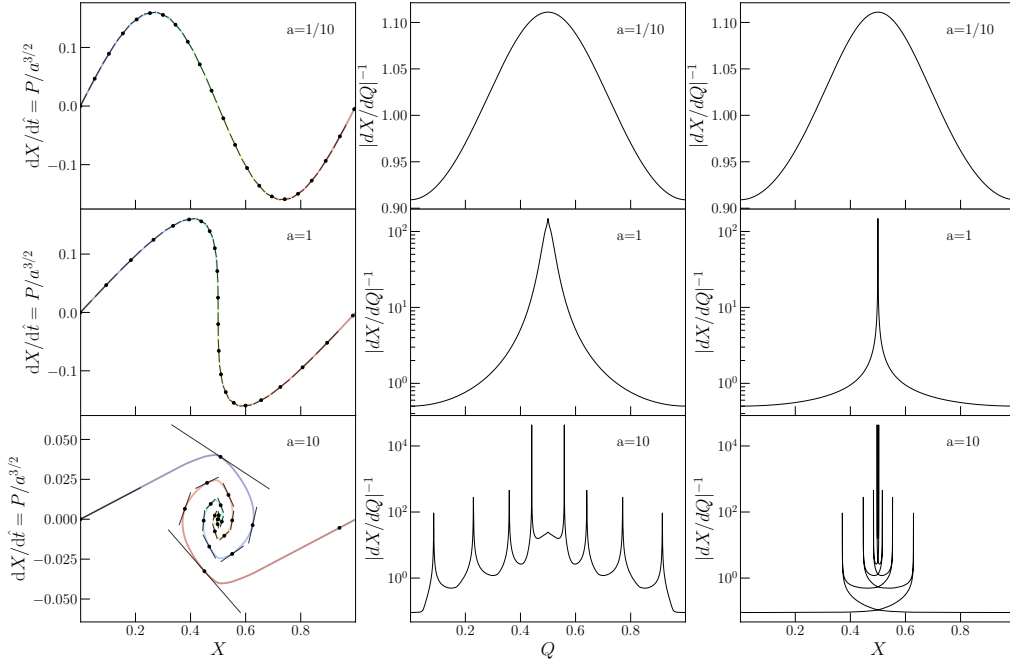


Figure 4.22: Evolution of the $\partial x / \partial q$ and $\partial p / \partial q$ tensors describing the tangent space to the cold distribution function. In the left panels, the tensors are shown as tangent lines for a subset of the N -body particles. The space-space part $\partial x / \partial q$ is the Jacobian matrix of the Lagrangian map and thus gives direct information about the density in the case of cold distribution functions. The middle panels plot this local particle density $|\det \partial x / \partial q|^{-1}$ as a function of the Lagrangian coordinate Q of the particles. The density is singular at caustic locations, i.e. where the determinant vanishes. In the right panels, this local particle density is shown as a function of the Eulerian coordinate. In this case it is evident that the Eulerian coordinates of the caustics coincide with a change in the number of streams. Both tensors and particle positions/momenta were evolved with a particle mesh method using 256 cells and 2048 particles in one dimension.

superconformal time

$$\frac{\partial x_i}{\partial q_j} = \delta_{ij} + \sum_{n=1}^{\infty} D_+^n \Psi_{ij}^{(n)} \quad (4.105a)$$

$$\frac{\partial p_i}{\partial q_j} = m \frac{dx_i}{dt} = m \frac{dD_+}{dt} \sum_{n=1}^{\infty} n D_+^{n-1} \Psi_{ij}^{(n)} \quad (4.105b)$$

Which fully specifies the “cold” (i.e. Lagrangian submanifold) part of the tensor D . and quantifies the tangent space to the Lagrangian manifold.

Evolution

The evolution of the $\partial x / \partial q$ part of D is shown in Figure 4.22. Tracking the evolution of the tangent space gives direct access to the (single stream) density at each particle location. It allows for the detection of shell-crossings. Whenever a particle passes through a caustic, one of the eigenvalues of $\partial x / \partial q$ flips its sign. These sign flips can be counted in order to obtain the number of caustic crossing

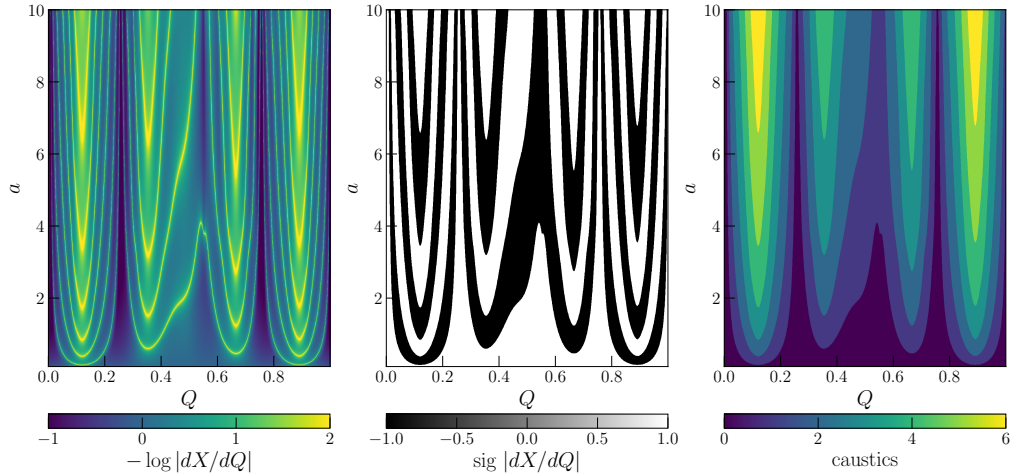


Figure 4.23: Evolution of the local particle density $|\partial X/\partial Q|^{-1}$ (left), the flip-flop field $\text{sig } \det \partial X / \partial Q$ (center) and the number of caustic crossing (right panel) as a function of time a and Lagrangian coordinate Q for the multi-wave perturbation from Figure 4.6. Caustics are associated with an infinite density and a sign flip of the determinant $\det \partial X / \partial Q$. The number of sign-flips experienced by each particle can be counted to yield the number of caustics a particle has crossed through. Note that this does not include passing through a caustic associated with other particles – excluding notably particles that are on first infall. Only when they turn around and begin [secondary infall](#) do they undergo a sign flip.

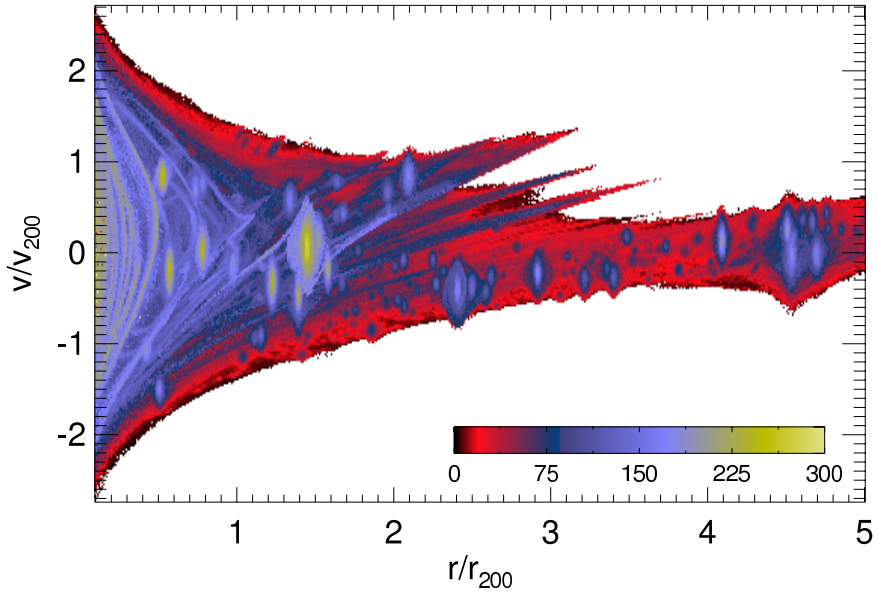


Figure 4.24: The caustic counts in a high-resolution three-dimensional simulation of a Milky-Way-like halo in radial phase space (i.e. the radial coordinate vs. the radial velocity component). [Subhalos](#) prominently show up as high caustic-count structures inside the main halo. While significantly more complex, the fundamental structure of a halo is quite similar to the lower-dimensional phase-space spirals. [Figure adapted from Vogelsberger and White (2011)]

that a particle has undergone. Both the flip-flop map and the number of caustic crossings is shown in Figure 4.23 for a one-dimensional simulation of multiple plane wave perturbations (the initial conditions used also in Fig. 4.6).

Tessellation methods

An alternative method first proposed by Abel et al. (2012); Shandarin et al. (2012) is similar in spirit to the metric methods, but fundamentally different in its construction. Rather than focusing on the particles, this approach treats them as vertices of a simplicial complex or n -dimensional triangulation. This yields a tessellated version of the Lagrangian manifold.

What do we mean by this? – Remember that the Lagrangian manifold (i.e. the sub-space of phase space occupied by the *cold* distribution function, is essentially really just $L_d \subset \mathbb{R}^d$). If we discretise L_d using particles (aka the N -body approximation), then we choose only discrete points $Q_i \in L_d$. Each particle being a point it is clear that they don't approximate L_d particularly well. A tessellation instead aims at covering all of L_d with simple d -dimensional shapes. In the simplest case, one can take the particles as vertices of the shapes providing such a tessellation and proceed as we describe next.

Tessellations

In one dimension, we have initially placed our N particles at discrete locations $Q_i = i \Delta Q$ with $\Delta Q = L_{\text{box}}/N$. The one-dimensional simplex is a line segment, and thus a one-dimensional tessellation is given by the set of line segments

$$\mathcal{T} = \left\{ \left(Q_i, Q_{(i+1) \bmod N} \right) \mid i = 0 \dots N-1 \right\}. \quad (4.106)$$

A standard simulation will of course give us also $X_i(t) = X(Q_i, t)$ and $P_i(t) = P(Q_i, t)$, which are the usual positions and momenta of N -body particles, but now promoted to vertices that determine the location of the segment (i.e. the simplex) in phase space. Consider now the fundamental matrix

$$A_i := \Delta Q^{-1} \begin{bmatrix} 1 & 1 \\ X_i & X_{i+1} \end{bmatrix} =: \Delta Q^{-1} J_i \quad (4.107)$$

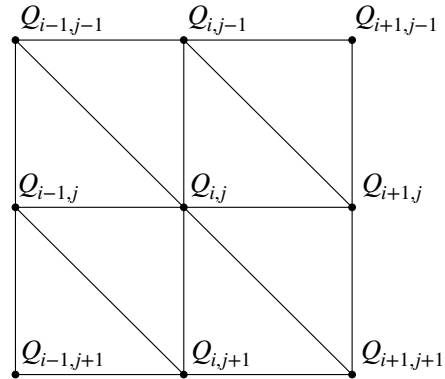
which allows us to approximate

$$\det \frac{\partial X}{\partial Q} \approx \det A_i \quad \text{for } Q_i < Q < Q_{i+1}. \quad (4.108)$$

It is quite obvious that this is just the first order accurate 'finite difference' approximation

$$\frac{\partial X}{\partial Q} \approx \frac{X_{i+1} - X_i}{Q_{i+1} - Q_i} + \text{h.o.t.} \quad (4.109)$$

This can be readily upgraded to higher dimensions. In 2+2D, Lagrangian space L_2 is two-dimensional and we can cover it for example with the two-dimensional simplices, which are triangles. This can be achieved as follows (but note that this choice introduces a global anisotropy and this choice is not unique):



Instead of line segments (Q_i, Q_{i+1}) , we obtain two triangles so that we can write the full tessellation as (be careful to orient vertices in a mathematically positive sense)

$$\mathcal{T} = \{(Q_{i,j}, Q_{i,j+1}, Q_{i+1,j+1}), (Q_{i,j}, Q_{i+1,j+1}, Q_{i+1,j}) \mid i, j = 0 \dots N-1\}. \quad (4.110)$$

\mathcal{T} tessellates the Lagrangian submanifold since we know the position $\mathbf{X}(Q_{i,j})$ and momentum $\mathbf{P}(Q_{i,j})$ vectors at every vertex $Q_{i,j}$. Let $(X, Y)_{0,1,2}^{(i)}$ be the x and y -coordinates of the three vertices of triangle $T_i \in \mathcal{T}$. Then we can define the fundamental matrix

$$\mathbf{A}_i := \frac{1}{2} \Delta Q^{-2} \begin{bmatrix} 1 & 1 & 1 \\ X_0^{(i)} & X_1^{(i)} & X_2^{(i)} \\ Y_0^{(i)} & Y_1^{(i)} & Y_2^{(i)} \end{bmatrix} =: \frac{1}{2} \Delta Q^{-2} \mathbf{J}_i \quad (4.111)$$

with

$$\det \frac{\partial \mathbf{X}}{\partial \mathbf{Q}} \approx \det \mathbf{A}_i \quad \text{for } \mathbf{Q} \in T_i. \quad (4.112)$$

This is the signed area of the triangle. Shell-crossing on the tessellation now corresponds to an area inversion of a triangle. The local particle density is then given by

$$\rho_i \approx \bar{\rho} |\det \mathbf{A}_i|^{-1}. \quad (4.113)$$

The construction for $3 + 3$ (or more) dimensions proceeds analogously.

Tessellations as an analysis tool

In Figure 4.25, we show the deformation of the two-dimensional tessellation under the Zeldovich map for an initial perturbation of the form $\phi^{\text{ini}} \propto \cos q_x + \cos q_y$ (left panels) along with the shape of the tessellated submanifold in a three-dimension cut of four-dimensional phase space, with the z -coordinate representing the x -velocity (top right) and the y -velocity (bottom right). Once shell-crossing occurs, also multi-streaming will occur, which means that multiple triangles will overlap any given point. Due to the preservation of connectivity in phase space, this will always be an odd number of triangles at any interior point (i.e. point that does not

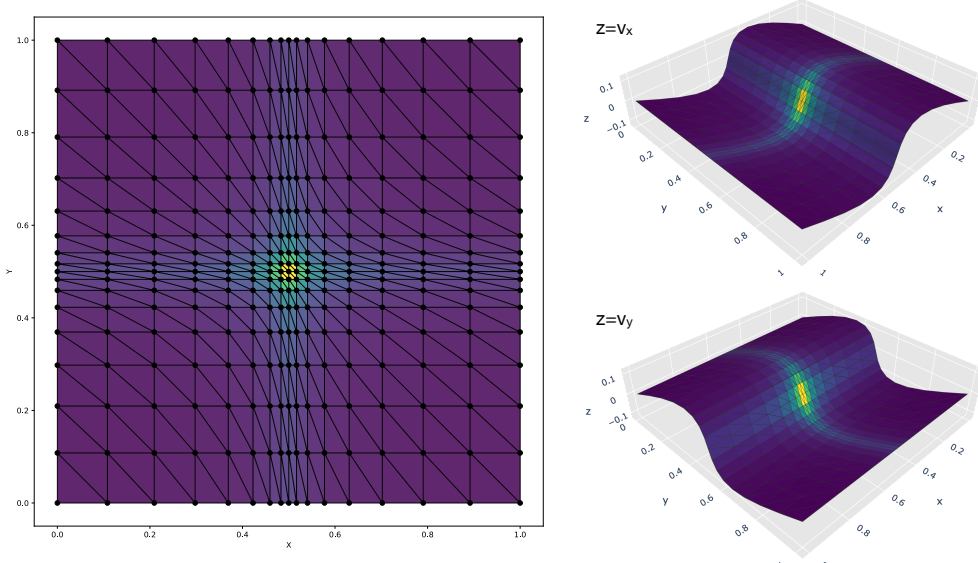


Figure 4.25: Left: Cosmic density field from a tessellation projected to configuration space. The Jacobian determinant equals the area of the projected triangle. The resulting density field is defined everywhere in space. Right: phase space projections. In 2+2D, the Lagrangian manifold occupies a two-dimensional surface embedded in four-dimensional space. The triangles provide a tessellation of this surface. In 3+3D the Lagrangian submanifold is three-dimensional and can be covered with tetrahedra (the simplices of 3D space) that occupy a 3D subvolume of 6D phase space. When multi-streaming occurs, several simplices may overlap a given point in Eulerian space. In this case, the properties of the various simplices need to be appropriately combined. The total density, e.g., is the sum of individual densities of all simplices overlapping a given point.

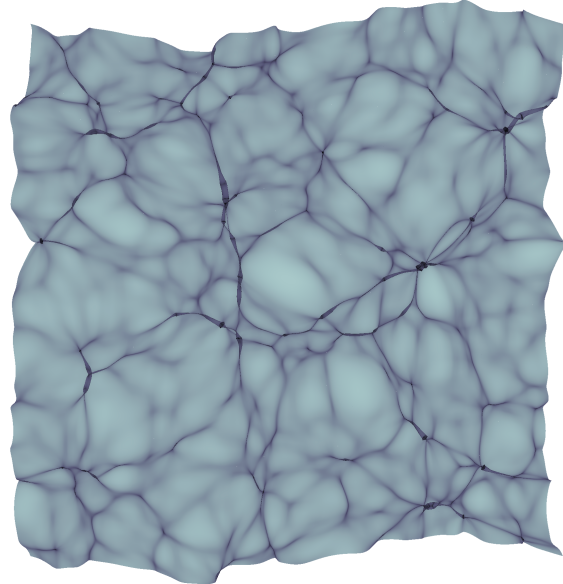


Figure 4.26: The density field obtained by projecting a two-dimensional tessellation and summing the densities of overlapping triangles at any given point. Periodic boundary conditions are applied in the computation but not in the rendering, so that one sees the distortion of the originally square shaped piece of Lagrangian space.

lie exactly on the edge of any of the triangles). In this case, the densities of all triangles overlapping the given Eulerian point need to be co-added, i.e. we have to find all simplices $\mathcal{S}(\mathbf{x})$ that contain a given Eulerian coordinate \mathbf{x} and then sum the individual ‘stream’ densities

$$\rho(\mathbf{x}) = \sum_{i, T_i \in \mathcal{S}(\mathbf{x})} \rho_i. \quad (4.114)$$

Since we know the density associated with each simplex, we can also linearly interpolate coordinates and momenta on each simplex. This is most easily achieved in [barocentric coordinates](#) ζ . They can be defined on a simplex in n -dimensions through the map

$$\zeta \mapsto \mathbf{x} : (1, \mathbf{x})^T = J \cdot \zeta, \quad (4.115)$$

where J is a $(n+1) \times (n+1)$ matrix constructed on the simplex as above, ζ is a $(n+1)$ -dimensional vector with

$$\sum_{k=0 \dots n} \zeta_k = 1, \quad (4.116)$$

a property that is easily verified. Any quantity F_k known at the $(n+1)$ -vertices of simplex i can then be linearly interpolated to any point \mathbf{x} using the interpolation formula on simplex i

$$\hat{F}_i(\mathbf{x}) = \sum_{k=0 \dots n} F_k \zeta_k \quad \text{with} \quad \zeta = J_i^{-1} \cdot (1, \mathbf{x})^T. \quad (4.117)$$

This allows us now to compute a whole lot of additional statistics that is not easily accessible from the particle data otherwise. E.g. the mean velocity field can be computed as

$$\langle \mathbf{v} \rangle(\mathbf{x}) = \frac{1}{m_N} \frac{\sum_{i, T_i \in \mathcal{S}(\mathbf{x})} \rho_i \hat{P}_i(\mathbf{x})}{\sum_{i, T_i \in \mathcal{S}(\mathbf{x})} \rho_i}, \quad (4.118)$$

i.e. averages are computed simply as weighted averages, with weights coming from the individual stream densities. This allows to evaluate accurately the mean velocity field also in between particles, both in single and multi-stream regions. The result of such a mean velocity field from a tessellation is shown in Figure 4.27.

Analysis of N -body simulations

Now that we know how to run an N -body simulation, we not only want to create visualisation, but we also want to use it to make statistical measurements.

Measuring the density field

The empirical [density field](#) is simply given by the projection of the [N-body distribution function](#). We already had in (4.24) that

$$\hat{n}_N(\mathbf{x}, t) := \int_{\mathbb{R}^d} d^d v f_N(\mathbf{x}, \mathbf{v}, t) = \frac{1}{N} \sum_{i=1}^N \delta_D(\mathbf{x} - \mathbf{X}_i(t)) \quad (4.119)$$

and therefore

$$\hat{\delta}_N(\mathbf{x}, t) := \hat{n}_N(\mathbf{x}, t) - 1. \quad (4.120)$$

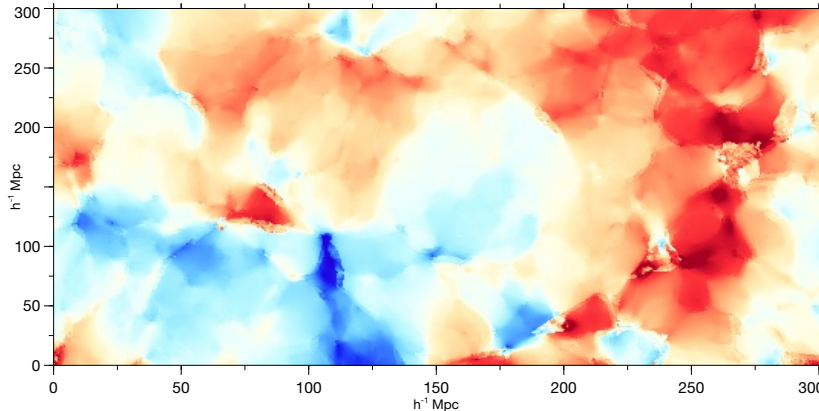


Figure 4.27: Velocity field obtained using the phase space tessellation method. Shown is the y -component from a 3D simulation: red corresponds to positive, mymiddleblue to negative velocities. The method gives a velocity field that is defined everywhere in Eulerian space, even where very few particles reside. In multi-stream regions, one computes the multi-stream average weighted by the individual contributing stream densities. [Adapted from Hahn et al. (2015)]

Point-based estimators The problem is that this estimator is not practical as it is zero almost everywhere, while the true density δ clearly is not. As for the force softening, it is therefore preferable to compute a kernel smoothed version

$$\hat{\delta}_K(\mathbf{x}) := (\hat{\delta}_N * K)(\mathbf{x}) = \frac{1}{Nh} \sum_{i=1}^N K\left(\|\mathbf{x} - \mathbf{X}_i\|/h\right) - 1 \quad (4.121)$$

which can be evaluated for N_g query points with algorithmic complexity $\mathcal{O}(N_g N)$. The **kernel bandwidth** h should be chosen so that sufficiently many particles contribute to the ‘measurement’. Having too few contribute increases the variance of the measurement error, having too many increases the bias. Since the point can be very non-uniformly distributed, it might even be preferable to use **adaptive softening**, where the bandwidth is varied at a particle by particle level, i.e. by setting

$$\hat{\delta}_{K,\text{adaptive}}(\mathbf{x}) := \frac{1}{N} \sum_{i=1}^N h_i^{-1} K\left(\|\mathbf{x} - \mathbf{X}_i\|/h_i\right) - 1 \quad (4.122)$$

and where h_i is estimated by computing a density estimate at the particle location using the constant bandwidth estimator first, or by setting h_i to the distance to the m -th neighbour, which then guarantees that always m particles are contained within h_i when evaluating at the particle locations.

Estimating one-point statistics The one-point statistics of the density field can then be recovered by evaluating one of the estimators above for a large set of random points $\mathbf{y}_{1,\dots,M}$ that are drawn from a Poisson process (i.e. each coordinate of \mathbf{y}_j is uniformly distributed in $[0, 1]$). In particular, with

$$\hat{\delta}_j := \hat{\delta}_K(\mathbf{y}_j) \quad (4.123)$$

we can compute also estimators for the moments and cumulants of the density fields as

$$\hat{c}_1 := \frac{1}{M} \sum_{j=1}^M \hat{\delta}_j = 0 \quad \text{by construction} \quad (4.124)$$

$$\hat{c}_2 := \frac{1}{M} \sum_{j=1}^M \hat{\delta}_j^2 \quad \hat{c}_3 := \frac{1}{M} \sum_{j=1}^M \hat{\delta}_j^3 \quad \hat{c}_4 := \frac{1}{M} \sum_{j=1}^M \hat{\delta}_j^4 - \hat{c}_2^2 \quad (4.125)$$

⋮

Grid-based estimators Instead of explicitly evaluating the kernels at a large number of locations M which consists of $\mathcal{O}(MN)$ operations, it is usually preferable (also a starting point for other statistics such as power spectra below) to estimate the density on the grid using one of the grid interpolation kernels as in (4.70)

$$\hat{\delta}[\mathbf{m}] = \frac{1}{N} \sum_{i=1}^N W(\mathbf{m} - \mathbf{X}_i/h \mid h) - 1 \quad (4.126)$$

where now $h = 1/n_g$ is the linear grid cell spacing and W is one of the particle interpolation kernels (4.68), e.g. the CIC kernel, just as when computing the source term for the Poisson equation in the PM/PIC method. In order to compute a filtered density, one can then apply another filter to the gridded density, i.e. by computing

$$\hat{\delta}_K[\mathbf{m}] = (\hat{\delta} \circledast K)[\mathbf{m}] \quad (4.127)$$

where \circledast is the discrete cyclic convolution that can be efficiently executed using the FFT. It is important to note that the grid assignment kernel W also acts as an additional filter. If this intrinsic filtering is undesired, it is possible to deconvolve with the grid assignment kernel, which is most easily performed in Fourier space by computing

$$\tilde{\delta}^{\text{dec}}[\mathbf{k}] := \begin{cases} \frac{\tilde{\delta}[\mathbf{k}]}{\tilde{W}[\mathbf{k}]} & \text{if } |\mathbf{k}_{1,\dots,d}| < \pi \\ 0 & \text{if } |\mathbf{k}_{1,\dots,d}| = \pi \end{cases} \quad (4.128)$$

where $\tilde{W}[\mathbf{k}]$ is the Fourier transform of the assignment kernel from (4.71).

Measuring power spectra and correlation functions

In order to relate our simulation results to the two-point statistics we had discussed earlier, we should find a way to compute e.g. power spectra for our simulations. In fact, given the density field above, we can directly compute the power in each mode to be

$$\hat{P}_d[\mathbf{k}] = \frac{1}{(2\pi)^d} |\tilde{\delta}[\mathbf{k}]|^2 \quad (4.129)$$

and over many realisations of our simulations we should recover the true power spectrum in the sense that the expectation value is the isotropic power spectrum

$$P(k) = \mathbb{E}[\hat{P}_d[\mathbf{k}]] \quad \forall \mathbf{k} = k. \quad (4.130)$$

It is of course not practical to average over many realisations of each mode to estimate the power spectrum. For this reason it is common practice to use an estimator where we replace the ensemble average with an average over modes. Let

$$\mathcal{M}(k_1, k_2) := \{k \mid k_1 \leq \|k\| < k_2\} \quad (4.131)$$

be the set of modes with a norm between k_1 and k_2 , then set

$$\hat{P}(k) := \langle \hat{P}_d[k] \rangle_{\mathcal{M}(k_1, k_2)} = \frac{1}{|\mathcal{M}(k_1, k_2)|} \sum_{k \in \mathcal{M}(k_1, k_2)} \hat{P}_d[k] \quad (4.132)$$

as the arithmetic mean of the amplitudes of modes in this range, and also k is chosen to coincide with the mean of modes in \mathcal{M} in the sense that

$$k \stackrel{!}{=} \langle \|k\| \rangle_{\mathcal{M}(k_1, k_2)} = \frac{1}{|\mathcal{M}(k_1, k_2)|} \sum_{k \in \mathcal{M}(k_1, k_2)} \|k\|. \quad (4.133)$$

If the data is given in terms of particles, one can directly compute the power spectrum from the particle data directly using the non-uniform FFT, as we have discussed earlier.

```

1 import finufft
2 import numpy as np
3
4 def compute_powerspectrum_3dnufft( X, Y, Z, Ng, eps=1e-3 ):
5     """Compute the isotropic power spectrum of a 3d point set using NUFFT
6     Parameters:
7         X,Y,Z (array)      : 1D arrays of particle positions in [0,1)
8         Ng (int)           : number of grid points along one dimension
9         eps (float)         : NUFFT tolerance parameter
10    Returns:
11        array              : k values
12        array              : power spectrum P(k) = 1/(2 pi)^3 /delta_k|^2
13    """
14
15    # set up weights for NUFFT = 1/N
16    w = np.ones_like( X, dtype=np.complex128)/len(X)
17
18    # compute the 3D NUFFT non-uniform to uniform (type 1)
19    f = finufft.nufft3d1(X * 2*np.pi, Y* 2*np.pi, Z * 2*np.pi, w, Ng, eps=eps)
20
21    # set up wave numbers (this is the same code as in the GRF generation)
22    k = (np.arange(Ng)-Ng//2) * 2 * np.pi
23    kmod = np.sqrt( k[:,None,None]**2 + k[None,:,None]**2 + k[None,None,:]**2 )
24
25    # compute the power spectrum P(k) = 1/(2 pi)**3 /delta_k|**2
26    P = np.abs( f )**2 / (2*np.pi)**3
27
28    ## compute isotropic average, to do this we average over shells in
29    ## k-space, i.e. P_iso(k) = <P(m)>_ / |m|=k, where <.> denotes
30    ## average over k-space shells, i.e. k < |m| < k+dk
31    # set up the shell radii
32    kmodes = np.linspace(2*np.pi,np.pi*Ng,num=Ng//2)
33    # determine which shell each mode is in
34    ibin = np.digitize(kmod.flat,kmodes)
35    # compute average power in each shell
36    Pavg = np.bincount(ibin,weights=P.flat)[1:-1]/np.bincount(ibin)[1:-1]
37    # get the k value at the centre of each shell
38    kmid = 0.5*(kmodes[1:]+kmodes[:-1])
39
40    return kmid, Pavg

```

Measuring the abundance of collapsed structures

Extracting gravitationally bound structures from N-body simulations One of the most important tasks in the post-processing of cosmological simulations is the identification of gravitationally bound structures: the haloes. The existence of a local minimum of the gravitational potential is a necessary condition for the existence of a bound structure. A local minimum of the potential however corresponds also to local maximum of the matter density field. Thus, most halo finders focus on determining the region of gravitational boundness around a density maximum. Many methods exist, below the most commonly used for isolated haloes are explained, and we discuss a few existing software packages after. Calculations using the model spherical collapse of a single top hat perturbation in EdS cosmology indicate that regions that are in virial equilibrium should have an overdensity ρ_{vir} of

$$\rho_{\text{vir}} = \Delta_{\text{vir}} \rho_c \quad \text{with} \quad \Delta_{\text{vir}} = 18\pi^2 \simeq 178 \quad (4.134)$$

where ρ_c is the critical density of the universe.

The Friends-of-Friends (FoF) Algorithm Davis et al. (1985) introduced the so-called [friends-of-friends \(FOF\)](#) algorithm that is particularly suited for N-body simulations. The algorithm builds equivalence classes among all particle pairs in the N-body simulation whose distance falls below a given threshold. The resulting equivalence classes thus comprise regions bounded by an isodensity surface. It is common practice to relate the distance threshold to the mean inter-particle distance b and adopt a value of $b = 0.2$. This choice can be roughly motivated by considering the density of an isothermal sphere at the virial radius. Expressed in units of the mean inter-particle separation, $b \sim (\Delta_{\text{vir}}/3)^{-1/3} \approx 0.25$ in this case. One main problem of the friends-of-friends algorithm is that it tends to spuriously connect nearby haloes that are linked by a bridge which may purely be a result of the stochastic nature of N-body simulations. This problem is most severe in regions of high environmental density.

However, friends-of-friends haloes are not constrained in their shape by the algorithm and mass functions obtained with this algorithm show a nearly universal behaviour across redshift.

The Spherical Overdensity (SO) Algorithm The second most commonly employed halo finding method is the spherical overdensity algorithm introduced by Lacey & Cole (1994). Here, particles are ranked according to their local density. Then a sphere is grown around the first particle until the mean density within that sphere falls below the virial overdensity, i.e. the virial radius R_{vir} is defined as $M_{\text{vir}} = M(< R_{\text{vir}})$ (where $M(< r)$ is the mass enclosed in a sphere of radius r) so that

$$\frac{M(< R_{\text{vir}})}{\frac{4\pi}{3} R_{\text{vir}}^3} = \Delta_{\text{vir}} \rho_c. \quad (4.135)$$

All particles within the sphere make up the first halo and are removed from the list of density ranked particles. The procedure is then repeated with the next highest density particle left in the list and stopped, when no more groups are found that contain a given minimum number of particles. The resulting haloes do not suffer from spurious linking of distinct haloes. They are however spherical by

definition which might not reflect the true shape of the gravitationally bound volume. A further advantage of the spherical overdensity method is that it can be readily used also in hydrodynamic simulations where particles and mesh cells come with basically arbitrary masses so that the simple friends-of-friends algorithm cannot be applied with a fixed distance threshold. Instead of ranking particles by their density, any method to identify peaks of the density field is sufficient to serve as the starting point before growing spheres around the peaks.

For simplicity, often 200 is used instead of 178 and haloes that are defined using this overdensity criterion are often denoted with an index $200c$, so that the usual mass definition for a halo is M_{200c} . In the sub-field of cosmology that uses galaxy clusters as cosmological probes, usually a higher density threshold of $500c$ is used that better correlates with the hot X-ray emitting region of the cluster halo. Sometimes also the mean density is used instead of the critical density so that $200m$ refers to $\rho_{\text{vir}} = 200\rho_m = 200\Omega_m\rho_c$. In the presence of a cosmological constant, in principle the overdensity criterion becomes time dependent and a convenient parameterisation has been given by Bryan & Norman Bryan and Norman (1998) as

$$\Delta_{\text{vir}}(a) = 18\pi^2 + 82x - 39x^2, \quad \text{with} \quad x := \frac{\Omega_m a^{-3}}{\Omega_m a^{-3} + \Omega_\Lambda} - 1. \quad (4.136)$$

Bibliography

Tom Abel, Oliver Hahn, and Ralf Kaehler. Tracing the dark matter sheet in phase space. *MNRAS*, 427(1):61–76, November 2012. doi: [10.1111/j.1365-2966.2012.21754.x](https://doi.org/10.1111/j.1365-2966.2012.21754.x).

R.J. Adler and J.E. Taylor. *Random Fields and Geometry*. Springer Monographs in Mathematics. Springer New York, 2009. ISBN 9780387481166. URL <https://books.google.at/books?id=R5BGvQ3ejloC>.

Robert J. Adler. *The Geometry of Random Fields (Probability & Mathematical Statistics S.)*. John Wiley & Sons Inc, June 1981. ISBN 0471278440.

A. W. Appel. An Efficient Program for Many-Body Simulation. *SIAM Journal on Scientific and Statistical Computing*, 6(1):85–103, January 1985.

Josh Barnes and Piet Hut. A hierarchical O(N log N) force-calculation algorithm. *Nature*, 324(6096):446–449, December 1986. doi: [10.1038/324446ao](https://doi.org/10.1038/324446ao).

Joshua E. Barnes. Gravitational softening as a smoothing operation. *MNRAS*, 425(2):1104–1120, September 2012. doi: [10.1111/j.1365-2966.2012.21462.x](https://doi.org/10.1111/j.1365-2966.2012.21462.x) [10.48550/arXiv.1205.2729](https://arxiv.org/abs/1205.2729).

A. H. Barnett. Aliasing error of the $\exp(\beta\sqrt{1-z^2})$ kernel in the nonuniform fast Fourier transform. *arXiv e-prints*, art. arXiv:2001.09405, January 2020. doi: [10.48550/arXiv.2001.09405](https://doi.org/10.48550/arXiv.2001.09405).

Alexander H. Barnett, Jeremy Magland, and Ludvig af Klinteberg. A Parallel Nonuniform Fast Fourier Transform Library Based on an “Exponential of Semicircle” Kernel. *SIAM Journal on Scientific Computing*, 41(5):C479–C504, January 2019. doi: [10.1137/18M120885X](https://doi.org/10.1137/18M120885X).

M. Berger. *A Panoramic View of Riemannian Geometry*. Springer Berlin Heidelberg, 2007. ISBN 9783540653172.

F. Bernardeau, S. Colombi, E. Gaztañaga, and R. Scoccimarro. Large-scale structure of the Universe and cosmological perturbation theory. *Phys. Rep.*, 367:1–3, 2002.

G. L. Bryan and M. L. Norman. Statistical Properties of X-Ray Clusters: Analytic and Numerical Comparisons. *ApJ*, 495:80–99, March 1998. doi: [10.1086/305262](https://doi.org/10.1086/305262).

Thomas Buchert. Lagrangian theory of gravitational instability of Friedman-Lemaitre cosmologies and the ‘Zel’dovich approximation’. *MNRAS*, 254:729–737, February 1992. doi: [10.1093/mnras/254.4.729](https://doi.org/10.1093/mnras/254.4.729).

Jordan Carlson, Beth Reid, and Martin White. Convolution Lagrangian perturbation theory for biased tracers. *MNRAS*, 429:1674, 2013. doi: [10.1093/mnras/sts457](https://doi.org/10.1093/mnras/sts457).

- J. J. M. Carrasco, M. P. Hertzberg, and L. Senatore. The effective field theory of cosmological large scale structures. *JHEP*, 9:82, 2012. doi: [10.1007/JHEP09\(2012\)082](https://doi.org/10.1007/JHEP09(2012)082).
- M. Davis, G. Efstathiou, C. S. Frenk, and S. D. M. White. The evolution of large-scale structure in a universe dominated by cold dark matter. *ApJ*, 292: 371–394, May 1985. doi: [10.1086/163168](https://doi.org/10.1086/163168).
- W. Dehnen and J. I. Read. N-body simulations of gravitational dynamics. *European Physical Journal Plus*, 126:55, May 2011. doi: [10.1140/epjp/i2011-11055-3](https://doi.org/10.1140/epjp/i2011-11055-3).
- Walter Dehnen. Towards optimal softening in three-dimensional N-body codes - I. Minimizing the force error. *MNRAS*, 324(2):273–291, June 2001. doi: [10.1046/j.1365-8711.2001.04237.x](https://doi.org/10.1046/j.1365-8711.2001.04237.x) arXiv:astro-ph/0011568.
- Walter Dehnen. A Hierarchical $\mathcal{O}(N^{\log_2 \epsilon})$ Force Calculation Algorithm. *Journal of Computational Physics*, 179(1):27–42, June 2002. doi: [10.1006/jcph.2002.7026](https://doi.org/10.1006/jcph.2002.7026).
- Marek Demianski, Zdzislaw A. Golda, and Andrzej Woszczyna. Evolution of density perturbations in a realistic universe. *Gen. Rel. Grav.*, 37:2063–2082, 2005. doi: [10.1007/s10714-005-0180-2](https://doi.org/10.1007/s10714-005-0180-2).
- A. G. Doroshkevich. The space structure of perturbations and the origin of rotation of galaxies in the theory of fluctuation. *Astrofizika*, 6:581–600, January 1970.
- Jurgen Ehlers and Thomas Buchert. Newtonian cosmology in Lagrangian formulation: Foundations and perturbation theory. *Gen. Rel. Grav.*, 29:733–764, 1997. doi: [10.1023/A:1018885922682](https://doi.org/10.1023/A:1018885922682).
- A. Friedmann. Über die Krümmung des Raumes. *Zeitschrift für Physik*, 10:377–386, 1922. doi: [10.1007/BF01332580](https://doi.org/10.1007/BF01332580).
- Lehman Garrison. *Computational Modeling of Large-Scale Structure With Abacus*. PhD thesis, Harvard U. (main), 2019.
- M. H. Goroff, Benjamin Grinstein, S. J. Rey, and Mark B. Wise. Coupling of Modes of Cosmological Mass Density Fluctuations. *Astrophys. J.*, 311:6–14, 1986. doi: [10.1086/164749](https://doi.org/10.1086/164749).
- L. Greengard and V. Rokhlin. A Fast Algorithm for Particle Simulations. *Journal of Computational Physics*, 73(2):325–348, December 1987. doi: [10.1016/0021-9991\(87\)90140-9](https://doi.org/10.1016/0021-9991(87)90140-9).
- Salman Habib and Robert D. Ryne. Symplectic Calculation of Lyapunov Exponents. *Phys. Rev. Lett.*, 74(1):70–73, January 1995. doi: [10.1103/PhysRevLett.74.70](https://doi.org/10.1103/PhysRevLett.74.70).
- O. Hahn, R. E. Angulo, and T. Abel. The properties of cosmic velocity fields. *MNRAS*, 454:3920–3937, December 2015. doi: [10.1093/mnras/stv2179](https://doi.org/10.1093/mnras/stv2179).
- R. W. Hockney and J. W. Eastwood. *Computer Simulation Using Particles*. Computer Simulation Using Particles, New York: McGraw-Hill, 1981, 1981.
- E. Hubble. A Relation between Distance and Radial Velocity among Extra-Galactic Nebulae. *Proceedings of the National Academy of Science*, 15:168–173, 1929. doi: [10.1073/pnas.15.3.168](https://doi.org/10.1073/pnas.15.3.168).

- J. H. Jeans. The Stability of a Spherical Nebula. *Philosophical Transactions of the Royal Society of London Series A*, 199:1–53, 1902. doi: [10.1098/rsta.1902.0012](https://doi.org/10.1098/rsta.1902.0012).
- M. Joyce, B. Marcos, A. Gabrielli, T. Baertschiger, and F. Sylos Labini. Gravitational Evolution of a Perturbed Lattice and its Fluid Limit. *Phys. Rev. Lett.*, 95(1):011304, June 2005. doi: [10.1103/PhysRevLett.95.011304](https://doi.org/10.1103/PhysRevLett.95.011304).
- M. Kac. On the average number of real roots of a random algebraic equation. *Bulletin of the American Mathematical Society*, 49(4):314 – 320, 1943. doi: [bams/1183505112](https://doi.org/10.1090/S0002-9904-1943-0118350-5). URL <https://doi.org/>.
- Michael K.-H. Kiessling. The “jeans swindle”: A true story—mathematically speaking. *Advances in Applied Mathematics*, 31(1):132–149, 2003. ISSN 0196-8858. doi: [https://doi.org/10.1016/S0196-8858\(02\)00556-0](https://doi.org/10.1016/S0196-8858(02)00556-0). URL <https://www.sciencedirect.com/science/article/pii/S0196885802005560>.
- Yu.L. Klimontovich. *The Statistical Theory of Non-equilibrium Processes in a Plasma*. M.I.T. Press, 1967.
- J. Kurzak and B. M. Pettitt. Fast multipole methods for particle dynamics. *Molecular Simulation*, 32(10-11):775–790, 2006. doi: [10.1080/08927020600991161](https://doi.org/10.1080/08927020600991161). PMID: 19194526. URL <https://doi.org/10.1080/08927020600991161>.
- C. Lacey and S. Cole. Merger Rates in Hierarchical Models of Galaxy Formation - Part Two - Comparison with N-Body Simulations. *MNRAS*, 271:676, 1994. doi: [10.1093/mnras/271.3.676](https://doi.org/10.1093/mnras/271.3.676).
- Ofer Lahav and Yasushi Suto. Measuring our universe from galaxy redshift surveys. *Living Reviews in Relativity*, 7(1):8, 2004. doi: [10.12942/lrr-2004-8](https://doi.org/10.12942/lrr-2004-8). URL <https://doi.org/10.12942/lrr-2004-8>.
- G. Lemaître. Un Univers homogène de masse constante et de rayon croissant rendant compte de la vitesse radiale des nébuleuses extra-galactiques. *Annales de la Société Scientifique de Bruxelles*, 47:49–59, 1927.
- Matthew Lewandowski, Ashley Perko, and Leonardo Senatore. Analytic Prediction of Baryonic Effects from the EFT of Large Scale Structures. *JCAP*, 05:019, 2015. doi: [10.1088/1475-7516/2015/05/019](https://doi.org/10.1088/1475-7516/2015/05/019).
- Giacomo Livan, Marcel Novaes, and Pierpaolo Vivo. Introduction to Random Matrices - Theory and Practice. *arXiv e-prints*, art. arXiv:1712.07903, December 2017.
- S.-K. Ma. *Statistical Mechanics*. World Scientific Singapore, 1985. ISBN 9971966077. doi: [10.1142/0073](https://doi.org/10.1142/0073).
- J. Marcinkiewicz. Sur une propriété de la loi de gauß. *Mathematische Zeitschrift*, 44(1):612–618, 1939. doi: [10.1007/BF01210677](https://doi.org/10.1007/BF01210677). URL <https://doi.org/10.1007/BF01210677>.
- B. Marcos. Vlasov limit and discreteness effects in cosmological N-body simulations. *Communications in Nonlinear Science and Numerical Simulations*, 13:119–124, February 2008. doi: [10.1016/j.cnsns.2007.03.026](https://doi.org/10.1016/j.cnsns.2007.03.026).

- B. Marcos, T. Baertschiger, M. Joyce, A. Gabrielli, and F. Sylos Labini. Linear perturbative theory of the discrete cosmological N-body problem. *Phys. Rev. D*, 73(10):103507, May 2006. doi: [10.1103/PhysRevD.73.103507](https://doi.org/10.1103/PhysRevD.73.103507).
- Takahiko Matsubara. Resumming Cosmological Perturbations via the Lagrangian Picture: One-loop Results in Real Space and in Redshift Space. *Phys. Rev.*, D77:063530, 2008. doi: [10.1103/PhysRevD.77.063530](https://doi.org/10.1103/PhysRevD.77.063530).
- Matthew McQuinn and Martin White. Cosmological perturbation theory in 1+1 dimensions. *J. Cosmology Astropart. Phys.*, 2016(1):043–043, January 2016. doi: [10.1088/1475-7516/2016/01/043](https://doi.org/10.1088/1475-7516/2016/01/043).
- Michaël Michaux, Oliver Hahn, Cornelius Rampf, and Raul E. Angulo. Accurate initial conditions for cosmological N-body simulations: minimizing truncation and discreteness errors. *MNRAS*, 500(1):663–683, 2021. doi: [10.1093/mnras/staa3149](https://doi.org/10.1093/mnras/staa3149).
- Takahiro Nishimichi, Guido D’Amico, Mikhail M. Ivanov, Leonardo Senatore, Marko Simonović, Masahiro Takada, Matias Zaldarriaga, and Pierre Zhang. Blinded challenge for precision cosmology with large-scale structure: results from effective field theory for the redshift-space galaxy power spectrum. *Phys. Rev. D*, 102(12):123541, 2020. doi: [10.1103/PhysRevD.102.123541](https://doi.org/10.1103/PhysRevD.102.123541).
- P. J. E. Peebles. *Principles of physical cosmology*. Princeton Series in Physics. Princeton University Press, Princeton, NJ, USA, 1993.
- Roger Penrose. *The road to reality : a complete guide to the laws of the universe*. Knopf, 2006.
- Oliver H. E. Philcox, Mikhail M. Ivanov, Marko Simonović, and Matias Zaldarriaga. Combining Full-Shape and BAO Analyses of Galaxy Power Spectra: A 1.6\% CMB-independent constraint on H_0 . *JCAP*, 05:032, 2020. doi: [10.1088/1475-7516/2020/05/032](https://doi.org/10.1088/1475-7516/2020/05/032).
- M. Pietroni. Structure formation beyond shell-crossing: nonperturbative expansions and late-time attractors. *J. Cosmology Astropart. Phys.*, 6:028, 2018. doi: [10.1088/1475-7516/2018/06/028](https://doi.org/10.1088/1475-7516/2018/06/028).
- Planck Collaboration, P. A. R. Ade, N. Aghanim, M. Arnaud, M. Ashdown, J. Aumont, C. Baccigalupi, A. J. Banday, R. B. Barreiro, J. G. Bartlett, and et al. Planck 2015 results. XIII. Cosmological parameters. *A&A*, 594:A13, 2016. doi: [10.1051/0004-6361/201525830](https://doi.org/10.1051/0004-6361/201525830).
- Planck Collaboration, N. Aghanim, Y. Akrami, F. Arroja, M. Ashdown, J. Aumont, C. Baccigalupi, M. Ballardini, A. J. Banday, R. B. Barreiro, N. Bartolo, S. Basak, R. Battye, K. Benabed, J. P. Bernard, M. Bersanelli, P. Bielewicz, J. J. Bock, J. R. Bond, J. Borrill, F. R. Bouchet, F. Boulanger, M. Bucher, C. Burigana, R. C. Butler, E. Calabrese, J. F. Cardoso, J. Carron, B. Casaponsa, A. Challinor, H. C. Chiang, L. P. L. Colombo, C. Combet, D. Contreras, B. P. Crill, F. Cuttaia, P. de Bernardis, G. de Zotti, J. Delabrouille, J. M. Delouis, F. X. Désert, E. Di Valentino, C. Dickinson, J. M. Diego, S. Donzelli, O. Doré, M. Douspis, A. Ducout, X. Dupac, G. Efstathiou, F. Elsner, T. A. Enßlin, H. K. Eriksen, E. Falgarone, Y. Fantaye, J. Fergusson, R. Fernandez-Cobos, F. Finelli, F. Forastieri, M. Frailis, E. Franceschi, A. Frolov, S. Galeotta, S. Galli, K. Ganga, R. T.

Génova-Santos, M. Gerbino, T. Ghosh, J. González-Nuevo, K. M. Górski, S. Gratton, A. Gruppuso, J. E. Gudmundsson, J. Hamann, W. Handley, F. K. Hansen, G. Helou, D. Herranz, S. R. Hildebrandt, E. Hivon, Z. Huang, A. H. Jaffe, W. C. Jones, A. Karakci, E. Keihänen, R. Keskitalo, K. Kiiveri, J. Kim, T. S. Kisner, L. Knox, N. Krachmalnicoff, M. Kunz, H. Kurki-Suonio, G. Lagache, J. M. Lamarre, M. Langer, A. Lasenby, M. Lattanzi, C. R. Lawrence, M. Le Jeune, J. P. Leahy, J. Lesgourgues, F. Levrier, A. Lewis, M. Liguori, P. B. Lilje, M. Lilley, V. Lindholm, M. López-Caniego, P. M. Lubin, Y. Z. Ma, J. F. Macías-Pérez, G. Maggio, D. Maino, N. Mandolesi, A. Mangilli, A. Marcos-Caballero, M. Maris, P. G. Martin, M. Martinelli, E. Martínez-González, S. Matarrese, N. Mauri, J. D. McEwen, P. D. Meerburg, P. R. Meinhold, A. Melchiorri, A. Mennella, M. Migliaccio, M. Millea, S. Mitra, M. A. Miville-Deschénes, D. Molinari, A. Moneti, L. Montier, G. Morgante, A. Moss, S. Mottet, M. Münchmeyer, P. Natoli, H. U. Nørgaard-Nielsen, C. A. Oxborrow, L. Pagano, D. Paoletti, B. Partridge, G. Patanchon, T. J. Pearson, M. Peel, H. V. Peiris, F. Perrotta, V. Pettorino, F. Piacentini, L. Polastri, G. Polenta, J. L. Puget, J. P. Rachén, M. Reinecke, M. Remazeilles, C. Renault, A. Renzi, G. Rocha, C. Rosset, G. Roudier, J. A. Rubiño-Martín, B. Ruiz-Granados, L. Salvati, M. Sandri, M. Savelainen, D. Scott, E. P. S. Shellard, M. Shiraishi, C. Sirignano, G. Sirri, L. D. Spencer, R. Sunyaev, A. S. Suur-Uski, J. A. Tauber, D. Tavagnacco, M. Tenti, L. Terenzi, L. Toffolatti, M. Tomasi, T. Trombetti, J. Valiviita, B. Van Tent, L. Vibert, P. Vielva, F. Villa, N. Vittorio, B. D. Wandelt, I. K. Wehus, M. White, S. D. M. White, A. Zacchei, and A. Zonca. Planck 2018 results. I. Overview and the cosmological legacy of Planck. *A&A*, 641:A1, September 2020. doi: [10.1051/0004-6361/201833880](https://doi.org/10.1051/0004-6361/201833880).

H. C. Plummer. On the problem of distribution in globular star clusters. *MNRAS*, 71:460–470, March 1911. doi: [10.1093/mnras/71.5.460](https://doi.org/10.1093/mnras/71.5.460).

Gábor Rácz, István Szapudi, István Csabai, and László Dobos. Compactified cosmological simulations of the infinite universe. *MNRAS*, 477(2):1949–1957, June 2018. doi: [10.1093/mnras/sty695](https://doi.org/10.1093/mnras/sty695).

Cornelius Rampf. Cosmological Vlasov-Poisson equations for dark matter. *Reviews of Modern Plasma Physics*, 5(1):10, December 2021. doi: [10.1007/s41614-021-00055-z](https://doi.org/10.1007/s41614-021-00055-z).

Cornelius Rampf and Oliver Hahn. Shell-crossing in a Λ CDM Universe. *MNRAS*, 501(1):L71–L75, 2021. doi: [10.1093/mnrasl/slaa198](https://doi.org/10.1093/mnrasl/slaa198).

Cornelius Rampf and Yvonne Y. Y. Wong. Lagrangian perturbations and the matter bispectrum II: the resummed one-loop correction to the matter bispectrum. *JCAP*, 1206:018, 2012. doi: [10.1088/1475-7516/2012/06/018](https://doi.org/10.1088/1475-7516/2012/06/018).

Cornelius Rampf, Uriel Frisch, and Oliver Hahn. Unveiling the singular dynamics in the cosmic large-scale structure. *Mon. Not. Roy. Astron. Soc.*, 505(1):L90–L94, 2021a. doi: [10.1093/mnrasl/slabb053](https://doi.org/10.1093/mnrasl/slabb053).

Cornelius Rampf, Cora Uhlemann, and Oliver Hahn. Cosmological perturbations for two cold fluids in Λ CDM. *MNRAS*, 503(1):406–425, 2021b. doi: [10.1093/mnras/staa3605](https://doi.org/10.1093/mnras/staa3605).

S. O. Rice. Mathematical analysis of random noise. *Bell System Technical Journal*, 23(3):282–332, 1944. doi: <https://doi.org/10.1002/j.1538-7305.1944.tb00874>.

- x. URL <https://onlinelibrary.wiley.com/doi/abs/10.1002/j.1538-7305.1944.tb00874.x>.
- S. O. Rice. Mathematical analysis of random noise. *Bell System Technical Journal*, 24(1):46–156, 1945. doi: <https://doi.org/10.1002/j.1538-7305.1945.tb00453.x>.
x. URL <https://onlinelibrary.wiley.com/doi/abs/10.1002/j.1538-7305.1945.tb00453.x>.
- Konrad Rudnicki. *Cosmological Principles*, pages 169–175. Springer US, Boston, MA, 1993. ISBN 978-1-4899-1225-1. doi: [10.1007/978-1-4899-1225-1_11](https://doi.org/10.1007/978-1-4899-1225-1_11). URL https://doi.org/10.1007/978-1-4899-1225-1_11.
- Sergei Shandarin, Salman Habib, and Katrin Heitmann. Cosmic web, multistream flows, and tessellations. *Phys. Rev. D*, 85(8):083005, April 2012. doi: [10.1103/PhysRevD.85.083005](https://doi.org/10.1103/PhysRevD.85.083005).
- M. F. Skrutskie, R. M. Cutri, R. Stiening, M. D. Weinberg, S. Schneider, J. M. Carpenter, C. Beichman, R. Capps, T. Chester, J. Elias, J. Huchra, J. Liebert, C. Lonsdale, D. G. Monet, S. Price, P. Seitzer, T. Jarrett, J. D. Kirkpatrick, J. E. Gizis, E. Howard, T. Evans, J. Fowler, L. Fullmer, R. Hurt, R. Light, E. L. Kopan, K. A. Marsh, H. L. McCallon, R. Tam, S. Van Dyk, and S. Wheelock. The Two Micron All Sky Survey (2MASS). *AJ*, 131(2):1163–1183, February 2006. doi: [10.1086/498708](https://doi.org/10.1086/498708).
- Volker Springel, Naoki Yoshida, and Simon D. M. White. GADGET: a code for collisionless and gasdynamical cosmological simulations. *New A*, 6(2):79–117, April 2001. doi: [10.1016/S1384-1076\(01\)00042-2](https://doi.org/10.1016/S1384-1076(01)00042-2).arXiv.astro-ph/0003162.
- Volker Springel, Rüdiger Pakmor, Oliver Zier, and Martin Reinecke. Simulating cosmic structure formation with the GADGET-4 code. *MNRAS*, 506(2):2871–2949, September 2021. doi: [10.1093/mnras/stab1855](https://doi.org/10.1093/mnras/stab1855).arXiv.2010.03567.
- Norbert Straumann. *General Relativity*. Graduate Texts in Physics,. Springer Netherlands :, Dordrecht :, 2nd ed. 2013. edition, 2013. URL <http://dx.doi.org/10.1007/978-94-007-5410-2>.
- Jens Stüber, Oliver Hahn, Raul E. Angulo, and Simon D. M. White. Simulating the complexity of the dark matter sheet I: numerical algorithms. *MNRAS*, 495(4):4943–4964, July 2020. doi: [10.1093/mnras/staa1468](https://doi.org/10.1093/mnras/staa1468).
- Yasushi Suto and Misao Sasaki. Quasi nonlinear theory of cosmological selfgravitating systems. *Phys. Rev. Lett.*, 66:264–267, 1991. doi: [10.1103/PhysRevLett.66.264](https://doi.org/10.1103/PhysRevLett.66.264).
- Atsushi Taruya, Takahiro Nishimichi, and Donghui Jeong. Grid-based calculation for perturbation theory of large-scale structure. *Phys. Rev. D*, 98(10):103532, 2018. doi: [10.1103/PhysRevD.98.103532](https://doi.org/10.1103/PhysRevD.98.103532).
- Atsushi Taruya, Takahiro Nishimichi, and Donghui Jeong. Grid-based calculations of redshift-space matter fluctuations from perturbation theory: Uv sensitivity and convergence at the field level. *Phys. Rev. D*, 105:103507, May 2022. doi: [10.1103/PhysRevD.105.103507](https://doi.org/10.1103/PhysRevD.105.103507). URL <https://link.aps.org/doi/10.1103/PhysRevD.105.103507>.

-
- William P. Thurston. Three dimensional manifolds, Kleinian groups and hyperbolic geometry. *Bulletin (New Series) of the American Mathematical Society*, 6(3):357 – 381, 1982.
- H. Tomita. Curvature Invariants of Random Interface Generated by Gaussian Fields. *Progress of Theoretical Physics*, 76(4):952–955, 1986. doi: [10.1143/PTP.76.952](https://doi.org/10.1143/PTP.76.952).
- P. Valageas. Impact of shell crossing and scope of perturbative approaches, in real and redshift space. *A&A*, 526:A67, February 2011. doi: [10.1051/0004-6361/201015658](https://doi.org/10.1051/0004-6361/201015658).
- M. Vogelsberger, S. D. M. White, A. Helmi, and V. Springel. The fine-grained phase-space structure of cold dark matter haloes. *MNRAS*, 385:236–254, March 2008. doi: [10.1111/j.1365-2966.2007.12746.x](https://doi.org/10.1111/j.1365-2966.2007.12746.x).
- Mark Vogelsberger and Simon D. M. White. Streams and caustics: the fine-grained structure of Λ cold dark matter haloes. *MNRAS*, 413(2):1419–1438, May 2011. doi: [10.1111/j.1365-2966.2011.18224.x](https://doi.org/10.1111/j.1365-2966.2011.18224.x).
- Martin White. The Zel'dovich approximation. *MNRAS*, 439(4):3630–3640, April 2014. doi: [10.1093/mnras/stu209](https://doi.org/10.1093/mnras/stu209).

Index

- Λ CDM Universe, 91
 - , 86, 114
 - , 96
 - , 86
- 3-torus topology, 107
- adaptive softening, 163
- advection equation, 109
- Aliasing, 55
- all-order recursion relations, 100
- anthropic principle, 7
- antialiasing, 135
- Barnes & Hut tree, 151
- barocentric coordinates, 162
- Box-Muller method, 52
- Bravais lattice, 154
 - characteristic curve, 109
 - characteristic function, 46
 - Cholesky factorization, 53
 - Christoffel symbols, 15
 - closure condition, 41
 - Cloud-in-Cell (CIC), 129
 - co-frame, 12
 - co-moving distance, 30
 - co-tangent space, 12
 - comoving coordinates, 25
 - conditional probability, 45
 - conformal time, 34
 - conservation law, 23
 - constant curvature, 18
 - continuity equation, 87
 - contracted Bianchi identity, 23
 - convolution product, 42
 - convolution theorem, 42
 - coordinate basis, 12
 - coordinates
 - co-moving, 25
 - coordinates, comoving, 25
 - coordinates, physical, 25
 - cosmic microwave background, 8
 - cosmological principle, 7, 107
- cosmological redshift, 29
- covariance matrix, 47
- covariant derivative, 15
- critical density of the Universe, 28
- critical point, 67
- cumulant expansion theorem, 75, 77, 98
- cumulants, 75, 84
- decaying-mode, 92
- deceleration parameter, 29
- density field, 162
- density parameter, 29
- Dirac- δ , 42
- discreteness errors, 113, 153
- domain decomposition, 148
- dual basis, 12
- effective field theory of cosmic large-scale structure (EFTofLSS), 101
- Einstein tensor, 23
- Einstein's biggest blunder, 25
- Einstein-de Sitter (EdS) universe, 90
- Einstein-Hilbert action, 23
- energy-momentum tensor, 23
- equation of state, 31
- Euler equation, 87
- event horizon, 35
- excursion set, 71
- expectation value, 46
- extended phase space, 116
- Fast Fourier Transform (FFT), 126
- fast multipole method (FMM), 151
- FLRW metric, 24
- FLRW space-time, 8
- fluid limit, 154
- force softening, 113
- Fourier space, 40
- Fourier transform, 40
- Friedmann equation, 26, 31
- friends-of-friends (FOF), 166
- galaxies, 10
- Gauss-Bonnet theorem, 74

-
- Gaussian, 47
 Gaussian filter, 59
 Gaussian random field, 48, 51
 geodesic, 16
 Gibbs phenomenon, 135
 Green's function, 113, 152
 grid spacing, 54
 growing-mode, 92
 growth factor, 153
- Hessian, 67
 hierarchical structure formation, 121
 homogeneous and isotropic, 49
 Hubble
 constant, 27
 dimensionless parameter, 27
 parameter, 26
 radius, 29, 35
 hyperspherical coordinates, 20
- inertial motion, 36
 integral geometry, 71
 Inverse Fourier transform, 43
 inverse of the metric tensor, 13
 Isserlis' theorem, 50
- Jeans scale, 90
 just in time (JIT) compilation, 132
- Karhunen-Loëve decomposition, 53
 kernel bandwidth, 163
 kinetic moments, 83
 Kolmogorov consistency, 48
 Kronecker-delta, 88
- Lagrangian coordinate, 111
 Lagrangian map, 94
 Lagrangian submanifold, 155
 leapfrog integrator, 116
 level set, 71
 light-cone, 22
 lightcone, 25
 load balancing, 148
 Lorentzian manifold, 14, 21
 Lyapunov exponents, 156
- manifold
 pseudo-Riemannian, 13
 Riemannian, 13
- Marcinkiewicz' theorem, 48
 marginal of the phase-space distribution, 80
- marginals, 83
 matter power spectrum, 101
 maximally symmetric, 24
 maximum of a GRF, 67
 metric
 signature, 21
 tensor, 13
 minimum of a GRF, 67
 Minkowski functionals, 71
 modified gravity, 24
 moment generating function, 46
 moments, 75
 moments of the distribution, 46
 multi-streaming, 80
 multi-streaming regime, 95
 multiply connected, 12
- N-body distribution function, 113, 151, 162
 Nearest-Grid-Point (NGP), 129
 Noether's theorem, 116
 non-uniform fast Fourier transform (NUFFT), 140
 normal coordinates, 14, 18
 null-geodesic, 23
 Nyquist frequency, 55
 Nyquist mode, 127, 133
- object-oriented programming, 145
- parallel transport, 16
 particle linear theory (PLT), 154
 particle-in-cell (PIC) method, 126
 particle-mesh (PM) method, 126
 peculiar distribution function, 86
 peculiar fluid equations, 88
 peculiar Vlasov–Poisson equations, 86
 periodic boundary conditions, 107
 phase mixing, 82
 physical coordinates, 25
 physical distribution function, 79
 physical Vlasov–Poisson equations, 80
 Plummer profile, 152
 Poisson noise, 133
 Poisson summation formula, 125
 probability density, 45, 47
- random field, 39
 recombination, 8
 reduced circumference polar coordinates, 19
 Ricci

scalar, 18
tensor, 18
Riemann tensor, 17, 18
Riemannian manifold, 14

saddle-point of a GRF, 67
scale factor, 25
secondary infall, 158
sectional curvatures, 18
shell-crossing, 95
signature, 14
simple cubic lattice, 154
simply connected, 12
smoothing kernel, 59
softened distribution function, 152
space-time, 21
spatial section, 12
special relativity, 21
spectral moments, 61
standard perturbation theory (SPT), 100,
 101
stochastic process, 39
Subhalos, 158
substructures, 121
superconformal time, 115

tangent space, 12
Taylor series, 67
tensor, 12
top-hat filter, 60
translation invariance, 41

UV cutoff, 60

variance, 59
velocity, 25
velocity dispersion tensor, 84
velocity divergence, 99
Vlasov hierarchy, 83
vorticity, 91

Wick's theorem, 50
Wiener-Khinchin theorem, 45

Zel'dovich map, 94
Zel'dovich solution, 96